

The Pennsylvania State University
The Graduate School
College of Earth and Mineral Sciences

**DEVELOPMENT OF A KNOWLEDGE BASE OF Ti-ALLOYS
FROM FIRST-PRINCIPLES AND COMPUTATIONAL
THERMODYNAMICS**

A Dissertation in
Materials Science and Engineering
by
Cassie Marker

© 2017 Cassie Marker

Submitted in Partial Fulfillment
of the Requirements
for the Degree of

Doctor of Philosophy

August 2017

The dissertation of Cassie Marker was reviewed and approved* by the following:

Zi-Kui Liu

Professor of Materials Science and Engineering

Thesis Advisor, Chair of Committee

Allison Beese

Assistant Professor of Materials Science and Engineering

Kristen Fichthorn

Merrell Fenskey Professor of Chemical Engineering and Professor of Physics

Michael Manley

Senior Researcher, Oak Ridge National Laboratory, Materials Science & Technology Division

Special Member

Susan Sinnott

Department Head and Professor of Materials Science and Engineering

*Signatures are on file in the Graduate School.

Abstract

An aging population with an active lifestyle requires the development of better load-bearing implants, which have high levels of biocompatibility and a low elastic modulus. Titanium alloys, in the body centered cubic phase, are great implant candidates, due to their mechanical properties and biocompatibility. The present work aims at investigating the thermodynamic and elastic properties of bcc Ti-alloys, using the integrated first-principles based on Density Functional Theory (DFT) and the CALculation of PHase Diagrams (CALPHAD) method. The use of integrated first-principles based on DFT and CALPHAD modeling has greatly reduced the need for trial and error metallurgy, which is ineffective and costly. The phase stability of Ti-alloys has been shown to greatly affect their elastic properties. Traditionally, CALPHAD modeling has been used to predict the equilibrium phase formation, but in the case of Ti-alloys, predicting the formation of two metastable phases ω and α'' is of great importance as these phases also drastically effect the elastic properties. To build a knowledge base of Ti-alloys, for biomedical load-bearing implants, the Ti-Mo-Nb-Sn-Ta-Zr system is studied because of the biocompatibility and the bcc stabilizing effects of some of the elements.

With the focus on bcc Ti-rich alloys, a database of thermodynamic descriptions of each phase for the pure elements, binary and Ti-rich ternary alloys is developed in the present work. Previous thermodynamic descriptions for the pure elements are adopted from the widely used SGTE database for global compatibility. The previous binary and ternary models from the literature are evaluated for accuracy and new thermodynamic descriptions are applied when necessary. The models are evaluated using available experimental data, as well as the enthalpy of formation of the bcc phase calculated from first-principles based on DFT. The thermodynamic descriptions are combined into a database ensuring that the sublattice models are compatible with each other.

For subsystems, such as the Sn-Ta system, where no thermodynamic description had been evaluated and minimal experimental data was available, first-principles based on DFT is used. The Sn-Ta system has two intermetallic phases, TaSn_2 and Ta_3Sn , with five solution phases: liquid, bcc, hexagonal close packed (hcp), body centered tetragonal (bct) and diamond. First-principles calculations are done on the intermetallic and solution phases. Special quasirandom structures (SQS) are used to obtain information about the solution phases across the entire composition range. The Debye-Grüneisen approach, as well as the quasiharmonic phonon method are used to obtain the finite-temperature data. Results from first-principles calculations and experiments are used to complete the thermodynamic description. The resulting phase diagram reproduced the first-principles calculations and experimental data accurately.

In order to determine the effect of alloying on the elastic properties, first-principles based on DFT are systematically done on the pure elements, five Ti-X binary systems and Ti-X-Y ternary systems ($X \neq Y = \text{Mo, Nb, Sn, Ta, Zr}$) in the bcc phase. The first-principles calculations predict the single crystal elastic stiffness constants c_{ij} 's. Correspondingly, the polycrystalline aggregate properties are also estimated from the c_{ij} 's, including bulk modulus B , shear modulus G and Young's modulus E . The calculated results show good agreement with experimental results. The CALPHAD method is then adapted to assist in the database development of the elastic properties as a function of composition. On average, the database predicts the elastic properties of higher order Ti-alloys within 5 GPa of the experimental results.

Finally, the metastable phase formation, ω and α'' is studied in the Ti-Ta and Ti-Nb systems. The formation energy of these phases, calculated from first-principles at 0 °K, shows that these phases must be stabilized by entropy. A new theoretic framework is introduced that allows the prediction of the increase in entropy due to the competition between the metastable and stable phase. Using this approach, the phase fraction of the phases are predicted for the Ti-Nb system. The predicted phase fractions are used to calculate the mixed force constants to obtain the phonon density of states. Results from inelastic neutron scattering experiments are compared to the predicted phase fractions and phonon density of states for accuracy. Then the predicted phase fractions are used to calculate the elastic properties using the rule of mixtures. The predicted elastic properties are compared with available experimental data.

This thesis provides a knowledge base of the thermodynamic and elastic properties of Ti-alloys from computational thermodynamics. The databases created will impact research focused on Ti-alloys and specifically efforts focused on Ti-alloys for biomedical applications.

Table of Contents

List of Figures	x
List of Tables	xviii
Acknowledgments	xxii
Chapter 1	
Introduction	1
1.1 Motivation	1
1.2 Overview	2
1.2.1 Equilibrium Phases	2
1.2.2 Elastic Properties	3
1.2.3 Metastable Phases	3
Chapter 2	
Methodology	11
2.1 First-Principles Calculations	11
2.1.1 Density Functional Theory at 0 °K	13
2.1.2 Finite-temperature thermodynamics	14
2.1.3 Elastic stiffness calculations	16
2.1.4 Special quasirandom structures (SQS)	17
2.1.5 High-throughput partition function	18
2.1.6 First-principles calculation error	19
2.2 CALPHAD method	19
2.2.1 Solution phases	20
2.2.2 Stoichiometric compounds	21
2.2.3 Elastic Properties	21
2.3 Experimental	22
2.3.1 Ti-Nb sample preparation	22
2.3.2 Neutron Scattering	23

2.3.2.1	ARCS	23
2.3.2.2	Data Analysis	23
Chapter 3		
	Ti-Mo-Nb-Sn-Ta-Zr Thermodynamic Database	27
3.1	Introduction	27
3.2	Computational details	28
3.3	Binary systems	28
3.3.1	Ti-Mo	29
3.3.2	Ti-Nb	30
3.3.3	Ti-Ta	30
3.3.4	Ti-Zr	31
3.3.5	Non Ti-containing binaries	31
3.4	Ti-containing ternary sections	33
3.4.1	Ti-Mo-Nb	33
3.4.2	Ti-Mo-Ta	34
3.4.3	Ti-Mo-Zr	35
3.4.4	Ti-Nb-Ta	35
3.4.5	Ti-Nb-Zr	36
3.4.6	Ti-Ta-Zr	37
3.5	Conclusion	37
Chapter 4		
	First-principles aided thermodynamic modeling of the Sn-Ta system	61
4.1	Introduction	61
4.2	Literature Review	62
4.3	Modeling and Calculations	63
4.3.1	First-principles details	63
4.3.2	CALPHAD	64
4.4	Results and discussion	64
4.4.1	First-principles	64
4.4.2	CALPHAD	66
4.5	Conclusion	68
Chapter 5		
	Effects of alloying elements on the elastic properties of bcc Ti-X alloys	84
5.1	Introduction	84
5.2	Modeling and Calculations	85

5.2.1	Calculation details	85
5.2.2	Modeling details	85
5.3	Results and discussion	86
5.3.1	Evaluation of calculation settings	86
5.3.2	Calculations of the Ti-X elastic properties	86
5.3.3	Extrapolation to ternary and higher ordered systems	90
5.4	Conclusion	91

Chapter 6

Effects of alloying elements on the elastic properties of bcc ternary and higher ordered Ti-alloys 108

6.1	Introduction	108
6.2	Modeling and Calculations	109
6.2.1	Calculation details	109
6.2.2	Modeling details	109
6.3	Results and discussion	110
6.3.1	Elastic calculation results	110
6.3.2	Extrapolation to higher ordered systems	113
6.4	Conclusion	114

Chapter 7

Phase stability and elastic properties study of the Ti-Ta and Ti-Nb systems 137

7.1	Introduction	137
7.2	Modeling and Calculations	138
7.2.1	Computational details	138
7.2.2	Modeling details	138
7.3	Results and discussion	139
7.3.1	First-principles calculations at 0 K	139
7.3.2	Elastic properties	139
7.3.3	Neutron scattering results	140
7.3.3.1	Phonon density of states at 300 K	140
7.3.3.2	Diffraction patterns at 300 K	140
7.3.3.3	Temperature dependent phonon density of states .	140
7.3.3.4	Temperature dependent diffraction patterns . . .	140
7.3.4	Partition function approach results	140
7.3.4.1	Phase fractions	140
7.3.4.2	Mixed force constants	140
7.3.5	Comparison of elastic properties	140
7.4	Conclusion	140

Chapter 8	
Conclusions and Future Work	151
8.1 Conclusions	151
8.2 Future Work	151
Appendix A	
Ti-Mo-Nb-Ta-Zr Database	152
Appendix B	
Sn-Ta Database	169
Appendix C	
Mathematica	
Interaction Parameter Fitting	177
Appendix D	
Ti Elastic Database	179
Appendix E	
Pycalphad script	186
Bibliography	196

List of Figures

1.1	Comparison of first-principles calculations [1, 2] and experimental measurements of the Young's modulus of Ti-Ta alloys [3–5]. The purple box refers to the composition range when the calculations and experimentally determined E do not match up due to the formation of two metastable phases ω and α''	9
1.2	Comparison of the present first-principles calculations and experimental measurements of the Young's modulus of Ti-Nb alloys [6–10]. The purple box refers to the composition range when the calculations and experimentally determined E do not match up due to the formation of two metastable phases ω and α''	10
2.1	Elastic stiffness constants of the bcc Ti-Ta binary system calculated with the GGA and PBE exchange correction functions, respectively.	26
3.1	Figure a on the left plots the previously modeled thermodynamic description of the Ti-Mo system versus available experimental data to ensure accuracy [11,12]. Figure b on the right plots the enthalpy of formation of the bcc phase predicted by the previous thermodynamic modeling (solid line) at 300 K versus the present first-principles calculations (circles) at 0 K.	47
3.2	Figure a on the left plots the previously modeled thermodynamic description of the Ti-Nb system versus available experimental data to ensure accuracy [13,14]. Figure b on the right plots the enthalpy of formation of the bcc phase predicted by the previous thermodynamic modeling (solid line) at 300 K versus the present first-principles calculations (circles) at 0 K.	48

3.3	Figure a on the left plots the previously modeled thermodynamic description of the Ti-Ta system versus available experimental data to ensure accuracy [11, 15]. Figure b on the right plots the enthalpy of formation of the bcc phase predicted by the previous thermodynamic modeling (solid line) at 300 K versus the present first-principles calculations (circles) at 0 K.	49
3.4	Figure a on the left plots the previously modeled thermodynamic description of the Ti-Zr system versus available experimental data to ensure accuracy [16]. Figure b on the right plots the enthalpy of formation of the bcc phase predicted by the previous thermodynamic modeling (solid line) at 300 K versus the present first-principles calculations (circles) at 0 K.	50
3.5	The previously modeled thermodynamic descriptions of the Mo-Nb (a) [17], Mo-Ta (b) [17] and Nb-Ta (c) [17] binary systems are evaluated by comparing with available phase boundary experimental data.	51
3.6	The previously modeled thermodynamic descriptions of the Mo-Zr [18], Nb-Zr [19,20] and Ta-Zr [21] binary systems are evaluated for accuracy by comparing the available experimental phase boundary data.	52
3.7	Figure a) on the left is a binary interpolation of the isothermal section of Ti-Mo-Nb plotted at 873 K. Figure b) plots the present calculations (circles) and binary interpolation (solid black line) of the enthalpy of formation of the bcc phase.	53
3.8	Figure a) on the left is a binary interpolation of the isothermal section of Ti-Mo-Ta plotted at 873 K. Figure b) plots the present calculations (circles), binary interpolation (solid black line) and ternary assessed (red dotted line) enthalpy of formation of the bcc phase.	54
3.9	Figure a) on the left is the isothermal plot of Ti-Mo-Ta at 873 K after evaluation of the ternary interaction parameters. Figure b) on the right is zoomed in to show the comparison with the experimental data [22].	55
3.10	Figure a) on the left is a binary interpolation of the isothermal section of Ti-Mo-Zr plotted at 1273 K with experimental phase data obtained at the same temperature [23,24]. Figure b) plots the present calculations (circles) and binary interpolation (solid black line) of the enthalpy of formation of the bcc phase.	56

3.11	Figure a) on the top left is a binary interpolation of the isothermal section of Ti-Nb-Ta plotted at 673 K. Figure b) is a binary interpolation of the isothermal section of Ti-Nb-Ta at 823 K. Both binary interpolations are compared with experimental phase boundary data [25]. Figure c) plots the present calculations (circles), binary interpolation (solid black line) and ternary assessed (red dotted line) enthalpy of formation of the bcc phase.	57
3.12	Figure a) on the left is the isothermal plot of Ti-Nb-Ta at 673 K after evaluation of the ternary interaction parameters. Figure b) is the evaluated isothermal plot of Ti-Nb-Ta at 823 K. Both plots have experimental phase boundary data [25].	58
3.13	Figure a) on the left is a binary interpolation of the isothermal section of Ti-Nb-Zr plotted at 843 K with experimental phase data [26]. Figure b) plots the present calculations (circles) and binary interpolation (solid black line) of the enthalpy of formation of the bcc phase.	59
3.14	Figure a) on the top left is a binary interpolation of the isothermal section of Ti-Ta-Zr plotted at 1273 K. Figure b) is a binary interpolation of the isothermal section of Ti-Ta-Zr at 1773 K. Both binary interpolations are compared with experimental data [27, 28]. Figure c) plots the present calculations (circles) and binary interpolation (solid black line) for the enthalpy of formation of the bcc phase.	60
4.1	Calculated phonon dispersion curve of bcc-Ta, compared with neutron diffraction experiments (\circ) [29] along with the phonon DOS.	73
4.2	Calculated phonon dispersion curve of bct-Sn on the left and phonon DOS on the right. The open squares (\square) are the LO and TO modes from Raman [30] and the filled squares the theoretical prediction of the LO and TO modes at the M point [30].	74
4.3	Calculated phonon dispersion curve for TaSn ₂ at 0 °K and the phonon DOS.	75
4.4	Calculated phonon dispersion curve of Ta ₃ Sn at 0 °K on the left and the phonon DOS on the right.	76
4.5	Comparison of the enthalpy and entropy of bcc-Ta from the Debye model (solid line) and the quasiharmonic phonon calculations (red dotted line) to the SGTE data (blue dashed line) [31].	77
4.6	Comparison of the Gibbs energy of bct-Sn from the Debye model (solid line) and the quasiharmonic phonon calculations (red dotted line) to the SGTE data (blue dashed line) [31].	78

4.7	Heat capacity, enthalpy and entropy of TaSn ₂ using the Debye model (solid line) and the quasiharmonic phonon calculation (red dotted line) from first-principles calculations, compared with those from the current CALPHAD modeling (blue dashed line).	79
4.8	Heat capacity, enthalpy and entropy of Ta ₃ Sn using the Debye model (solid line) and the quasiharmonic phonon calculation (red dotted line) compared with those from the current CALPHAD modeling (blue dashed line).	80
4.9	Heat capacity, enthalpy and entropy of Ta ₃ Sn using the Debye model (solid line) and the quasiharmonic phonon calculation (red dotted line) compared with those from the current CALPHAD modeling (blue dashed line).	81
4.10	Calculated Sn-Ta phase diagram using the present thermodynamic description.	82
4.11	Enthalpy of mixing of the liquid phase as a function of composition at 298 °K and ambient pressure in the Sn-Ta system.	83
5.1	Elastic stiffness constants for the bcc Ti-Mo binary system calculated with strains, 0.01, 0.03 and 0.07, respectively, showing comparable results.	98
5.2	Young's modulus E of the Ti-X binary systems. The present calculations are plotted as the filled circles with the error bars. The dotted purple line is the Voigt upper Young's modulus bound, the gold dot dashed line is the lower Reuss Young's modulus bound and the black line is the Hill Young's modulus average. The experimental values [1–5, 7, 8, 32–34] are also included for comparison.	99
5.3	Young's modulus calculated from the model parameters (see ??) and Eq. Y as a function of composition from bcc Ti to bcc X.	100
5.4	Calculated \bar{C}_{11} values (circles) plotted with their errors as well as the pure element extrapolation (red dashed line) and the present modeling (black dashed line) for five Ti-X binary systems (X = Mo, Nb, Ta, Sn, Zr). Ti-Mo, Ti-Nb, and Ti-Ta alloys are compared with previous calculations from Ikehata et al. [2].	101
5.5	Calculated \bar{C}_{12} values (circles) plotted with their errors as well as the pure element extrapolation (red dashed line) and the present modeling (black dashed line) for five Ti-X binary systems (X = Mo, Nb, Ta, Sn, Zr). Ti-Mo, Ti-Nb, and Ti-Ta alloys are compared with previous calculations from Ikehata et al. [2].	102

5.6	Calculated \bar{C}_{44} values (circles) plotted with their errors as well as the pure element extrapolation (red dashed line) and the present modeling (black dashed line) for five Ti-X binary systems (X = Mo, Nb, Ta, Sn, Zr). Ti-Mo, Ti-Nb, and Ti-Ta alloys are compared with previous calculations from Ikehata et al. [2].	103
5.7	Calculated \bar{C}_{11} - \bar{C}_{12} values (circles) plotted with the present modeling (solid lines) for five Ti-X binary systems (X = Mo, Nb, Ta, Sn, Zr). The C11-C12 shows the stability of the bcc phase. When the \bar{C}_{11} - \bar{C}_{12} value is negative the bcc phase is not stable in the corresponding compositions range.	104
5.8	Bulk modulus B of the Ti-X binary systems. The present calculations are plotted as the filled circles with the error bars. The dotted purple line is the Voigt upper bulk modulus bound, the gold dot dashed line is the lower Reuss bulk modulus bound and the black line is the Hill bulk modulus average.	105
5.9	Shear modulus G of the Ti-X binary systems. The present calculations are plotted as the filled circles with the error bars. The dotted purple line is the Voigt upper shear modulus bound, the gold dot dashed line is the lower Reuss shear modulus bound and the black line is the Hill shear modulus average.	106
5.10	Young's modulus values of multicomponent bcc Ti alloys measured experimentally plotted against the predicted Young's modulus from the pure elements and binary interaction parameters with the black diagonal line showing the exact correlation between the experimental and calculated values. Error bars in the experiments and the bounds from Reuss and Voigt approximations are plotted as vertical and horizontal lines, respectively. The variance in the first calculations from Eq. Y-Eq. Y was averaged and plotted as the grey region to show the variance in the first-principles calculations. More information on the alloys is in Table ?? [35–37]	107
6.1	Young's modulus E of five of the Ti-X-Y ternary systems are plotted from a 50-50 mixture of the alloying elements to Ti in the bcc phase. The present calculations are plotted as filled circles with the error bars. The red dotted line is the extrapolation for the pure elements and binary interaction parameters only. The dotted purple line is the Voigt upper YoungâŽs modulus bound, the gold dot dashed line is the lower Reuss YoungâŽs modulus bound and the black line is the Hill YoungâŽs modulus average. Experimental values are include for comparison [36–39].	121

6.2	Young's modulus E of five of the Ti-X-Y ternary systems are plotted from a 50-50 mixture of the alloying elements to Ti in the bcc phase. The present calculations are plotted as filled circles with the error bars. The red dotted line is the extrapolation for the pure elements and binary interaction parameters only. The dotted purple line is the Voigt upper YoungâŽs modulus bound, the gold dot dashed line is the lower Reuss YoungâŽs modulus bound and the black line is the Hill YoungâŽs modulus average. Experimental values are include for comparison [36–39].	122
6.3	Calculated \bar{C}_{11} values (circles) plotted with their errors as well as the interpolation from the binary interaction parameters (red dashed line) and the ternary fitting (black dashed line) for five of the Ti-X-Y binary systems from a 50-50 mixture of the alloying elements X and Y to Ti ($X \neq Y = Mo, Nb, Ta, Sn, Zr$).	123
6.4	Calculated \bar{C}_{11} values (circles) plotted with their errors as well as the interpolation from the binary interaction parameters (red dashed line) and the ternary fitting (black dashed line) for five of the Ti-X-Y binary systems from a 50-50 mixture of the alloying elements X and Y to Ti ($X \neq Y = Mo, Nb, Ta, Sn, Zr$).	124
6.5	Calculated \bar{C}_{12} values (circles) plotted with their errors as well as the interpolation from the binary interaction parameters (red dashed line) and the ternary fitting (black dashed line) for five of the Ti-X-Y binary systems from a 50-50 mixture of the alloying elements X and Y to Ti ($X \neq Y = Mo, Nb, Ta, Sn, Zr$).	125
6.6	Calculated \bar{C}_{12} values (circles) plotted with their errors as well as the interpolation from the binary interaction parameters (red dashed line) and the ternary fitting (black dashed line) for five of the Ti-X-Y binary systems from a 50-50 mixture of the alloying elements X and Y to Ti ($X \neq Y = Mo, Nb, Ta, Sn, Zr$).	126
6.7	Calculated \bar{C}_{44} values (circles) plotted with their errors as well as the interpolation from the binary interaction parameters (red dashed line) and the ternary fitting (black dashed line) for five of the Ti-X-Y binary systems from a 50-50 mixture of the alloying elements X and Y to Ti ($X \neq Y = Mo, Nb, Ta, Sn, Zr$).	127
6.8	Calculated \bar{C}_{44} values (circles) plotted with their errors as well as the interpolation from the binary interaction parameters (red dashed line) and the ternary fitting (black dashed line) for five of the Ti-X-Y binary systems from a 50-50 mixture of the alloying elements X and Y to Ti ($X \neq Y = Mo, Nb, Ta, Sn, Zr$).	128

6.9	Calculated \overline{C}_{11} - \overline{C}_{12} values (circles) plotted with the present modeling (solid lines) for the Ti-X-Y ternary systems ($X \neq Y = Mo, Nb, Ta, Sn, Zr$). The \overline{C}_{11} - \overline{C}_{12} shows the stability of the bcc phase, when the value is negative the bcc phase is not stable in the corresponding composition ranges.	129
6.10	Bulk modulus B calculations of five of the Ti-X-Y ternary systems ($X \neq Y = Mo, Nb, Ta, Sn, Zr$). The present calculations are plotted as the filled circles with error bars as well as the interpolation from the binary interaction parameters (red dashed line). The dotted purple line is the Voigt upper bulk modulus bound, the gold dashed line is the lower Reuss bulk modulus bound and the black line is the Hill bulk modulus average plotted from a 50-50 mixture of the alloying elements X and Y to Ti.	130
6.11	Bulk modulus B calculations of five of the Ti-X-Y ternary systems ($X \neq Y = Mo, Nb, Ta, Sn, Zr$). The present calculations are plotted as the filled circles with error bars as well as the interpolation from the binary interaction parameters (red dashed line). The dotted purple line is the Voigt upper bulk modulus bound, the gold dashed line is the lower Reuss bulk modulus bound and the black line is the Hill bulk modulus average plotted from a 50-50 mixture of the alloying elements X and Y to Ti.	131
6.12	Shear modulus G calculations of five of the Ti-X-Y ternary systems ($X \neq Y = Mo, Nb, Ta, Sn, Zr$). The present calculations are plotted as the filled circles with error bars as well as the interpolation from the binary interaction parameters (red dashed line). The dotted purple line is the Voigt upper shear modulus bound, the gold dashed line is the lower Reuss shear modulus bound and the black line is the Hill shear modulus average plotted from a 50-50 mixture of the alloying elements X and Y to Ti.	132
6.13	Shear modulus G calculations of five of the Ti-X-Y ternary systems ($X \neq Y = Mo, Nb, Ta, Sn, Zr$). The present calculations are plotted as the filled circles with error bars as well as the interpolation from the binary interaction parameters (red dashed line). The dotted purple line is the Voigt upper shear modulus bound, the gold dashed line is the lower Reuss shear modulus bound and the black line is the Hill shear modulus average plotted from a 50-50 mixture of the alloying elements X and Y to Ti.	133
6.14	The Young's modulus is mapped as a function of composition in GPa for the Ti-Mo-Nb, Ti-Mo-Sn, Ti-Mo-Ta, Ti-Mo-Zr and Ti-Nb-Sn alloy systems using pycalphad [40].	134

6.15	The Young's modulus is mapped as a function of composition in GPa for the Ti-Mo-Nb, Ti-Mo-Sn, Ti-Mo-Ta, Ti-Mo-Zr and Ti-Nb-Sn alloy systems using pycalphad [40].	135
6.16	<i>E</i> of multicomponent bcc Ti alloys predicted from the completed database are compared with measured experimental results. Error bars plotted are from the variation in experimentally determined YoungâŽ's modulus values for the specific multi-component alloy. The grey region refers to the error in the first-principles calculations. More information on the alloys is Table 6.3 [35-37].	136
7.1	The relative energy of the bcc, hcp, ω , α'' phases in the Ti-Nb system are plotted from 100 at. % Ti to 100 at. % Nb.	144
7.2	The relative energy of the bcc, hcp, ω , α'' phases in the Ti-Ta system are plotted from 100 at. % Ti to 100 at. % Ta.	145
7.3	The elastic properites of the bcc, hcp, ω , α'' phases in the Ti-Nb system calculated from first-principles based on DFT are plotted as symbols. The CALPHAD fitting are plotted as the dashed lines. The figure is plotted from 100 at. % Ti to 100 at. % Nb.	146
7.4	The phonon density of states is plotted for the TiNb alloy at 20 at. % Nb. The dashed line represents the slow cooled sample while the solid line represents the quenched sample.	147
7.5	The phonon density of states is plotted for the TiNb alloy at 18 at. % Nb. The dashed line represents the slow cooled sample while the solid line represents the quenched sample.	148
7.6	The phonon density of states is plotted for the TiNb alloy at 12 at. % Nb. The dashed line represents the slow cooled sample while the solid line represents the quenched sample.	149
7.7	The phonon density of states is plotted for the TiNb alloy at 10 at. % Nb. The dashed line represents the slow cooled sample while the solid line represents the quenched sample.	150
C.1	178

List of Tables

1.1	Young's modulus of common implant materials compared with the Young's modulus of bone [41].	8
3.1	Bulk modulus B and enthalpy are listed for each pure element in their SER phase listed. The sv and pv refer to the electrons chosen as valance according to the VASP recommendations. The results are compared with available experimental data.	39
3.2	First-principles calculations of the enthalpy of formation of the bcc phase in kJ/mol-atom for different atomic percent compositions of the Ti-X binary systems at 0 K.	40
3.2	First-principles calculations of the enthalpy of formation of the bcc phase in kJ/mol-atom for different atomic percent compositions of the Ti-X binary systems at 0 K.	41
3.3	Thermodynamic parameters for the Ti-Mo-Nb-Ta-Zr system. The thermodynamic description of the pure elements is not included. The pure elements were adopted from the SGTE database and are listed in the supplementary tdb file [41].	42
3.3	Thermodynamic parameters for the Ti-Mo-Nb-Ta-Zr system. The thermodynamic description of the pure elements is not included. The pure elements were adopted from the SGTE database and are listed in the supplementary tdb file [41].	43
3.3	Thermodynamic parameters for the Ti-Mo-Nb-Ta-Zr system. The thermodynamic description of the pure elements is not included. The pure elements were adopted from the SGTE database and are listed in the supplementary tdb file [41].	44
3.3	Thermodynamic parameters for the Ti-Mo-Nb-Ta-Zr system. The thermodynamic description of the pure elements is not included. The pure elements were adopted from the SGTE database and are listed in the supplementary tdb file [41].	45

3.3	Thermodynamic parameters for the Ti-Mo-Nb-Ta-Zr system. The thermodynamic description of the pure elements is not included. The pure elements were adopted from the SGTE database and are listed in the supplementary tdb file [41].	46
4.1	Lattice parameters from first-principles calculations compared with experimental values.	69
4.2	Equilibrium volume V_0 , bulk modulus B_{EOS} , and the first derivative of bulk modulus with respect to pressure B'_{EOS} , from fitted equilibrium properties from the EOS at 0 °K compared to experimental work and previous DFT studies.	70
4.3	Elastic stiffness constants and elastic properties predicted using the Hill approach and the scaling factors used in the Debye model, calculated from the Poisson ratio, see Eq. 2.11. To ensure the accuracy of the calculated scaling factor, the bulk modulus (B) calculated from the elastic constants was compared to the B_{EOS} calculated from the EOS fitting Eq. 2.6.	71
4.4	Modeled parameters in SI units in the present work for the phases in the Sn-Ta binary system. These parameters were incorporated with the SGTE data for the pure elements [31].	72
5.1	Calculated pure element elastic stiffness constants and the bulk modulus B (in GPa) by X-C functional of PBE are compared with the previous first-principles calculations (FP) by X-C functional PW91 and experiments (Expt). Sv, pv and d refereeing to the s, p, and d states being treated as valance, respectively.	92
5.2	Evaluated interaction parameters L_0 and L_1 using the R-K polynomial Eq. Y for the elastic stiffness constants for the Ti-X binary systems.	93
5.3	First-principles calculations of the elastic stiffness constants, bulk modulus B , shear modulus G , and Young's modulus E in GPa for different atomic percent compositions of the bcc Ti-X binary systems at 0 °K. As well as experimental data for the Young's modulus obtained at 300 °K by the reference stated.	94
5.3	First-principles calculations of the elastic stiffness constants, bulk modulus B , shear modulus G , and Young's modulus E in GPa for different atomic percent compositions of the bcc Ti-X binary systems at 0 °K. As well as experimental data for the Young's modulus obtained at 300 °K by the reference stated.	95

5.3	First-principles calculations of the elastic stiffness constants, bulk modulus B , shear modulus G , and Young's modulus E in GPa for different atomic percent compositions of the bcc Ti-X binary systems at 0 °K. As well as experimental data for the Young's modulus obtained at 300 °K by the reference stated.	96
5.4	Predicted Young's modulus (in GPa) of higher order alloys in the bcc phase compared to experimental values found with both the weight percent and atomic percent listed. The predicted Young's modulus was found using the pure elements and binary interaction parameter data.	97
6.1	First-principles calculations of the elastic stiffness constants, bulk modulus B , shear modulus G , and Young's modulus E in GPa for different atomic percent compositions of the bcc Ti-X-Y ternary systems at 0 °K. As well as experimental data obtained for the Young's modulus at 300 °K by the reference stated.	116
6.1	First-principles calculations of the elastic stiffness constants, bulk modulus B , shear modulus G , and Young's modulus E in GPa for different atomic percent compositions of the bcc Ti-X-Y ternary systems at 0 °K. As well as experimental data obtained for the Young's modulus at 300 °K by the reference stated.	117
6.1	First-principles calculations of the elastic stiffness constants, bulk modulus B , shear modulus G , and Young's modulus E in GPa for different atomic percent compositions of the bcc Ti-X-Y ternary systems at 0 °K. As well as experimental data obtained for the Young's modulus at 300 °K by the reference stated.	118
6.2	Evaluated interactions parameters (L_2 , Eq. Y) for the elastic stiffness constants of the Ti-containing ternary alloys.	119
6.3	Predicted Young's modulus (in GPa) of higher order alloys in the bcc phase compared to experimental values found with both the weight percent and atomic percent listed. The predicted Young's modulus was found using the completed database with the pure elements, binary and ternary interaction parameters.	120
7.1	First-principles calculations of the elastic stiffness constants in GPa for different atomic percent compositions in the α'' , bcc, hcp, and ω phases in the Ti-Nb system at 0 °K.	141
7.1	First-principles calculations of the elastic stiffness constants in GPa for different atomic percent compositions in the α'' , bcc, hcp, and ω phases in the Ti-Nb system at 0 °K.	142

7.2 Evaluated interaction parameters L_0 and L_1 , using Eq. 2.35, for the elastic stiffness constants of the bcc, hcp, α'' and ω phases in the Ti-Nb systems.	143
---	-----

Acknowledgments

Dedication

Chapter 1

Introduction

1.1 Motivation

Titanium (Ti) and its alloys have been used in biomedical applications for many years because of their biocompatibility and corrosion resistance properties [41]. In recent years, there has been an increasing interest in developing better materials for load-bearing implants, due to the increase in total knee and hip replacements. Krutz et al. predicted that the total number of hip and knee replacements would increase by 174% and 673%, respectively, from 2005 to 2030, leading to 572,000 hip and 3.48 million knee procedures in the United States in 2030 [42]. Two of the driving factors for this situation involve the increasing number of younger individuals requiring replacements and the fact that the average life of these implants is only about 7-12 years [43]. These factors contribute significantly to the necessity for better implant materials. The primary considerations for biomedical implants, such as load-bearing knee and hip implants, are biocompatibility, corrosion resistance, fatigue strength, and Young's modulus (E) [41]. In previous years, the most common implants for these applications have been Ti-6Al-4V, stainless steels, and MoCoCr alloys [38,44]. However, there have been issues with these materials, such as cytotoxicity that has been observed with alloys containing aluminum and vanadium [45]. Another important impediment concerning the common implant materials is stress shielding, which can lead to implant failure. Stress shielding occurs when the E of the implant is higher than that of bone. Due to the difference in E , load applications to the joint result in the implant material absorbing all of the stress and causing the bone surrounding the implant to atrophy, which leads to a loss in bone density, and can

result in implant loosening and failure [41]. Table 1.1 summarizes the comparison of the E of common implant materials (> 100 GPa) to bone (10-40 GPa) [41] and shows the extreme elasticity mismatch between the various materials. Using computational thermodynamics to develop a knowledge base of Ti and its alloys is an extremely useful tool in overcoming these challenges.

This work focuses on investigating the thermodynamic and elastic properties of the biocompatible Ti-Mo-Nb-Sn-Ta-Zr system. The thermodynamic and elastic properties are calculated using first-principles based on Density Functional Theory (DFT). The parametrization of the properties is completed using the CALPHAD modeling approach. The combination of these two methodologies has been shown to eliminate the need for trial-and-error metallurgy, thus saving time, money and resources. A new computational methodology to predict the metastable phase formation are presented and verified by neutron scattering experiments. The culmination of this work provides a fundamental understanding of the thermodynamics and elastic properties for the Ti-Mo-Nb-Sn-Ta-Zr system.

1.2 Overview

The phase stability of Ti alloys has been shown to greatly affect the mechanical properties of these materials, so predicting and understanding this aspect of a Ti alloy will greatly impact its effectiveness as a biomedical implant.

1.2.1 Equilibrium Phases

Titanium is stable in the α (hexagonal close packed, hcp) phase (space group $P6_3/mmc$) under standard temperature and pressure. However, β (body centered cubic, bcc) phase (space group $Im\bar{3}m$) Ti alloys have received a good deal of attention because of their low E and high specific strength, so they have been targeted for biomedical applications [46, 47]. Mo, Nb and Ta are biocompatible elements and strong β -stabilizers, while Zr is a bio-compatible weak β -stabilizer individually but strong stabilizer when in combination with other elements, such as Mo, Nb, and Ta [41]. In conjunction with their biocompatibility, studies have shown excellent Mo, Nb, Ta and Zr have excellent corrosion resistance and no allergy problems [48]. Recently, Sn has also been studied for use in Ti-alloys, due

to its low cost [38]. When alloyed in small concentrations, Sn does not effect the biocompatibility of the alloy. Therefore, the present study focuses on determining the effects of alloying Ti with Mo, Nb, Sn, Ta and Zr on the thermodynamic properties. The combined DFT and CALPHAD approach is used to evaluate previous models and build new models for the binary and ternary alloys in the Ti-Mo-Nb-Sn-Ta-Zr system to build a completed database describing the thermodynamic properties of the system.

1.2.2 Elastic Properties

The mechanical properties, and phase stabilities have been experimentally determined for alloys such as Ti-13Nb-13Zr, Ti-35Nb-5Ta-7Zr-0.4O, Ti-29Nb-Ta-Zr and Ti-25Nb-Ta-Zr with Young's moduli between 71 and 57 GPa, approaching the E of bone [35,41,48]. While new metallic alloys are continually being designed, the ability to predict the elastic properties before attempting to develop alloys for biomedical implants will reduce the need for trial and error and narrow the scope of alloys being selected. In this dissertation, first-principles calculations are used to complete an extensive systematic study of the elastic properties of the pure elements, Ti-X systems and Ti-X-Y systems ($X \neq Y = \text{Mo, Nb, Sn, Ta, Zr}$) in the bcc phase. Multiple calculations are done across the entire composition range, using SQS to mimic the behavior of randomly substituted compositions. The first-principles results, are used to introduce interaction parameters that allow for the prediction of the elastic properties as a function of composition.

1.2.3 Metastable Phases

At this point, the completed thermodynamic database will predict the formation of the equilibrium phases and alloys in the bcc phase can then be targeted and their elastic properties predicted. However, Ti and its alloys form two metastable phases, α'' and ω . α'' is an orthorhombic martensitic phase (space group Cmcm). The martensitic transformation is displacive and closely related to the system critical phenomenon [49, 50]. Thermodynamically the martensitic transformation is first-order and initiated due to some supercooling defined by $T_0 - M_S$ where T_0 is the temperature where bcc goes to hcp and M_S is the martensitic temperature where the martensitic transformation begins. An applied stress can also contribute

to the driving force for a martensitic transformation. Kinetically the martensitic transformation propagates in an athermal manner which suggests that the velocity of the interface and the force causing its movement contain an instability. The ω phase is a metastable hexagonal phase (space group P6/mmm) of Ti that has lattice parameters closely matching that of bcc Ti. The ω phase has been seen to form athermally when Ti is alloyed with β stabilizing elements such as Mo, Nb and Ta. It has been shown that different cooling techniques, of alloys at certain compositions in the Ti-Mo, Ti-Nb and Ti-Ta systems, from a temperature in the single-phase bcc region to room temperature causes either the α'' phase or the ω phase with the untransformed bcc phase. Quenching the samples leads to the formation of α'' , while slow cooling the sample leads to the ω phase. The formation of these phases causes variations to the predicted elastic properties as seen in Figure 1.1 and 1.2 where the closed symbols represent the calculated E and the open symbols represent the experimentally determined E . The calculations and experiments match up well on the Ti-rich and Ta-rich sides of the graph but in the purple boxed region, the experiments show a much higher E than predicted. This is due to the formation of α'' and ω . While the formation of the metastable phases greatly effects the properties of the Ti-alloys, the properties of unstable structures cannot be efficiently predicted by DFT-based first-principles calculations. In this dissertation, the phase stability and effect on the elastic properties of the α'' and ω phases are studied for the Ti-Nb and Ti-Ta systems. Initially, the ground state energy and elastic properties of multiple structures in the α'' , ω , bcc and hcp were calculated, across all compositions, for the Ti-Ta and Ti-Nb systems. The partition function approach was then adapted to predict the concentrations and phases fractions where the metastable phases will form. The predicted phase fractions were then used to predict the elastic modulus and phonon density of states using a rule of mixtures. Inelastic neutron scattering was then used to determine diffraction patterns and phonon density of states. By looking at the diffraction patterns obtained at 300 °K, the phase fractions can be obtained and compared to the predicted phase fractions. The phonon density of states (DOS) obtained from neutron scattering experiments at 300 °K can be compared with a mixed force constant first-principles phonon density of states. The plotting of the phonon density of states obtained through neutron scattering at different temperatures will be analyzed to help further understand the transformations taking place. The

predicted E was compared with experimental value in literature.

This completed thesis will consist of the following main tasks:

1. Using first-principles calculations based on DFT and the CALPHAD method to investigate the thermodynamics of the Ti-Mo-Nb-Sn-Ta-Zr system.
 - (a) The previous binary models were evaluated with the available experimental data as well as the first-principles calculated enthalpy of formation of the bcc phase
 - (b) The thermodynamic description of the Sn-Ta binary alloy was modeled
 - (c) The thermodynamic descriptions of the Ti-containing ternary alloys was modeled
2. Using first-principles calculations, the elastic properties of the Ti-Mo-Nb-Sn-Ta-Zr system in the bcc phase were systematically studied. The results, as well as the CALPHAD method, was used to build a database to predict the elastic properties as a function of composition.
3. The metastable phase formation in Ti alloys was investigated through first-principles calculations, the CALPHAD method and experiments done on the Ti-Nb and Ti-Ta systems
 - (a) The ground state energy and elastic properties of the Ti-Nb and Ti-Ta systems in the hcp, bcc, ω and α'' was predicted using first-principles calculations
 - (b) From first-principles the:
 - i. Adapted partition function approach was used to predict the phase fractions
 - ii. The phase fractions were used in a rule of mixtures to plot the phonon density of states and elastic properties
 - (c) From neutron scattering:
 - i. The phase fractions were determined and compared to the predictions

- ii. The phonon density of states was plotted at 300 °K to compare to the mixed force constant predicted phonon density of states
- iii. The temperature dependent phonon density of states will be plotted to study the transformation

Table 1.1. Young's modulus of common implant materials compared with the Young's modulus of bone [41].

Alloy	Young's Modulus (GPa)
Bone	10-40
cp-Ti*	105
Ti-6Al-4V	110
Stainless Steel	200
CoCrMo	200-230

*cp-commercially pure titanium

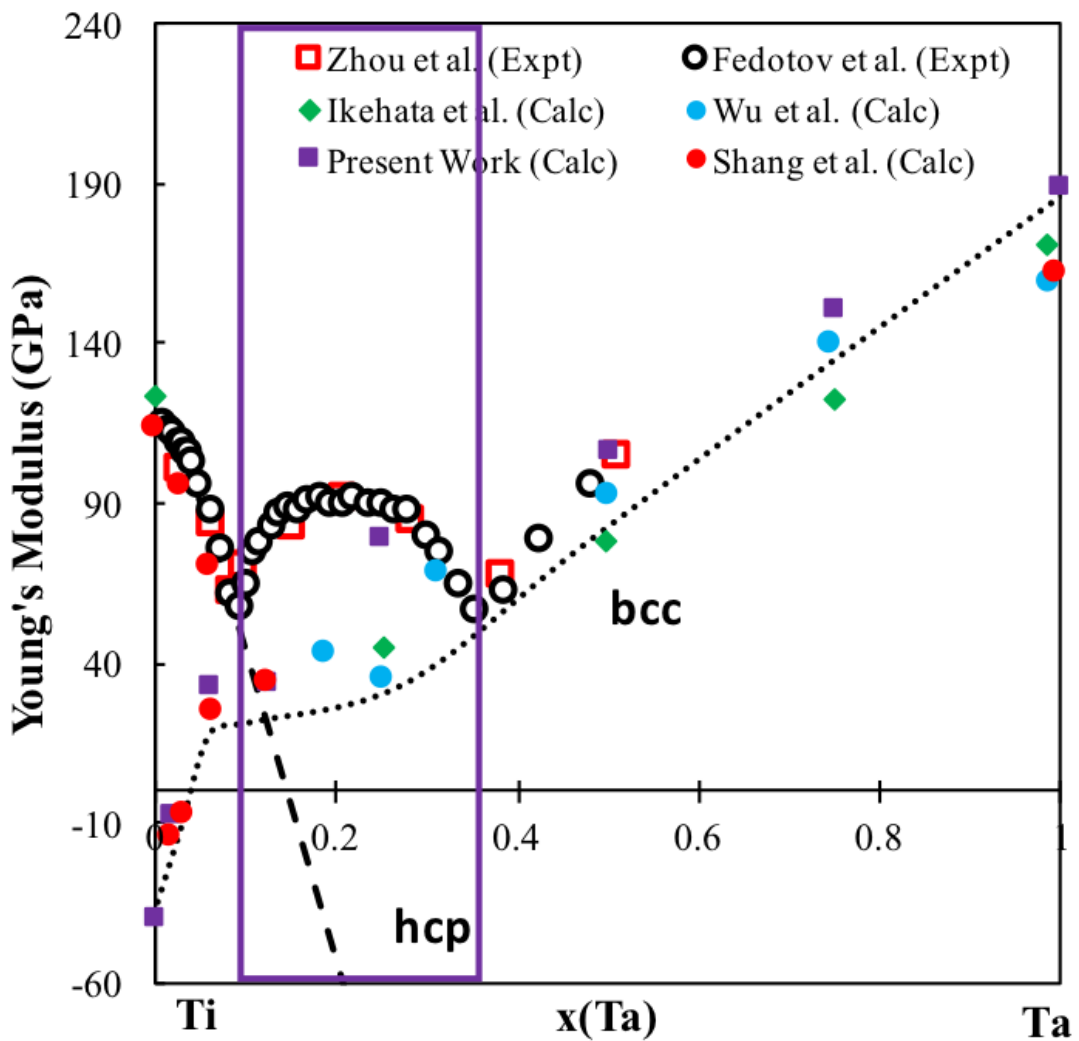


Figure 1.1. Comparison of first-principles calculations [1, 2] and experimental measurements of the Young's modulus of Ti-Ta alloys [3–5]. The purple box refers to the composition range when the calculations and experimentally determined E do not match up due to the formation of two metastable phases ω and α''

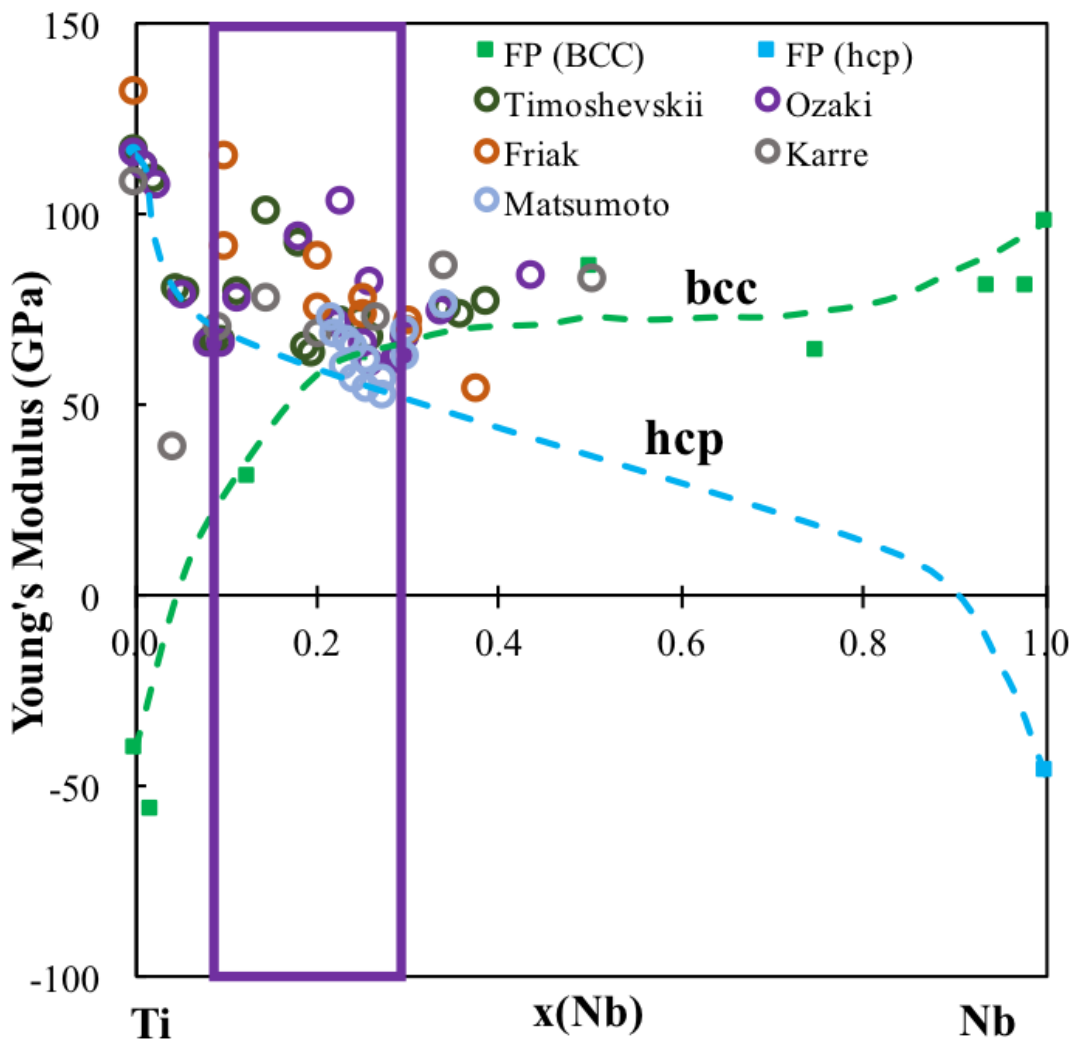


Figure 1.2. Comparison of the present first-principles calculations and experimental measurements of the Young's modulus of Ti-Nb alloys [6–10]. The purple box refers to the composition range when the calculations and experimentally determined E do not match up due to the formation of two metastable phases ω and α''

Chapter 2

Methodology

2.1 First-Principles Calculations

In this dissertation, the ground state energy structures, thermodynamic properties and mechanical properties were calculated using first-principles based on Density Functional Theory. The first-principles refers to the calculations originating from "first-principles", meaning that the inputs were the atomic coordinates and atomic numbers. This method computes the interactions between atoms in a periodic supercell. This was determined using quantum mechanical electronic theory that is based on the electronic charge density and does not rely on any empirical data. This section provides a description of the DFT methodology.

Schrödinger's time-independent non-relativistic equation is a solution to the many-body problem of calculating the interactions of positively charged nuclei and negatively charged electrons. The Schrödinger equation is:

$$\left[\sum_{i=1}^N \left(-\frac{\hbar^2}{2m} \nabla_i^2 + V_{ext}(r_i) \right) + \sum_{i < j} U(r_i, r_j) \right] \Psi = E_s \Psi \quad (2.1)$$

where the first bracketed part represents the Hamiltonian (\hat{H}), Ψ describes the wave function of electrons, E_s describes the systems energy. The \hat{H} of the system is described by three parts, the first part represents the kinetic energy with N being the total number of electrons in the system, \hbar being Planck's constant and m the mass of an electron. The second term V_{ext} gives the external potential and U is the potential of the electron-electron repulsion.

Eq. 2.1 can be solved for Ψ with the lowest energy E_s being the ground state

energy, assuming the nuclei-nuclei interactions are neglected due to the Born-Oppenheimer approximation. The Born-Oppenheimer approximation allows us to assume the nuclei are stationary and ignore the motion of the nuclei on the electronic timescale, due to the mass difference, with nuclei being $\sim 10^3$ to 10^5 larger than electrons. However, even with this approximation solving Eq. 2.1 is difficult to deal with due to the electron-electron Columb interactions making the electronic motion correlated and the fact that the many-body problem results in too many variables because there are $3N$ degrees of freedom.

Hohenberg-Kohn formulated two theorems to simplify this problem [51]. The first theorem states that the external potential is a unique functional of the electron density. The second theorem states that the density that minimizes the total energy is the exact ground state density and thus the ground state is obtained variationaly. With these theorems, Kohn-Sham proved that the problem can be solved as if the electrons are not interacting and still obtain the density as if they were, by [52]:

$$\left[-\frac{\hbar^2}{2m} \nabla^2 + V_{ext}(r) + V_{Hartree}(r) + V_{XC}(r) \right] \phi_1(r) = \epsilon_i \psi_i(r) \quad (2.2)$$

where $V_{ext}(r)$ describes the electron-nuclei interaction similar as in Eq. 2.1:

$$V_{ext} = -e^2 \sum_a \frac{Z_a}{|r_i - R_a|} \quad (2.3)$$

where r_i represents the position of electron i and R_a represents the position of nucleus a with a charge valance of Z_a . The electron-electron interactions are represented by $V_{Hartree}$:

$$V_{Hartree}(r) = e^2 \int \frac{\rho(r)}{|r - r_j|} d^3r \quad (2.4)$$

where r and r_j represent the electrons and $\rho(r)$ is described by :

$$\rho(r) = \sum_i^N |\psi_i(r)|^2 \quad (2.5)$$

The final term of V_{xc} is the exchange correlation potential that is described in terms of an exchange-correlation energy. While there is no exact solution to the exchange-correlation (X-C) energy available, there are multiple different approximations. Each approximation is done to account for different things. In the present work, the

generalized gradient approximation by Perdew and Wang (PW91) [53] and the generalized gradient approximation by Perdew, Burke and Ernzerhoff (PBE) [54] were used. The generalized gradient approach improves the total energies, atomization energies as opposed to other methods such as the local density approximation [55] but can over-correct for the expansion and softening of bonds. The generalized gradient approximation (GGA) is favored for densities that are inhomogeneous. Based on previous research done by Perdew et al. [54], GGA's are considered to be adequate approximations for calculating metals [54]. The use of PW91 vs PBE was compared when looking at the elastic properties of the Ti-Ta system in Figure 2.1. The results showed little difference in calculated elastic properties. The PW91 X-C functional was designed to satisfy as many exact conditions as possible and thus has some issues. Perdew introduced the PBE X-C functional as an improvement to PW91 which satisfied less exact conditions and only looked at the ones that were energetically significant for metals. Due to this and the fact the results vary so little, the PBE X-C functional was chosen to be used for the present thesis work. By implementing the theorems and the Kohn-Sham equation, the energy of the system can thus be calculated.

2.1.1 Density Functional Theory at 0 °K

The ground state energy at 0 °K without the contribution of zero-point vibrational energy was calculated by using the equation of states (EOS) fitting for the relationship between the energy and volume of the structure. The EOS fitting was achieved through an energy-volume ($E_0 - V$) curve of 5 or more relaxed volumes and using the four-parameter Birch-Murnaghan (BM4) EOS [56]:

$$E_0(V) = a + bV^{-\frac{2}{3}} + cV^{-4/3} + dV^{-2} \quad (2.6)$$

where a , b , c and d are fitting parameters. From this, the volume V_0 , ground state energy E_0 , bulk modulus B_{EOS} , and first derivative with respect to pressure B'_{EOS} can be calculated.

From the ground state energies, the energy of formation and enthalpy of formation at 0 °K was calculated by finding the difference between the structures energy and a reference state, normally the standard element reference (SER) state at standard pressure and temperature. The valance configuration for each element

was selected based on the VASP recommendations. The p electrons were treated as valance for the Mo and Ta, the d electrons were treated as valance for Sn and the s electrons were treated as valance for Ti, Nb, and Zr [57, 58].

2.1.2 Finite-temperature thermodynamics

The Helmholtz energy, $F(V, T)$ was calulated, with DFT, as a function of temperature T and volume V :

$$F(V, T) = E_0(V) + F_{vib}(V, T) + F_{T-el}(V, T) \quad (2.7)$$

where E_0 is the static contribution at 0 °K calculated from Eq. 2.6, F_{vib} is the temperature-dependent vibrational contribution, and F_{T-el} is the thermal electronic contribution. At ambient pressure, the Helmholtz energy of the system is equal to the Gibbs energy, which is used in the CALPHAD modeling. The vibrational contribution was obtained through the phonon quasiharmonic supercell (phonon approach) or the Debye-Grüneisen method (Debye). The phonon approach is a more accurate approach compared to the Debye model but it is also more computationally expensive. In the present work, both the phonon and Debye models are used in different sections. The vibrational contribution obtained through phonon calculations of at least five different volumes is expressed by [59]:

$$F_{vib}(V, T) = k_b T \int_0^\infty \ln \left[2 \sinh \frac{\hbar \varrho}{2k_B T} \right] g(\varrho) d\varrho \quad (2.8)$$

where $g(\varrho)$ is the phonon density of states as a function of phonon frequency ϱ at volume V . ϱ is normally expressed in literature as ω , however, due to the extensive discussion of the ω phase in this work the phonon frequency is expressed as ϱ to avoid confusion. In addition, the Debye model is used to estimate the vibrational contribution [56]:

$$F_{vib}(V, T) = \frac{9}{8} k_b \theta_D(V) + k_B T \left[3 \ln \left(1 - e^{-\frac{\theta_D}{T}} \right) - D \left(\frac{\theta_D}{T} \right) \right] \quad (2.9)$$

where θ_D is the Debye temperature, T is the temperature, and $D \left[\frac{\theta_D}{T} \right]$ is the Debye function. θ_D is calculated through:

$$\theta_D = s \frac{(6\pi^2)^{\frac{1}{3}} \hbar}{k_B} V_0^{\frac{1}{6}} \left(\frac{B}{M} \right)^{\frac{1}{2}} \left(\frac{V_0}{V} \right)^\gamma \quad (2.10)$$

where s is the Debye temperature scaling factor, γ is the Grüneisen parameter determined by the pressure derivative of bulk modulus (B'_{EOS}), B_{EOS} is the bulk modulus, M is the atomic mass, and V_0 is the equilibrium volume. Here the equilibrium properties V_0 , B_{EOS} , and B'_{EOS} are estimated from the EOS of Eq. 2.6. The Debye temperature scaling factor was determined by Moruzzi et al. [60] to be 0.617 for nonmagnetic metals. However, this value has been shown to be less accurate for other materials. Liu et al. extensively looked at the Debye scaling factor and how to calculate the scaling factor based on the Poisson's ratio of a material [61]. The methodology by Liu et al. [61] was used for the present work to calculate the scaling factor:

$$s(\nu) = 3^{\frac{5}{6}} \left[4\sqrt{2} \left(\frac{1+\nu}{1-\nu} \right)^{\frac{3}{2}} + \left(\frac{1+\nu}{1-\nu} \right)^{\frac{-1}{3}} \right] \quad (2.11)$$

where ν is the Poisson's ratio, which can be calculated from the elastic stiffness constants.

The thermal electronic contribution is based on the electronic density of states and calculated with the Fermi-Dirac statistics [56, 62]:

$$F_{T-el} = E_{T-el} - TS_{T-el} \quad (2.12)$$

The E_{T-el} and S_{T-el} represent the energy and entropy of the thermal electron excitations, respectively. The E_{T-el} is expressed by:

$$E_{T-el}(V, T) = \int n(\epsilon, V) f(\epsilon, T) \epsilon d\epsilon - \int^{\epsilon_f} n(\epsilon) \epsilon d\epsilon \quad (2.13)$$

and the entropy S_{T-el} is expressed by:

$$S_{T-el}(V, T) = -k_B \int n(\epsilon, V) [ln f(\epsilon, T) + (1 - f(\epsilon, T)) ln(1 - f(\epsilon, T))] d\epsilon \quad (2.14)$$

where $n(\epsilon, V)$ is the electronic density of states (DOS) at energy ϵ , $f(\epsilon, T)$ is the Fermi-Dirac distribution, ϵ_f is the Fermi energy level and k_B is Boltzmann's

constant. The Fermi-Dirac distribution $f(\epsilon, T)$ is expressed by:

$$f(\epsilon, T) = \left[\exp\left(\frac{\epsilon - \mu}{k_B T}\right) + 1 \right]^{-1} \quad (2.15)$$

and μ is the chemical potential of the electrons.

2.1.3 Elastic stiffness calculations

The single crystal elastic stiffness constants ($c_{ij}'s$) were calculated from the ground state energy structure using a stress-strain method developed by Shang et al. [63]. With this method, a set of independent strains $\varepsilon = (\varepsilon_1, \varepsilon_2, \varepsilon_3, \varepsilon_4, \varepsilon_5, \varepsilon_6)$ were imposed on the crystal lattice, where $\varepsilon_1, \varepsilon_2$, and ε_3 are the normal strains, $\varepsilon_4, \varepsilon_5$, and ε_6 the shear strains, and a set of stresses $\sigma = (\sigma_1, \sigma_2, \sigma_3, \sigma_4, \sigma_5, \sigma_6)$ were generated. Hooke's law is then used to calculate the elastic stiffness constants:

$$\begin{pmatrix} c_{11} & c_{12} & c_{13} & 0 & 0 & 0 \\ c_{12} & c_{22} & c_{23} & 0 & 0 & 0 \\ c_{13} & c_{23} & c_{33} & 0 & 0 & 0 \\ 0 & 0 & 0 & c_{44} & 0 & 0 \\ 0 & 0 & 0 & 0 & c_{55} & 0 \\ 0 & 0 & 0 & 0 & 0 & c_{66} \end{pmatrix} = \begin{pmatrix} \varepsilon_{1,1} & \dots & \varepsilon_{1,n} \\ \varepsilon_{2,1} & \dots & \varepsilon_{2,n} \\ \varepsilon_{3,1} & \dots & \varepsilon_{3,n} \\ \varepsilon_{4,1} & \dots & \varepsilon_{4,n} \\ \varepsilon_{5,1} & \dots & \varepsilon_{5,n} \\ \varepsilon_{6,1} & \dots & \varepsilon_{6,n} \end{pmatrix}^{-1} \begin{pmatrix} \sigma_{1,1} & \dots & \sigma_{1,n} \\ \sigma_{2,1} & \dots & \sigma_{2,n} \\ \sigma_{3,1} & \dots & \sigma_{3,n} \\ \sigma_{4,1} & \dots & \sigma_{4,n} \\ \sigma_{5,1} & \dots & \sigma_{5,n} \\ \sigma_{6,1} & \dots & \sigma_{6,n} \end{pmatrix} \quad (2.16)$$

where "-1" represents the pseudo-inverse. Due to symmetry, the bcc structure only has three independent elastic stiffness constants. However, with a lack of bcc stability for some of the calculations, all of the elastic stiffness constants were calculated and the average \bar{C}_{11} , \bar{C}_{12} and \bar{C}_{44} values were used:

$$\bar{C}_{11} = \frac{(c_{11} + c_{12} + c_{44})}{3} \quad (2.17)$$

$$\bar{C}_{12} = \frac{(c_{12} + c_{13} + c_{23})}{3} \quad (2.18)$$

$$\bar{C}_{44} = \frac{(c_{44} + c_{55} + c_{66})}{3} \quad (2.19)$$

This case is for the unstable bcc elastic calculations to mimic the behavior of a cubic

structure. The largest variance between the similar elastic stiffness constants, when calculating the average, was used to show the deviation from the bcc symmetry in the calculations, shown as error bars. The stable bcc structures show no variance and thus no error bars. To examine the effects of different strain on the elastic properties, three groups of non-zero strain magnitudes, ± 0.01 , ± 0.03 , and ± 0.07 , were tested in chapter 5 and it can be noted that the results have negligible changes with respect to the three groups of strains tested herein. Therefore, ± 0.01 was used for all the calculations. The polycrystalline elastic properties including bulk (B), shear (G), and E modulus were calculated from the elastic stiffness constants, based on the Voigt-Reuss-Hill approach [64]. The Voigt gives the upper elastic bound due to the assumption of constant strain in all grains, the Reuss gives the lower elastic bound due to the assumption of constant stress in all grains, and the Hill approach is the average of Voigt and Reuss and is closer to real case [65, 66]. The Hill approach is hence what is listed in the results section. The Voigt and Reuss bounds were also plotted in the figures to give the bounds of the moduli values.

In order to fully investigate the effects of the alloying elements on the Ti-alloys, the mechanical stability of the bcc phase was studied. The mechanical stability was given by on Born's criteria for a cubic crystal [67, 68]:

$$\bar{C}_{11} - |\bar{C}_{12}| > 0 \quad (2.20)$$

$$\bar{C}_{11} + 2\bar{C}_{12} > 0 \quad (2.21)$$

$$\bar{C}_{44} > 0 \quad (2.22)$$

Based on Born's criteria, when $\bar{C}_{11} - \bar{C}_{12}$ becomes negative then the phase, bcc in this case, loses mechanical stability and thus $\bar{C}_{11} - \bar{C}_{12}$ is plotted in the results section.

2.1.4 Special quasirandom structures (SQS)

To calculate the energies, enthalpies of formation and elastic properties across the entire binary and ternary composition range, varying compositions of special quasirandom structures (SQS) were used. The SQS are small supercells used to mimic randomly substituted structures in terms of correlation functions. The binary

and ternary bcc SQS, used in the present work, were previously generated by Jiang et al. [69, 70]. The relaxation of these structures is complicated because local atomic relaxations can cause the structure to lose the bcc lattice symmetry. To preserve structural symmetry, the calculations were carried out with different relaxation schemes only alloying the cell shape and cell volume to be relaxed to determine the lowest energy structure. In order to ensure the bcc symmetry was preserved the energies were plotted as a function of composition. Then the symmetry was verified. There are two ways to verify whether the SQS is still bcc or not after the relaxation. The first is to merge different elements into one element for the SQS structure, and then, use codes available to check the symmetry or space group (such as VASP and phonopy codes). The second is to visualize the structure directly using a visualization software such as VESTA and compare the symmetry to the unrelaxed bcc structure. For the present work, the relaxed structures were plotted in the visualization software and compared to the unrelaxed structure. In some cases, even without comparing, it was very obvious that the structure had lost bcc symmetry. For the cases where it wasn't obvious the comparison was done using symmetry codes (VASP, phonopy, etc). After the relaxation, at least five different volume structures are generated and the ions were allowed to relax. This yields the different volumes needed for the EOS fitting described above, which allows a better prediction of the different properties as a function of composition.

2.1.5 High-throughput partition function

This section introduces a theoretic framework to predict the formation of a solid with a mixture of multiple microstates. The combined potential energy can be expressed by [71]:

$$E_c = E_g + \sum p_i (E_i - E_g) \quad (2.23)$$

where E_g is the ground state energy and E_i is the energy of metastable phase i . All of the energies were calculated from first-principles based on DFT using the EOS fitting in Eq. 2.6. p_i is expressed by:

$$p_i = \frac{Z_i}{Z_c} \quad (2.24)$$

where Z_i and Z_c are calculated by:

$$Z_c = \sum_j e^{-\frac{E_c}{k_B T}} \quad (2.25)$$

From Eq. 2.23-2.25 the combined Helmholtz energy is calculated by:

$$F_c = -k_B T \left(\sum \frac{Z_i}{Z_c} \ln Z_i - \sum \frac{Z_i}{Z_c} \ln \frac{Z_i}{Z_c} \right) \quad (2.26)$$

From the combined helmholtz the phase fractions MORE

2.1.6 First-principles calculation error

The error between the previous results (experimental or calculation) and present results was calculated using:

$$\sqrt{\frac{\sum[(A_{calc} - A_{ref})]^2}{\kappa}} = Difference \quad (2.27)$$

where A_{calc} is from the present calculation and A_{ref} is from the previous experiment or calculation, and κ is the total number of data points.

2.2 CALPHAD method

The CALPHAD method evaluates parameters to represent the Gibbs energy of individual phases as a function of temperature, pressure and composition. Thermo-chemical and phase boundary data obtained from experiments and first-principles calculations were used in the PARROT module of Thermo-Calc to evaluate the thermodynamic interaction parameters [72]. The Gibbs free energy is described by enthalpy H , temperature T and entropy S as follows:

$$G = H - TS \quad (2.28)$$

The Gibbs energy is then parameterized and expressed by:

$$G - H^{SER} = a + bT + cT \ln T + dT^2 + \sum_2^n e_n T^n \quad (2.29)$$

where H^{SER} refers to the elemental enthalpy in the SER state and a, b, c, d, e are coefficients. Other thermodynamic properties such as, enthalpy, entropy and heat capacity can be derived from this equation. The parameterized equations for the pure elements have been determined and widely adopted from the SGTE to ensure global compatibility between different databases [31].

2.2.1 Solution phases

The databases were built upon the pure elements and then the effects of the binary and ternary interactions are modeled. Normally, the effects of alloying are modeled as solution phases or stoichiometric phases. The solution phases with one sublattice were described by:

$$G_m^\phi = \sum x_A^0 G_A^\phi + RT \sum x_A \ln x_A + {}^{XS}G_m^\phi \quad (2.30)$$

where x_A is the mole fraction of element A and ${}^0G_A^\phi$ is the molar Gibbs energy of pure element A in the specific phase (ϕ) being modeled, the second term describes the ideal interaction between elements. The last term represents the excess mixing energy, representing the non-ideal interactions between species A and B . The excess mixing energy can be expressed by the Redlich-Kister polynomial as [73]:

$${}^{XS}G_m^\phi = \sum x_A x_B \sum_{k=0}^k L_{A,B}^\phi (x_A - x_B)^k \quad (2.31)$$

where ${}^kL_{A,B}^\phi$ represents the interaction parameter for elements A and B in phase ϕ described by:

$$L_{A,B}^\phi = {}^k a + {}^k b T \quad (2.32)$$

in which ${}^k a$ and ${}^k b$ are evaluated model parameters. Eq. 2.31 can be extended to multi-component systems as:

$$\begin{aligned} {}^{XS}G_m^\phi &= \sum x_A x_B \sum_{k=0}^k L_{A,B}^\phi (x_A - x_B)^k + \sum x_A x_B x_C \\ &\quad \left[{}^0L_{A,B,C}^\phi (x_A + \delta_{A,B,C} + {}^1L_{A,B,C}^\phi (x_B + \delta_{A,B,C} + {}^2L_{A,B,C}^\phi (x_C + \delta_{A,B,C})) \right] \end{aligned} \quad (2.33)$$

where the ternary interaction parameters $L_{A,B,C}^\phi$ are described the same as the binary interaction parameters in Eq. 2.32 and $\delta_{A,B,C}$ is defined as $\delta_{A,B,C} = (1 - x_A - x_B - x_C)/3$

In the present thesis, while no order-disorder modeling was done, the order-disorder model was used in many of the previous models evaluated. At low temperatures in many of the Ti-containing binary alloys, the randomly substituted bcc-A2 phase goes through a second order transition to become the ordered simple cubic B2 phase (CsCl-type). This modeling was discussed extensively in the COST 507 by Ansara [11].

2.2.2 Stoichiometric compounds

The Gibbs energy of stoichiometric compounds was modeled in per mole unit formula. For the stoichiometric compound, A_pB_q , the Gibbs energy is expressed by [74]:

$${}^0G_m^{A_pB_q} = a + bT + p * {}^0G_A^{SER} + q * {}^0G_B^{SER} \quad (2.34)$$

where a and b are the evaluated parameters, ${}^0G_A^{SER}$ is the Gibbs energy of pure element A in the SER phase, ${}^0G_B^{SER}$ is the Gibbs energy of pure element B in the SER phase, p is the number of atoms per unit formula of element A and q is the number of atoms per unit formula of element B .

2.2.3 Elastic Properties

To obtain the elastic properties as a function of composition, the CALPHAD modeling approach was adopted and the Redlich-Kister polynomial was used to describe the elastic stiffness constants by [73, 75]:

$$E(x) = \sum x_A E_A^\phi + \sum x_A x_B^k L_{A,B}^\phi + \sum x_A x_B x_C^0 L_{A,B,C}^\phi \quad (2.35)$$

where similar to Eq. 2.31 and 2.33 the x_A , x_B , and x_C refer to the mole fraction of element A , B , and C respectively, E_A is the elastic property of element A , ${}^kL_{A,B}^\phi$ and ${}^kL_{A,B,C}^\phi$ are the binary and ternary interaction parameters, respectively. The binary and ternary interaction parameters were described in terms of Eq. 2.32 but with solely an a coefficient. For the binary modeling, the addition of one and two

interaction parameters were studied to ensure the best fit. For the ternary systems, only one interaction parameter was introduced. This is due to the fact that only one ternary interaction parameter is needed to describe the interaction between the ternary systems on the Ti-rich side. The fittings of the binary and ternary interaction parameters were completed using the Mathematica code in Appendix C. The binary interaction parameters were fit using the difference between the pure elements extrapolation and the first-principles results for each Ti-X ($X = \text{Mo}, \text{Nb}, \text{Sn}, \text{Ta}, \text{Zr}$). The ternary interaction were fit using the difference between the interpolaiton calculated from the pure elements and binary interaction parameters and the results. The interaction parameters determined to describe the elastic stiffness constants were incorporated into a database. Pycalphd [40] was then used to calculate the moduli values as a function of compostion based on the Voigt-Reuss-Hill approach.

2.3 Experimental

To study the effect of the metastable phase formation, Ti-Nb alloys at different compositions were made by arc melting. Two samples were made at each composition. One set of samples was quenched to form the α'' and the second set of samples was slow cooled to form the ω phase. The samples were then studied using inelastic neutron scattering.

2.3.1 Ti-Nb sample preparation

The first set of samples, which hereafter be referred to as set 1, included four Ti-Nb samples made from pieces of titanium (Alfa Aesar, Stock No. 14004) and niobium (Alfa Aesar, Stock No. 00241) at 0.1, 0.12, 0.18, 0.2 mole fraction of Nb. The second set of samples, which hereafter will be reffered to as set 2, included four Ti-Nb samples made from pieces of titanium (Sigma Aldrich, Stock No. 305812) and niobium (Alfa Aesar, Stock No. 00241) at 0.1, 0.12, 0.18, 0.2 mole fraction of Nb. Two different titanium pieces were used because the Alfa Aesar titnaium pieces were out of stock but they both had the same purity and thus should not lead to any issues with the data analysis. The alloyed samples were made using the MAM1, Edmund Buhler GmbH arc melter under argon atmosphere. The

alloys were machined into a cylindrical shape (0.7 inches in diameter and 0.7 inches in thickness). The samples were then heat treated using a Lindberg 59544 tube furnace. The tube was made of Al_2O_3 and was under vacuum. The samples were annealed at 1273 °K for 24 hours. The samples from set 1 were quenched in a water solution. The samples in set 2 were slow cooled.

2.3.2 Neutron Scattering

2.3.2.1 ARCS

The inelastic neutron scattering measurements were carried out using the Wide Angular-Range Chopper Spectrometer (ARCS) at the Spallation Neutron Source (SNS) at Oak Ridge National Laboratory. ARCS is a time-of-flight spectrometer so the neutrons original position and energy are fixed and neutrons final position and the time elapse are recorded. From this information, the momentum and energy of the neutrons was calculated and plotted. The samples were loaded into a customized vanadium sample holder. Vanadium was chosen due to the high temperatures measured. The empty vanadium sample holder was measured at the same conditions at each temperature. The holder was mounted into the furnace and kept under vacuum throughout all measurements. Two incident neutron energies, $E_i = 25\text{meV}$ and $E_i = 50\text{meV}$, were used at each temperature (300, 500, 700, 900, 1110 K). The data was corrected for the empty can scattering as well as the ARCS background. The diffraction patterns and phonon density of states were then obtained.

2.3.2.2 Data Analysis

After the empty sample holder and background were subtracted from the data, the diffraction patterns and phonon density of states were investigated. Diffraction is prominently an elastic scattering process. The intensity of the diffraction patterns obtained were compared with intensities of Ti and Nb single-phase diffraction patterns in the α'' , ω , bcc and hcp from literature. The single-phase diffraction patterns from literature are not always at the right compositions, but by comparing the intensities the phase fractions can be predicted fairly accurately. First the distance between scattering planes is taken into account for each phase. The

intensity at each momentum was calculated and modeled as a Gaussian function for each phase and then the data was fitted with the literature data [76, 77].

The phonon DOS contains the one-phonon and multi-phonon contributions; however, the one-phonon density of states is what is needed. An iterative process was done starting with a trial phonon DOS to separate the multi-phonon and one phonon contributions. This is accomplished by summing over the entire detector angle range (2θ) and calculating the total incoherent dynamic structure factor expressed by [78]:

$$\bar{S}_{calc}^{inc}(\varrho) = \sum_{\theta} \frac{1}{2\pi\hbar} e^{-Q^2(\theta,\varrho)\langle u^2 \rangle} \int_{-\infty}^{\infty} dt e^{-i\varrho t} e^{\hbar^2 Q^2(\theta,\varrho)G(t)/2M} \left[e^{\frac{-t^2}{2}\left(\frac{\Delta E(\varrho)}{2\hbar}\right)^2} \right] \quad (2.36)$$

where $\langle u^2 \rangle$ is the Debye-Waller factor describing the mean square atomic displacement. The anisotropy in the Debye-Waller factor was neglected because the resulting errors were negligible [78]. The ΔE is the Gaussian instrument energy resolution of variable width. M is the mass of a neutron, $G(t)$ is the time dependent self-correlation function which is expressed by [78]:

$$G(t) = \int_{-\infty}^{\infty} d\varrho \frac{Z(\varrho)}{\varrho} n(\varrho) e^{-i\varrho t} \quad (2.37)$$

where $g(\varrho)$ is the phonon density of states as a function of phonon frequency ϱ and $n(\varrho)$ is the thermal occupancy factor. Finally, Q is defined by [78]:

$$Q(\theta, \varrho) = \sqrt{\frac{2M}{\hbar^2} \left(2E - \hbar\varrho - 2E\sqrt{1 - \frac{\hbar\varrho}{E}} \cos(2\theta) \right)} \quad (2.38)$$

The calculated $\bar{S}_{0,calc}^{inc}$ and the elastic scattering was then subtracted from the total scattering which leaves us with the angle-averaged multiphonon structure factor which is a good starting approximation for the multiphonon coherent scattering [78].

The elastic peak was then subtracted from the measured total dynamical structure factor. Then the total dynamical structure factor was averaged over 2θ and scaled so the multiphonon coherent scattering could be subtracted. After the subtractions, the new phonon DOS was determined and was then used to recalculate the multiphonon contribution and the procedure was repeated. The procedure was repeated three times to converge the phonon DOS based on previous

recommendations that showed three iterations were enough to converge within statistical errors [78].

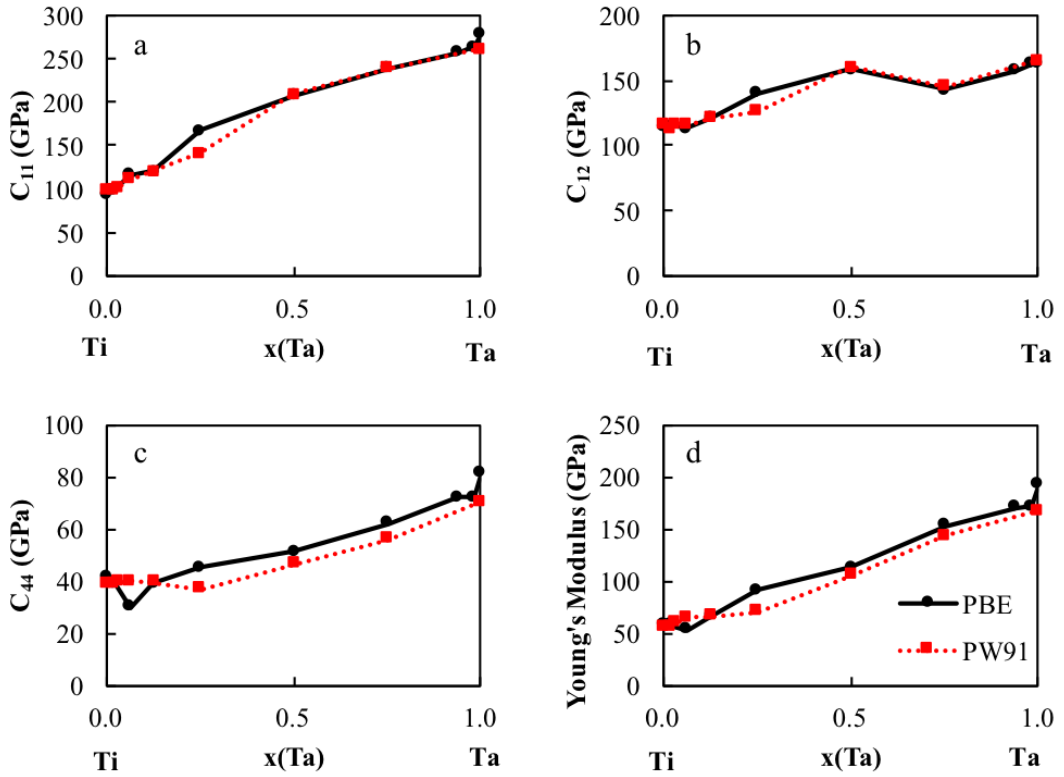


Figure 2.1. Elastic stiffness constants of the bcc Ti-Ta binary system calculated with the GGA and PBE exchange correction functions, respectively.

Chapter 3 |

Ti-Mo-Nb-Sn-Ta-Zr Thermodynamic Database

3.1 Introduction

The design of Ti-alloys for biomedical applications necessitates a completed thermodynamic database that will facilitate the prediction of phase compositions and fractions as a function of composition and temperature. However, there is no completed thermodynamic database for the Ti-Mo-Nb-Sn-Ta-Zr system and thus the present work aims at building a complete database with special focus on the Ti-rich alloys and bcc phase models. With this in mind the pure elements have been extensively studied and are widely adopted from the SGTE database [31]. The modeling of the binary systems has been widely documented with the exception of the Ta-Sn and Mo-Sn systems, while experimental phase boundary data is available for the ternary systems but little to no modeling has been completed. The Mo-Sn and Sn-Ta subsystems have high melting temperatures and little to no experimental data. In these cases, first-principles calculations based on DFT can be used to aid in modeling and supplement the lack of experimental data. The complete modeling of the Ta-Sn system is discussed in Ch3. In the present chapter, the thermodynamic descriptions of the Ti-Mo-Nb-Ta-Zr system are described.

While many of the alloys in this Ti system have been studied experimentally, yielding phase equilibrium data, only limited calorimetry data is available. With the present work focuses on bcc Ti-rich alloys, first-principles calculations based on DFT of the enthalpy of formation of the bcc phase were calculated. The thermodynamic

descriptions were built or evaluated using available experimental phase boundary data and present calculated thermochemical data. This work looks at evaluating new and previous models for the binary and Ti-containing ternary systems.

3.2 Computational details

First-principles results based on Density Functional Theory (DFT) are used to predict the enthalpy of formation of specific phases. In the present work, the enthalpy of formation of the bcc phase was calculated for the Ti-X and Ti-X-Y ($X \neq Y = Mo, Nb, Ta, Zr$) using the calculated energy of the pure elements in their SER states. For each Ti-containing binary system at least 5 composition energy structures were calculated and three compositions for the Ti-containing ternary system. For each system, three special quasirandom structures (SQS) of varying compositions were relaxed to get an accurate representation of the enthalpy of formation across the composition range. For the binary phases the compositions are each 16-atom unit cells at Ti_4X_{12} , Ti_8X_8 , and $Ti_{12}X_4$ and the ternary phase compositions of $Ti_{12}X_{12}Y_{12}$ (36-atom), $Ti_{16}X_8Y_8$ (32-atom), $Ti_{48}X_8Y_8$ (64-atom) structures are used with one X_8Y_8 (16-atom), where X and Y are the alloying elements. These SQS in the bcc phase that were implemented were developed by Jiang et al. [69, 70]. Relaxation of these structures is complicated and explained in the methodology section. The DFT calculations are completed using VASP (Vienna ab-initio Simulation Package) [57]. The ion-electron interactions were described using the projector augmented wave (PAW) [58, 79] method. Based on the work of comparing X-C functionals (Figure 2.1) the exchange-correlation functional of the generalized gradient approach depicted by Perdew, Burke, and Ernzerhof (PBE) was employed [54]. For consistency, a 310 eV energy cutoff was adopted for all calculations, which is roughly 1.3 times higher than the default value. The energy convergence criterion was 10⁻⁶ eV/atom, and the Monkhorst-Pack scheme is used for Brillouin zone sampling [57, 80].

3.3 Binary systems

In order to build the database, as discussed above, the pure elements were adapted from the SGTE database [31]. After the incorporation of the pure elements, all the

binary systems were then evaluated. When applicable, previous models of the binary systems were evaluated for accuracy and model compatibility and incorporated into the database. After incorporation of all binary systems, the Ti-containing ternary systems were evaluated, with the exception of Mo-Nb-Ta which had a previous model available by Xiong et al. [17] and was incorporated into this work. To do the binary and ternary evaluations, the enthalpy of formation of the bcc phase for the Ti-containing alloys was calculated across the composition ranges. To calculate the enthalpy of formation of the bcc phase, the enthalpy of the pure elements had to be calculated in their standard element reference states (SER). The phases and results are listed in Table 3.1. In order to ensure the accuracy of the calculations, the bulk modulus B calculated in the present work was compared with the experimental data. The experimental B varied on average by 1 GPa from the calculated B . This discrepancy is not large and is attributed with the temperature difference thus these calculations prove to be accurate.

The previous thermodynamic descriptions for the Ti-containing binaries were evaluated with experimental data as well as looking at the enthalpy of formation of the bcc phase using present first-principles calculations. The enthalpy of formation of the bcc phase calculated for each Ti-containing binary from first-principles is listed in Table 3.2.

3.3.1 Ti-Mo

The Ti-Mo binary evaluation was taken from the COST 507 database and the thermodynamic description was evaluated by Saunders [11]. This model was chosen because it is the modeled incorporated into the Ti-Mo-Zr modeling done by Kar et al. [23]. Interaction parameters were evaluated for the liquid, fcc (face centered cubic), hcp, bcc#1, bcc#2 ordered and disordered phases, AlM-D019, AlM-D022, and the AlTi-L10 phases. Figure 3.1a shows the comparison of the available phase boundary data from Murray et al. [12] with the Saunders model. The phase boundary data is reproduced in the with the Saunders model. Figure 3.1b shows the enthalpy of formation of the bcc phase predicted from the model at 300 K compared with the present first-principles results at 0 °K. The enthalpy of formation of the bcc phase predicted varies from the first-principles calculations drastically between 20 and 80 at % Mo. This discrepancy is seen due to the disagreement on the existence

of a bcc miscibility gap. Previous research has shown the need for a bcc miscibility gap which would fit what is seen in the first-principles calculations [81, 82]. Kar et al. showed that the experimental data from higher-component systems fit better with the description containing no miscibility gap. Based on this, the model by Saunders was adopted for the database with no changes.

3.3.2 Ti-Nb

The Ti-Nb binary evaluation was taken from Zhang et al. [13] and plotted in Figure 3.2a. Originally the binary evaluation was taken from Kumar et al. [14]. The figure shows solidus data (\square) and hcp and bcc solvus data (\circ) used in the Kumar et al. evaluation. The model from Kumar was used in the modeling of the Ti-Nb-Zr. The phase diagram was evaluated using phase boundary data on the Ti-rich side and liquidus data. Not only was the binary evaluation adapted due to the use in the Ti-Nb-Zr ternary but it also reproduced the experimental phase boundary data reasonably well. However, the model was changed to the new model by Zhang et al. (\triangle) due to the new phase boundary data on the Nb rich side. The present first-principles calculations of the enthalpy of formation of the bcc phase are plotted in Figure 3.2b. The present DFT results (circles) are at 0 °K while the CALPHAD prediction (solid line) is at 300 °K which explains the average variance of 0.17 kJ/mol-atom between the DFT and CALPHAD predictions. However, even with the variance the CALPHAD prediction compares well with the DFT results and the sublattice models are similar to the database being built. With the reproduction of experimental data and the first-principles results no alterations were made to the thermodynamic evaluation.

3.3.3 Ti-Ta

The Ti-Ta binary was taken from the COST 507 database and evaluated by Saunders [11]. The phase diagram is shown in Figure 3.3a. The figure is plotted with liquidus and solidus experimental data (\diamond , Y) as well as bcc and hcp solvus data (\triangle , \square , \circ). The evaluation includes interaction parameters for the fcc, hcp, liquid, AIM-D019, AIM-D022, AlTi-L10 and the bcc#1 and bcc#2 ordered and disordered phases. The thermodynamic description reproduces the phase boundary experimental data from Murray et al. [15]. The first-principles results (circles) and

the enthalpy of formation of the bcc phase predicted by the CALPHAD modeling is shown in Figure 3.3b. The CALPHAD prediction of the enthalpy of formation reproduces the results from first-principles reasonably well on the Ti-rich and Ta-rich sides. The first-principles results between 10 and 60 at % Ta vary on an average by 0.17 kJ/mol-atom. However, the CALPHAD prediction is at 300 °K and the first-principles are at 0 °K which explains the variance and the CALPHAD prediction follows the same trend that is seen in the first-principle results. The modeling and sublattices used were compatible with the database being built and thus the thermodynamic description by Saunders was not altered.

3.3.4 Ti-Zr

The thermodynamic description of the Ti-Zr alloy system evaluated by Kumar et al. [16] is used in the present work. The model by Kumar et al. was used in the ternary modeling of the Ti-Mo-Zr and Ti-Nb-Zr ternary alloys. The sublattice modeling was consistent with the previous binary systems. The evaluation introduced interaction parameters for the liquid, bcc, and hcp solution phases. Figure 3.4a plots the evaluation compared with phase boundary data for the bcc to hcp phase (\circ) transformation and solidus (\diamond). The thermodynamic description accurately reproduces the phase boundary data. The evaluation also included heat of transformation data shown in the paper by Kumar et al. [16]. Figure 3.4b plots the first-principles results (circles) versus the CALPHAD prediction (solid line) for the enthalpy of formation of the bcc phase. The DFT results and CALPHAD modeling vary on average by 1.2 kJ/mol-atom. The variance is larger than the other binary alloys due to the instability of the bcc phase at both 0 °K and 300 °K for the Ti-Zr alloy but the calculations and CALPHAD prediction follow the same trend. Based on the agreement between the experimental data, first-principles and CALPHAD prediction no alterations were made to the thermodynamic description.

3.3.5 Non Ti-containing binaries

Figure 3.5 shows the evaluation of the Mo-Nb, Mo-Ta, and Nb-Ta alloys. The Mo-Nb, Mo-Ta and Nb-Ta binary descriptions were adapted from the Mo-Nb-Ta ternary paper by Xiong et al. [17]. Xiong et al. introduced binary interaction parameters for the liquid and bcc solution phases. The Mo-Nb evaluation was

completed using differential thermal analysis experiments that measured both the liquidus and solidus temperature. Multiple authors measured experiments and Xiong et al. picked the experiments (shown in the figure as X, +) that estimated the pure elements reasonably well to build the evaluation on. Xiong et al. saw that the experiments shown by \circ , \triangle , \square agreed well with the thermodynamic description. The remaining work (\diamond , *) was too low and thus wasn't included in the evaluation of the binary alloy. The Mo-Ta alloy evaluation was done using two sets of experimental data (\triangle , *, \diamond , \square) for the evaluation that agree well with the accepted melting temperatures of Mo and Ta. The remaining experimental data (\circ) was higher than the other experimental work by 70 °C and thus was not used for the evaluation. The Nb-Ta binary evaluation was done using the melting temperature experimental data (\circ , \triangle , \square) because it predicted the melting temperatures of Nb and Ta accurately. The remaining experimental work which measured the solidus temperature (*) was not used because the melting temperatures of Nb and Ta showed discrepancy. The remaining experimental work (\diamond) was not included in the evaluation because similarly to the Mo-Ta alloy the experimental work was 70 °C higher than the other work. These three evaluations were chosen because these binaries were evaluated to make up the Mo-Nb-Ta ternary alloy and the modeling was done consistently using the same sublattices models. The evaluations fit well with available experimental data and thus they can be added to the database without any changes.

Figure 3.6 shows the Mo-Zr, Nb-Zr, and Ta-Zr alloys. For the Mo-Zr binary alloy system, there were multiple previous thermodynamic descriptions and experimental results available. In the present work, the evaluation by Perez et al. [18] was chosen. The experimental data plotted was determined for the single-phase region, two-phase region, phase boundaries and peritectic and eutectoid reactions. Perez et al. goes into more detail on the available experimental data and was included in the evaluation of the thermodynamic description. The thermodynamic description generally reproduces all experimental data and is compatible with the sublattice modeling used in the database. The Perez et al. model was also incorporated into the Ti-Mo-Zr ternary modeling. Perez et al. introduced interaction parameters for the liquid, bcc, hcp and MZr_2 (laves_c15) phases. The Nb-Zr alloy thermodynamic description evaluated by Guillermet [19] was chosen for the present work. The figure shows the solidus experimental data (\diamond , *) as well as the hcp solvus (Y , \circ) and bcc

miscibility gap (\square , $+$, \triangle)data. The description includes interaction parameters for the liquid, bcc and hcp solution phases. The thermodynamic description was chosen because it was the description that Kumar et al. [16] included in his modeling of the Ti-Nb-Zr alloy system. The experimental phase boundary and liquidus data from Abriata et al. [20] fits well with the model. The Ta-Zr binary evaluated by Guillermet [21] was chosen for the present database. As Guillermet discusses there was quite a lot of experimental data, shown in the figure. Guillermet discusses the experimental data more in his paper. The figure plots single-phase, two-phase, phase boundary, and solidus experimental data. Interaction parameters were introduced for the bcc, hcp and liquid phases. Guillermet had phase boundary results from at least 5 different authors and thermodynamic results from three different authors. The evaluation reproduced the data fairly well. The sublattice modeling fit with the database and thus this binary was selected. The interaction parameters for all the binary systems are listed in Table ??.

3.4 Ti-containing ternary sections

3.4.1 Ti-Mo-Nb

A thermodynamic description for the Ti-Mo-Nb ternary system has never been evaluated. Two experimental investigations were done on the Ti-Mo-Nb system at 873 °K and 1373 °K [24, 83]. While both investigations agree that the isothermal section at 1373 °K is solely the bcc phase, the investigations differed on the phase boundary data at 873 °K. It is suspected that at such a low temperature the samples did not reach equilibrium which accounts for the discrepancy. Based on this, the binary interpolation of the isothermal sections at 1373 °K and 873 °K were plotted. The phase diagram at 1373 °K agreed with the experimentally determined phase diagram to be solely the bcc phase. The phase diagram at 873 °K is plotted in Figure 3.7a. The discrepancy at 873 °K, is the existence of the bcc miscibility gaps as well as what compositions the phase boundary lines lie at. First-principles calculations of the enthalpy of formation of the bcc phase are plotted against the binary interpolation in Figure 3.7b. While the first-principles calculations are at 0 °K and the binary interpolation is at 300 °K the calculation results are reproduced with the CALPHAD prediction. The prediction varies by less than 1.5 kJ/mol-

atom for all the calculations except at $\text{Mo}_{0.5}\text{Nb}_{0.5}$. While the calculation varies substantially from the prediction at $\text{Mo}_{0.5}\text{Nb}_{0.5}$, in order to improve this, the Mo-Nb binary system would have to be adjusted. In the present work, no thermochemical data was used to ensure the accuracy of the non Ti-containing binary systems but the previous binary models were able to reproduce the phase boundary data as discussed above. Based on the discrepancy between the experimental data and the fact that the thermochemical first-principles calculations are reproduced well by the binary interpolation, no ternary interaction parameters were evaluated.

3.4.2 Ti-Mo-Ta

The thermodynamic description of the Ti-Mo-Ta alloys system had not been previously modeled. The binary interpolation of the Ti-Mo-Ta alloy is plotted in Figure 3.8a at 873 °K and compared with experimental data from Nikitin et al. [22]. At 873 °K, the Ti-Mo-Ta alloy has the bcc and hcp solution phases. The experimental data showed a two-phase bcc-hcp region in the Ti-rich corner, while the binary interpolation shows a bcc miscibility gap which forms a tie triangle with the hcp phase. Figure 3.8b shows the first-principles calculations (circles) of the enthalpy of formation of the bcc phase compared with the binary interpolation from the CALPHAD prediction. The first-principles calculations line up fairly well with the CALPHAD prediction. However, due to the discrepancy of the experimental data, ternary interaction parameters were evaluated using the experimental and first-principles results. Interaction parameters for the hcp and bcc phases were investigated. The evaluated interaction parameters are listed in Table 3.3. After assessing the ternary interaction parameters, the isothermal section was again plotted and compared with experimental data in Figure 3.9a and the enthalpy of formation of the newly assessed bcc phase is plotted as a dashed line in Figure 3.8b. The assessment reproduces the first-principles results. With the introduction of the interaction parameters the isothermal section fits with the experimental data. Figure 3.9b is zoomed in on the Ti-rich corner. The work by Nikitin determined hcp phase boundary data plotted as (○) and two phase experimental data as (●). The two phase experimental data is reproduced by the current model. The hcp phase boundary data is not reproduced. However, reliable solid phase boundary data is difficult to obtain at such a low temperature and if the evaluation is altered

to fit the data it then over fits and stabilizes non-equilibrium phases.

3.4.3 Ti-Mo-Zr

The thermodynamic description of the Ti-Mo-Zr alloy system was previously modeled by Kar et al. [23]. The same binary phases used in the modeling by Kar et al. were included in the database. The phases in this system are liquid, bcc, hcp and laves_c15. After interpolating the ternary system from the binary models and comparing to two sets of available experimental data, Kar et al. introduced interaction parameters for the laves_c15 phase. Using the model by Kar et al., the present work plotted the ternary isothermal section at 1273 °K comparing to phase boundary data plotted in Figure 3.10a. As discussed by Kar et al. there is phase boundary data from two authors. The sets of phase boundary data conflict on how far out the two-phase region should extend toward the Ti-rich corner and whether there is a bcc miscibility gap. After plotting the data, Kar et al. decided not to introduce any bcc, liquid or hcp interaction parameters. Only one set of phase boundary data is plotted [24]. The phase boundary data fits well on the Zr-Mo binary side. The predicted enthalpy of formation of the bcc phase is plotted with the first-principles results in Figure 3.10b. The first-principles results vary on average by 0.025 kJ/mol-atom. Based on the available experimental data, first-principles calculations and the conclusions from Kar et al. the present work agrees with the introduction of the ternary laves_c15 interaction parameters and lack of liquid, bcc and hcp ternary interaction parameters. The ternary laves_c15 interaction parameters are listed in Table 3.3.

3.4.4 Ti-Nb-Ta

A thermodynamic description of the Ti-Nb-Ta had not been evaluated but different isothermal sections had been estimated by Na et al. [25] using phase boundary data. The phase boundary data was obtained through XRD. Na et al. looked at samples at 823 °K and 673 °K. The authors discussed that it is likely that the alloys at 673 °K never reached equilibrium conditions. The experimental results were plotted on the binary interpolation in Figure 3.11a and Figure 3.11b. The bcc phase boundary data does not match with the binary interpolation. Figure 3.11c plots the enthalpy of formation of the bcc phase predicted by the CALPHAD

modeling and compared with the first-principles results. The first-principles results vary from the CALPHAD prediction. The variance of the first-principles results and the variance of the experimental data lead to the evaluation of ternary interaction parameters for the bcc and hcp phases. The evaluation was done using the 823 °K experimental data and first-principles calculations. Due to the conclusion by Na et al. that the 673 °K samples did not reach equilibrium the data was neglected during the evaluation. The evaluation led to only one bcc ternary interaction parameter needed and it is listed in Table 3.3. After evaluation, the ternary isothermal sections are plotted with the phase boundary data in Figure 3.12a and Figure 3.12b. The isothermal sections at both 673 and 823 °K reproduces the experimental data reasonably well. The prediction of the enthalpy of formation of the bcc phase also improved to accurately predict the first-principles results.

3.4.5 Ti-Nb-Zr

The Ti-Nb-Zr was previously evaluated by multiple authors. In the present work the ternary isothermal sections were compared with work by Kumar et al. [16] and Tokunaga et al. [26]. The Ti-Zr and Nb-Zr binary alloys were the same modeled binaries as chosen by Kumar et al. The Ti-Nb binary however was changed to a newer evaluation by Zhang et al. [13] which was discussed above. In the evaluation done by Kumar et al. [16], the liquidus projection and various isothermal sections were interpolated from the binary alloys but not compared with experimental data. In the present work, the binary interpolation was used to plot the isothermal sections at the same temperature as Kumar et al. The ternary isothermal sections varied due to the change in the Ti-Nb binary. The binary interpolation of the isothermal section at 843 °K is plotted in Figure 3.13a and compared with experimental data for the tie triangle (\triangle) and two-phase region (\square) shown in the paper by Tokunaga et al. [26]. The binary interpolation reproduced the hcp and bcc disordered and ordered tie triangle phase boundary data and the two-phase bcc miscibility gap region. The enthalpy of formation of the bcc phase is plotted in Figure 3.3b. The CALPHAD prediction varies on an average by 1.34 kJ/mol-atom. While it the CALPHAD prediction varies more drastically than the other enthalpies of formation from the calculated first-principles results, it follows the same trend and fits well with the experimental data. So, the conclusion was reached to not introduce ternary

interaction parameters.

3.4.6 Ti-Ta-Zr

For the Ti-Ta-Zr alloys system, Lin et al. [27] calculated the isothermal sections using binary interpolations and introduced no interaction parameters. The isothermal sections at 1273 and 1773 °K are plotted in Figure 3.14a and Figure 3.14b. Experimental phase boundary data (○) along the bcc miscibility gap at 1273 °K and single phase ● and two phase region ◉ data using x-ray diffraction at 1773 °K are plotted to compare with the binary interpolation [27, 28]. The phase boundary data is reproduced excellently. The single-phase data fits well with the interpolation with the two-phase region falling on the phase boundary line. Figure 3.14c is the enthalpy of formation of the bcc predicted from first-principles calculations and the binary interpolation. On average the first-principles varies by 3.69 kJ/mol-atom. While this variance is larger than other plots it can be attributed to the temperature difference and instability of the bcc phase at 300 °K and 0 °K. Since the experimental data is reproduced, it was concluded that no overfitting to the first-principles calculations was needed and thus none were evaluated. After evaluation, the thermodynamic descriptions of all the binary systems and Ti-containing ternary systems are listed in Table 3.3 and combined into a single tdb database in the appendix.

3.5 Conclusion

The present work builds a thermodynamic database for the Ti-Mo-Nb-Ta-Zr system using descriptions of the pure elements, binary systems and Ti-containing ternary systems. The thermodynamic descriptions of the pure elements was adapted from the SGTE database [31]. The previous models for the binary systems were evaluated for compatibility and accuracy. With the present application focusing on Ti-alloys, first-principles results for the enthalpy of formation of the bcc phase was used to ensure the accuracy of the thermodynamic descriptions in predicting thermochemical data. Binary interpolations were predicted for the Ti-containing ternary systems and compared with isothermal experimental data as well as first-principles of enthalpy of formation of the bcc phase. When needed the ternary interaction, parameters were evaluated. The compatible thermodynamic descriptions were

complied into a single tdb database. The raw first-principles data as well as the tdb database are in appendix A.

Table 3.1. Bulk modulus B and enthalpy are listed for each pure element in their SER phase listed. The sv and pv refer to the electrons chosen as valance according to the VASP recommendations. The results are compared with available experimental data.

Pure Elements	Reference	Phase	Enthalpy (kJ/mol-atom)	B (GPa)
Ti_sv	Shang [84]	hcp	-7.89	113
	Expt 300 K [85]			110
Mo_pv	This work 0 K	bcc	-10.84	262
	Expt 300 K [86]			261
Nb_sv	This work	bcc	-10.22	171
	Expt 300 K [87]			172
Ta_pv	This work 0 K	bcc	-11.85	196
	Expt 300 K [87]			196
Zr_sv	Shang 0 K [84]	hcp	-8.51	94
	Calc 0 K [88–91]			94

Table 3.2: First-principles calculations of the enthalpy of formation of the bcc phase in kJ/mol-atom for different atomic percent compositions of the Ti-X binary systems at 0 K.

BCC Phase 0 K	x(Ti)	x(X)	HForm (kJ/mol-atom)
Ti	1.000	0.000	7.29
Ti15Mo	0.937	0.063	3.08
Ti7Mo	0.875	0.125	2.82
Ti75Mo25	0.750	0.250	1.12
Ti50Mo50	0.500	0.500	-3.67
Ti25Mo75	0.250	0.750	-5.18
TiMo15	0.063	0.937	1.79
TiMo53	0.019	0.981	5.82
Mo	0.000	1.000	0.00
Ti53Nb	0.981	0.019	6.92
Ti7Nb	0.875	0.125	5.88
Ti75Nb25	0.750	0.250	7.57
Ti50Nb50	0.500	0.500	8.54
Ti25Nb75	0.250	0.750	1.15
TiNb15	0.063	0.938	0.59
TiNb53	0.019	0.981	0.20
Nb	0.000	1.000	0.00
Ti53Ta	0.981	0.019	7.21
Ti15Ta	0.938	0.063	7.04
Ti7Ta	0.875	0.125	9.28
Ti75Ta25	0.750	0.250	4.89
Ti50Ta50	0.500	0.500	3.94
Ti25Ta75	0.250	0.750	3.10
TiTa15	0.063	0.938	0.94
TiTa53	0.019	0.981	0.28
Ta	0.000	1.000	0.00
Ti53Zr	0.981	0.019	5.49
Ti75Zr25	0.750	0.250	4.59

Table 3.2: First-principles calculations of the enthalpy of formation of the bcc phase in kJ/mol-atom for different atomic percent compositions of the Ti-X binary systems at 0 K.

BCC Phase 0 K	x(Ti)	x(X)	HForm (kJ/mol-atom)
Ti50Zr50	0.500	0.500	1.94
Ti25Zr75	0.250	0.750	3.50
TiZr15	0.063	0.938	5.72
Zr	0.000	1.000	8.19

Table 3.3: Thermodynamic parameters for the Ti-Mo-Nb-Ta-Zr system. The thermodynamic description of the pure elements is not included. The pure elements were adopted from the SGTE database and are listed in the supplementary tdb file [41].

Phase	Reference	Interaction Parameter
Liquid	[11]	$0_{Ti,Mo}^L = -9000.0 + 2.00 * T$
	[13]	$0_{Ti,Nb}^L = 7406.1$
	[11]	$0_{Ti,Ta}^L = 1000.0$
	[11]	$0_{Ti,Ta}^L = -7000.0$
	[16]	$0_{Ti,Zr}^L = -967.7$
	[17]	$0_{Mo,Nb}^L = 15253.7$
	[17]	$1_{Mo,Nb}^L = 10594.2$
	[17]	$0_{Mo,Ta}^L = 13978.9$
	[18]	$0_{Mo,Zr}^L = -24055.1 + 8.146 * T$
	[18]	$1_{Mo,Zr}^L = -5132.17 + 4.804 * T$
	[19]	$0_{Nb,Zr}^L = 10311.0$
	[19]	$1_{Nb,Zr}^L = 6709.0$
	[21]	$0_{Ta,Zr}^L = 13832.1$
	[21]	$1_{Ta,Zr}^L = -7150$
	[11]	$0_{Ti,Mo}^L = 2000.0$
	[11]	$1_{Ti,Mo}^L = -2000.0$
	[13]	$0_{Ti,Nb}^L = 13045.3$
	[11]	$0_{Ti,Ta}^L = 12000.0$
	[11]	$1_{Ti,Ta}^L = -2500.0$
	[16]	$0_{Ti,Zr}^L = -4346.2 + 5.49 * T$
	[17]	$0_{Mo,Nb}^L = -68202.6 + 29.86 * T$
	[17]	$1_{Mo,Nb}^L = 8201.3$
	[17]	$0_{Mo,Ta}^L = -75129.2 + 30.00 * T$
	[17]	$1_{Mo,Ta}^L = 6039.2$
	[18]	$0_{Mo,Zr}^L = 17936.0 + 3.10 * T$
	[18]	$1_{Mo,Zr}^L = -991.0 + 4.30 * T$
	[17]	$0_{Nb,Ta}^L = 1298.0$

Table 3.3: Thermodynamic parameters for the Ti-Mo-Nb-Ta-Zr system. The thermodynamic description of the pure elements is not included. The pure elements were adopted from the SGTE database and are listed in the supplementary tdb file [41].

Phase	Reference	Interaction Parameter
HCP	[19]	$0_{Nb,Zr}^L = 15911.0 + 3.35 * T$
	[19]	$1_{Nb,Zr}^L = 3919.0 - 1.09 * T$
	[21]	$0_{Ta,Zr}^L = 29499.6 + 2.67 * T$
	[21]	$1_{Ta,Zr}^L = -4396.2 + 4.43 * T$
	[21]	$2_{Ta,Zr}^L = -6353.3 + 4.91 * T$
	This work	$0_{Ti,Mo,Ta}^L = -154731.2$
	This work	$0_{Nb,Ta,Ti}^L = -136603.3$
	This work	$1_{Nb,Ta,Ti}^L = -136602.7$
	[11]	$0_{Ti,Mo}^L = 22760.0 - 6.00 * T$
	[13]	$0_{Ti,Nb}^L = 11742.4$
FCC	[11]	$0_{Ti,Ta}^L = 8500.0$
	[16]	$0_{Ti,Zr}^L = 5133.0$
	[18]	$0_{Mo,Zr}^L = 26753.8 + 4.56 * T$
	[19]	$0_{Nb,Zr}^L = 24411.0$
Al3M_D022	[21]	$0_{Ta,Zr}^L = 30051.7$
	[11]	$0_{Ti,Mo}^L = 16500.0$
	[11]	$0_{Ti,Ta}^L = 8500.0$
AlM_D019	[11]	$0_{Ti:Ti}^L = 4 * GFCTTI$
	[11]	$0_{Mo:Mo}^L = 4 * GFCCMO$
	[11]	$0_{Ti:Mo}^L = GFCCMO + 3.0 * GFCTTI$
	[11]	$0_{Mo:Ti}^L = 3.0 * GFCCMO + GFCTTI$
	[11]	$0_{Ti:Ta}^L = GFCTTA + 3.0 * GFCTTI$
	[11]	$0_{Ti:Ti}^L = 4.0 + 4.0 * GHSERTI$
	[11]	$0_{Mo:Mo}^L = 4.0 * GHCPMO$
	[11]	$0_{Ta:Ta}^L = 4.0 * GHCPТА$
	[11]	$0_{Ti:Mo}^L = 17072.0 - 4.5 * T + GHCPMO + 3.0 * GHSERTI$
	[11]	$0_{Mo:Ti}^L = 17072.0 - 4.5 * T + 3.0 * GHCPMO + GHSERTI$

Table 3.3: Thermodynamic parameters for the Ti-Mo-Nb-Ta-Zr system. The thermodynamic description of the pure elements is not included. The pure elements were adopted from the SGTE database and are listed in the supplementary tdb file [41].

Phase	Reference	Interaction Parameter
AlTi	[11]	$0_{Ti:Ta}^L = 6376.0 + GHCPA + 3.0 * GHSERTI$
	[11]	$0_{Ta:Ti}^L = 6376.0 + 3.0 * GHCPA + GHSERTI$
	[11]	$0_{Ti:Mo}^L = 51212.0 - 13.5 * T$
	[11]	$0_{Mo,Ti:Ti}^L = 51212.0 - 13.5 * T$
	[11]	$0_{Mo:Mo,Ti}^L = 5692.0 - 1.5 * T$
	[11]	$0_{Ti:Ti,Mo}^L = 5692.0 - 1.5 * T$
	[11]	$0_{Ta,Ti:Ta}^L = 19128.0$
	[11]	$0_{Ta,Ti:Ti}^L = 19128.0$
	[11]	$0_{Ta:Ta,Ti}^L = 2128.0$
	[11]	$0_{Ti:Ta,Ti}^L = 2128.0$
BCC_B2	[11]	$0_{Ti:Ti}^L = 2.0 * GFCTI$
	[11]	$0_{Mo:Mo}^L = 2.0 * GFCCMO$
	[11]	$0_{Ta:Ta}^L = 2.0 * GFCTA$
	[11]	$0_{Ti:Mo}^L = 8250.0 + GFCCMO + GFCTI$
	[11]	$0_{Mo:Ti}^L = 8250.0 + GFCCMO + GFCTI$
	[11]	$0_{Ti:Ta}^L = 4250.0 + GFCTA + GFCTI$
	[11]	$0_{Ta:Ti}^L = 4250.0 + GFCTA + GFCTI$
	[11]	$0_{Mo,Ti:Mo}^L = 8250.0$
	[11]	$0_{Mo,Ti:Ti}^L = 8250.0$
	[11]	$0_{Mo:Mo,Ti}^L = 8250.0$
disordered phase	[11]	$0_{Ti:Mo}^L = 10000.0$
	[11]	$0_{Mo:Ti}^L = 10000.0$

Table 3.3: Thermodynamic parameters for the Ti-Mo-Nb-Ta-Zr system. The thermodynamic description of the pure elements is not included. The pure elements were adopted from the SGTE database and are listed in the supplementary tdb file [41].

Phase	Reference	Interaction Parameter
LAVES_C15	[11]	$0_{Ti:Ta}^L = 5000.0$
	[11]	$0_{Ta:Ti}^L = 5000.0$
	[23]	$0_{Ti:Ti}^L = 15000.0 + 3.0 * GHSERTI$
	[18]	$0_{Mo:Mo}^L = 15000.0 + 3.0 * GHSERMO$
	[18]	$0_{Zr:Zr}^L = 15000.0 + 3.0 * GHSERZR$
	[23]	$0_{Ti:Mo}^L = 15000.0 + GHSERMO$ + $2.0 * GHSERTI$
	[23]	$0_{Mo:Ti}^L = 15000.0$ + $2.0 * GHSERMO + GHSERTI$
	[23]	$0_{Ti:Zr}^L = 9000.0$ + $GHSERZR + 2.0 * GHSERTI$
	[23]	$0_{Zr:Ti}^L = 15000.0 + 2.0 * GHSERZR + GHSERTI$
	[18]	$0_{Mo:Zr}^L = -21734.8 + 0.14 * T$ + $GHSERZR + 2.0 * GHSERMO$
OMEGA	[18]	$0_{Zr:Mo}^L = 21734.8 - 0.14 * T$ + $2.0 * GHSERZR + GHSERMO$
	[18]	$0_{Mo:Mo,Zr}^L = 60000.0$
	[18]	$0_{Zr:Mo,Zr}^L = 60000.0$
	[18]	$0_{Mo,Zr:Mo}^L = 100000.0$
	[18]	$0_{Mo,Zr:Zr}^L = 100000.0$
	[23]	$0_{Ti:Mo,Zr}^L = 60000.0$
	[23]	$0_{Mo,Zr:Ti}^L = 100000.0$
	[13]	$0_{Ti}^L = 1886.7 - 0.15 * T + GHSERTI$
	[13]	$0_{Nb}^L = 15000.0 + 2.4 * T + GHSERNB$
	[31]	$0_{Zr}^L = -8878.082 + 144.432234 * T$ - $26.8556 * T * LN(T) - .002799446 * T2 + 38376 * T - 1$
		$298.15 < T < 2128$

Table 3.3: Thermodynamic parameters for the Ti-Mo-Nb-Ta-Zr system. The thermodynamic description of the pure elements is not included. The pure elements were adopted from the SGTE database and are listed in the supplementary tdb file [41].

Phase	Reference	Interaction Parameter
	[13]	$-29500.524 + 265.290858 * T - 42.144 * T * LN(T)$ $+ 7.17445E + 31 * T - 9$ $2128 < T < 6000$ $0LTi, Nb = -3775.9$

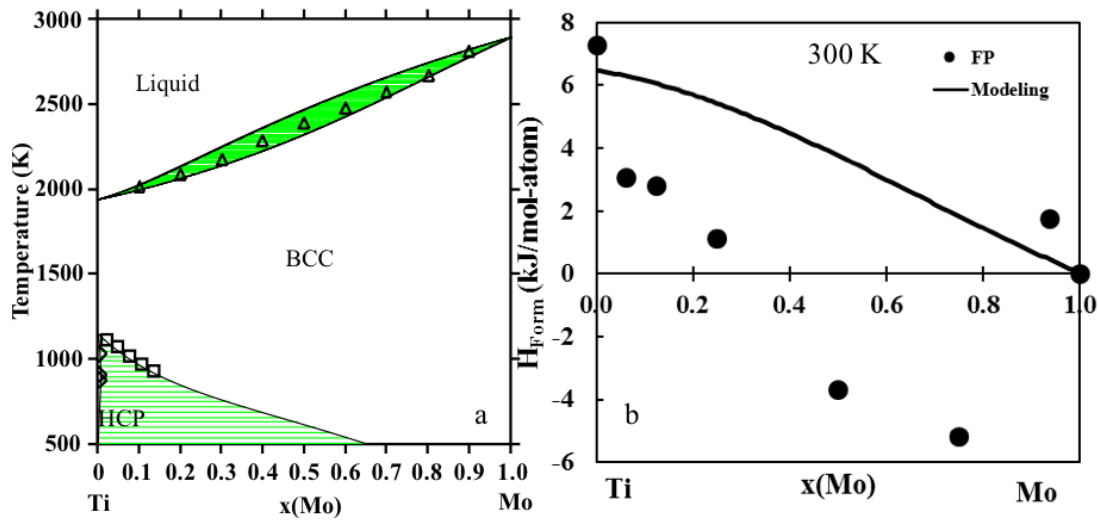


Figure 3.1. Figure a on the left plots the previously modeled thermodynamic description of the Ti-Mo system versus available experimental data to ensure accuracy [11, 12]. Figure b on the right plots the enthalpy of formation of the bcc phase predicted by the previous thermodynamic modeling (solid line) at 300 K versus the present first-principles calculations (circles) at 0 K.

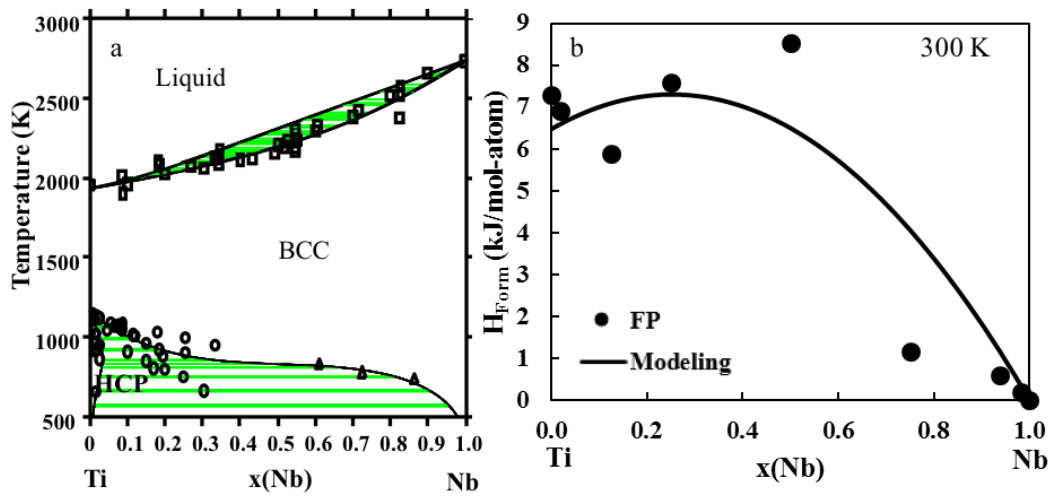


Figure 3.2. Figure a on the left plots the previously modeled thermodynamic description of the Ti-Nb system versus available experimental data to ensure accuracy [13, 14]. Figure b on the right plots the enthalpy of formation of the bcc phase predicted by the previous thermodynamic modeling (solid line) at 300 K versus the present first-principles calculations (circles) at 0 K.

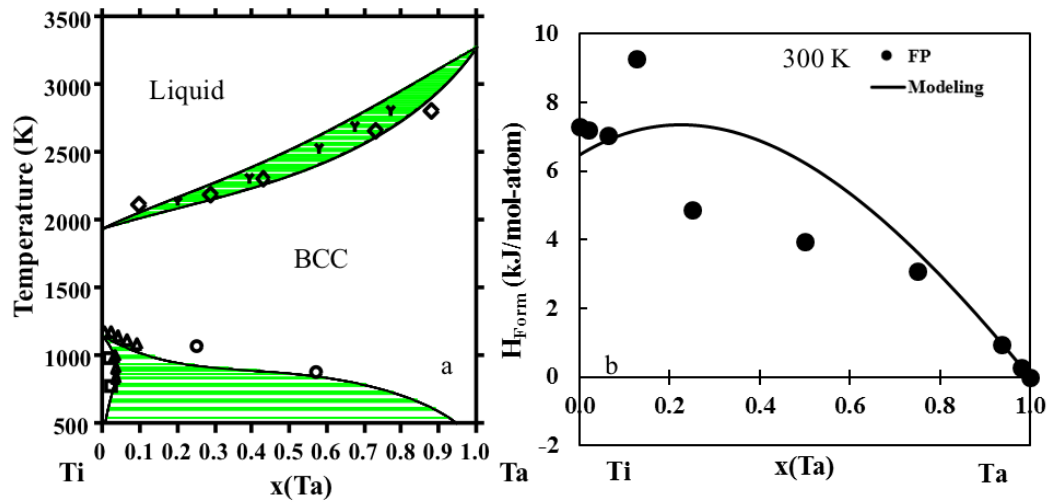


Figure 3.3. Figure a on the left plots the previously modeled thermodynamic description of the Ti-Ta system versus available experimental data to ensure accuracy [11, 15]. Figure b on the right plots the enthalpy of formation of the bcc phase predicted by the previous thermodynamic modeling (solid line) at 300 K versus the present first-principles calculations (circles) at 0 K.

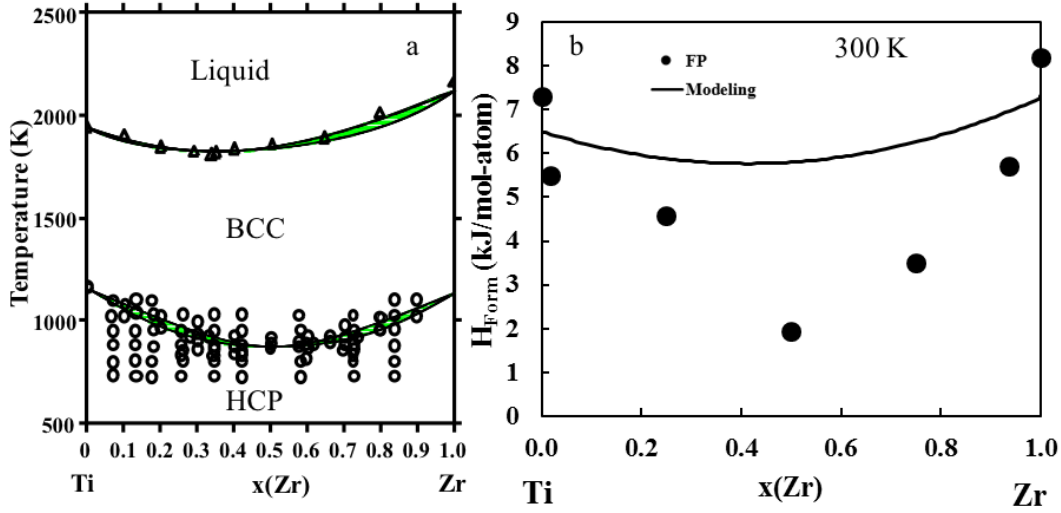


Figure 3.4. Figure a on the left plots the previously modeled thermodynamic description of the Ti-Zr system versus available experimental data to ensure accuracy [16]. Figure b on the right plots the enthalpy of formation of the bcc phase predicted by the previous thermodynamic modeling (solid line) at 300 K versus the present first-principles calculations (circles) at 0 K.

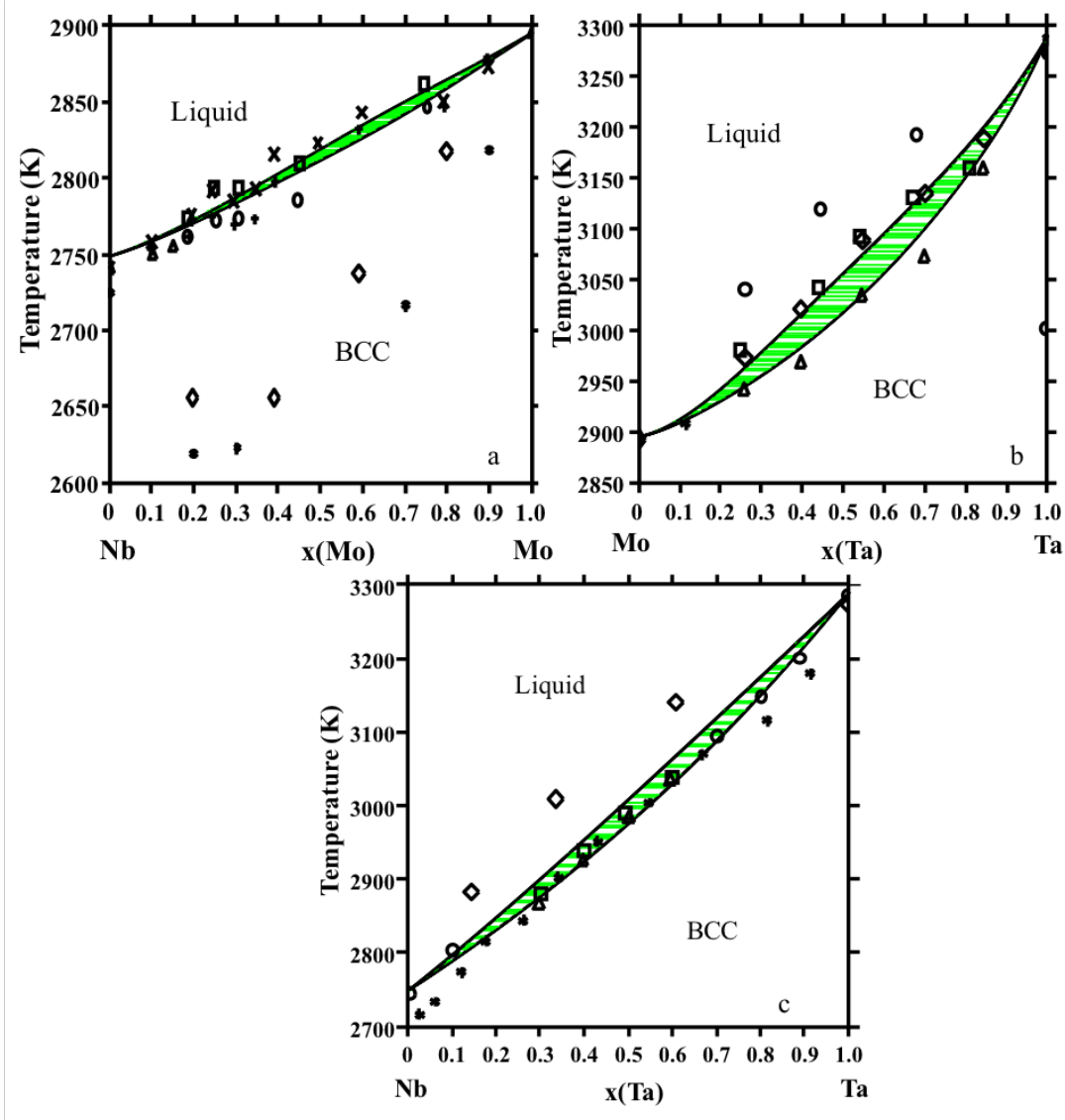


Figure 3.5. The previously modeled thermodynamic descriptions of the Mo-Nb (a) [17], Mo-Ta (b) [17] and Nb-Ta (c) [17] binary systems are evaluated by comparing with available phase boundary experimental data.

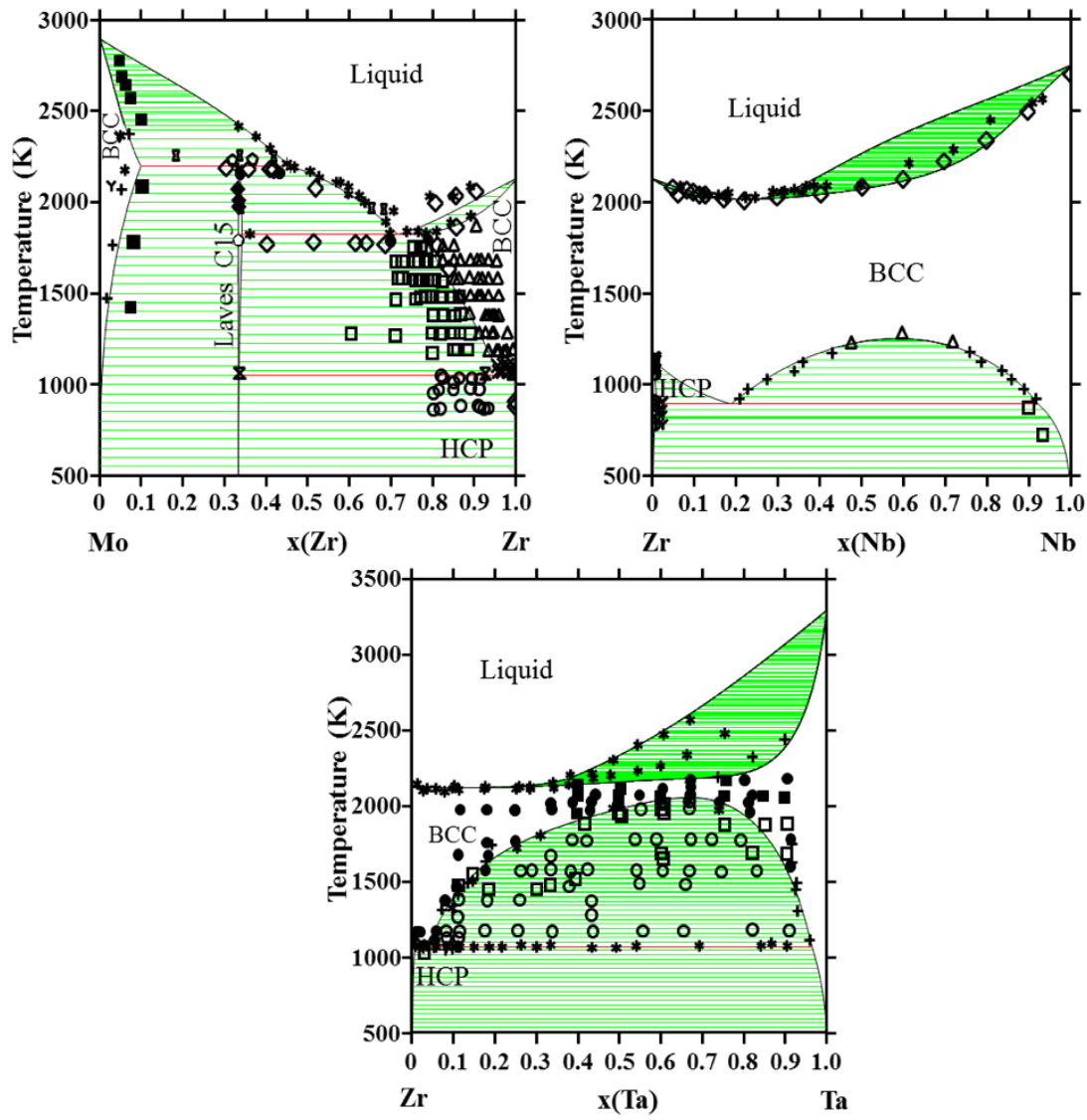


Figure 3.6. The previously modeled thermodynamic descriptions of the Mo-Zr [18], Nb-Zr [19, 20] and Ta-Zr [21] binary systems are evaluated for accuracy by comparing the available experimental phase boundary data.

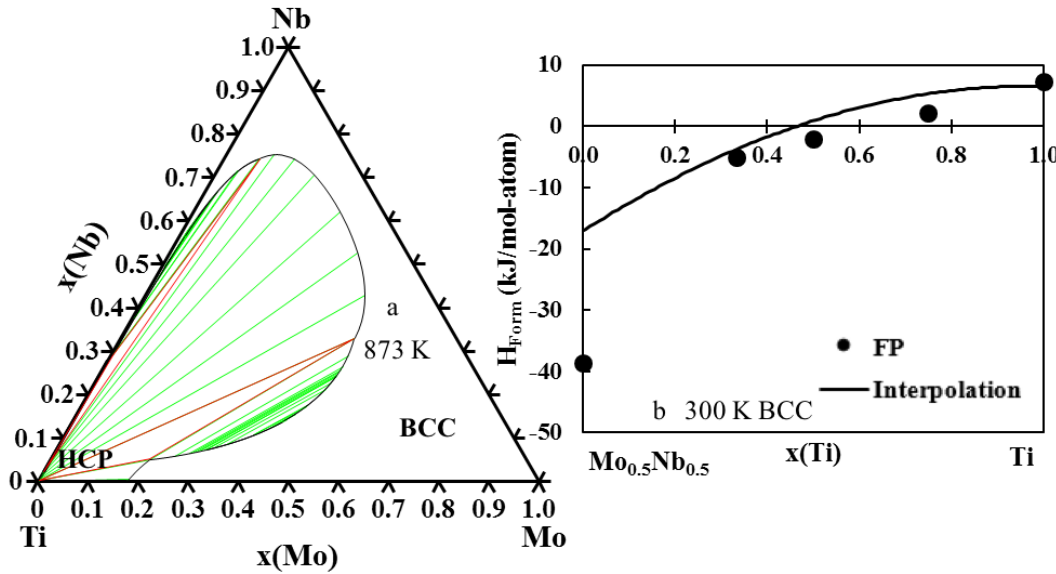


Figure 3.7. Figure a) on the left is a binary interpolation of the isothermal section of Ti-Mo-Nb plotted at 873 K. Figure b) plots the present calculations (circles) and binary interpolation (solid black line) of the enthalpy of formation of the bcc phase.

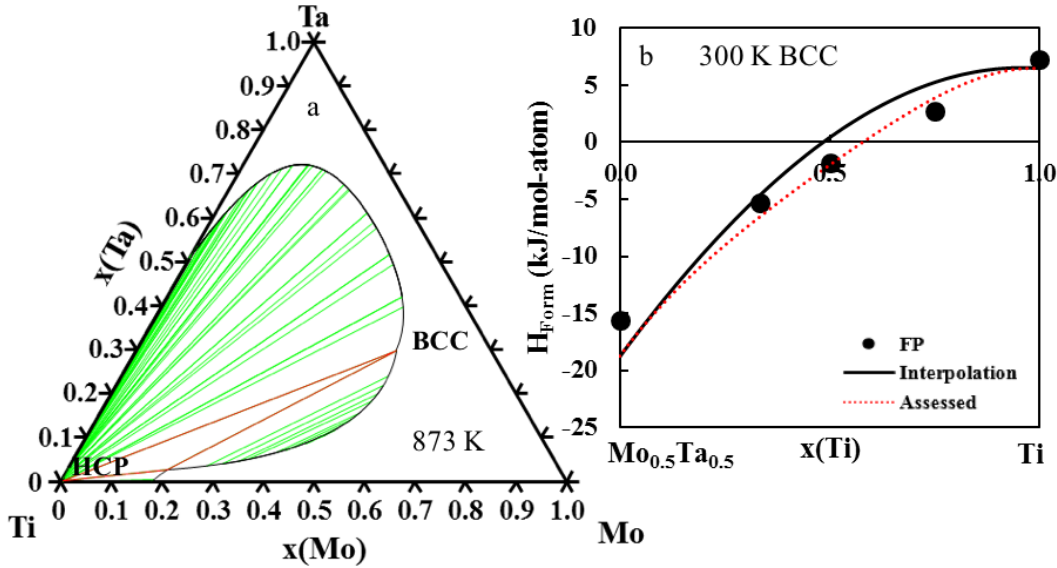


Figure 3.8. Figure a) on the left is a binary interpolation of the isothermal section of Ti-Mo-Ta plotted at 873 K. Figure b) plots the present calculations (circles), binary interpolation (solid black line) and ternary assessed (red dotted line) enthalpy of formation of the bcc phase.

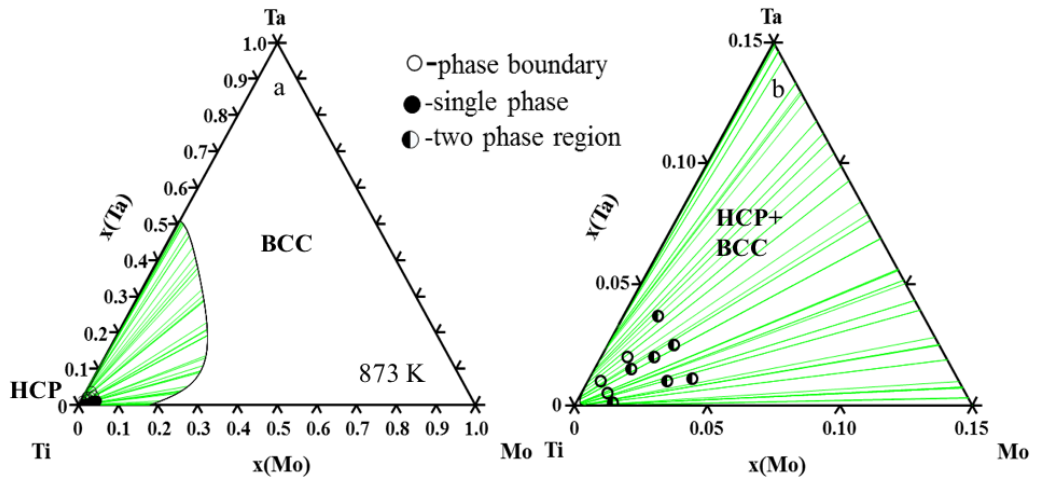


Figure 3.9. Figure a) on the left is the isothermal plot of Ti-Mo-Ta at 873 K after evaluation of the ternary interaction parameters. Figure b) on the right is zoomed in to show the comparison with the experimental data [22].

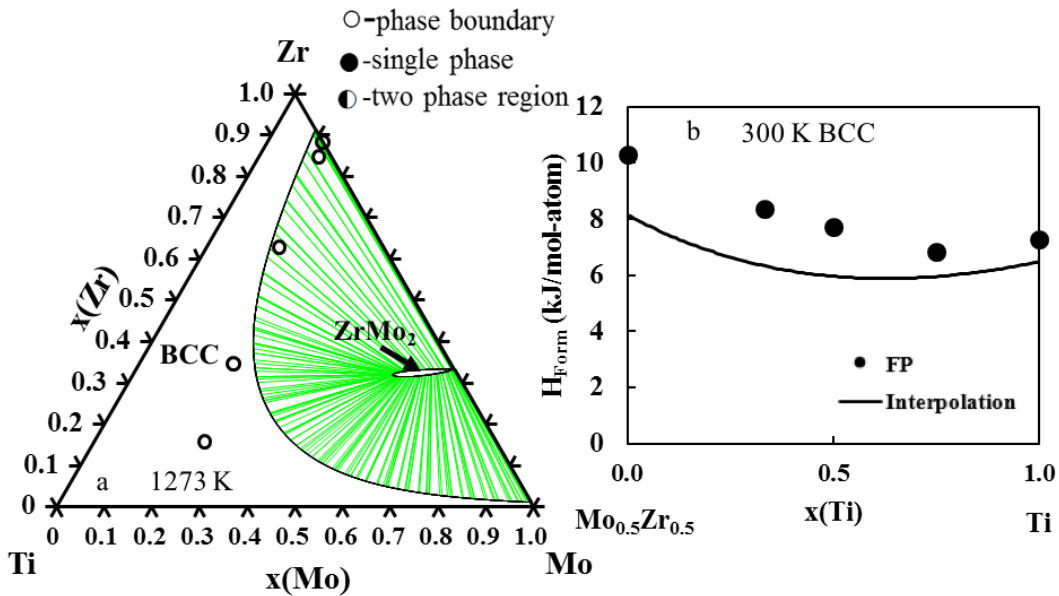


Figure 3.10. Figure a) on the left is a binary interpolation of the isothermal section of Ti-Mo-Zr plotted at 1273 K with experimental phase data obtained at the same temperature [23, 24]. Figure b) plots the present calculations (circles) and binary interpolation (solid black line) of the enthalpy of formation of the bcc phase.

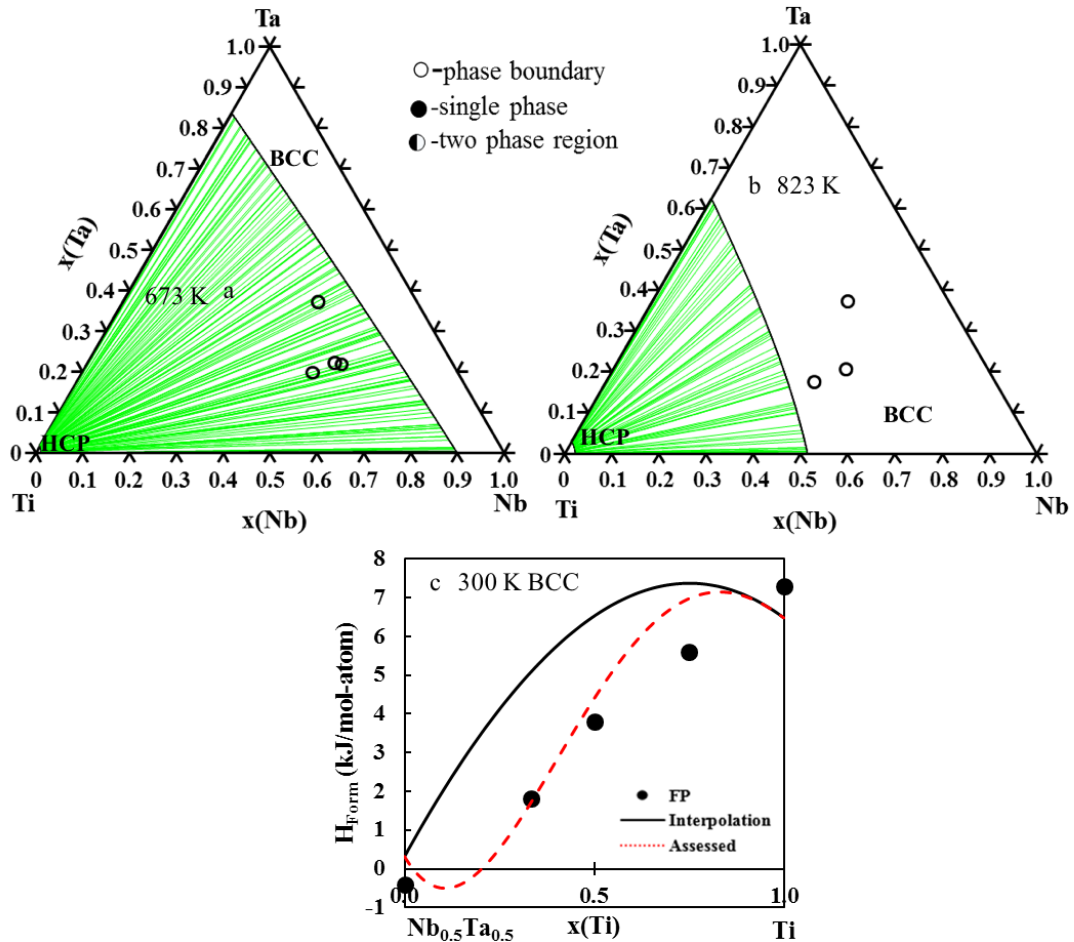


Figure 3.11. Figure a) on the top left is a binary interpolation of the isothermal section of Ti-Nb-Ta plotted at 673 K. Figure b) is a binary interpolation of the isothermal section of Ti-Nb-Ta at 823 K. Both binary interpolations are compared with experimental phase boundary data [25]. Figure c) plots the present calculations (circles), binary interpolation (solid black line) and ternary assessed (red dotted line) enthalpy of formation of the bcc phase.

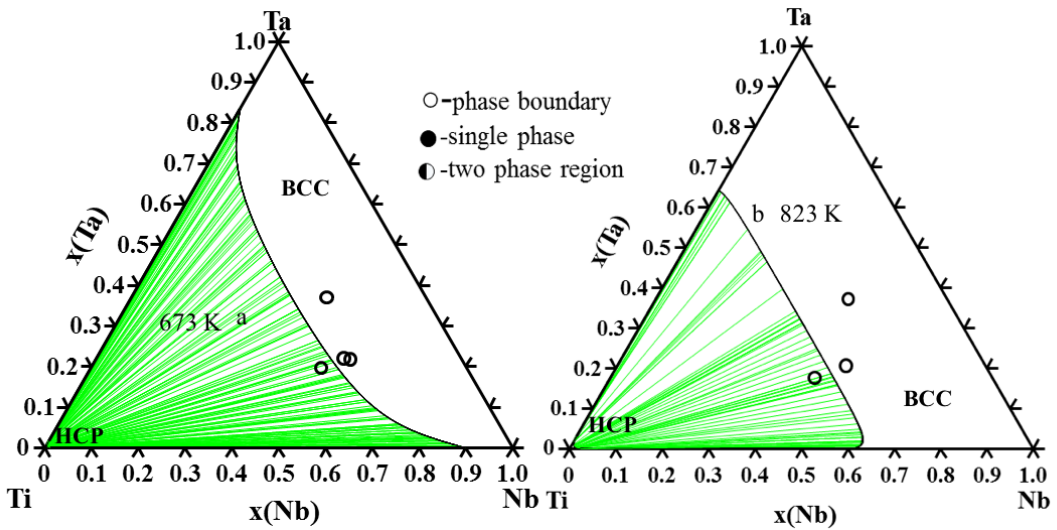


Figure 3.12. Figure a) on the left is the isothermal plot of Ti-Nb-Ta at 673 K after evaluation of the ternary interaction parameters. Figure b) is the evaluated isothermal plot of Ti-Nb-Ta at 823 K. Both plots have experimental phase boundary data [25].

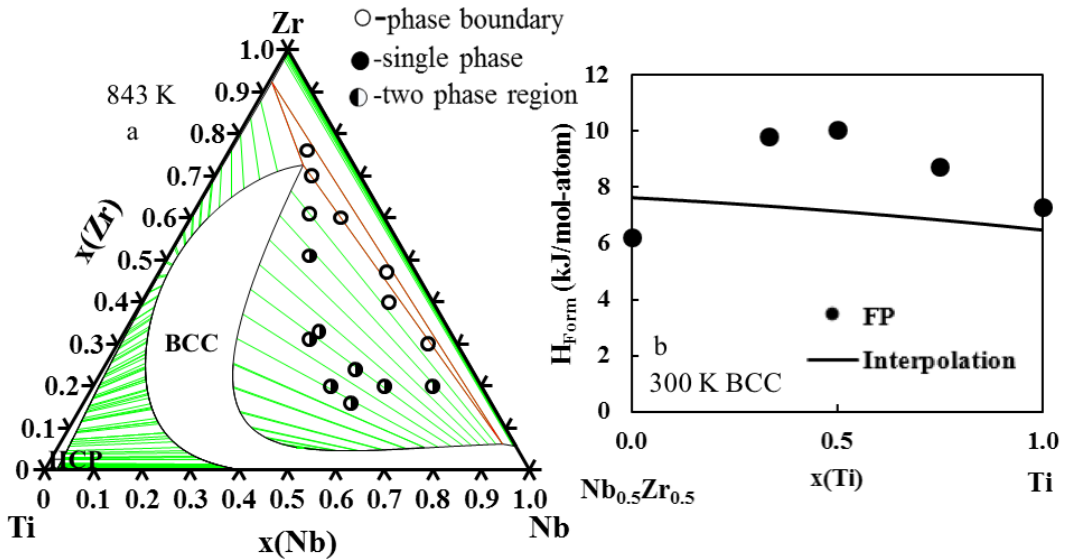


Figure 3.13. Figure a) on the left is a binary interpolation of the isothermal section of Ti-Nb-Zr plotted at 843 K with experimental phase data [26]. Figure b) plots the present calculations (circles) and binary interpolation (solid black line) of the enthalpy of formation of the bcc phase.

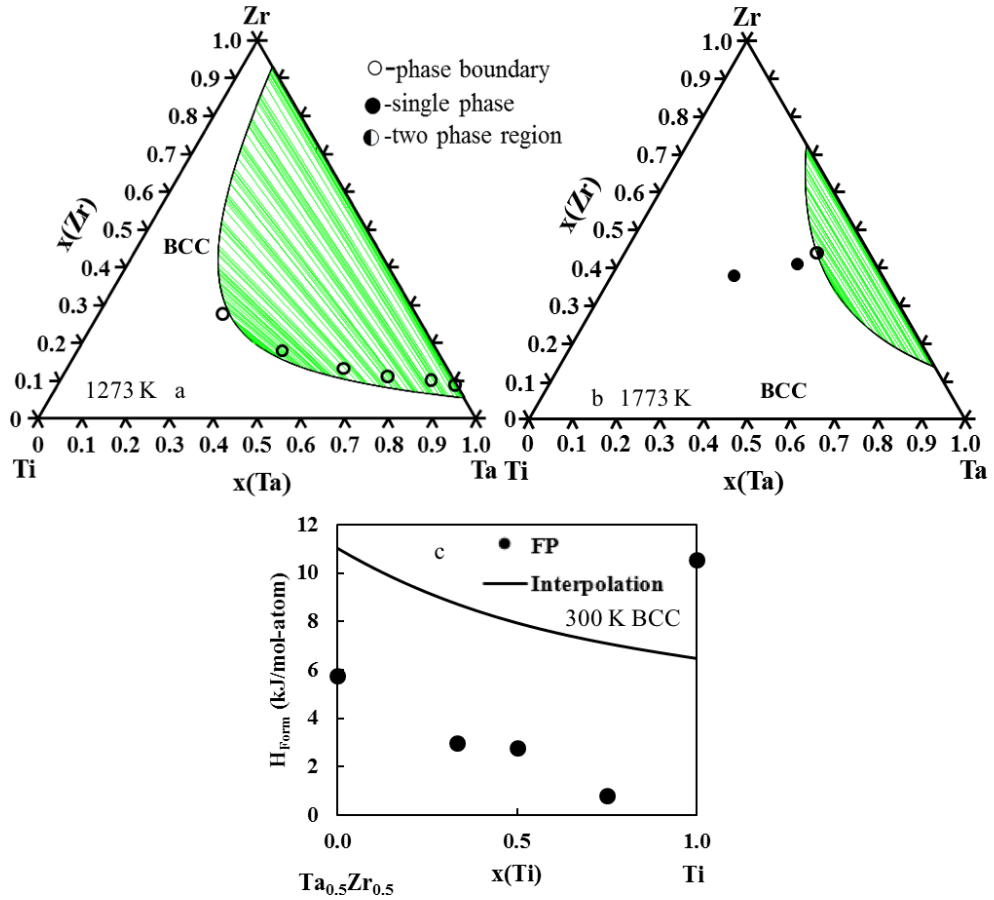


Figure 3.14. Figure a) on the top left is a binary interpolation of the isothermal section of Ti-Ta-Zr plotted at 1273 K. Figure b) is a binary interpolation of the isothermal section of Ti-Ta-Zr at 1773 K. Both binary interpolations are compared with experimental data [27, 28]. Figure c) plots the present calculations (circles) and binary interpolation (solid black line) for the enthalpy of formation of the bcc phase.

Chapter 4

First-principles aided thermodynamic modeling of the Sn-Ta system

4.1 Introduction

Currently, the biomaterial implant research of Ti alloys is focused on biocompatible elements that stabilize the body centered cubic (bcc, β) phase of Ti and help to lower its elastic modulus. Tantalum (Ta) is a biocompatible element and is considered to be a strong -stabilizers [47]. Recently, tin (Sn) has also been researched for use in Ti-alloys due to its biocompatibility and low cost [38]. Kuroba et al. [92] studied various Ti-alloys such as Ti-29-Nb-13Ta-2Sn (weight percentage, and similarly hereinafter unless specified otherwise), Ti-29Nb-13Ta-4Mo, and Ti-29Nb-13Ta-6Sn for use as biocompatible implant materials. Kuroba and Hagiwara [93] also studied new Ti-Cu-Ni-Sn-Ta alloys for the artificial materials used in orthopedic surgeries. The Sn-Ta system is thus an important sub-system for this purpose [94]. A complete knowledge base of the thermodynamic description of Sn-Ta can be used to examine the effects of temperature and composition on phase stability for higher order systems and help to tailor experimental alloy selections to viable options. The CALPHAD technique, in combination with first-principles and phonon calculations based on the DFT, has been proven to provide valuable data to model the thermodynamic properties of binary such as Ta-Sn that lack sufficient experimental data [95]. The Sn-Ta system has three solid solution phases and two intermetallic compounds,

i.e. the bcc, body centered tetragonal (bct), and diamond solution phases, and the intermetallic compounds Ta_3Sn with space group $Pm\bar{3}n$ and $TaSn_2$ ($Ta_{1.2}Sn_{1.8}$) with space group $Fddd$ [96].

In the present work, thermodynamic data was predicted using first-principles calculations for the two intermetallics and for the bcc, bct and diamond solution phases. The finite temperature properties of the phases were obtained using the Debye-Grüneisen model [56] and phonon calculations based on the supercell approach [59]. The DFT data was used to model the parameters of the Gibbs energy of each phase using the CALPHAD technique.

4.2 Literature Review

The Sn-Ta binary system was studied by Okamoto [96], Studnitzky and Schmid-Fetzer [97], and Basile [98]. Both of the intermetallic phases, Ta_3Sn and $TaSn_2$, were shown to have a very narrow homogeneity range. Basile [98] observed that $TaSn_2$ is located around $Ta_{1.2}Sn_{1.8}$ which was then designated as Ta_2Sn_3 by Okamoto [96]. It seems that $TaSn_2$ is a more compatible description of the stoichiometric compound based on the descriptions of similar systems (V-Sn, and Nb-Sn) [99–101], and thus will be used in the present work. Basile [98] determined $TaSn_2$ has a peritectic reaction at 595 °C and used X-ray diffraction (XRD) to elucidate the lattice parameters of $TaSn_2$.

Studnitzky and Schmid-Fetzer [97] used powder samples to study the Ta_3Sn intermetallic phase and verified the results previously reported by Basile [98]. They cold pressed the pure element powders at 600 MPa and then heated the pellets at 1000 °C for up to 48 hours. The resulting pellet was then cold pressed at 600 MPa again. Under these conditions $TaSn_4$ was observed at 400 °C, but was not present as the temperature increased to 600 °C. In the work by Courtney et al. [102], Ta_3Sn was studied to see how the temperature affects the long-range ordering parameter. In Courtney et al.’s work, Ta_3Sn powder samples were sintered at 600, 700, 950, 1200, and 1450 °C for 2, 4, 7, and 16 days, respectively. Each sample was then studied using XRD at room temperature to examine the phases present and the long-range ordering. They concluded that the transition temperature of superconductivity for Ta_3Sn varied by a maximum of 4 °K based on heat treatment and sintering times due to long-range ordering that occurred. Courtney et al. also

measured the lattice parameter of each sample and reported the average value of this cubic phase being 5.285 Å.

4.3 Modeling and Calculations

4.3.1 First-principles details

In the present work, the Vienna ab-initio Simulation Package (VASP) was used to perform the first-principles calculations [57]. The projector augmented-wave (PAW) [58, 79] method was used to describe the electron-ion interactions. Based on the work of comparing X-C functionals (Figure 2.1) the exchange-correlation functional of the generalized gradient approach depicted by Perdew, Burke, and Ernzerhof (PBE) was employed [54]. A sigma value of 0.2 eV and a plane wave energy cutoff of 1.3 times higher than the highest default cutoff was adopted. The Brillouin zone sampling was done with Blöchl corrections [79] using a gamma centered Monkhorst-Pack (MP) scheme [80]. The k-points grid for diamondSn, bcc-Ta, TaSn₂, and bcc-Sn were 4x4x4, 6x6x6, 10x10x5, and 6x6x6 respectively. The k-point grids for the bct-Sn, Ta₃Sn and bcc SQS calculations used an automated k-point mesh generator in VASP with the length of the subdivisions specified as 80. The energy convergence criterion of the electronic self-consistency is set as 10⁻⁴ eV/atom and 10⁻⁴ eV/A was set as the stopping criteria for the ionic relaxation loop for all of the calculations.

To calculate the enthalpy of formation of the bcc phase across the entire composition range, the enthalpy of formation of Ta and Sn in the bcc phase were calculated with five different compositions of Ta_{1-x}Sn_x, where x=0.0185 (Ta₅₃Sn, 54 atoms), 0.25, 0.5, 0.75, and 0.9815 (TaSn₅₃, 54 atoms). For x=0.0185 and 0.9815, calculations were performed on a diluted 54 atom cell where all atoms but one was Sn or Ta (Ta₅₃Sn and TaSn₅₃). For x=0.25, 0.5, and 0.75, 16-atom special quasirandom structures (SQS) in the bcc phase developed by Jiang et al. [69] were used to mimic the behavior of random structures. The relaxation of these structures is complicated and discussed in the methodology section. The enthalpy of formation was plotted as a function of composition and then used for the modeling.

4.3.2 CALPHAD

The Gibbs energy functions of pure elements were adopted from the SGTE (SSUB) database [31]. In the present work, the bcc and liquid phases were modeled in conjunction with the two intermetallics Ta_3Sn and $TaSn_2$. Dilute first-principles calculations of Ta in Sn were done for the diamond and bct phases. However, there is little solubility of Ta in these phases and there is no description of pure Ta in these phases available in SGTE. So, no binary interaction parameters were introduced in the modeling similar to other Sn systems such as Nb-Sn and V-Sn [99, 101]. The energy of the liquid and bcc solution phases were modeled using Eq. 2.30 and 2.31, while Ta_3Sn and $TaSn_2$ were modeled according to Eq. 2.34.

4.4 Results and discussion

4.4.1 First-principles

To evaluate the accuracy of phonon calculations for the present system, both the dispersion curves and the phonon DOS are plotted for bcc-Ta, bct-Sn, $TaSn_2$, and Ta_3Sn in Figure 4.1, Figure 4.2, Figure 4.3, and Figure 4.4, respectively. The bcc-Ta phonon dispersion curve in Figure 4.1 is compared with values obtained by Taioli et al. [29] using neutron scattering, showing good agreement. The longitudinal modes (LO) and the transverse modes (TO) measured by Raman spectroscopy [30] (open square) along with the previous theoretical predictions at the M point (filled square) for bct-Sn are compared with the calculated phonon dispersion curve in Figure 4.2. The substantial difference for the LO mode may be due to the temperature and pressure differences as pointed out by Olijnyk [30]. No imaginary phonon frequencies are obtained in the phonon DOS plots for bcc-Ta, bct-Sn, $TaSn_2$, Ta_3Sn , indicating that they are all mechanically and dynamically stable at 0 °K.

The calculated lattice parameters at 0 °K from the EOS fitting and with the Debye and phonon models at 298 °K are compared to available experimental and previous DFT results in Table 4.1. The lattice parameters of Ta are compared with the experimental lattice parameters by Predmore and Arsenault [103] at room temperature and the previous 0 °K DFT results by Shang et al. [84] who used the GGA-PW91 exchange correlation functional. The Sn lattice parameters are

compared to experimental work by Allen et al. [104] at 298 °K and calculations by Arróyave et al. [105]. The properties of the TaSn₂ and Ta₃Sn intermetallics have not been calculated previously and are compared to experimental values by Calvert et al. [106] and Courtney et al. [102], respectively. The results show a less than 0.5% difference when compared with other DFT results at 0 °K. There is a less than 2% difference between the DFT 0 °K results and the experiments, which are listed in Table 4.1. The variance is due to the fact that the calculations are at 0 °K and the experiments are at a higher temperature. When comparing the calculated lattice parameters at 298 °K to the experiments, all of the predictions improve to show a less than 1% difference with the exception of Sn, which shows a less than 2% difference.

Table 4.2 shows the equilibrium volume, V_0 , bulk modulus, B_{EOS} , and the derivative of bulk modulus B'_{EOS} obtained by the EOS E-V fitting of the first-principles data at 0 °K. The Sn and Ta calculations are compared with previous first-principles calculations and available experiments. The volume shows a less than 0.5% difference between the previous DFT results and current DFT results for both Sn and Ta [103, 107]. The comparison of the DFT results at 0 °K and the experimental results at 298 K for volume show a slightly higher variance of less than 5 % due to the different in temperature [84, 107]. The B_{EOS} comparison of previous 0 °K DFT results and the present 0 °K DFT results show a less than 7 GPa difference and the DFT results at 0 °K vary by less than 11 GPa from the experimental results at 298 °K [84, 103, 107]. The difference between the current calculations and the previous values may be due to many reasons; e.g. the different choices in input parameters used by Peltzer et al. [107] and different exchange correlation functionals. Another reason is due to the temperature difference 0 °K (calculations) versus 298 °K (experiments). Figure 4.5 shows the enthalpy and entropy of Ta from the Debye and phonon approaches in comparison with the data from the SGTE pure element database [31]. Figure 4.6 shows the comparison of the enthalpy and entropy calculated for Sn from the phonon and Debye model to the SGTE pure element database [31]. Both show excellent agreement.

The elastic stiffness constants and polycrystalline elastic properties calculated by the Hill approach and the scaling factors for the Debye model are shown in Table 4.3. To ensure the accuracy of the scaling factor, the elastic stiffness constants and moduli are compared with previous first-principles results [89–91, 108, 109]. The

previous calculation results and present calculation results only vary slightly for the TaSn₂ structure. The present work calculated the elastic stiffness constants for the Ta₃Sn structure at 2 different atom sizes and compared the results with previous calculations by the Materials Project [89–91, 108, 109]. The present elastic stiffness results are quite similar. There is a larger variance between the present results and the Materials Project results. This can be attributed to the different input parameters and exchange correlation functional used (PBE in the present work and GGA-PW91 in Materials Project). B calculated from the c_{ij} methodology is compared with the B_{EOS} obtained from the EOS fitting, showing a difference of less than 3%. Since the B_{EOS} from the EOS fitting is already compared to experiments, the elastic calculations and the scaling factor for the Debye model are thus deemed accurate.

4.4.2 CALPHAD

The PARROT module in the Thermo-Calc software [72] is used to optimize the parameters of the Gibbs energy function of the TaSn₂ and Ta₃Sn intermetallics as well as the binary interaction parameters for the bcc and liquid phases. The Gibbs energy parameters of the intermetallics are first estimated from the thermodynamic properties obtained by the phonon supercell method because the phonon calculations are regarded as more accurate than the Debye model. While the decomposition temperature of the TaSn₂ intermetallic is known to be 868 °K from experiments, the decomposition of the Ta₃Sn intermetallic has not been reported in the literature. It is noted that both the Nb-Sn and V-Sn systems, which are quite similar to the Ta-Sn system, have the X₃Sn phase forming through a peritectic reaction of bcc+Liquid→X₃Sn [99–101]. Based on the assumption from similar works that Ta₃Sn is also formed through a peritectic reaction, the Ta₃Sn parameters are adjusted and the parameters for the liquid phase are evaluated. The evaluation of the Gibbs parameters along with the results from the Debye model and the phonon quasiharmonic approach for TaSn₂ and Ta₃Sn are plotted in Figure 4.7 and Figure 4.8, respectively. As seen in both figures, the data from the phonon method correlates well with the current CALPHAD modeling. This is to be expected since this data was used to evaluate the parameters. It is noted in Figure 4.7, that the heat capacity and entropy of TaSn₂ from the current CALPHAD modeling is higher

than those from the first-principles calculations. This is due to the fact that the enthalpy and entropy values from DFT were adjusted with the experimental data of the peritectic temperature.

The bct and diamond phases are treated as ideal due to the little solubility. As previously stated, the enthalpies of formation of the bcc phase for five different Sn-Ta compositions are calculated and plotted in Figure 4.9, showing asymmetrical behavior. There is a discrepancy between the first-principles value and the CALPHAD modeling for the lattice stability of bcc-Sn. The first-principles predicts a value of 15.48 kJ/mol-atom and the CALPHAD model gives 4.42 kJ/mol-atom. This difference is expected to be due to the instability of Sn in the bcc phase. Wang et al. [110] concluded and discussed the same discrepancy when comparing first-principles DFT results to SGTE data for Os and Ru. Wang et al. calculated the lattice stability of bcc and fcc (face centered cubic) structure for Os and Ru, both stable in the hexagonal close packed phase at standard temperature and pressure, and concluded a difference of approximately 40 and 60 kJ/mol for Ru and Os, respectively. Wang et al. attributed this difference to the fact that when using first-principles calculations of unstable structures, frequencies of some of the phonon modes would become imaginary and thus the results would be less accurate. On the other hand, the CALPHAD technique can extrapolate lattice stabilities from binary solutions for which an alloying element has stabilized the otherwise unstable structure. These enthalpies of formation calculated from the SQS first-principles calculations are used to evaluate the bcc binary interaction parameters in the present CALPHAD modeling. The enthalpy of formation of the bcc phase is negative at the Ta rich side and becomes positive at the Sn rich side. This is common for X-Sn systems [99,101], such as the Nb-Sn system [101] shown in Figure 4.9. It should be noted that Toffolon et al. [100,101] used experimental data on the Sn-rich bcc phase to evaluate the Nb-Sn system's bcc interaction parameters. Due to the asymmetry of enthalpy of formation for the bcc phase, a subregular ^1L interaction parameters is introduced.

The interaction parameters obtained in the present work are listed in Table 4.4. Based on these model parameters, the phase diagram is calculated and shown in Figure 4.10. The melting temperature of Ta_3Sn is predicted to be 2884 °K. Both the intermetallics decompose incongruently similar to those in the Nb-Sn and V-Sn systems. As seen in Table 4.4, both intermetallic phases have a negative enthalpy

of formation and a negative entropy of formation. This goes along with previous predictions by Arroyave and Liu [111] where they showed that the enthalpy and entropy of formation have the same sign. The calculated enthalpy of mixing of the liquid phase is plotted in Figure 4.11. The interaction parameter for the liquid phase allows for an accurate representation of the phase stability in Figure 4.10 but may need to be slightly adjusted if experimental data would come available.

4.5 Conclusion

The present work incorporates the thermodynamic data from DFT-based first-principles calculations and the available experimental data in the literature to model the Gibbs energies for the bcc and liquid solution phases and the stoichiometric Ta_3Sn and TaSn_2 phases of the Sn-Ta system. First-principles calculations are used to predict the enthalpy of formation of the bcc phase for the evaluation of interaction parameters in the phase. The decomposition temperature of Ta_3Sn is predicted to be 2884 °K. The completed thermodynamic description is complied into a tdb file. The tdb file and raw data from the first-principles calculations are in appendix b.

Table 4.1. Lattice parameters from first-principles calculations compared with experimental values.

Phase	Space Group	<i>a</i> (Å)	<i>b</i> (Å)	<i>c</i> (Å)	Reference
bcc-Ta	Im $\bar{3}$ m	3.316			This work (0 °K)
		3.328			This work phonon (298 °K)
		3.330			This work Debye (298 °K)
		3.30			Expt. [103]
		3.32			DFT (0 °K) [84]
bct-Sn	I4 ₁ /amd	5.939	3.214		This work (0 °K)
		5.959	3.236		This work phonon (298 °K)
		5.954	3.222		This work Debye (298 °K)
		5.83	3.18		Expt. [104]
		5.93	3.23		DFT (0 °K) [105]
TaSn ₂	Fd ³ d	5.641	9.766	19.200	This work (0 °K)
		5.652	9.786	19.238	This work phonon (298 °K)
		5.652	9.785	19.238	This work Debye (298 °K)
		5.63	9.80	19.18	Expt. [106]
Ta ₃ Sn	Pm $\bar{3}$ n	5.304			This work (0 °K)
		5.319			This work phonon (298 °K)
		5.319			This work Debye (298 °K)
		5.29			Expt. [102]

Table 4.2. Equilibrium volume V_0 , bulk modulus B_{EOS} , and the first derivative of bulk modulus with respect to pressure B'_{EOS} , from fitted equilibrium properties from the EOS at 0 °K compared to experimental work and previous DFT studies.

Phase	V_0 ($\text{\AA}^3/\text{atom}$)	B_{EOS} (GPa)	B'_{EOS}	Reference
bcc-Ta	18.241	193.7	3.84	This work
	17.9685	200		Expt. [103]
	18.313	195.3	3.82	DFT [84]
bct-Sn	28.431	47.7	4.61	This work
	27.055	58.0		Expt. [107]
	28.396	54.0		DFT [107]
TaSn ₂	22.631	104.3	4.80	This work
Ta ₃ Sn	18.668	182.4	4.27	This work

Table 4.3. Elastic stiffness constants and elastic properties predicted using the Hill approach and the scaling factors used in the Debye model, calculated from the Poisson ratio, see Eq. 2.11. To ensure the accuracy of the calculated scaling factor, the bulk modulus (B) calculated from the elastic constants was compared to the B_{EOS} calculated from the EOS fitting Eq. 2.6.

	TaSn ₂		Ta ₃ Sn		
	Present Work	FP	Present Work	Present Work	FP
		[89–91, 108]	8 atoms	32 atoms	[89–91, 109]
C ₁₁ (GPa)	166	161	297	310	226
C ₁₂ (GPa)	79	78	127	131	155
C ₁₃ (GPa)	62	57			
C ₂₂ (GPa)	189	182			
C ₂₃ (GPa)	68	68			
C ₃₃ (GPa)	187	183			
C ₄₄ (GPa)	37	35	65	68	22
C ₅₅ (GPa)	59	55			
C ₆₆ (GPa)	61	60			
E (GPa)	135		210	202	
G (GPa)	53	51	80	76	27
Poisson Ratio	0.288	0.29	0.32	0.32	0.43
Scaling factor	0.789		0.71	0.71	
B (GPa)	107	107	184	190	179
B_{EOS} (GPa)	104		182		

Table 4.4. Modeled parameters in SI units in the present work for the phases in the Sn-Ta binary system. These parameters were incorporated with the SGTE data for the pure elements [31].

Phase (model)	Modeled Paramters
bcc-A2(Sn,Ta)	${}^0L_{Ta,Sn}^b cc = + 70451$ ${}^1L_{Ta,Sn}^b cc = + 112237$
Liquid (Sn,Ta)	${}^0L_{Ta,Sn}^L iq = 17118$
TaSn ₂	$G^{TaSn_2} = {}^0G_{Sn}^{bct} + {}^0G_{Ta}^{bcc} = -29678 - 4.202T$
Ta ₃ Sn	$G^{Ta_3Sn} = {}^0G_{Sn}^{bct} + 3{}^0G_{Ta}^{bcc} = -68844 - 6.000T$

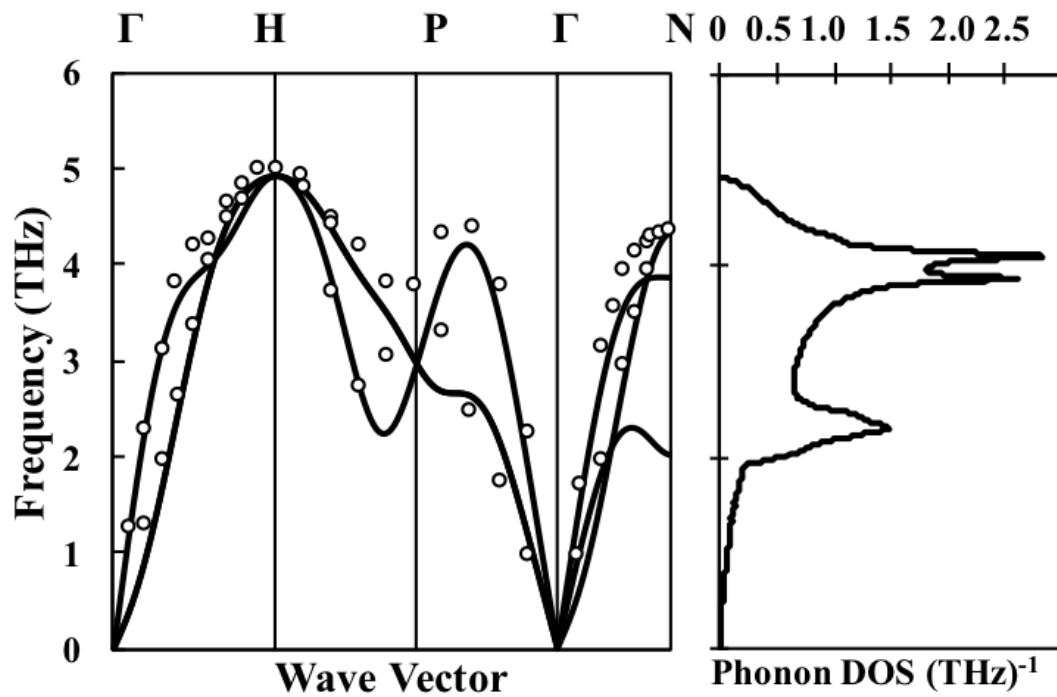


Figure 4.1. Calculated phonon dispersion curve of bcc-Ta, compared with neutron diffraction experiments (○) [29] along with the phonon DOS.

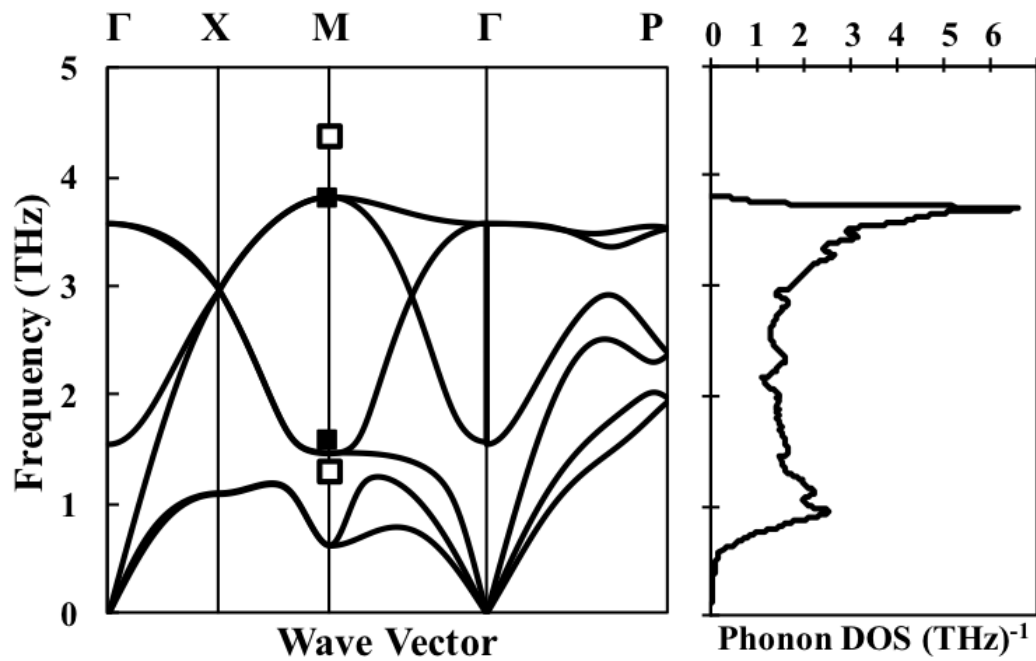


Figure 4.2. Calculated phonon dispersion curve of bct-Sn on the left and phonon DOS on the right. The open squares (\square) are the LO and TO modes from Raman [30] and the filled squares the theoretical prediction of the LO and TO modes at the M point [30].

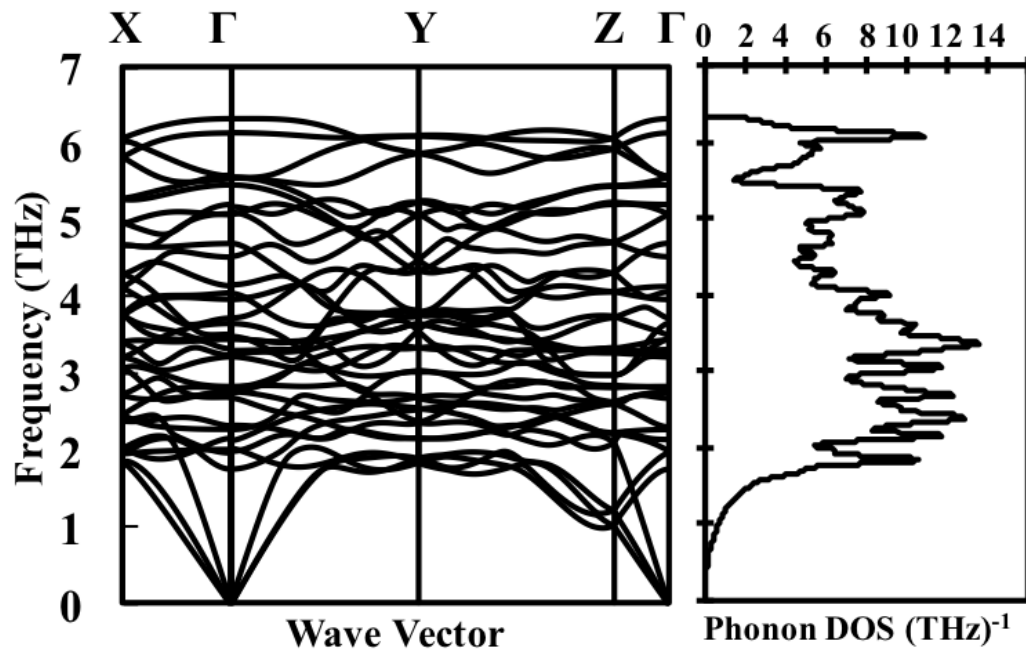


Figure 4.3. Calculated phonon dispersion curve for TaSn_2 at 0 $^{\circ}\text{K}$ and the phonon DOS.

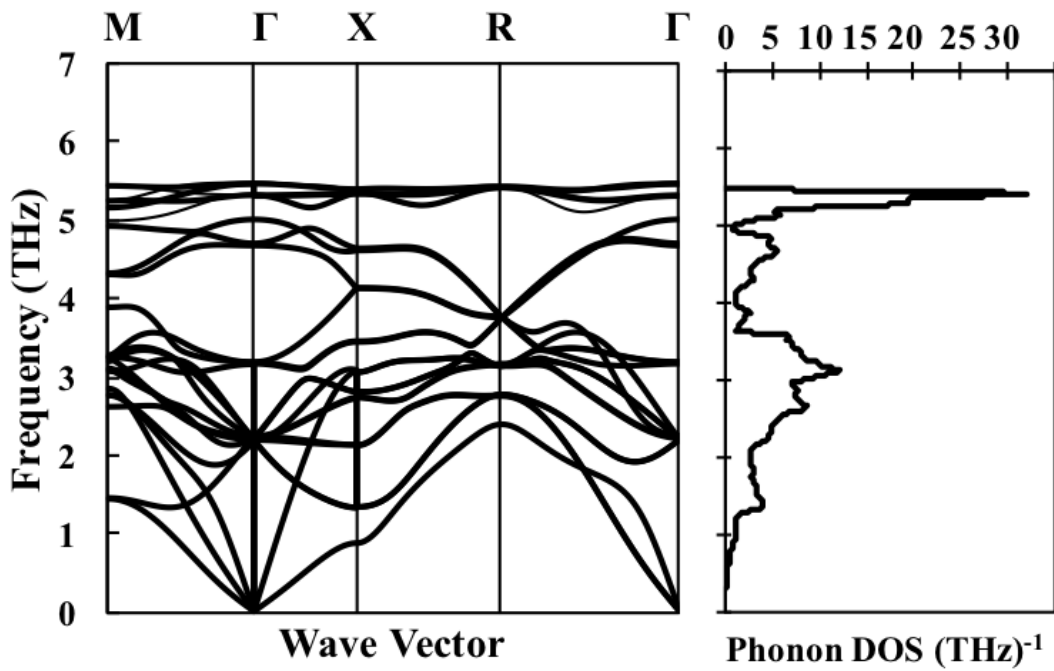


Figure 4.4. Calculated phonon dispersion curve of Ta₃Sn at 0 °K on the left and the phonon DOS on the right.

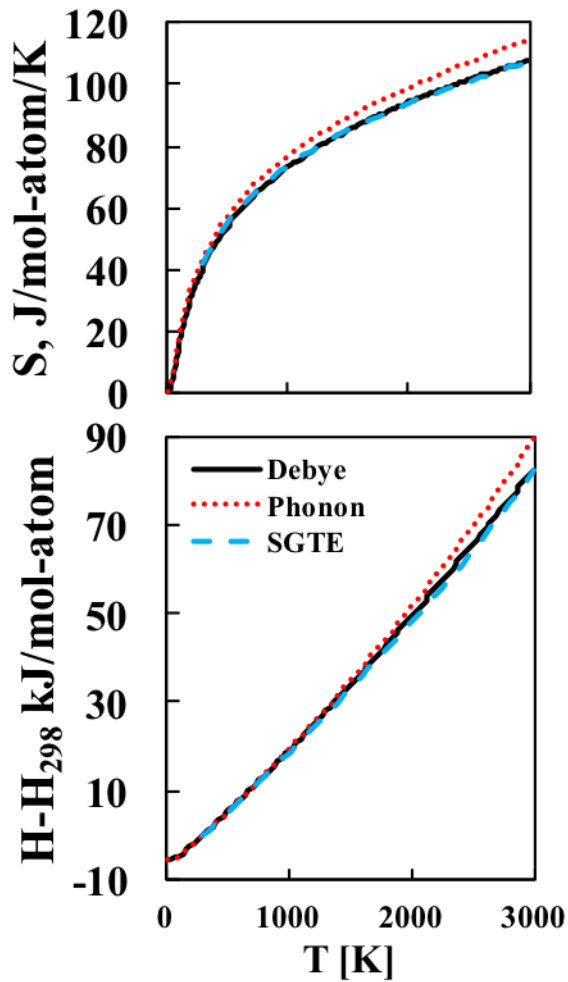


Figure 4.5. Comparison of the enthalpy and entropy of bcc-Ta from the Debye model (solid line) and the quasiharmonic phonon calculations (red dotted line) to the SGTE data (blue dashed line) [31].

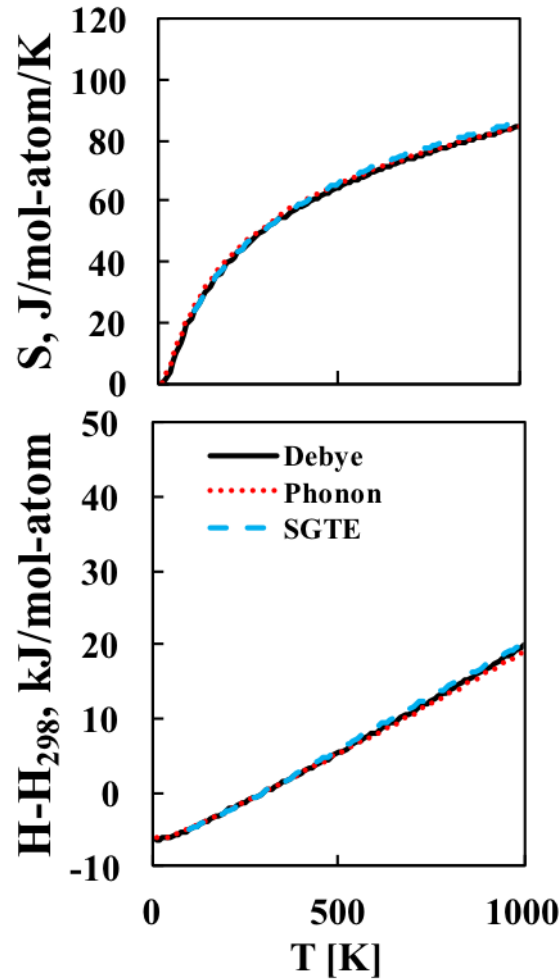


Figure 4.6. Comparison of the Gibbs energy of bct-Sn from the Debye model (solid line) and the quasiharmonic phonon calculations (red dotted line) to the SGTE data (blue dashed line) [31].

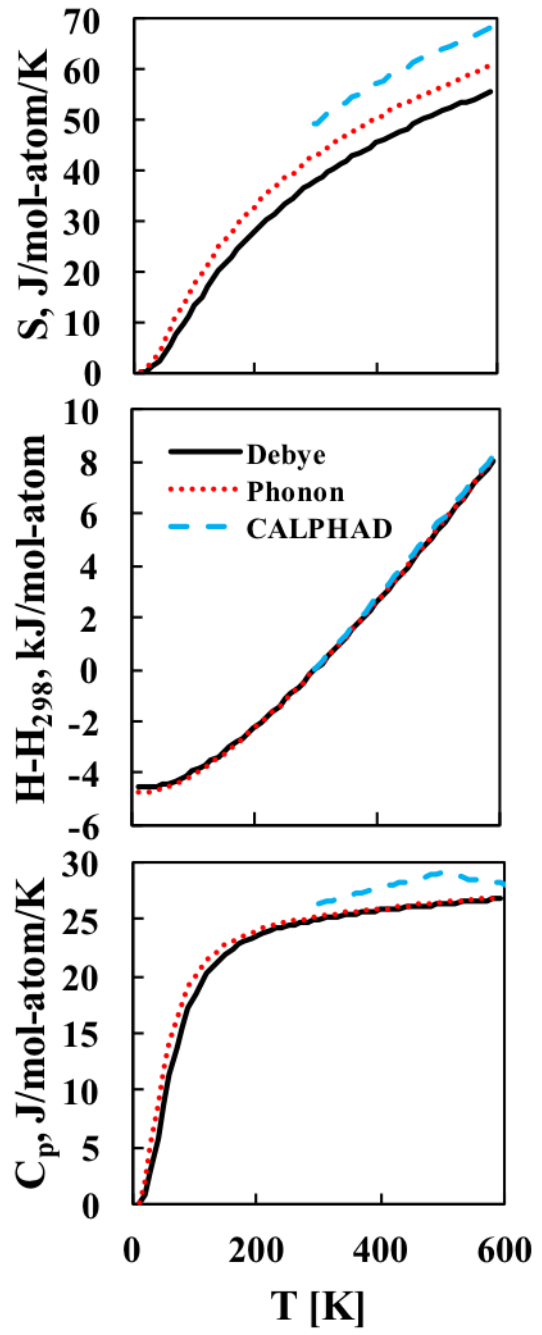


Figure 4.7. Heat capacity, enthalpy and entropy of TaSn_2 using the Debye model (solid line) and the quasiharmonic phonon calculation (red dotted line) from first-principles calculations, compared with those from the current CALPHAD modeling (blue dashed line).

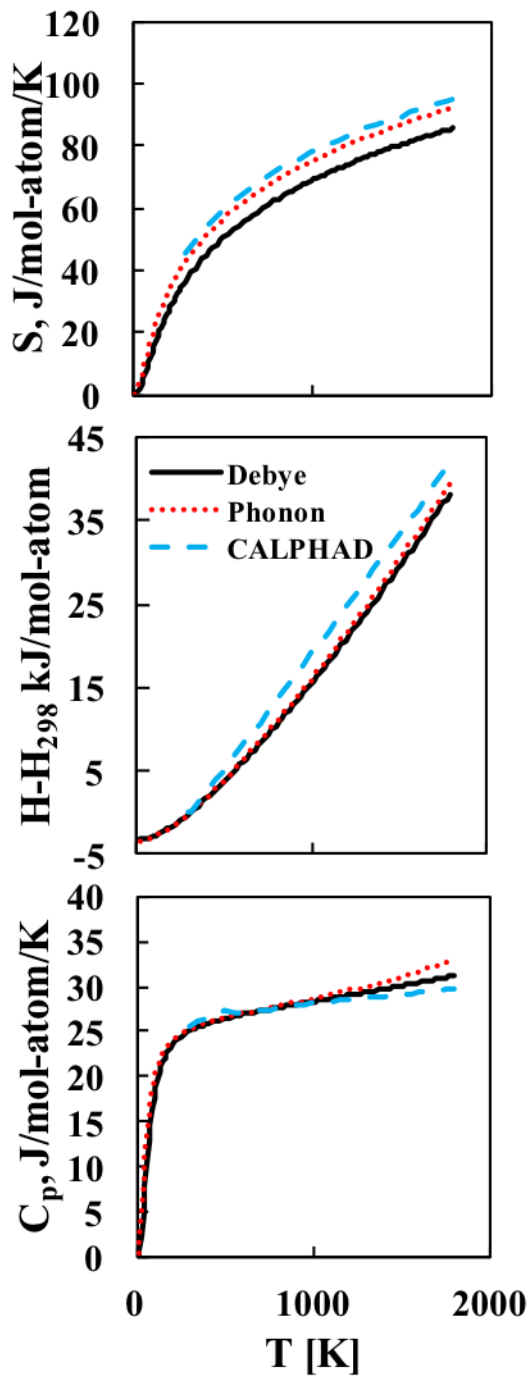


Figure 4.8. Heat capacity, enthalpy and entropy of Ta_3Sn using the Debye model (solid line) and the quasiharmonic phonon calculation (red dotted line) compared with those from the current CALPHAD modeling (blue dashed line).

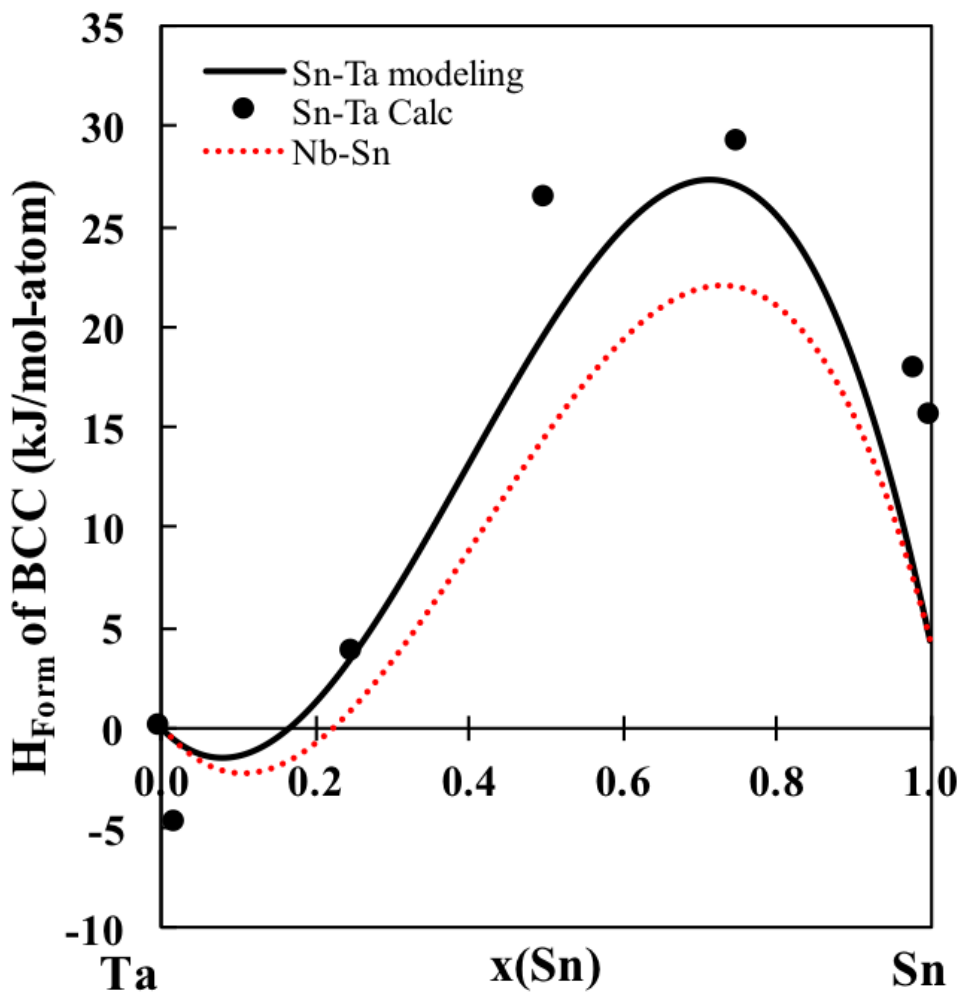


Figure 4.9. Heat capacity, enthalpy and entropy of Ta_3Sn using the Debye model (solid line) and the quasiharmonic phonon calculation (red dotted line) compared with those from the current CALPHAD modeling (blue dashed line).

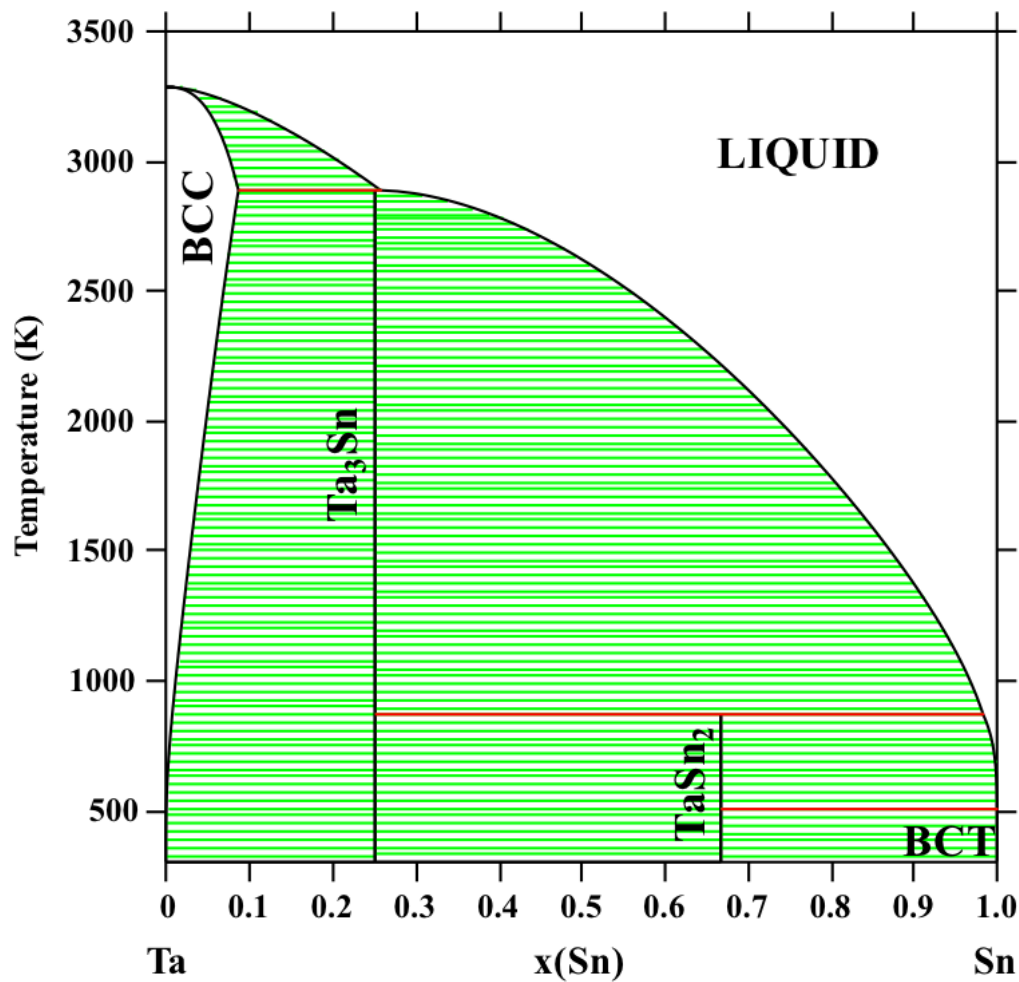


Figure 4.10. Calculated Sn-Ta phase diagram using the present thermodynamic description.

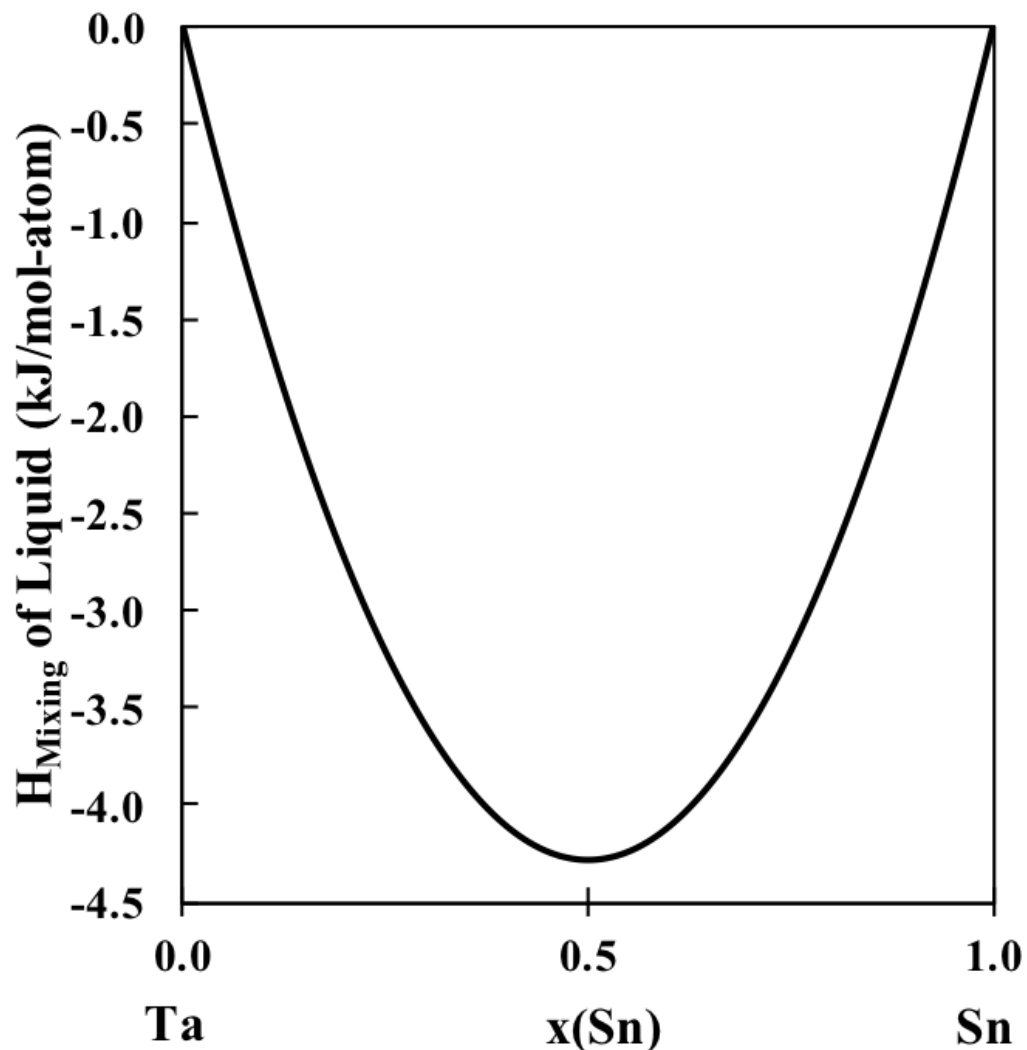


Figure 4.11. Enthalpy of mixing of the liquid phase as a function of composition at 298 °K and ambient pressure in the Sn-Ta system.

Chapter 5 |

Effects of alloying elements on the elastic properties of bcc Ti- X alloys

5.1 Introduction

The present chapter is aimed at studying the effects of alloying elements on the mechanical properties of Ti-alloys as well as completing a database to calculate the elastic properties as a function of composition. This is accomplished by systematically studying the single crystal elastic stiffness constants (c_{ij} 's) and polycrystalline aggregate properties of bcc Ti-X (X = Mo, Nb, Ta, Sn, Zr) alloys. The elastic properties are calculated using first-principles calculations based on density functional theory (DFT). The composition dependence of elastic properties of Ti-X alloys is explored through the dilute solutions and special quasirandom structures (SQS) [69] for concentrated solutions using the methodologies outlined in the methodology chapter. The obtained elastic properties are then fit using the CALPHAD method and extrapolated to higher order Ti-alloys.

5.2 Modeling and Calculations

5.2.1 Calculation details

In the present work the Vienna ab-initio Simulation Package (VASP) [57] was employed to calculate the elastic properties of pure elements and Ti-containing binary systems in the bcc phase. The ion-electron interactions were described using the projector augmented wave (PAW) [58, 79] method and based on the previous work of comparing X-C functionals (Figure 2.1) the exchange-correlation functional of the generalized gradient approach depicted by Perdew, Burke, and Ernzerhof (PBE-GGA) was employed [54]. Three magnitudes of strain were compared by doing the same calculations on the Ti-Mo system using the ± 0.01 , ± 0.013 and ± 0.007 magnitudes of strain. The three magnitudes of strain showed little variance in results, thus the calculations were done with PBE and ± 0.01 strains. For consistency, a 310 eV energy cutoff was adopted for all calculations, which is roughly 1.3 times higher than the default value. The energy convergence criterion was 10^{-6} eV/atom, and the Monkhorst-Pack scheme is used for Brillouin zone sampling [57, 80].

For the Ti-X binary systems, calculations for both dilute and SQS solutions were carried out. Three SQS cells with mole fractions of X atoms at 0.25, 0.5, and 0.75 were employed. Five dilute solutions were calculated for each Ti-X binary alloy using supercell sizes, i.e., $Ti_{53}X$ (54-atom), $Ti_{15}X$ (16-atom), Ti_7X (8-atom), $X_{15}Ti$ (16-atom), and $X_{53}Ti$ (54-atom). The interaction paramters for the elastic stiffness constants were then determined according to the methodology laid out in chapter 2.

5.2.2 Modeling details

The first-principles results were then used to model the elastic stiffness constants. The modeling was completed by calculating the difference between the first-principles calculations and a linear extrapolation between pure elements. The differences were then used to fit to the interaction parameters. Due to the limitations within the PARROT module, a mathematica script was used to fit the interaction parameters. The mathematica script is appended in appendix C. With the focus being Ti-rich alloys, the first-principles results with 70 at. % Ti or higher

were weighted heavier (x6, according to the authors' practices) than the other points for the fittings. The best fit was found by comparing the fittings obtained with one interaction parameter or with two interaction parameters. The moduli values were then calculated from the elastic stiffness constants according to Eq. Y in the methodology chapter.

5.3 Results and discussion

5.3.1 Evaluation of calculation settings

The X-C functionals of PW91 and PBE were tested on the Ti-Ta binary system. The results are plotted in Figure ???. It is shown that the c_{44} values of Ti-Ta alloys consistently differ around 10 GPa or less between the PW91 and PBE calculations. The c_{11} and c_{12} calculations differ less than 5 GPa. The c_{11} and c_{12} values with 25 at.% Ta from SQS calculations vary by 26 GPa and 13 GPa, respectively. Since overall the values vary by an error of less than 0.2 (calculated with Eq. Y), it is concluded that the X-C functional choice does not make a significant difference in the results. The PBE functional was created after PW91 and meant to be an improvement on the PW91 and was chosen for the present work.

Three magnitudes of strain were tested on the Ti-Mo binary system and plotted in 5.1. The results show that the different strain magnitudes do not affect the results. For example, the data calculated using ± 0.01 , ± 0.013 , and ± 0.007 strains at Mo_{15}Ti for c_{11} was 451 GPa, 450 GPa, and 450 GPa, respectively, varying within 1 GPa ($< 1\%$), similar to the variance in the c_{12} and c_{44} results. Overall, the variance in the c_{11} and c_{12} is less than 0.02 (Eq. Y). The largest variance is seen in the $\text{Ti}_{50}\text{Mo}_{50}$, the c_{44} values are 42 GPa, 42 GPa, and 65 GPa calculated with ± 0.01 , ± 0.013 , and ± 0.007 strains, respectively. Overall, the strain magnitude does not seem to affect the calculated results, and the ± 0.01 strain magnitude is thus used for all the calculations.

5.3.2 Calculations of the Ti-X elastic properties

The elastic stiffness constants and bulk modulus B are calculated from c_{ij} of pure elements in the bcc structure and reported in 5.1. The results in the present work

were all obtained at 0 °K without considering the effect of zero-point vibrational energy as discussed in the section of methodology. The results for Mo, Nb and Ta, which are stable in the bcc structure at low temperatures, are compared with experimental data at temperatures specified in the table [86, 87]. The error (Eq. Y) between the present results and previous results for Mo, Nb and Ta are 2.61, 7.5, and 4.25 %, respectively [64, 86, 87]. This discrepancy is partially due to the experimental values being obtained at higher temperatures than the calculations at 0 °K.

Ti and Zr are stable in the hcp structure at low temperatures, and Sn is stable in the body centered tetragonal and diamond structures at low temperatures. Due to the instability of Ti, Sn and Zr in the bcc structure at low temperatures, their elastic stiffness coefficients are compared with previous first-principles calculations at 0 °K [84] used the PW91 functional, and the errors are 2.4, 52.8 and 5.1 %, respectively. The differences are related to the instability of the bcc structure, the different exchange correlation functionals and the different input parameters chosen. Due to the bcc instability, multiple relaxation schemes were run in the present work to find the lowest energy structure retaining the bcc symmetry, making the results the most accurate representation of the bcc pure elements.

Figure 5.2 summarizes the present Young's modulus results for each Ti-X binary system (circles). The solid lines are from the Voigt-Reuss-Hill approach with the elastic coefficients from the current modeling using Eq. Y and the model parameters shown in Table 5.2. The Hill average is plotted as a solid black line while the Voigt (high bound) and Reuss (low bound) are plotted as dotted lines and dashed lines, respectively. When the structures are stable the Voigt and Reuss do not vary drastically but when the structures are unstable the Voigt and Reuss show the high and low bounds of the modulus calculations with the Hill average being what the database will predict. The results calculated for the Ti-Mo, Ti-Nb, and Ti-Ta systems are compared with previous calculated results from Ikehata et al. [2], and the difference is due to the different input parameters and structures used at each composition. Ikehata et al. used the s electrons as the valance electrons for Ti and used the B2 structure for their $Ti_{0.5}X_{0.5}$ with Ti at the body centered site and X at the corner site. For the $Ti_{0.25}X_{0.75}$ and $Ti_{0.75}X_{0.25}$ structures they used the DO₃ structure with space group $Fm\bar{3}m$, as opposed to the BCC space group of $Im\bar{3}m$. While the present work used the p electrons as valance for Ti

based on updated work and new recommendations by VASP and 16-atom SQS structures from Jiang et al. [69]. The SQS structures mimic the random substitution of elements that represent the atomic structures of solution phases better. The Ti-Mo, Ti-Nb and Ti-Ta alloy results are also compared with available experimental results [3–5, 7, 32–34] in Table 5.3.

Figure 5.2a compares the present results for the Ti-Mo alloy system with experimental data from Zhang et al. [32], Collings et al. [33], and Sung et al. [34]. It can be seen that the Young's modulus increases from pure Ti to pure Mo. The results from Sung et al. [34] differ by about 60 GPa from the present work. However, during the XRD and TEM investigations by Sung et al., one of the metastable phases, α'' and ω , in addition to the bcc phase was observed in the samples. The ω phase is a hexagonal phase (space group P6/mmm) with lattice parameters closely matching those of the bcc phase, and the α'' phase is a martensitic orthorhombic phase (space group Cmcm). The formation of the α'' and ω phases causes variations in the mechanical properties and thus the mechanical properties are expected to vary from the elastic properties of the single bcc phase. Zhang et al. [32] and Collings et al. [33] did not observe the formation of either metastable phase. The Young's modulus determined by Zhang et al. and Collings et al. are predicted with the present Voigt-Reuss bounds but have an error of 0.39 (Eq. Y) from the Hill average Young's modulus.

The present Young's moduli of the Ti-Nb alloy system are compared with data from Ozaki et al. [7] and Collings et al. [33] in Figure 5.2b, showing an increase in Young's modulus with an increase in Nb concentration. The analyses of the samples from the work by Ozaki et al. and Collings et al. showed that the alloys all contained the single bcc phase. The Young's modulus from the present first-principles calculations show an error of 0.09 (Eq. Y) from the Young's modulus determined by Ozaki et al. and Collings et al.

The Young's modulus calculation results for the Ti-Ta alloy system are plotted in Figure 5.2d. Figure 5.2d also plots the Young's modulus values that were experimentally determined from Fedotov et al. [5] and Zhou et al. [3,4]. The present Young's moduli calculated have an error of 0.19 (Eq. Y) from the experimental Young's moduli determined by Fedotov et al and Zhou et al. The Young's modulus in the Ti-Ta alloy system increases from pure Ti to pure Ta.

The error between the Young's moduli determined experimentally and the

Young's moduli calculated using DFT is expected due to the temperature difference (calculations at 0 °K and experiments at 298 °K). The Young's modulus results determined experimentally fit well within the Voigt and Reuss bounds and the present calculations provide good prediction of the elastic properties of the Ti-Mo, Ti-Nb and Ti-Ta alloys as a function of composition.

For the Young's modulus of the Ti-Sn (Figure 5.2c) and Ti-Zr (Figure 5.2e) systems there is no experimental data to compare with due to the instability in the bcc phase. For the Ti-Sn alloy system the Young's modulus increases until around 35 at % Sn when the Young's modulus than decreases to pure Sn. The Young's modulus data, for the Ti-Zr alloy system, increases up to 40 at.% Zr, and then the Young's modulus decreases to pure Zr. Figure 5.3 plots the Young's modulus as a function of composition from pure Ti in the bcc structure to the alloying element (X = Mo, Nb, Sn, Ta, Zr) to be able to compare the effects of each alloying element on the Young's modulus.

Figure 5.4 to Figure 5.6 plots the calculated elastic stiffness constants, \bar{C}_{11} , \bar{C}_{12} , \bar{C}_{44} (circles) and compares it with the elastic stiffness constants fitting (solid line) and linear extrapolation between the pure elements for each binary alloy, Ti-Mo, Ti-Nb, Ti-Sn, Ti-Ta, and Ti-Zr. The previous results from Ikehata et al. [2] are plotted for comparison for the Ti-Mo, Ti-Nb, and Ti-Ta alloys. The trend seen in the elastic stiffness constants data depict that Mo, Nb and Ta affect the elastic stiffness constants in a similar fashion. As shown in Figure 5.4a, b and d the $i\bar{C}_{11}$ increases from Ti to X (Mo, Nb, Ta) and in Figure 5.6a, b and d the \bar{C}_{44} values first decrease and then increase with the addition of the alloying element Mo, Nb and Ta respectively. The calculated \bar{C}_{12} increases by the addition of Mo and Ta (Figure 5.5a and Figure 5.5d, respectively), and the \bar{C}_{44} first decreases and then increases by the addition of Nb (Figure 5.5b). A similar trend is shown in the \bar{C}_{11} and \bar{C}_{12} data for the Ti-Sn system (Figure 5.4c and Figure 5.5c). The \bar{C}_{11} and \bar{C}_{11} values increase and then decrease from pure Ti to pure Sn. The trend of the \bar{C}_{44} seen in Figure 5.6c increases, decreases, and then increases from pure Ti to pure Sn. In the Ti-Zr system, the \bar{C}_{11} and \bar{C}_{44} values increase and then decrease with increasing Zr concentration (Figure 5.4e and Figure 5.6e). The calculated \bar{C}_{12} values for the Ti-Zr system decrease and then increase shown in Figure 5.5e.

The instability in the bcc phase can be seen from Figure 5.7, which shows the \bar{C}_{11} - \bar{C}_{12} values from first-principles calculations and the present modeling. The

bcc phase is mechanical unstable at concentrations less than 5.5, 11.5, 51.5, 9.5 and 4.0 at. % for Mo, Nb, Sn, Ta and Zr, respectively. Figure 5.8 and Figure 5.9 show the bulk and shear moduli plotted similarly to the Young's modulus in Figure 5.2 with the present results (circles), the Hill average (solid black line), and Voigt (purple dashed line) and Reuss (yellow dashed line) bounds. Similar trends in the B and G data are seen for the Ti-Mo, Ti-Nb and Ti-Ta systems. The B and G increase with increasing Mo, Nb and Ta concentration, as shown in Figure 5.8 and Figure 5.9, respectively. The bulk and shear moduli values increase and then decrease from pure Ti to pure Sn in the Ti-Sn system (Figure 5.8c and Figure 5.9c). In the Ti-Zr system, the B decreases from pure Ti to pure Zr (Figure 5.8e) and the G first increases and then decreases from pure Ti to pure Zr (Figure 5.9e).

5.3.3 Extrapolation to ternary and higher ordered systems

The interaction parameters in Table 5.2 can be used to predict the elastic stiffness constants of higher order Ti-alloys by summing the interaction parameters of each binary alloy contained in the multi-component alloy from Eq. Y. The predicted elastic stiffness constants of the multi-component alloys can be used to calculate Young's modulus as a function of composition as shown in Figure 5.3. The Hill average is plotted as solid lines while the Voigt and Reuss bounds are plotted as dotted and dashed lines, respectively. The accuracy of prediction of the elastic properties of higher ordered Ti alloys can be evaluated by comparing the predicted results with previous experimental results [35–38] as shown in Figure 5.10 and Table 5.4. The black diagonal line represents a perfect correlation between the predicted and experimental Young's modulus. The grey region is the error (3 GPa) in the first-principles calculations. The error in the first-principles is the average variance in \bar{C}_{11} , \bar{C}_{12} , and \bar{C}_{44} from Eq. Y-Eq. Y.

As it can be seen, the difference between experimental Young's modulus at the same composition from Niinomi et al. [38], Geetha et al. [36], Tane et al. [35] and Mohammad et al. [37] varies from 2 GPa to 46 GPa based on the heat treatments and measuring techniques. The scattering in the Young's modulus among experimental measurements is denoted by the vertical error bars in Figure 5.10. The horizontal error bars show the Reuss and Voigt Young's modulus ranges with the Hill average marked by the circle. The experimental Young's moduli vary from the present

predictions anywhere from 0.69 to 14 GPa. This difference is partially due to the temperature difference between the first-principles data and the experimental results. Considering the fact that the experimental results at the same composition vary drastically, the first-principles calculations give a good representation of the elastic properties of higher order Ti-alloys. Introducing the binary interaction parameters of non-Ti containing alloys in the system and the ternary interaction parameters can further improve the database predictions.

5.4 Conclusion

The effects of five alloying elements on the elastic properties of bcc Ti-X (X = Mo, Nb, Sn, Ta, Zr) alloys, including the elastic stiffness constants, bulk modulus, shear modulus, and Young's modulus, were systematically studied using first-principles calculations. The CALPAHD methodology was used to evaluate interaction parameters so that the elastic properties can be predicted as a function of composition. The present calculations showed that 5.5 at.%, 11.5 at.%, 51.5 at.%, 9.5 at.% and 4.0 at.% of Mo, Nb, Sn, Ta and Zr, respectively, were needed to stabilize the bcc phase according to the Born criteria. The trends observed were summarized for each Ti-X (X= Mo, Nb, Sn, Ta, Zr) binary system. Alloying with Mo, Nb and Ta showed to produce similar trends which is presumably due to Mo, Nb, and Ta being stable in the bcc structure at room temperature and being strong bcc stabilizers. The interaction parameters determined in the current work were used to predict the elastic properties of higher order alloys. The accuracy of database predictions of the Young's modulus was determined by comparing with the calculated and experimental Young's moduli. Overall, the database provides good predictions of the elastic properties of Ti-alloys in the bcc phase as a function of composition. To improve the database predictions, the non-Ti containing binary interaction parameters and the ternary interactions parameters should be determined.

Table 5.1. Calculated pure element elastic stiffness constants and the bulk modulus B (in GPa) by X-C functional of PBE are compared with the previous first-principles calculations (FP) by X-C functional PW91 and experiments (Expt). Sv, pv and d refereeing to the s, p, and d states being treated as valance, respectively.

Pure Elements		\bar{C}_{11}	\bar{C}_{11}	\bar{C}_{11}	B
Ti_sv	This work 0 K	93	115	41	108
	Calc 0 K [84]	96	116	40	107
Mo_pv	This work 0 K	475	164	108	268
	Expt 73 K [64]	473	156	111	
	Expt 300 K [86]	473	160	109	261
Nb_sv	This work 0 K	245	144	27	178
	Expt 4 K [64]	253	133	31	
	Expt 300 K [87]	247	135	29	172
Sn_d	This work 0 K	50	52	29	51
	Calc 0 K [84]	30	60	18	48
Ta_pv	This work 0 K	278	164	81	202
	Expt 0 K [64]	266	158	87	
	Expt 300 K [87]	267	161	83	196
Zr_sv	This work 0 K	86	91	32	89
	Calc 0 K [84]	82	94	30	90

Table 5.2. Evaluated interaction parameters L_0 and L_1 using the R-K polynomial Eq. Y for the elastic stiffness constants for the Ti-X binary systems.

Alloy	Interaction Parameter	Ti-Mo	Ti-Nb	Ti-Sn	Ti-Ta	Ti-Zr
\bar{C}_{11}	L_0	-22.16	40.46	119.46	83.65	246.97
	L_1	0	0	0	-67.76	-135.95
\bar{C}_{12}	L_0	-36.40	-32.39	15.90	38.05	-110.53
	L_1	0	0	-146.80	0	78.00
\bar{C}_{44}	L_0	-142.9	-41.54	59.79	-51.96	70.06
	L_1	0	-41.95	-94.38	0	0

Table 5.3: First-principles calculations of the elastic stiffness constants, bulk modulus B , shear modulus G , and Young's modulus E in GPa for different atomic percent compositions of the bcc Ti-X binary systems at 0 °K. As well as experimental data for the Young's modulus obtained at 300 °K by the reference stated.

Reference	$Ti_{1-b}X_b$	\bar{C}_{11}	\bar{C}_{12}	\bar{C}_{44}	B	G	E
This work	Ti	93	115	41	108	-12.91	-40.34
This work	TiMo _{6.3}	124	111	38	115	20	54
This work	TiMo _{12.5}	146	113	29	124	23	65
This work	TiMo ₂₅	178 ±3	123 ±15	32 ±11	141 ±15	30 ±15	84 ±15
This work	TiMo ₅₀	268 ±9	136 ±19	42 ±9	180 ±19	51 ±19	138 ±19
This work	TiMo ₇₅	385 ±9	146 ±6	66 ±6	226 ±9	84 ±9	224 ±9
This work	TiMo _{93.8}	451	158	96	256	114	397
This work	TiMo _{98.1}	464	163	100	263	118	308
This work	Mo	475	164	108	268	125	325
Expt 300 K [32]	TiMo ₈						83
Expt 300 K [32]	TiMo ₁₂						90
Expt 300 K [33]	TiMo ₈						84
Expt 300 K [33]	TiMo ₁₁						89
Expt 300 K [33]	TiMo ₁₈						101
This work	TiNb _{1.9}	93	115	35	108	-18	-56
This work	TiNb _{12.5}	116	116	37	116	11	31
This work	TiNb ₂₅	140 ±11	116 ±13	34 ±10	124 ±13	22 ±13	63 ±13
This work	TiNb ₅₀	181 ±9	121 ±2	31 ±10	141 ±9	31 ±10	86 ±10
This work	TiNb ₇₅	208 ±3	130 ±4	15 ±10	156 ±4	22 ±10	64 ±10
This work	TiNb _{93.8}	242	134	18	170	28	81
This work	TiNb _{98.1}	242	134	18	170	28	81
This work	Nb	245	144	27	178	35	98
Expt 300 K [7]	TiNb ₂₉						67
Expt 300 K [7]	TiNb ₃₄						74
Expt 300 K [7]	TiNb ₄₄						84
Expt 300 K [33]	TiNb ₂₆						64

Table 5.3: First-principles calculations of the elastic stiffness constants, bulk modulus B , shear modulus G , and Young's modulus E in GPa for different atomic percent compositions of the bcc Ti-X binary systems at 0 °K. As well as experimental data for the Young's modulus obtained at 300 °K by the reference stated.

Reference	$Ti_{1-b}X_b$	\bar{C}_{11}	\bar{C}_{12}	\bar{C}_{44}	B	G	E
Expt 300 K [33]	TiNb ₃₀						65
Expt 300 K [33]	TiNb ₃₄						73
Expt 300 K [33]	TiNb ₄₄						83
This work	TiSn _{6.3}	100	122	46	115	-10	-30
This work	TiSn ₂₅	105 ±5	114 ±2	60 ±4	111 ±5	11 ±5	31 ±5
This work	TiSn ₅₀	88 ±9	93 ±9	46 ±4	91 ±9	10 ±9	29 ±9
This work	TiSn ₇₅	92 ±9	55 ±7	35 ±8	67 ±9	27 ±9	72 ±9
This work	Sn	50	52	29	51	7	21
This work	TiTa _{1.9}	100	115	39	110	-3	-9
This work	TiTa _{6.3}	116	113	30	114	11	32
This work	TiTa _{12.5}	120	121	39	121	11	32
This work	TiTa ₂₅	167 ±1	140 ±3	45	149 ±3	28 ±3	78 ±3
This work	TiTa ₅₀	208 ±1	159	51 ±3	175 ±1	38 ±3	106 ±3
This work	TiTa ₇₅	239 ±7	143 ±5	62 ±3	175 ±7	56 ±7	152 ±7
This work	TiTa _{93.8}	257	158	72	191	62	168
This work	TiTa _{98.1}	264	163	72	197	62	169
This work	Ta	278	164	81	202	70	189
Expt 300 K [5]	TiTa ₃₈						62
Expt 300 K [5]	TiTa ₄₂						79
Expt 300 K [5]	TiTa ₄₈						95
Expt 300 K [3]	TiTa ₃₈						67
Expt 300 K [3]	TiTa ₅₁						105
This work	TiZr _{1.9}	112	106	43	108	17	48
This work	TiZr ₂₅	148 ±14	82 ±7	54 ±7	104 ±14	44 ±14	116 ±14
This work	TiZr ₅₀	152 ±17	76 ±12	48 ±12	101 ±17	44 ±17	115 ±17
This work	TiZr ₇₅	126 ±12	82 ±3	45 ±3	97 ±12	34 ±12	91 ±12

Table 5.3: First-principles calculations of the elastic stiffness constants, bulk modulus B , shear modulus G , and Young's modulus E in GPa for different atomic percent compositions of the bcc Ti-X binary systems at 0 °K. As well as experimental data for the Young's modulus obtained at 300 °K by the reference stated.

Reference	$\text{Ti}_{1-b}\text{X}_b$	\overline{C}_{11}	\overline{C}_{12}	\overline{C}_{44}	B	G	E
This work	$\text{TiZr}_{93.8}$	89	90	34	90	9	27
This work	Zr	86	91	32	89	6	16

Table 5.4. Predicted Young's modulus (in GPa) of higher order alloys in the bcc phase compared to experimental values found with both the weight percent and atomic percent listed. The predicted Young's modulus was found using the pure elements and binary interaction parameter data.

Alloy Name (%wt)	at %	Calc <i>E</i>	Expt <i>E</i>
Ti-35Nb-7Zr-5Ta [36]	Ti-24Nb-5Zr-2Ta	81	80
Ti-29Nb-13Ta-4.6Zr [36]	Ti-20Nb-5Ta-3Zr	76	75
Ti-29Nb-13Ta-6Sn [36]	Ti-21Nb-5Ta-3Sn	68	74
Ti-29Nb-13Ta-4.6Sn [36]	Ti-20Nb-5Ta-3Sn	67	66
Ti-29Nb-13Ta-4.5Zr [36]	Ti-20Nb-5Ta-3Zr	76	65
Ti-29Nb-13Ta-4.6Zr [35]	Ti-21Nb-5Ta-3Zr	76	64
Ti-30Nb-10Ta-5Zr [35]	Ti-23Nb-4Ta-3Zr	77	64
Ti-35Nb-10Ta-5Zr [35]	Ti-25Nb-4Ta-4Zr	80	65
Ti-24Nb-4Zr-7.9Sn [37]	Ti-15Nb-3Zr-4Sn	65	54
Ti-35Nb-2Ta-3Zr [37]	Ti-23Nb-1Ta-2Zr	69	61
Ti-29Nb-11Ta-5Zr [37]	Ti-20Nb-6Ta-2Zr	74	60
Ti-10Zr-5Ta-5Nb [37]	Ti-6Zr-1Ta-3Nb	64	52
Ti-29Nb-13Ta-2Sn [37]	Ti-20Nb-5Ta-1Sn	66	62

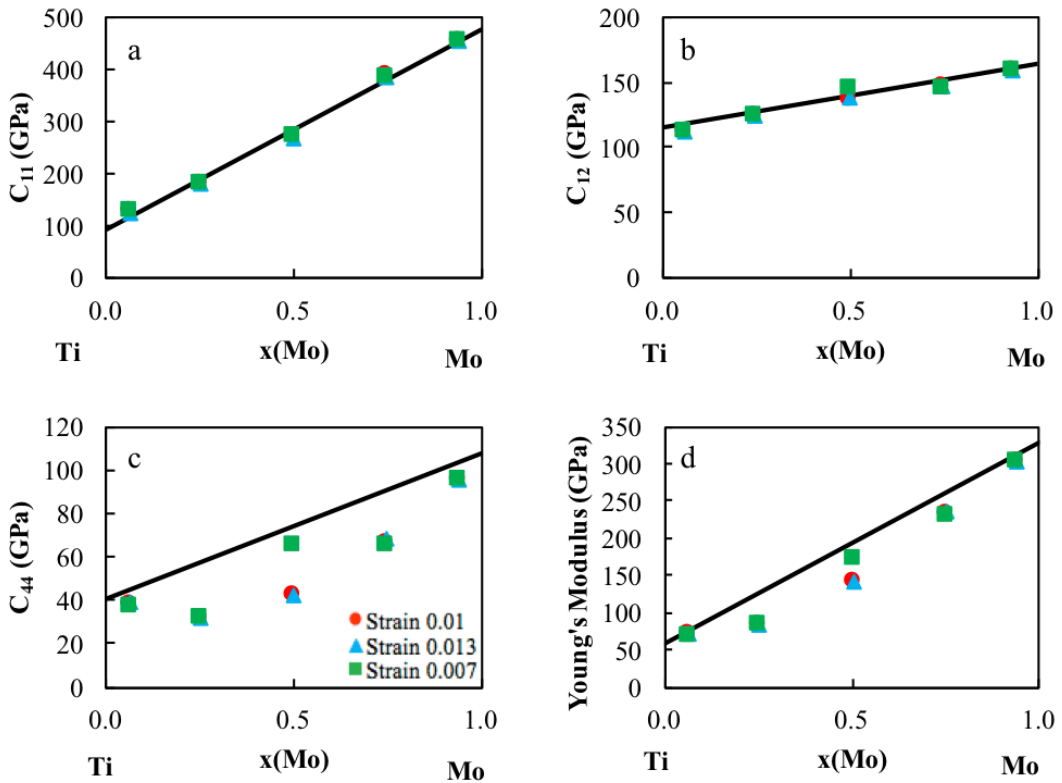


Figure 5.1. Elastic stiffness constants for the bcc Ti-Mo binary system calculated with strains, 0.01, 0.03 and 0.07, respectively, showing comparable results.

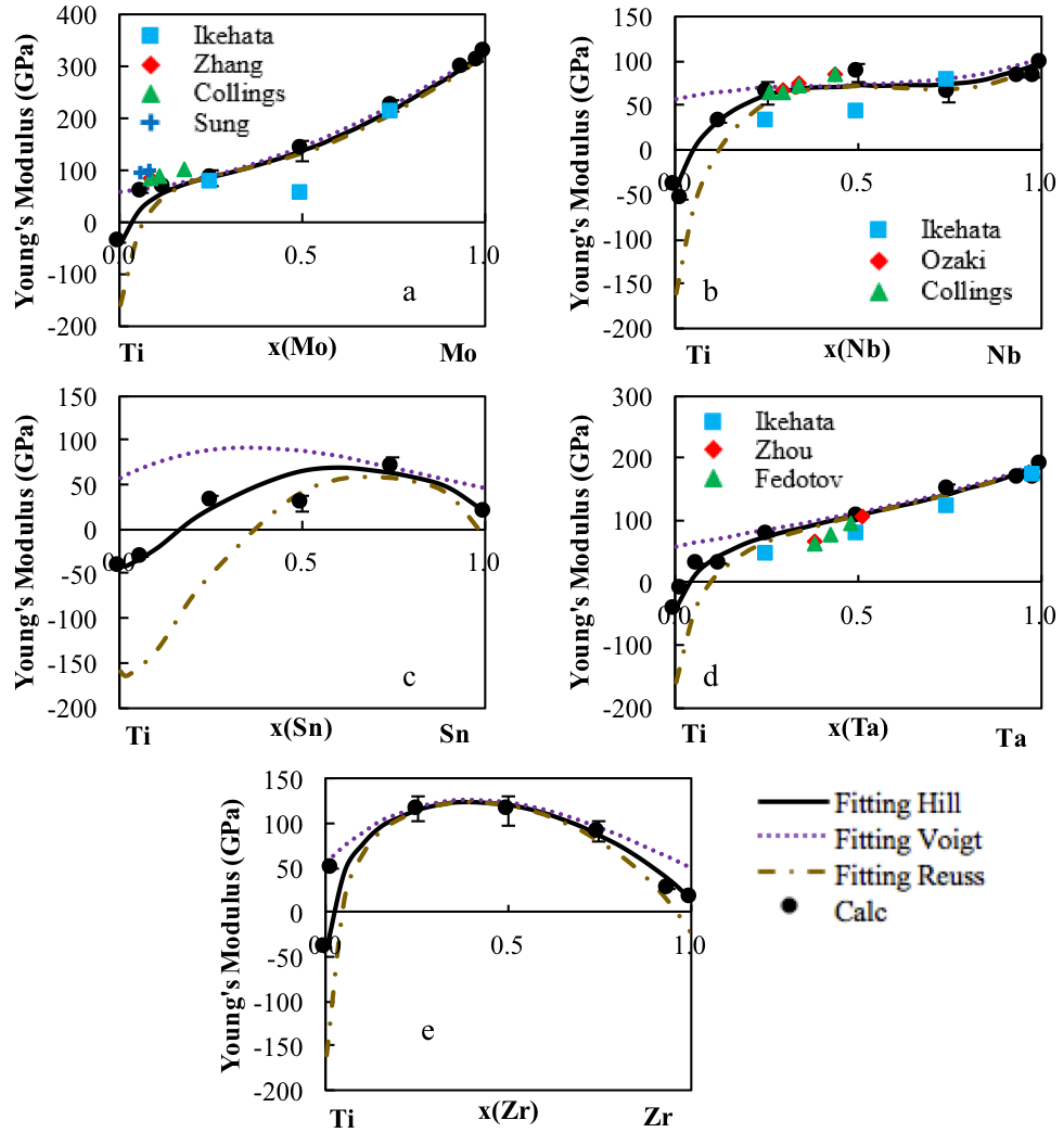


Figure 5.2. Young's modulus E of the Ti-X binary systems. The present calculations are plotted as the filled circles with the error bars. The dotted purple line is the Voigt upper Young's modulus bound, the gold dot dashed line is the lower Reuss Young's modulus bound and the black line is the Hill Young's modulus average. The experimental values [1–5, 7, 8, 32–34] are also included for comparison.

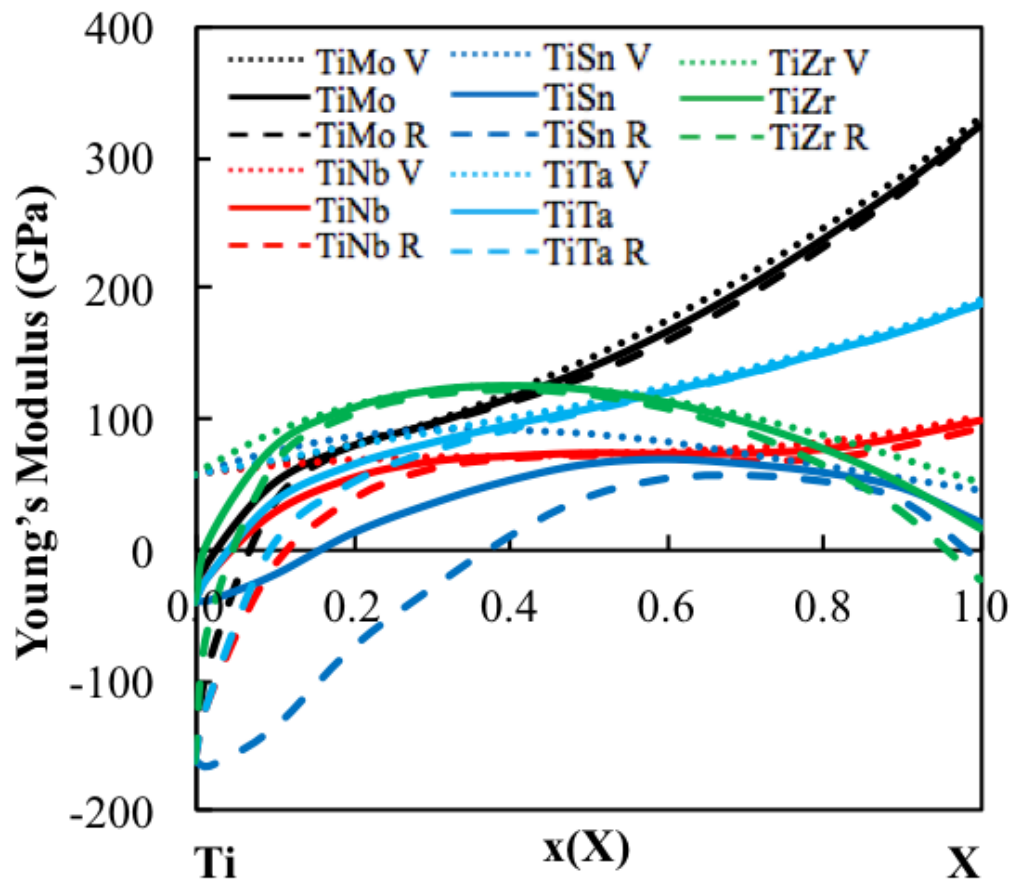


Figure 5.3. Young's modulus calculated from the model parameters (see ??) and Eq. Y as a function of composition from bcc Ti to bcc X.

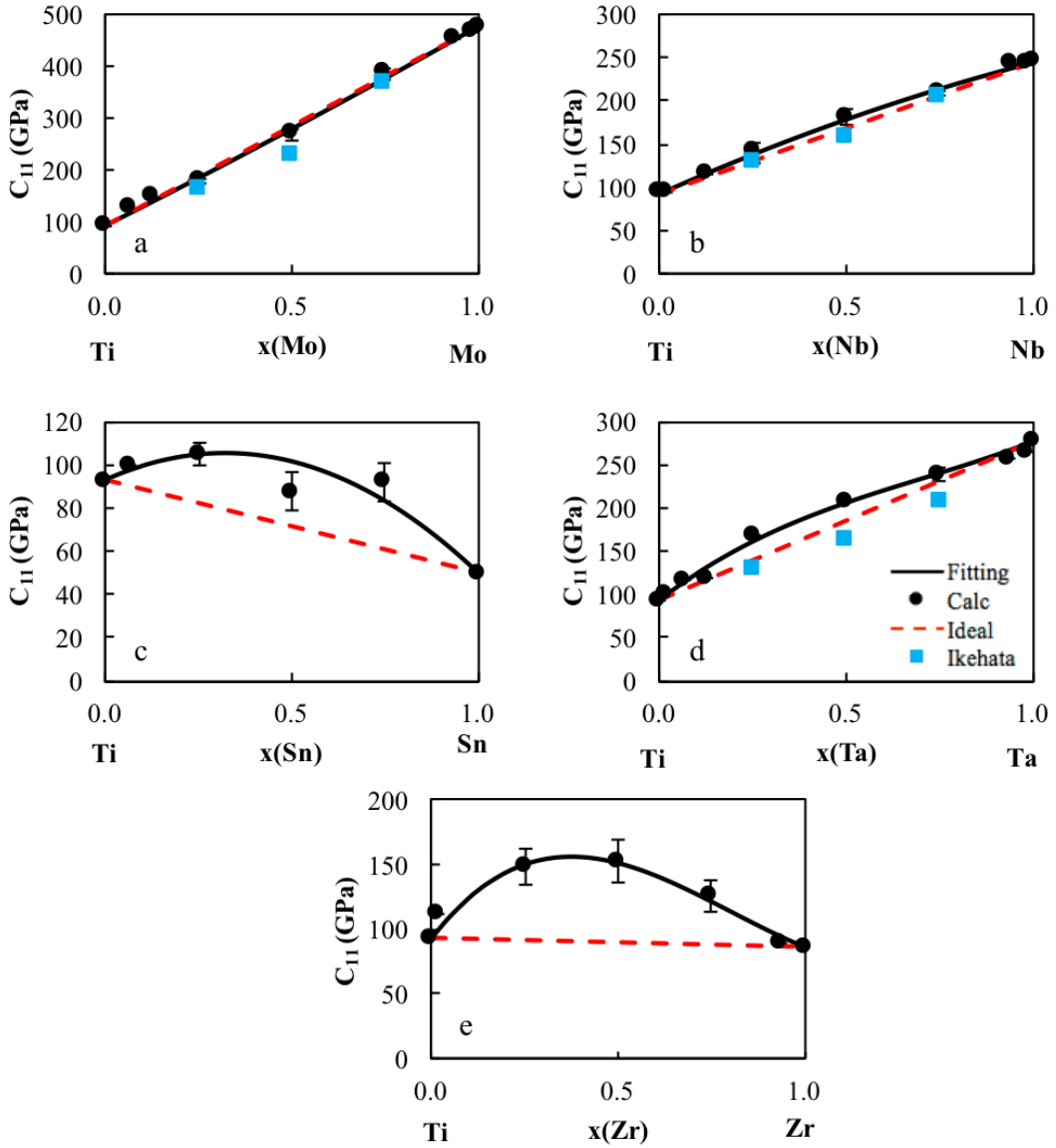


Figure 5.4. Calculated \bar{C}_{11} values (circles) plotted with their errors as well as the pure element extrapolation (red dashed line) and the present modeling (black dashed line) for five Ti-X binary systems ($X = \text{Mo}, \text{Nb}, \text{Ta}, \text{Sn}, \text{Zr}$). Ti-Mo, Ti-Nb, and Ti-Ta alloys are compared with previous calculations from Ikehata et al. [2].

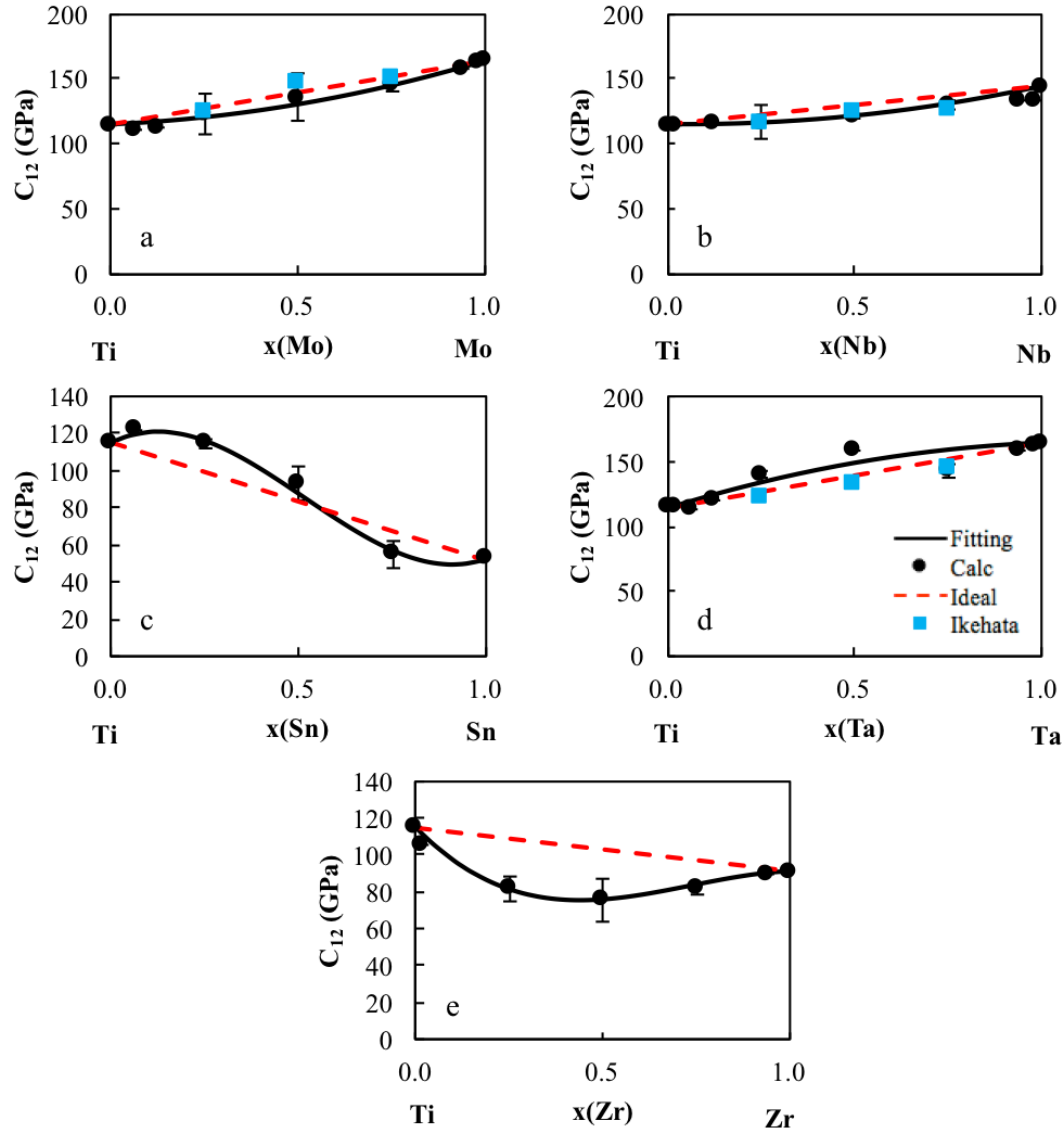


Figure 5.5. Calculated \bar{C}_{12} values (circles) plotted with their errors as well as the pure element extrapolation (red dashed line) and the present modeling (black dashed line) for five Ti-X binary systems ($X = \text{Mo}, \text{Nb}, \text{Ta}, \text{Sn}, \text{Zr}$). Ti-Mo, Ti-Nb, and Ti-Ta alloys are compared with previous calculations from Ikehata et al. [2].

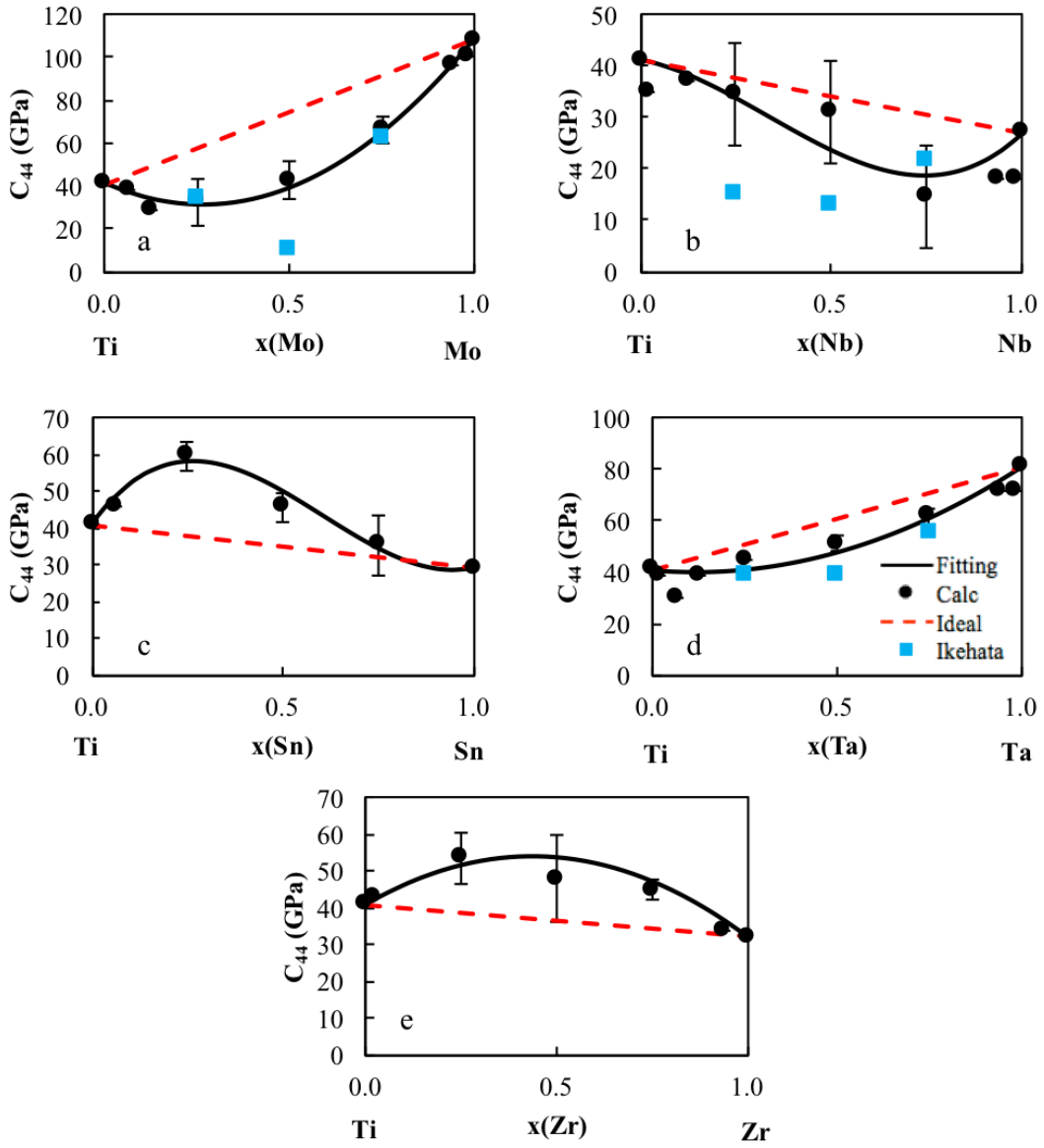


Figure 5.6. Calculated \bar{C}_{44} values (circles) plotted with their errors as well as the pure element extrapolation (red dashed line) and the present modeling (black dashed line) for five Ti-X binary systems ($X = \text{Mo}, \text{Nb}, \text{Ta}, \text{Sn}, \text{Zr}$). Ti-Mo, Ti-Nb, and Ti-Ta alloys are compared with previous calculations from Ikehata et al. [2].

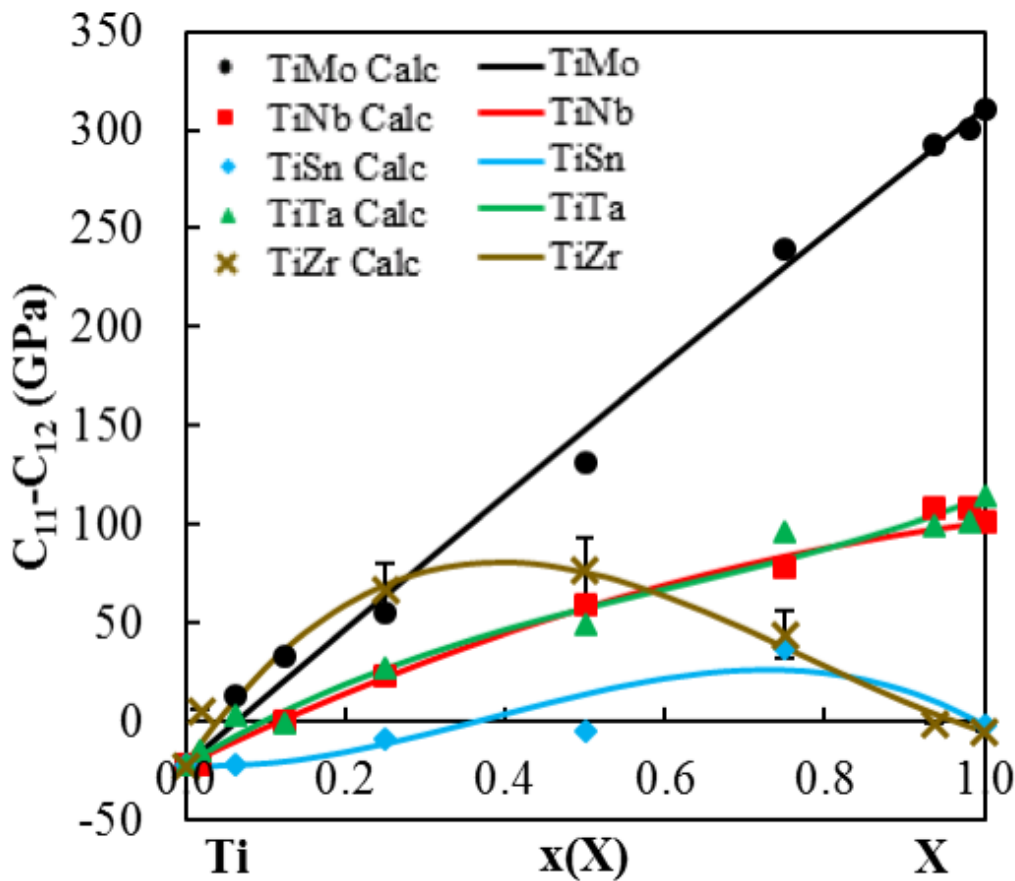


Figure 5.7. Calculated \bar{C}_{11} - \bar{C}_{12} values (circles) plotted with the present modeling (solid lines) for five Ti-X binary systems ($X = \text{Mo, Nb, Ta, Sn, Zr}$). The C_{11} - C_{12} shows the stability of the bcc phase. When the \bar{C}_{11} - \bar{C}_{12} value is negative the bcc phase is not stable in the corresponding compositions range.

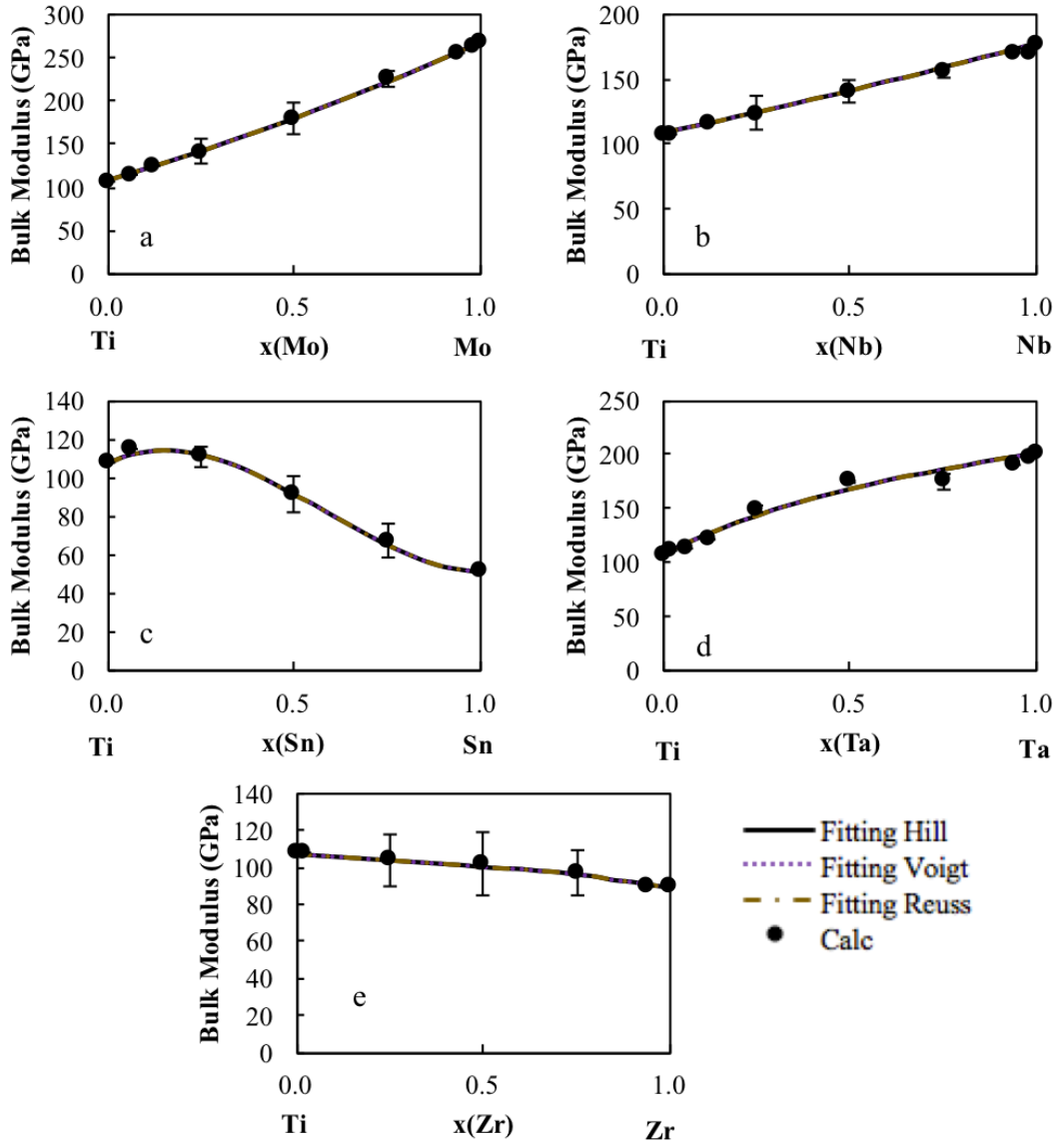


Figure 5.8. Bulk modulus B of the Ti-X binary systems. The present calculations are plotted as the filled circles with the error bars. The dotted purple line is the Voigt upper bulk modulus bound, the gold dot dashed line is the lower Reuss bulk modulus bound and the black line is the Hill bulk modulus average.

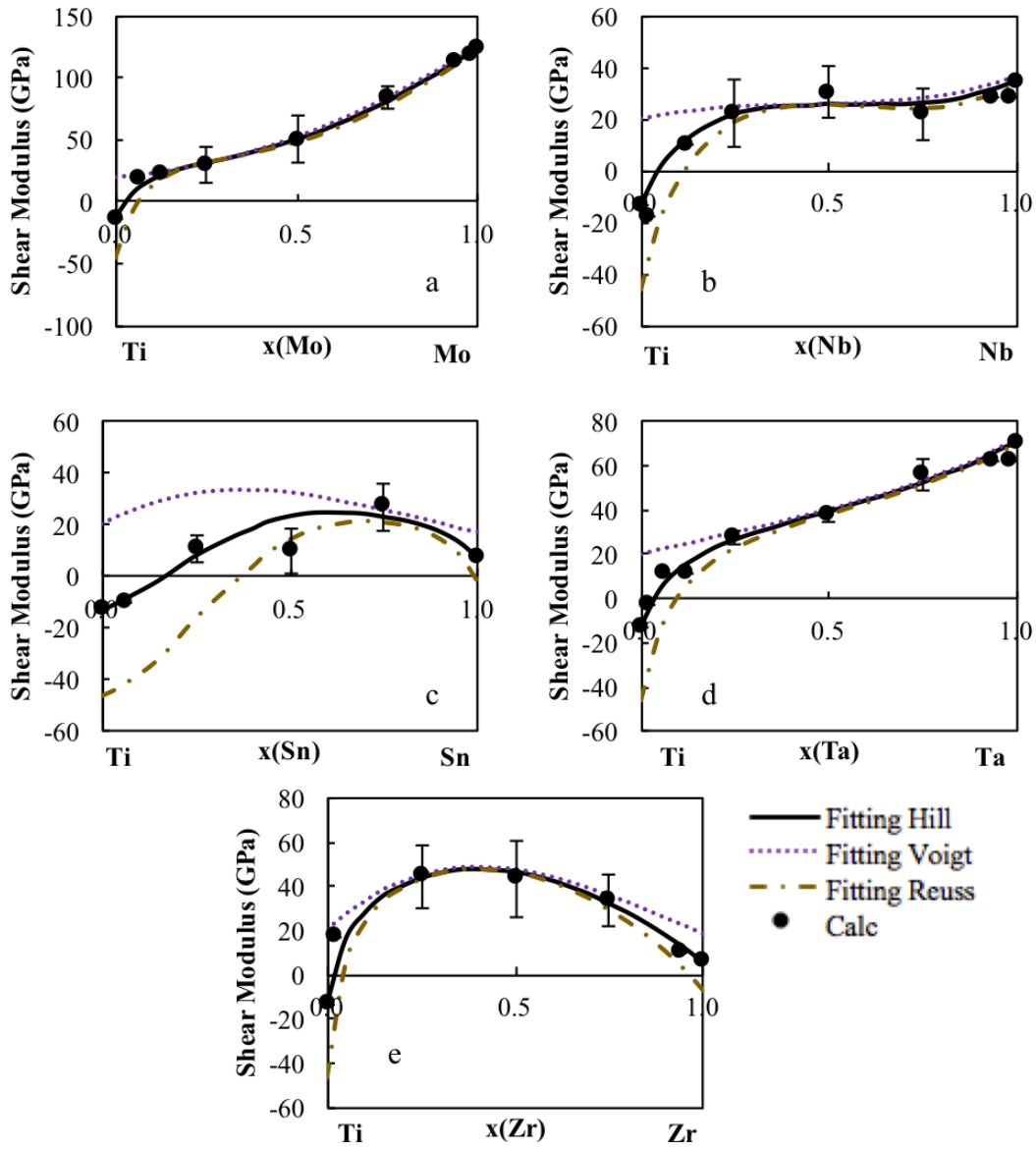


Figure 5.9. Shear modulus G of the Ti-X binary systems. The present calculations are plotted as the filled circles with the error bars. The dotted purple line is the Voigt upper shear modulus bound, the gold dot dashed line is the lower Reuss shear modulus bound and the black line is the Hill shear modulus average.

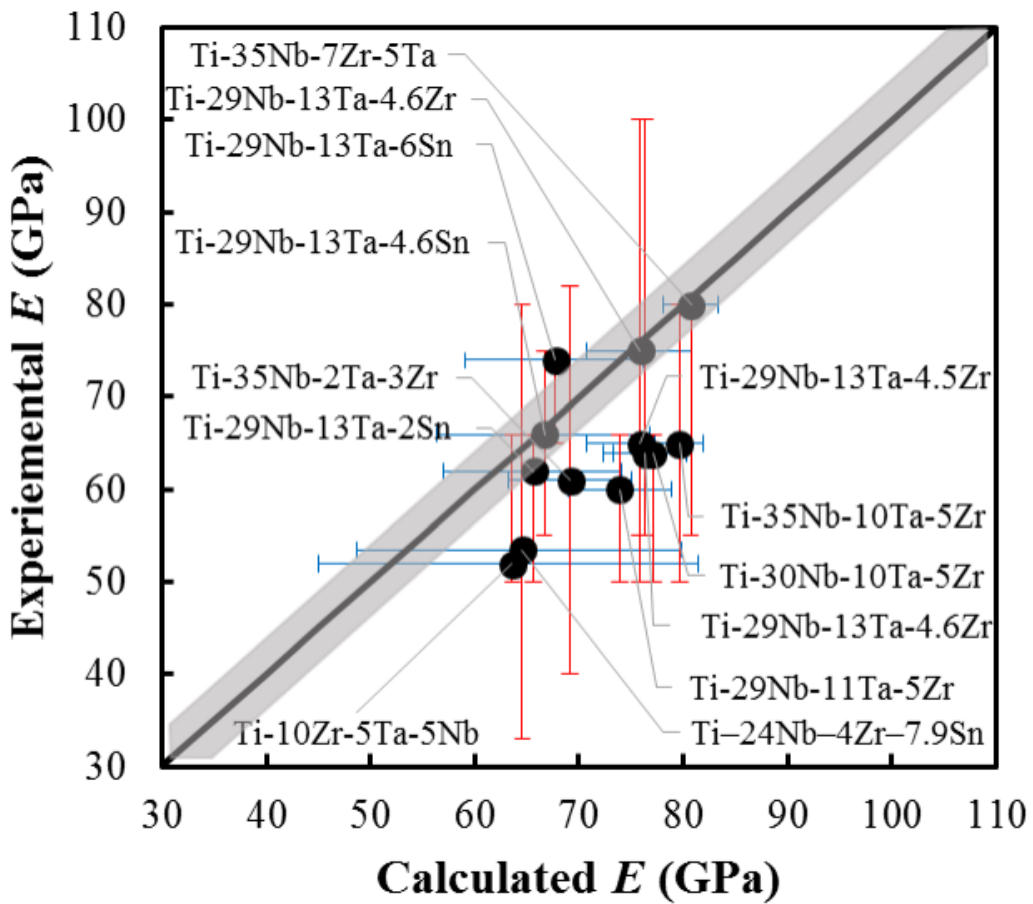


Figure 5.10. Young's modulus values of multicomponent bcc Ti alloys measured experimentally plotted against the predicted Young's modulus from the pure elements and binary interaction parameters with the black diagonal line showing the exact correlation between the experimental and calculated values. Error bars in the experiments and the bounds from Reuss and Voigt approximations are plotted as vertical and horizontal lines, respectively. The variance in the first calculations from Eq. Y-Eq. Y was averaged and plotted as the grey region to show the variance in the first-principles calculations. More information on the alloys is in Table ?? [35–37]

Chapter 6 |

Effects of alloying elements on the elastic properties of bcc ternary and higher ordered Ti-alloys

6.1 Introduction

In order to develop a better understanding about alloying effect on the elastic properties of Ti alloys, the present work is developing an elastic database for the Ti-Mo-Nb-Sn-Ta-Zr system. With the focus being on bcc Ti-alloys, the effects of alloying elements on the pure elements and Ti-X binary alloys in the bcc phase were calculated in chapter 5. After extrapolating to higher order systems, it was hypothesized that studying the effects of alloying on the elastic properties of ternary alloys would improve the database. The present work focuses on studying the elastic properties of the Ti-X-Y ($X \neq Y = \text{Mo, Nb, Ta, Sn, and Zr}$) ternary alloys in the bcc phase. The single crystal elastic stiffness constants ($c_{ij}\AA^3$ s) and polycrystalline aggregate properties are predicted across the composition range using Density Functional Theory (DFT) at 0 °K outlined in the methodology chapter. Based on the DFT results, the CALPHAD approach outlined in the methodology is used to evaluate ternary interaction parameters. The interaction parameters are then incorporated into the database and the database accuracy is again tested similarly to the testing in chapter 5. The completed database is used to map the elastic modulus as a function of composition.

6.2 Modeling and Calculations

6.2.1 Calculation details

To study the elastic properties of the ternary bcc Ti alloys in the Ti-Mo-Nb-Sn-Ta-Zr system, first-principles calculations based on density functional theory were completed using the VASP (Vienna ab-initio simulation package) [57, 58]. Four calculations were done for each ternary alloy Ti-X-Y, with the varying compositions of $X_{0.5}Y_{0.5}$ (16-atom supercell), $TiXY$ (36 atoms), Ti_2XY (32 atoms), Ti_6XY (64 atoms). The structures were all special quasirandom structures (SQS) that were previously generated by Jiang et al. [69, 70]. Due to instability of some of these structures in the bcc phase, different relaxation schemes were used to retain the strucutral symmetry while obtaining the lowest energy structure. These relaxation schemes are outlined in the methodology chapter under the SQS section. The projector augmented wave (PAW) method was used to describe the ion-electron interaction. Based on the work of comparing X-C functionals (Figure 2.1) the exchange-correlation functional of the generalized gradient approach depicted by Perdew, Burke, and Ernzerhof (PBE) was employed [54]. An energy cutoff roughly 1.3 times higher than the default value, 310, was used for all calculations. The valance configuration for each element was selected based on the VASP recommendations and is listed in the methodology chapter. The Brillouin zone sampling is done using the gamma centered Monkhorst-Pack scheme [80]. The elastic calculations were completed using a strain magnitude of ± 0.01 based on the study done in chapter 5 and the results seen in Figure 5.1.

6.2.2 Modeling details

The first-principles results are then used to model the elastic stiffness constants. The modeling was completed by plotting the binary interpolation from the working database build in chapter 5. The plots started at $X_{0.5}Y_{0.5}$ and plotted ot pure Ti. The difference between the binary interpolation and the first-principles results were calculated. The differences were then used to obtain a single fitting parameter using the mathematica code in appendix c. With the focus being Ti-rich alloys and wanting to follow the same modeling technique used on the binary alloys, the first-principles results with 70 at.% Ti or higher were weighted heavier (x6,

according to the authors' practices) than the other points for the fittings. The best fit was found and the ternary interaction parameters were incorporated into the database. The databases was then used to predict the moduli values of the ternary alloys.

6.3 Results and discussion

6.3.1 Elastic calculation results

The calculated elastic stiffness constants and moduli values are listed in Table 6.1 with the experimental values used for comparison. Figure 6.1 and 6.2 plot the Young's modulus calculations (circles) for each Ti-X-Y ternary system ($X \neq Y = Mo, Nb, Sn, Ta, Zr$) starting from a 50-50 mixture of the two alloying elements to Ti. The red dashed line is an interpolation from the binary interaction parameters shown in Table 5.2. The Voigt high bound is plotted as a purple dotted line with the Reuss low bound plotted as a gold dotted-dashed line and the Hill average is plotted as a solid black line. The Voigt and Reuss bounds vary more drastically when the bcc structure is unstable as opposed to when the bcc structure is stable. The database predicts the Hill average. When possible E data obtained experimentally is plotted for comparison.

The present E results for the Ti-Mo-Nb (Figure 6.1a) alloy system are compared with E data from Niinomi et al. [38] obtained experimentally. The error between the previous results and present results was calculated using Eq. Y. The E results from Niinomi et al. are closer to the Voigt bound than Hill average and has an error of 0.65. The present data shows that the E decreases from $Mo_{0.5}Nb_{0.5}$ to Ti. From the literature search, no bcc Ti-Mo-Sn (Figure 6.1b) experimental E results were available to compare with the present work. The E trend shows a decrease in value from $Mo_{0.5}Sn_{0.5}$ to Ti. The calculated E results for the Ti-Mo-Ta alloy system (Figure 6.1c) are compared with experimental data from Niinomi et al. [38] and Mohammad et al. [37] showing an error of 0.46 (Eq. Y). The E values from Niinomi et al. and Mohammad fit well with the present Voigt bound. The E data decreases in value from $Mo_{0.5}Ta_{0.5}$ to Ti. The Young's modulus of the Ti-Mo-Zr alloy system (Figure 6.1d) is compared with experimental E values from Mohammad et al. [37]. The experimental E from Mohammad et al. and the present

E vary by less than 6 GPa and shows the Young's modulus values decreases from $\text{Mo}_{0.5}\text{Zr}_{0.5}$ to Ti. Experimental E results from Niinomi et al. [38], Mohammad et al. [37], and Nozoe et al. [39] are compared with the present E calculations for the Ti-Nb-Sn alloy system (Figure 6.1e). The experimental E results from Niinomi et al., Mohammad et al. and Nozoe et al. fit within the present Voigt-Reuss bounds and have an error of 0.39 from the present Hill average E values. The data trend in the E values shows an increase in the E value from $\text{Nb}_{0.5}\text{Sn}_{0.5}$ to 50 at % Ti and then a decrease in value to Ti.

Figure 6.2 continues to plot the E of the Ti-X-Y ternary alloy systems. Figure 6.2a, plots the present E results for the Ti-Nb-Ta alloy system, versus the E results from Mohammad et al. [37]. The E results from Mohammad et al. fit along the Reuss bound and using Eq. Y have an error of 0.28 from the present E values. The Young's modulus decreases from $\text{Nb}_{0.5}\text{Ta}_{0.5}$ to Ti. The present E for the Ti-Nb-Zr (Figure 6.2b) alloy system is compared with E results obtained experimentally by Geetha et al. [36], Mohammad et al. [37], and Niinomi et al. [38]. The E results from Geetha, Mohammad and Niinomi fit well between the Voigt-Reuss bounds and have an error of 0.08 from the present Hill average E results. The E shows an increase in value from $\text{Nb}_{0.5}\text{Zr}_{0.5}$ to 70 at % Ti and then a decrease to Ti. The Ti-Sn-Ta, Ti-Sn-Zr and Ti-Ta-Zr alloy systems are not compared with any experimental data in Figure 6.2c, d and e respectively. The trend in the E data for the Ti-Sn-Ta alloy system shows that the E decreases from $\text{Sn}_{0.5}\text{Ta}_{0.5}$ to Ti. The Ti-Sn-Zr alloy system data shows an increase in the E values from $\text{Sn}_{0.5}\text{Zr}_{0.5}$ to 60 at % Ti and then the E decreases to Ti. The E values, for the Ti-Ta-Zr alloy system, show the E decreases to 15 at % Ti where the E begins increasing to 30 at % Ti and then decreases to Ti.

The error between the experimentally determined E and the present first-principles calculated E results is expected to occur due to the fact that the CALPHAD fittings are done using elastic stiffness constants calculations done at 0 °K on single crystal structures while the experiments are done measuring polycrystalline samples at 300 °K. While there is some error, the experiments fit well within the bounds set by Reuss and Voigt and the Hill average generally reproduces the experimentally determined E data for the Ti-X-Y ternary alloys.

The elastic stiffness constants, \bar{C}_{11} , \bar{C}_{12} , and \bar{C}_{44} are plotted in Figure 6.3 to Figure 6.8. The \bar{C}_{11} data showed similar trends for most of the Ti-X-Y systems

where the \bar{C}_{11} values decrease from $X_{0.5}Y_{0.5}$ to Ti (seen in Figure 6.3 and Figure 6.4). The data trends vary for the Ti-Sn-Zr and Ti-Ta-Zr alloy systems in Figure 6.4d and e, respectively. The \bar{C}_{11} values, for Ti-Sn-Zr system, increases to 60 at % Ti and then decreases to Ti, while the \bar{C}_{11} values, in the Ti-Ta-Zr system, increase to 35 at % Ti and then decreases to Ti.

The \bar{C}_{12} values plotted in Figure 6.5 and 6.6, decrease from $X_{0.5}Y_{0.5}$ to Ti similarly for the Ti-Mo-Nb, Ti-Mo-Ta and Ti-Nb-Ta systems. The Ti-Mo-Sn and Ti-Nb-Sn systems saw a decrease in \bar{C}_{12} value from $X_{0.5}Y_{0.5}$ to 15 at % Ti then and increase to 85 % Ti and then a decrease to Ti. The Ti-Mo-Zr and Ti-Nb-Zr systems show a decrease in \bar{C}_{12} value from $X_{0.5}Y_{0.5}$ to 60 at % Ti and then an increase to Ti. The \bar{C}_{12} values increase from $X_{0.5}Y_{0.5}$ to 70 at % Ti and then decrease to Ti for the Ti-Sn-Ta system. For the Ti-Sn-Zr system, the \bar{C}_{12} values increase from $X_{0.5}Y_{0.5}$ to Ti and the \bar{C}_{12} values, for the Ti-Ta-Zr system, decrease to 70 at % Ti and then increase.

The \bar{C}_{44} data plotted in Figure 6.7 and Figure 6.8 shows that the values similarly decrease from $X_{0.5}Y_{0.5}$ to Ti for the Ti-Mo-Sn and Ti-Ta-Zr systems. The Ti-Mo-Zr and Ti-Mo-Ta systems show that the \bar{C}_{44} values decrease from $X_{0.5}Y_{0.5}$ to 80 at % Ti and then increase to Ti. The \bar{C}_{44} values, for the Ti-Mo-Nb and Ti-Nb-Ta systems, show a decrease from $X_{0.5}Y_{0.5}$ to 65 at % Ti and then increasing to Ti. The \bar{C}_{44} values show an increase from $X_{0.5}Y_{0.5}$ to 80 at % Ti and then a decrease to Ti for the Ti-Nb-Sn and Ti-Nb-Zr systems. The \bar{C}_{44} values, for the Ti-Sn-Ta system, decrease from $X_{0.5}Y_{0.5}$ until 20 at % Ti, then increase to 50 at % Ti and then decrease to Ti. Finally the Ti-Sn-Zr system shows an increase in \bar{C}_{44} value from $X_{0.5}Y_{0.5}$ to 60 at % Ti and then decrease to Ti.

The $\bar{C}_{11} - \bar{C}_{12}$ is plotted in Figure 6.9. The $\bar{C}_{11} - \bar{C}_{12}$ plot shows the limit of mechanical stability of the bcc phase for each ternary alloy. Based on Borná Á Žs criteria when the $\bar{C}_{11} - \bar{C}_{12}$ values are negative then the phase, bcc in this case, loses mechanical stability. Based on the present results in Figure 6.9, the bcc phase loses mechanical stability in Ti-Mo-Nb, Ti-Mo-Ta, Ti-Mo-Zr, Ti-Nb-Zr, Ti-Sn-Zr, and Ti-Ta-Zr systems when the Ti concentration is more than 90 at %, with the values being 91, 92, 95, 93, 91, and 94 at % Ti respectively. The bcc phase loses mechanical stability at Ti concentrations of 87, 77, 89, and 80 at % Ti for Ti-Mo-Sn, Ti-Nb-Sn, Ti-Nb-Ta and Ti-Sn-Ta systems. The B and G moduli data are plotted similarly to the Young's modulus in Figure 6.10 to Figure 6.13. The

present B and G calculations (circles) are plotted with at interpolation from the binary interaction parameters (red dashed line), the Voigt (purple dotted line) and Reuss (gold dash-dotted line) bounds and the Hill average (solid black line). The B data showed the same trend, decreasing in value from $X_{0.5}Y_{0.5}$ to Ti, for all the Ti-X-Y ternaries except Ti-Nb-Sn, Ti-Sn-Ta and Ti-Sn-Zr seen in Figure 6.10 and Figure 6.11. The B data for the Ti-Nb-Sn and Ti-Sn-Ta systems, decrease in value from $X_{0.5}Y_{0.5}$ to 10 at % Ti and then increase to 55 at % Ti and then decrease to Ti. The B values, in the Ti-Sn-Zr alloy system, showed an increase in value from $X_{0.5}Y_{0.5}$ to 85 at % Ti and then a decrease to Ti. The G decrease in value from $X_{0.5}Y_{0.5}$ to Ti for all the ternary systems except Ti-Nb-Sn, Ti-Nb-Zr, Ti-Sn-Zr and Ti-Ta-Zr (Figure 6.12 and Figure 6.13). The G values increase from $X_{0.5}Y_{0.5}$ to 60 at % Ti and then decrease to Ti for the Ti-Nb-Sn, Ti-Nb-Zr systems. The G data for the Ti-Sn-Zr system increases in value and the G decreases in value from $X_{0.5}Y_{0.5}$ to 5 at % Ti and then increases to 35 at % Ti before decreasing to Ti for the Ti-Ta-Zr system.

6.3.2 Extrapolation to higher ordered systems

Using the completed database and interaction parameters in Table 5.2 and Table 6.2, the elastic stiffness constants can be predicted and then the moduli values can be calculated and mapped. Figure 6.14 and Figure 6.15 uses the global minimization tools in pycalphad [40] to map the Young's modulus based on composition for Ti-X-Y ternaries. The mapping can thus allow for regions with specific moduli values to be targeted.

The Young's modulus is predicted and compared with experimental results for higher order Ti alloys and the results are shown in Table 6.3 and Figure 6.16. The same comparison was made in chapter 5 but using only the pure elements and binary interaction parameters. As in Chapter 5, Figure 6.16 plots the calculated E versus the experimentally determined E [35–37]. The black diagonal line would be a perfect correlation between the predictions and experiments. The grey region is the average variance in the first-principles calculations when calculating the average elastic stiffness constants using Eq. Y-Eq. Y. The same higher order alloys were picked to compare the effect that introducing the ternary interaction parameters had. As discussed previously, the error bars plotted for the experiments come from

the variance that was seen when comparing the experimentally determined E at the same composition from Niinomi et al. [38], Geetha et al. [36], Tane et al. [35], and Mohammad et al. [37]. The horizontal error bars are the Voigt and Reuss bounds. Previously, with no ternary interaction parameters the predictions and experimental results varied anywhere between 0.69 and 14 GPa and on average by 7 GPa. This was attributed to the fact that the single crystal elastic stiffness constants that are fit to obtain the moduli values were at 0 °K while the experiments on the polycrystalline samples are done at 300 °K. It was predicted that introducing non-Ti containing binary interaction parameters and ternary interaction parameters would improve the database. The introduction of the ternary interaction parameters improved the predictions to vary anywhere from 0.39 to 13 GPa from the experimental values with an average variance of only 5 GPa. Thus the introduction of Ti-containing ternary interaction parameters improved the predictions and the database can accurately predict the Young's modulus of higher order Ti alloys.

6.4 Conclusion

The present work systematically calculates the elastic properties of the bcc Ti ternary alloys, including the elastic stiffness constants, bulk modulus, shear modulus, and Young's modulus. Six alloying elements, Mo, Nb, Sn, Ta and Zr were studied. The CALPHAD method was used to fit ternary interaction parameters. The fittings were done by calculating the difference between the first-principles calculations and the binary interpolations from the pure elements and binary interaction parameters previously determined. The differences were then used to determine the ternary interaction parameters. The present calculations showed that the bcc phase was mechanically stabilized at compositions less than 91, 92, 95, 93, 91, 94, 87, 77, 89, and 80 at % Ti for the Ti-Mo-Nb, Ti-Mo-Ta, Ti-Mo-Zr, Ti-Nb-Zr, Ti-Sn-Zr, Ti-Ta-Zr, Ti-Mo-Sn, Ti-Nb-St, Ti-Nb-Ta and Ti-Sn-Ta alloys respectively.

The Ti-Mo-Nb, Ti-Mo-Ta, Ti-Mo-Zr, and Ti-Nb-Ta alloys saw similar fitting trends. The ternary interaction parameters were combined with the previously determined pure elements and binary interaction parameters into one complete tdb database. The fittings were used to map some of the possible alloy compositions to find potential materials with a Young's modulus in the target range for biomedical load bearing implants. Overall, the introduction of the ternary interaction

parameters improved the database's ability to predict the Young's modulus of higher ordered alloys and the database is able to accurately predict the Young's modulus of Ti-alloys. It is hypothesized that the introduction of non-Ti containing interaction parameters would improve the database even further. The tdb file is attached in appendix d.

Table 6.1: First-principles calculations of the elastic stiffness constants, bulk modulus B , shear modulus G , and Young's modulus E in GPa for different atomic percent compositions of the bcc Ti-X-Y ternary systems at 0 °K. As well as experimental data obtained for the Young's modulus at 300 °K by the reference stated.

Reference	$Ti_{1-2b}X_bY_b$	\overline{C}_{11}	\overline{C}_{11}	\overline{C}_{11}	B	G	E
This work	Ti	93	115	41	108	-12.91	-40.34
This work	TiMo _{12.5} Nb _{12.5}	155	121 ±4	34 ±4	132 ±4	26 ±4	73 ±4
This work	TiMo _{25.0} Nb _{25.0}	222 ±3	129 ±3	33 ±3	160 ±3	38 ±3	105 ±3
This work	TiMo _{33.3} Nb _{33.3}	269 ±5	134 ±3	42 ±4	179 ±5	51 ±5	139 ±5
This work	Mo ₅₀ Nb ₅₀	414 ±6	165 ±3	68	248 ±6	87 ±6	233 ±6
Expt 300 K [38]	TiMo ₆ Nb ₂						110
This work	TiMo _{12.5} Sn _{12.5}	137 ±15	121 ±2	56 ±13	126 ±15	27 ±15	75 ±15
This work	TiMo _{25.0} Sn _{25.0}	160 ±3	130 ±8	71 ±2	140 ±8	39 ±8	106 ±8
This work	TiMo _{33.3} Sn _{33.3}	167 ±8	133 ±6	75 ±2	144 ±8	42 ±8	114 ±8
This work	Mo ₅₀ Sn ₅₀	192 ±28	130 ±36	40 ±31	151 ±36	36 ±36	100 ±36
This work	TiMo _{12.5} Ta _{12.5}	153 ±1	125 ±4	38 ±3	134 ±4	25 ±4	72 ±4
This work	TiMo _{25.0} Ta _{25.0}	222 ±2	136 ±1	45 ±3	165 ±2	44 ±3	122 ±3
This work	TiMo _{33.3} Ta _{33.3}	263 ±4	145 ±6	49 ±4	184 ±6	53 ±6	145 ±
This work	Mo ₅₀ Ta ₅₀	370 ±13	163 ±4	63 ±4	232 ±13	77 ±13	208 ±13
Expt 300 K [37]	TiMo ₇ Ta ₁						74
Expt 300 K [38]	TiMo ₇ Ta ₁						74
This work	TiMo _{12.5} Zr _{12.5}	125 ±1	109 ±8	35 ±1	114 ±8	20 ±8	55 ±8
This work	TiMo _{25.0} Zr _{25.0}	160 ±1	116 ±5	34 ±2	131 ±5	29 ±5	80 ±5
This work	TiMo _{33.3} Zr _{33.3}	182 ±1	116 ±2	31 ±8	138 ±2	32 ±8	89 ±8
This work	Mo ₅₀ Zr ₅₀	231 ±7	118 ±5	33 ±8	156 ±7	41 ±8	113 ±8
Expt 300 K [37]	TiMo ₇ Zr ₃						64
This work	TiNb _{12.5} Sn _{12.5}	115 ±4	118 ±3	55	117 ±4	14 ±4	41 ±4
This work	TiNb _{25.0} Sn _{25.0}	131 ±9	121 ±6	64 ±3	124 ±9	26 ±9	72 ±9
This work	TiNb _{33.3} Sn _{33.3}	134 ±2	122 ±3	67 ±6	126 ±6	28 ±6	78 ±6
This work	Nb ₅₀ Sn ₅₀	132 ±4	118 ±8	56 ±4	123 ±8	26 ±8	72 ±8
Expt 300 K [37]	TiNb ₂₂ Sn ₂						44

Table 6.1: First-principles calculations of the elastic stiffness constants, bulk modulus B , shear modulus G , and Young's modulus E in GPa for different atomic percent compositions of the bcc Ti-X-Y ternary systems at 0 °K. As well as experimental data obtained for the Young's modulus at 300 °K by the reference stated.

Reference	$Ti_{1-2b}X_bY_b$	\overline{C}_{11}	\overline{C}_{11}	\overline{C}_{11}	B	G	E
Expt 300 K [38]	TiNb ₂₂ Sn ₂						50
Expt 300 K [39]	TiNb ₉ Sn ₃						58
This work	TiNb _{12.5} Ta _{12.5}	130 ±3	124 ±4	37 ±3	126 ±4	15 ±4	43 ±4
This work	TiNb _{25.0} Ta _{25.0}	182 ±1	129 ±4	43 ±6	147 ±6	35 ±6	98 ±6
This work	TiNb _{33.3} Ta _{33.3}	208	135 ±1	44 ±1	159 ±1	41 ±1	113 ±1
This work	Nb ₅₀ Ta ₅₀	260 ±2	148 ±3	47 ±3	185 ±3	50 ±3	140 ±3
Expt 300 K [37]	TiNb ₁₀ Ta ₁₉						55
This work	TiNb _{12.5} Zr _{12.5}	101 ±2	113 ±4	32 ±3	109 ±4	-2 ±4	-6 ±4
This work	TiNb _{25.0} Zr _{25.0}	122 ±1	113 ±3	28 ±3	116 ±3	14 ±3	40 ±3
This work	TiNb _{33.3} Zr _{33.3}	143 ±2	107 ±5	28 ±3	119 ±5	23 ±5	66 ±5
This work	Nb ₅₀ Zr ₅₀	154 ±5	110 ±3	15 ±2	125 ±5	17 ±5	50 ±5
Expt 300 K [37]	TiNb ₈ Zr ₈						77
Expt 300 K [37]	TiNb ₁₂ Zr ₉						14
Expt 300 K [37]	TiNb ₁₁ Zr ₃						50
Expt 300 K [38]	TiNb ₁₇ Zr ₅						78
Expt 300 K [36]	TiNb ₈ Zr ₈						81
This work	TiSn _{12.5} Ta _{12.5}	115 ±6	121 ±4	60 ±2	119 ±6	13 ±6	39 ±6
This work	TiSn _{25.0} Ta _{25.0}	138 ±13	125 ±4	75 ±4	129 ±13	31 ±13	86 ±13
This work	TiSn _{33.3} Ta _{33.3}	138 ±6	131 ±8	78 ±1	133 ±8	28 ±8	79 ±8
This work	Sn ₅₀ Ta ₅₀	133 ±8	130 ±4	60 ±4	131 ±8	20 ±8	57 ±8
This work	TiSn _{12.5} Zr _{12.5}	97 ±5	111 ±4	55 ±2	106 ±5	4 ±5	13 ±5
This work	TiSn _{25.0} Zr _{25.0}	99 ±12	103 ±4	59 ±7	102 ±12	15 ±12	42 ±12
This work	TiSn _{33.3} Zr _{33.3}	96 ±7	98 ±3	55 ±3	97 ±7	15 ±7	43 ±7
This work	Sn ₅₀ Zr ₅₀	85 ±7	87 ±9	42 ±3	86 ±9	11 ±9	32 ±9
This work	TiTa _{12.5} Zr _{12.5}	136 ±36	103 ±21	44 ±5	114 ±21	30 ±21	82 ±21
This work	TiTa _{25.0} Zr _{25.0}	130 ±3	117 ±4	42 ±7	121 ±4	20 ±7	58 ±7

Table 6.1: First-principles calculations of the elastic stiffness constants, bulk modulus B , shear modulus G , and Young's modulus E in GPa for different atomic percent compositions of the bcc Ti-X-Y ternary systems at 0 °K. As well as experimental data obtained for the Young's modulus at 300 °K by the reference stated.

Reference	$\text{Ti}_{1-2b}\text{X}_b\text{Y}_b$	\overline{C}_{11}	\overline{C}_{11}	\overline{C}_{11}	B	G	E
This work	$\text{TiTa}_{33.3}\text{Zr}_{33.3}$	148 ± 1	115 ± 2	44 ± 2	126 ± 2	30 ± 2	83 ± 2
This work	$\text{Ta}_{50}\text{Zr}_{50}$	157 ± 2	123 ± 3	35 ± 3	134 ± 3	26 ± 3	74 ± 3

Table 6.2. Evaluated interactions parameters (L_2 , Eq. Y) for the elastic stiffness constants of the Ti-containing ternary alloys.

Alloy	Interaction Parameter	\bar{C}_{11}	\bar{C}_{12}	\bar{C}_{44}
Ti-Mo-Nb	L_2	-29.97	13.97	9.72
Ti-Mo-Sn	L_2	-83.85	31.80	74.73
Ti-Mo-Ta	L_2	-106.53	-12.35	5.27
Ti-Mo-Zr	L_2	-245.27	50.43	-44.96
Ti-Nb-Sn	L_2	-41.52	25.52	67.85
Ti-Nb-Ta	L_2	-93.77	-15.80	4.25
Ti-Nb-Zr	L_2	-220.35	72.10	-55.29
Ti-Sn-Ta	L_2	-95.39	-10.94	67.85
Ti-Sn-Zr	L_2	-155.34	68.86	3.85
Ti-Ta-Zr	L_2	-149.67	-8.91	-23.70

Table 6.3. Predicted Young's modulus (in GPa) of higher order alloys in the bcc phase compared to experimental values found with both the weight percent and atomic percent listed. The predicted Young's modulus was found using the completed database with the pure elements, binary and ternary interaction parameters.

Alloy Name (%wt)	at %	Calc E	Expt E
Ti-35Nb-7Zr-5Ta [36]	Ti-24Nb-5Zr-2Ta	78	80
Ti-29Nb-13Ta-4.6Zr [36]	Ti-20Nb-5Ta-3Zr	73	75
Ti-29Nb-13Ta-6Sn [36]	Ti-21Nb-5Ta-3Sn	68	74
Ti-29Nb-13Ta-4.6Sn [36]	Ti-20Nb-5Ta-3Sn	66	66
Ti-29Nb-13Ta-4.5Zr [36]	Ti-20Nb-5Ta-3Zr	73	65
Ti-29Nb-13Ta-4.6Zr [35]	Ti-21Nb-5Ta-3Zr	75	64
Ti-30Nb-10Ta-5Zr [35]	Ti-23Nb-4Ta-3Zr	74	64
Ti-35Nb-10Ta-5Zr [35]	Ti-25Nb-4Ta-4Zr	78	65
Ti-24Nb-4Zr-7.9Sn [37]	Ti-15Nb-3Zr-4Sn	62	54
Ti-35Nb-2Ta-3Zr [37]	Ti-23Nb-1Ta-2Zr	68	61
Ti-29Nb-11Ta-5Zr [37]	Ti-20Nb-6Ta-2Zr	72	60
Ti-10Zr-5Ta-5Nb [37]	Ti-6Zr-1Ta-3Nb	62	52
Ti-29Nb-13Ta-2Sn [37]	Ti-20Nb-5Ta-1Sn	65	62

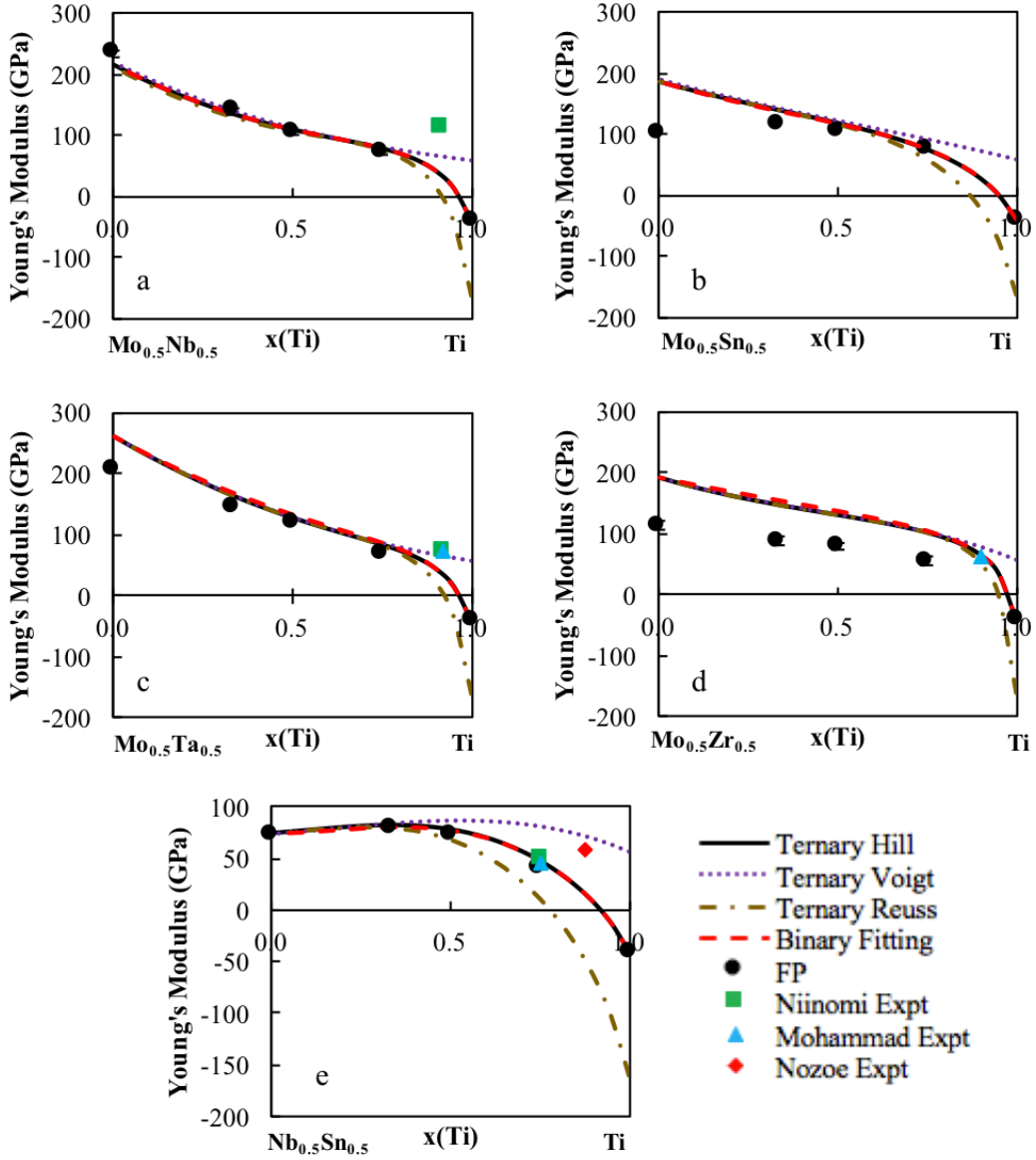


Figure 6.1. Young's modulus E of five of the Ti-X-Y ternary systems are plotted from a 50-50 mixture of the alloying elements to Ti in the bcc phase. The present calculations are plotted as filled circles with the error bars. The red dotted line is the extrapolation for the pure elements and binary interaction parameters only. The dotted purple line is the Voigt upper YoungâŽs modulus bound, the gold dot dashed line is the lower Reuss YoungâŽs modulus bound and the black line is the Hill YoungâŽs modulus average. Experimental values are include for comparison [36–39].

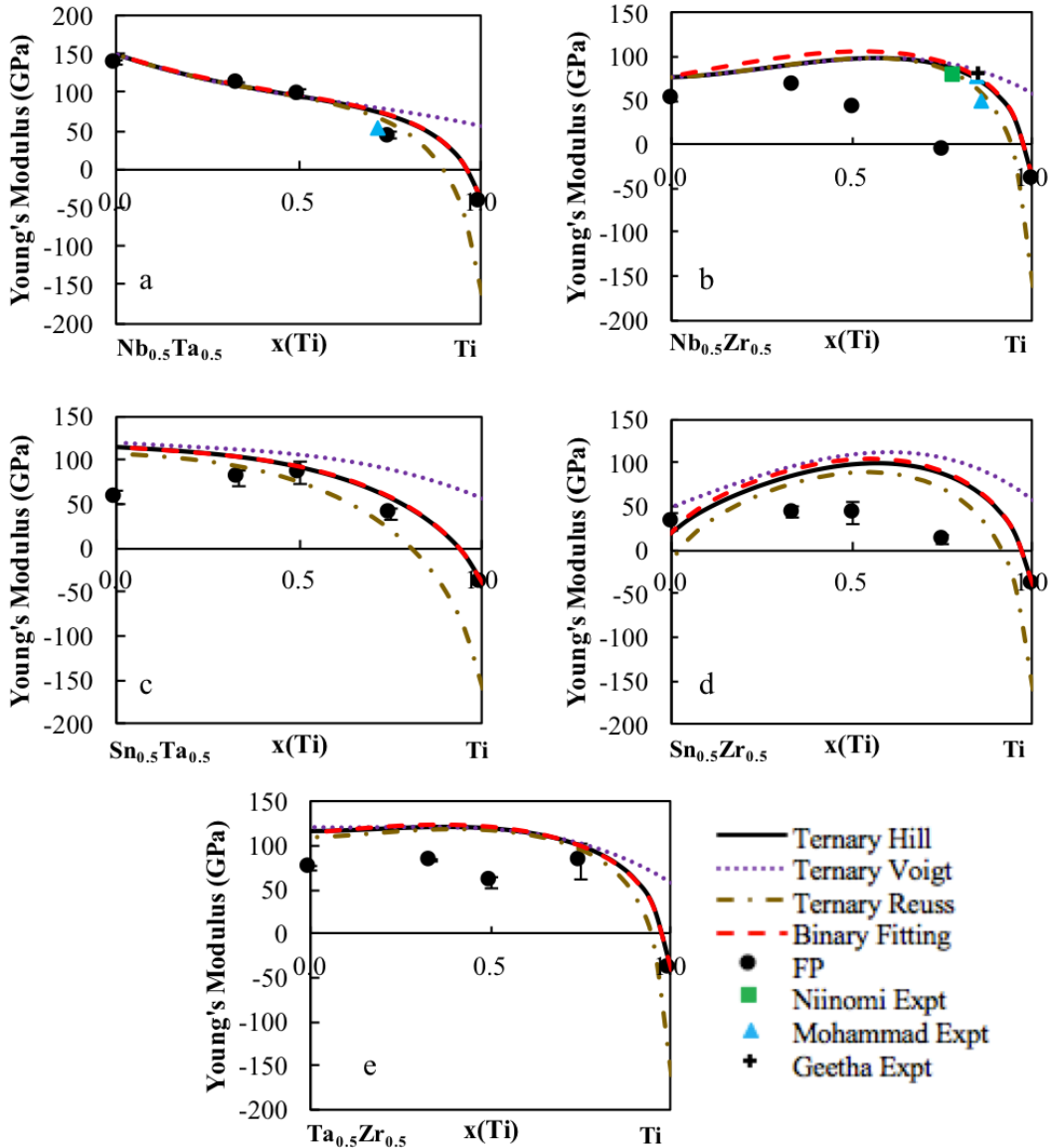


Figure 6.2. Young's modulus E of five of the Ti-X-Y ternary systems are plotted from a 50-50 mixture of the alloying elements to Ti in the bcc phase. The present calculations are plotted as filled circles with the error bars. The red dotted line is the extrapolation for the pure elements and binary interaction parameters only. The dotted purple line is the Voigt upper YoungâŽ's modulus bound, the gold dot dashed line is the lower Reuss YoungâŽ's modulus bound and the black line is the Hill YoungâŽ's modulus average. Experimental values are include for comparison [36–39].

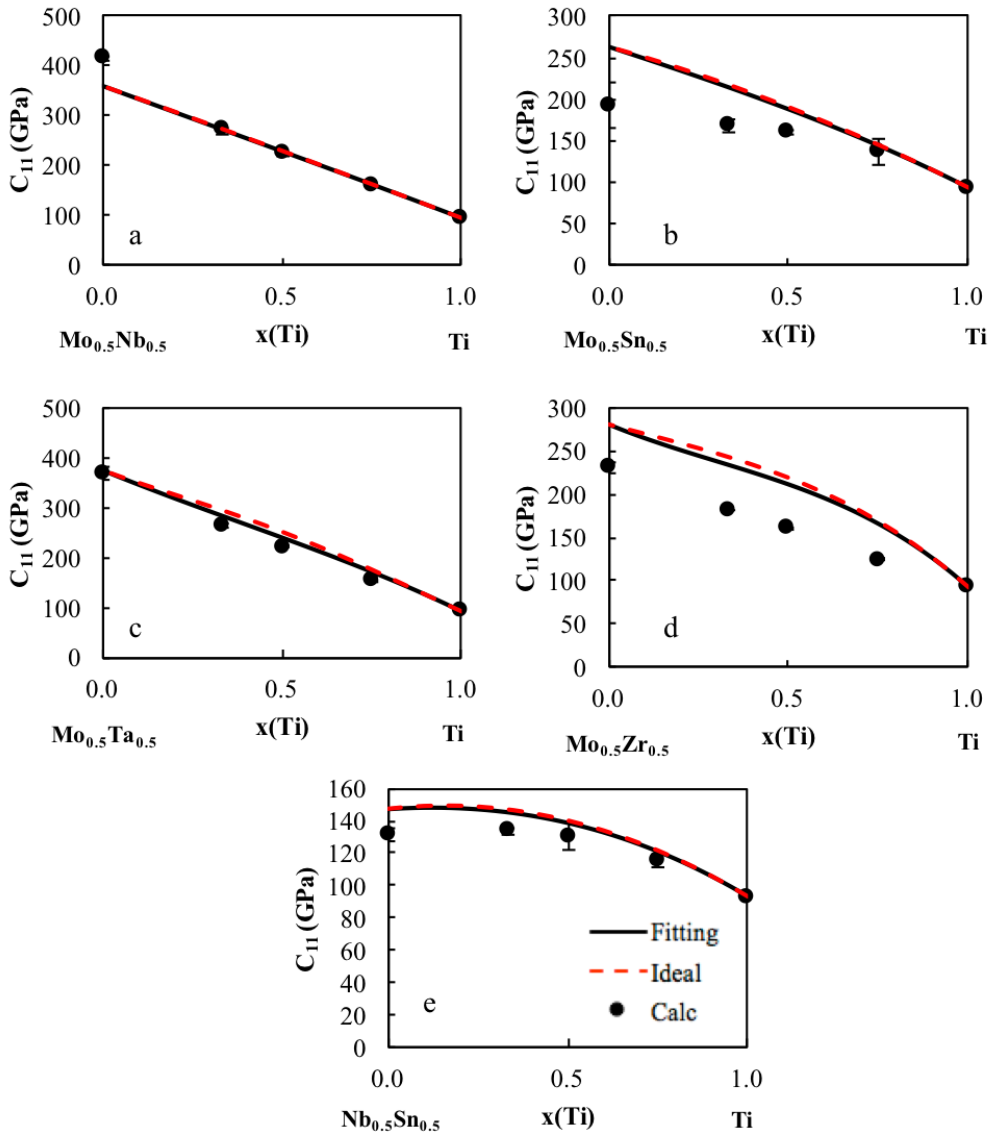


Figure 6.3. Calculated \bar{C}_{11} values (circles) plotted with their errors as well as the interpolation from the binary interaction parameters (red dashed line) and the ternary fitting (black dashed line) for five of the Ti-X-Y binary systems from a 50-50 mixture of the alloying elements X and Y to Ti ($X \neq Y = \text{Mo, Nb, Ta, Sn, Zr}$).

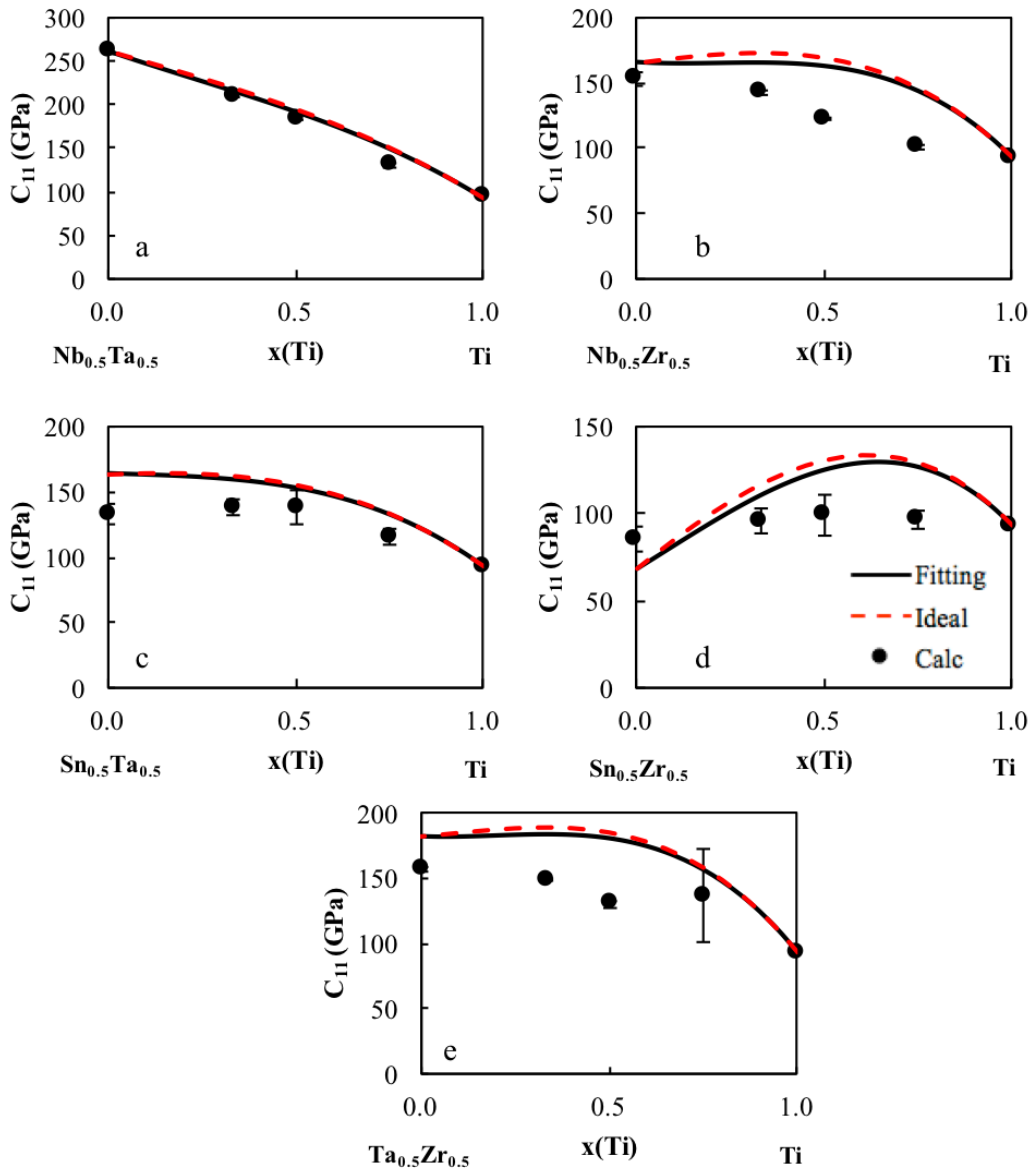


Figure 6.4. Calculated \bar{C}_{11} values (circles) plotted with their errors as well as the interpolation from the binary interaction parameters (red dashed line) and the ternary fitting (black dashed line) for five of the Ti-X-Y binary systems from a 50-50 mixture of the alloying elements X and Y to Ti ($X \neq Y = \text{Mo, Nb, Ta, Sn, Zr}$).

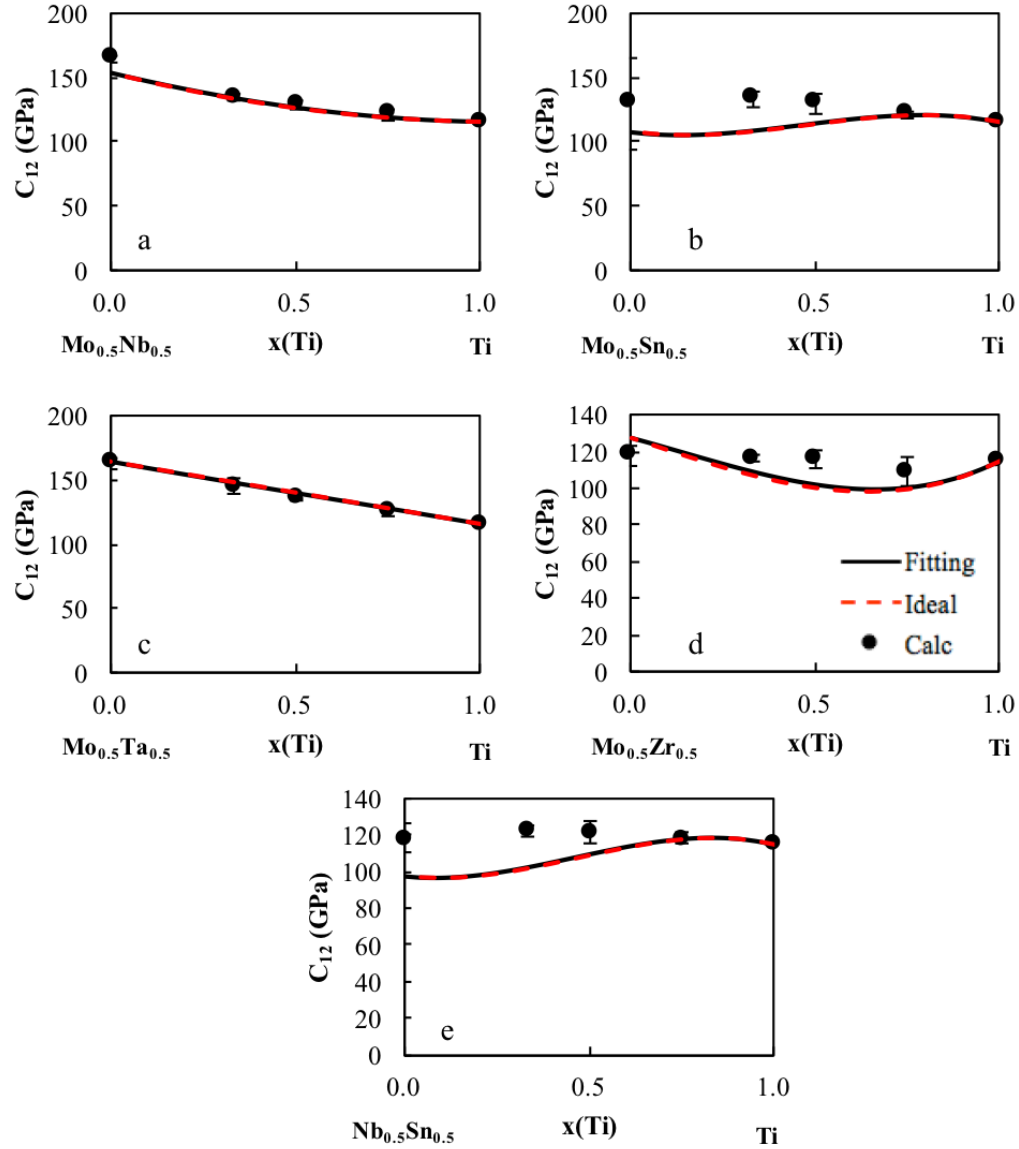


Figure 6.5. Calculated \bar{C}_{12} values (circles) plotted with their errors as well as the interpolation from the binary interaction parameters (red dashed line) and the ternary fitting (black dashed line) for five of the Ti-X-Y binary systems from a 50-50 mixture of the alloying elements X and Y to Ti ($X \neq Y = \text{Mo, Nb, Ta, Sn, Zr}$).

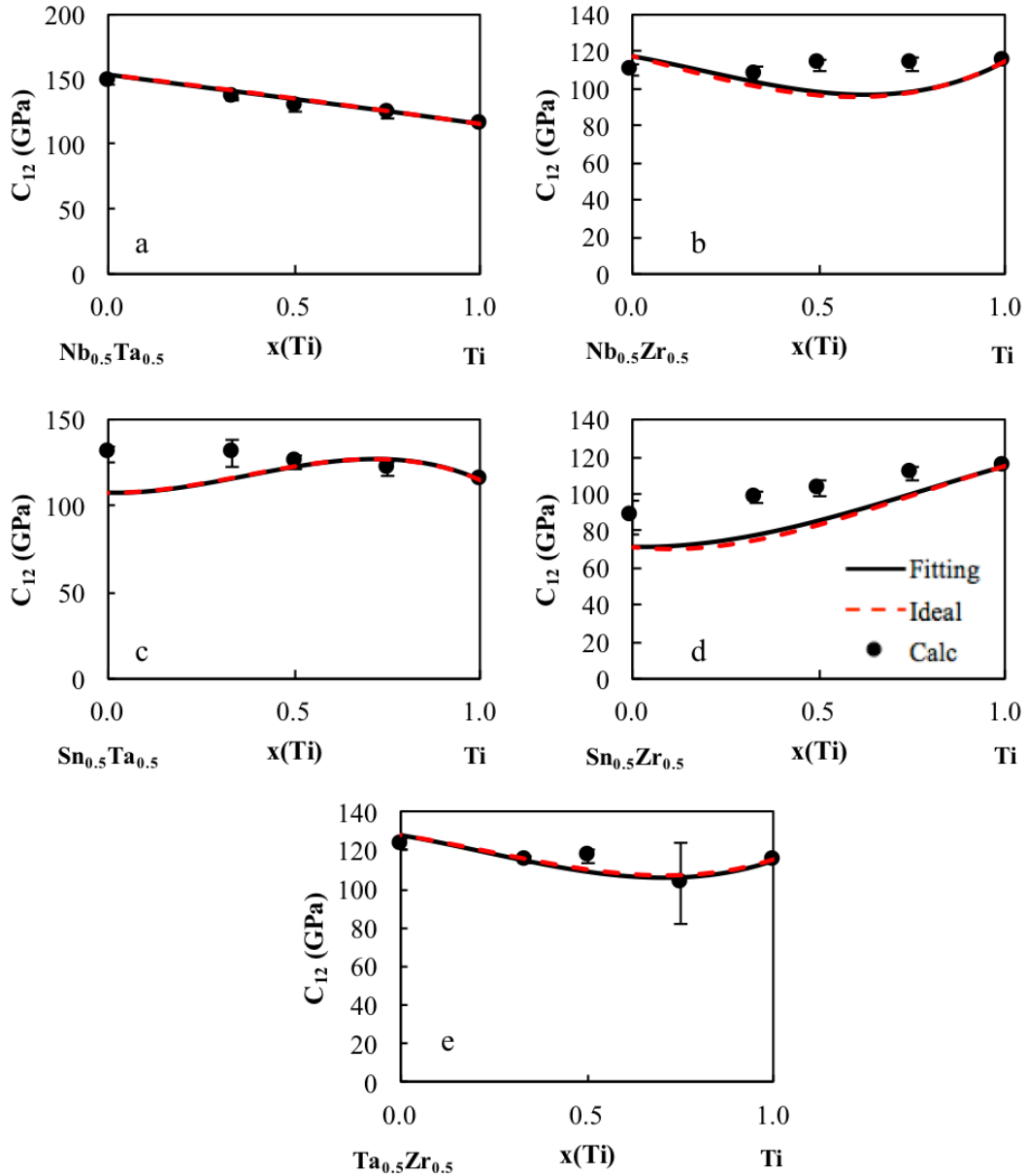


Figure 6.6. Calculated \bar{C}_{12} values (circles) plotted with their errors as well as the interpolation from the binary interaction parameters (red dashed line) and the ternary fitting (black dashed line) for five of the Ti-X-Y binary systems from a 50-50 mixture of the alloying elements X and Y to Ti ($X \neq Y = Mo, Nb, Ta, Sn, Zr$).

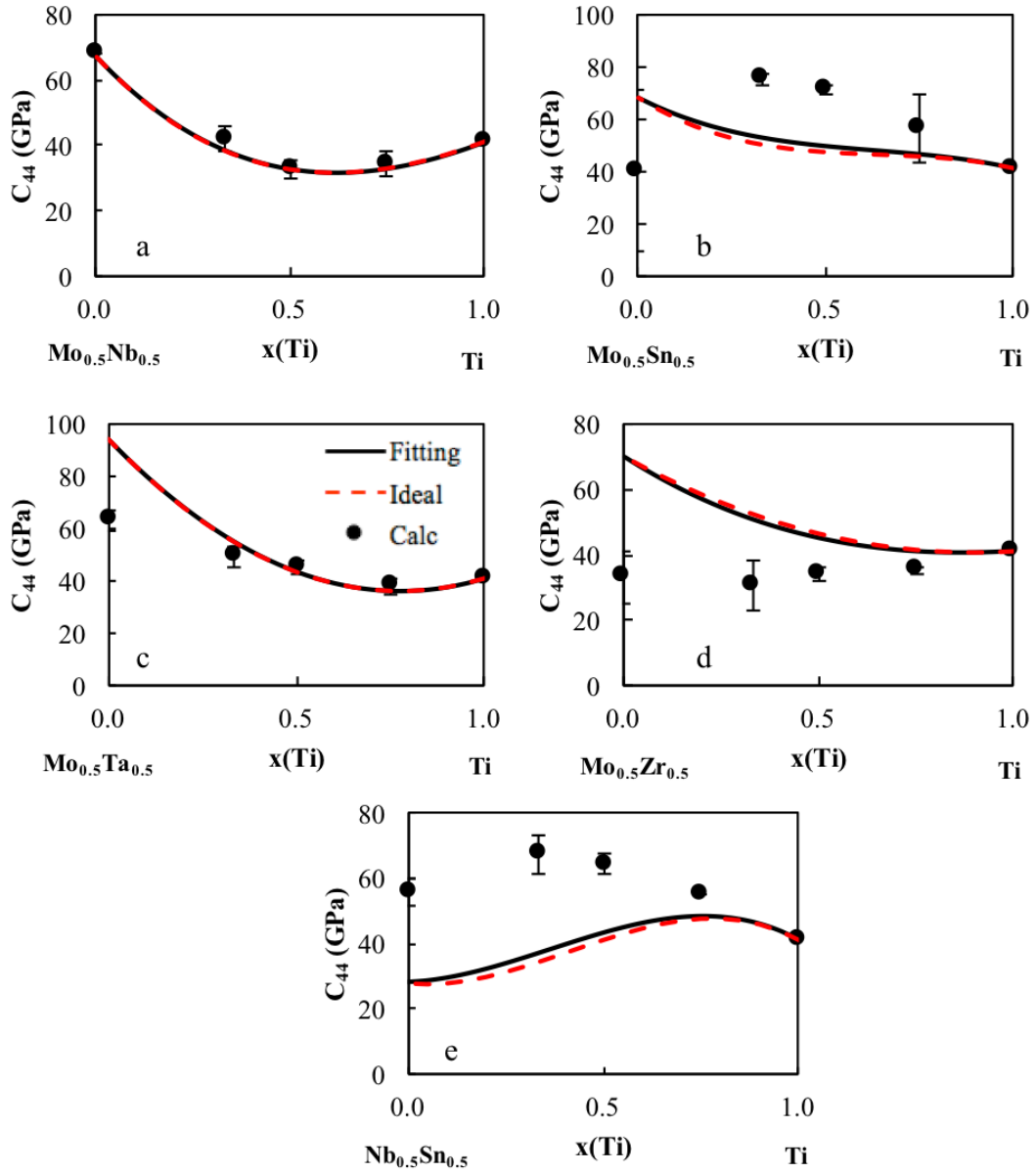


Figure 6.7. Calculated \bar{C}_{44} values (circles) plotted with their errors as well as the interpolation from the binary interaction parameters (red dashed line) and the ternary fitting (black dashed line) for five of the Ti-X-Y binary systems from a 50-50 mixture of the alloying elements X and Y to Ti ($X \neq Y = \text{Mo, Nb, Ta, Sn, Zr}$).

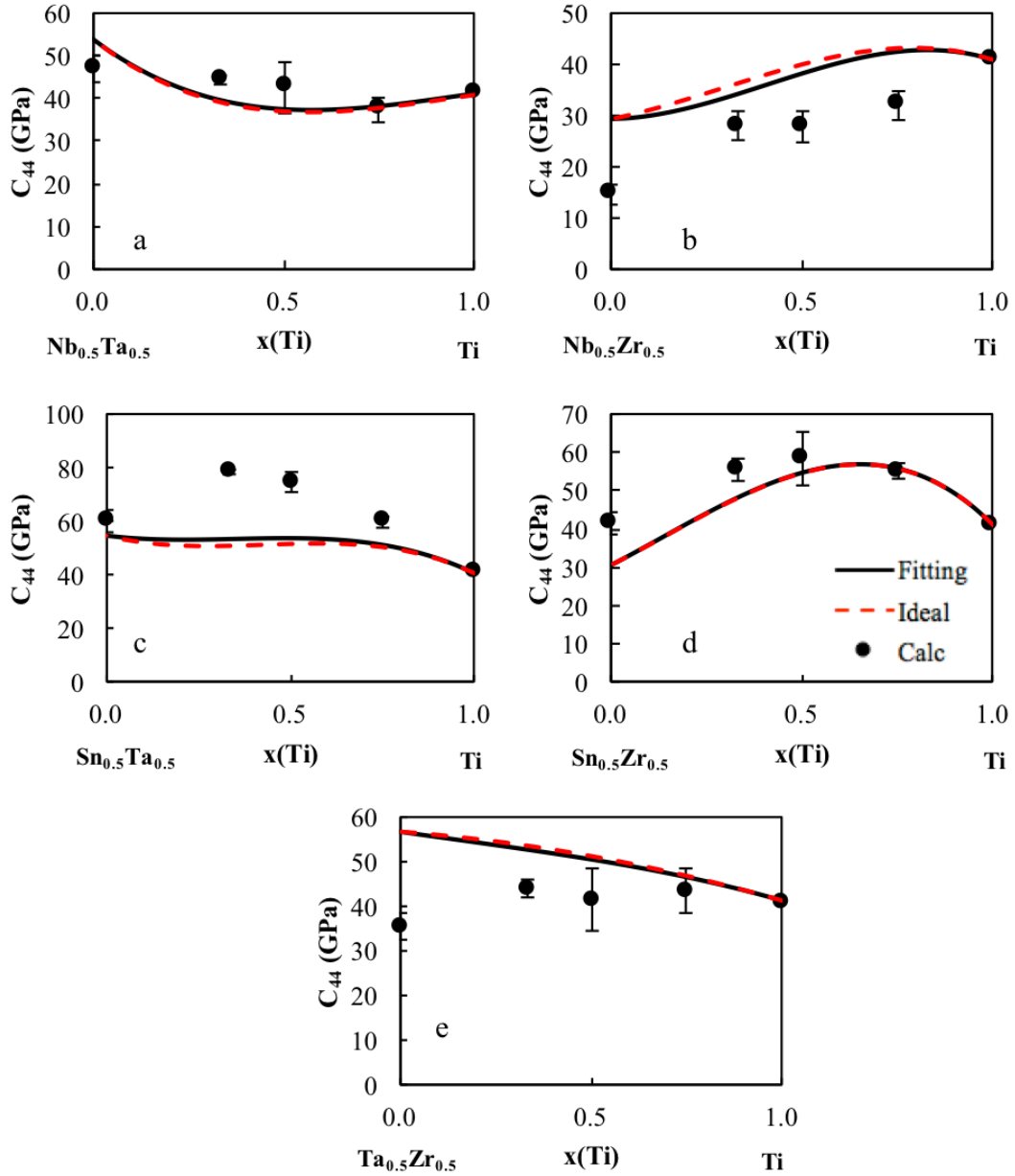


Figure 6.8. Calculated \bar{C}_{44} values (circles) plotted with their errors as well as the interpolation from the binary interaction parameters (red dashed line) and the ternary fitting (black dashed line) for five of the Ti-X-Y binary systems from a 50-50 mixture of the alloying elements X and Y to Ti ($X \neq Y = Mo, Nb, Ta, Sn, Zr$).

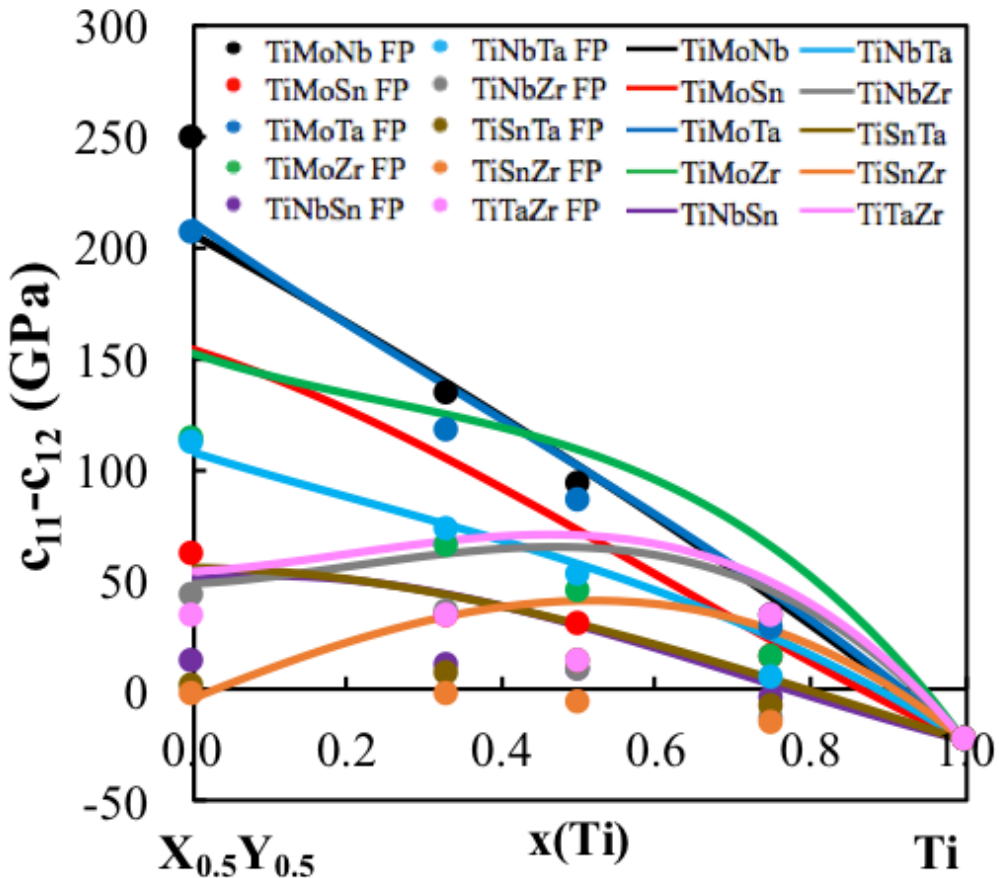


Figure 6.9. Calculated $\bar{C}_{11} - \bar{C}_{12}$ values (circles) plotted with the present modeling (solid lines) for the Ti-X-Y ternary systems ($X \neq Y = \text{Mo, Nb, Ta, Sn, Zr}$). The $\bar{C}_{11} - \bar{C}_{12}$ shows the stability of the bcc phase, when the value is negative the bcc phase is not stable in the corresponding composition ranges.

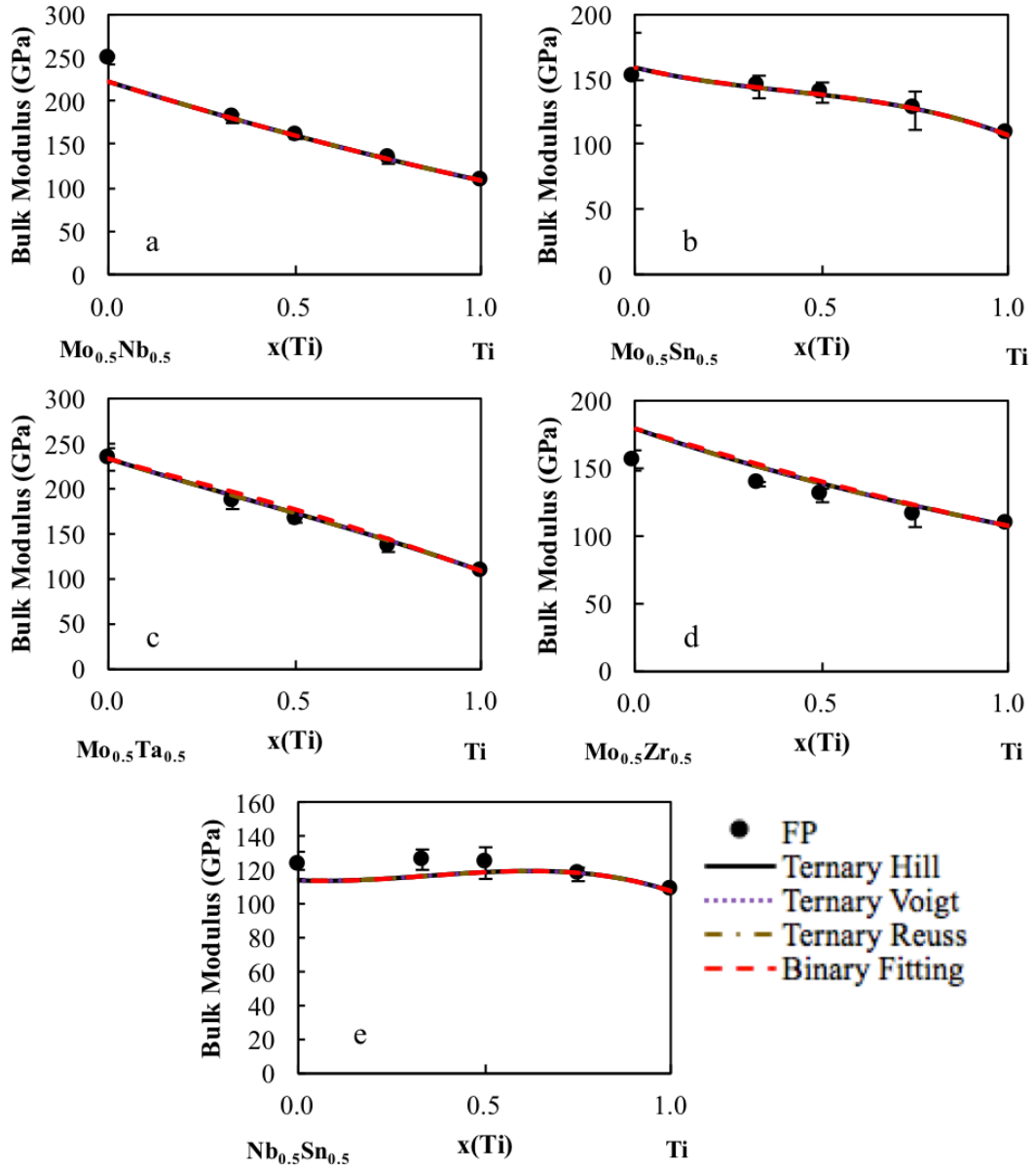


Figure 6.10. Bulk modulus B calculations of five of the Ti-X-Y ternary systems ($X \neq Y = \text{Mo, Nb, Ta, Sn, Zr}$). The present calculations are plotted as the filled circles with error bars as well as the interpolation from the binary interaction parameters (red dashed line). The dotted purple line is the Voigt upper bulk modulus bound, the gold dashed line is the lower Reuss bulk modulus bound and the black line is the Hill bulk modulus average plotted from a 50-50 mixture of the alloying elements X and Y to Ti.

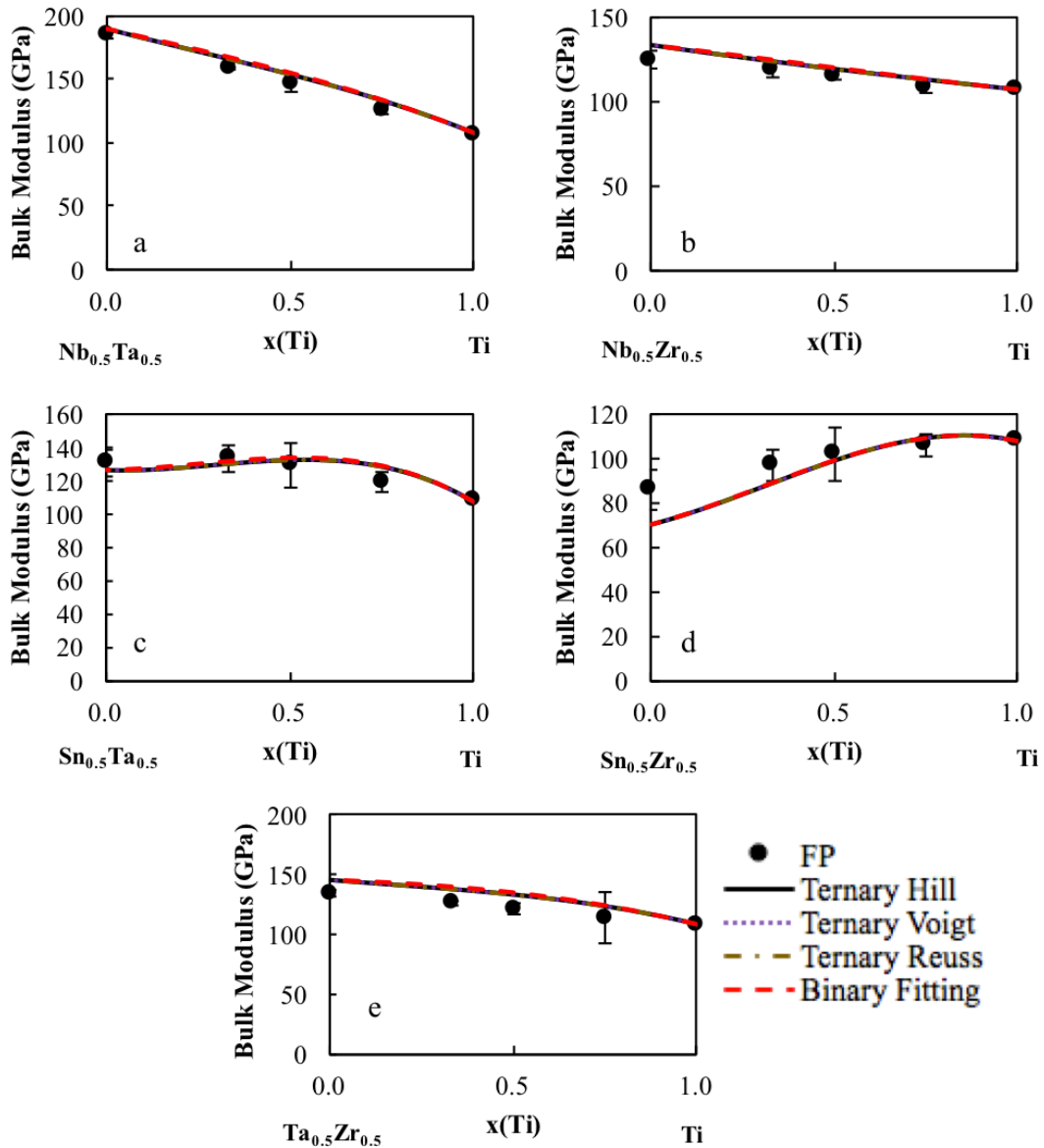


Figure 6.11. Bulk modulus B calculations of five of the Ti-X-Y ternary systems ($X \neq Y = \text{Mo, Nb, Ta, Sn, Zr}$). The present calculations are plotted as the filled circles with error bars as well as the interpolation from the binary interaction parameters (red dashed line). The dotted purple line is the Voigt upper bulk modulus bound, the gold dashed line is the lower Reuss bulk modulus bound and the black line is the Hill bulk modulus average plotted from a 50-50 mixture of the alloying elements X and Y to Ti.

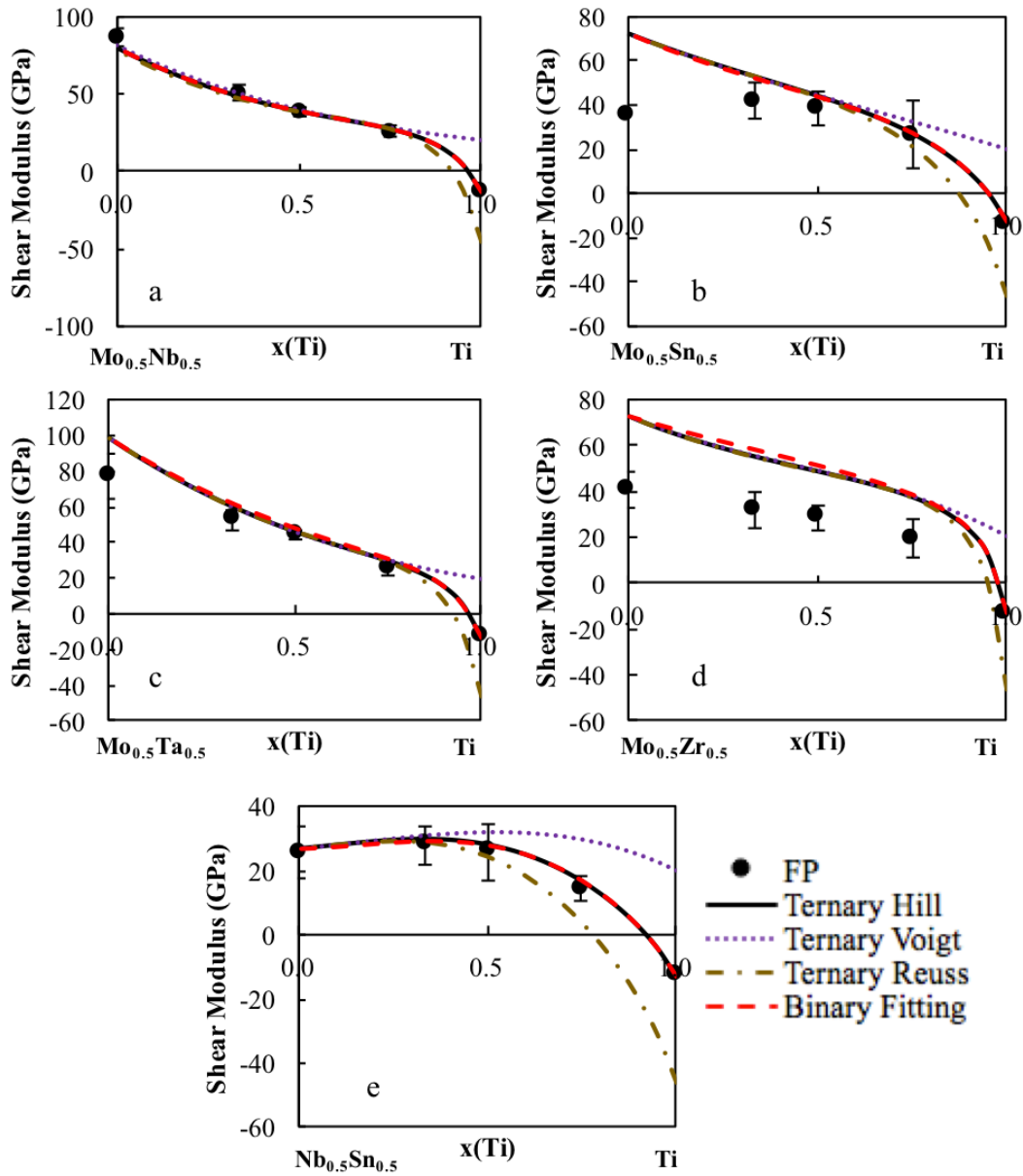


Figure 6.12. Shear modulus G calculations of five of the Ti-X-Y ternary systems ($X \neq Y = \text{Mo, Nb, Ta, Sn, Zr}$). The present calculations are plotted as the filled circles with error bars as well as the interpolation from the binary interaction parameters (red dashed line). The dotted purple line is the Voigt upper shear modulus bound, the gold dashed line is the lower Reuss shear modulus bound and the black line is the Hill shear modulus average plotted from a 50-50 mixture of the alloying elements X and Y to Ti.

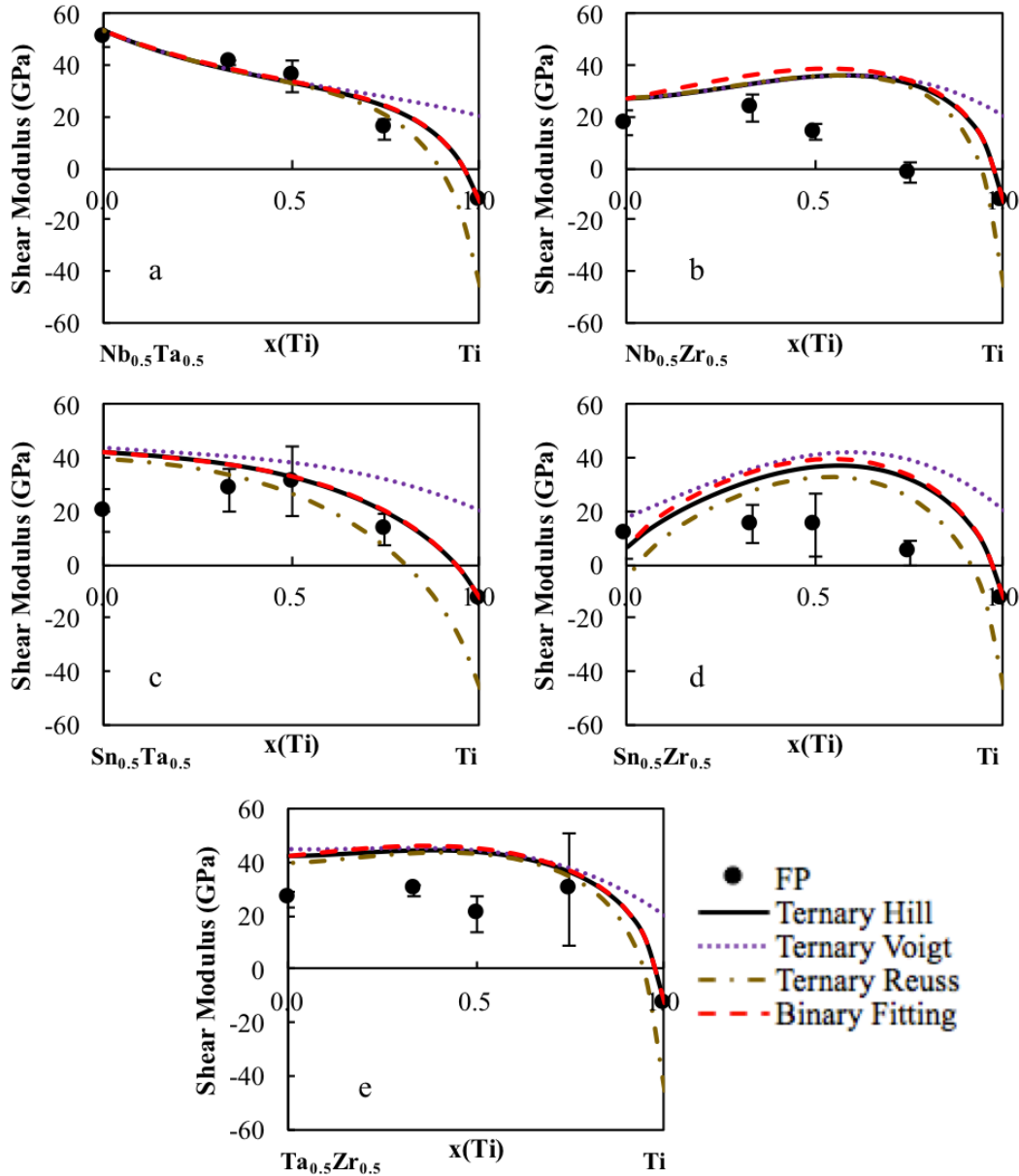


Figure 6.13. Shear modulus G calculations of five of the Ti-X-Y ternary systems ($X \neq Y = \text{Mo, Nb, Ta, Sn, Zr}$). The present calculations are plotted as the filled circles with error bars as well as the interpolation from the binary interaction parameters (red dashed line). The dotted purple line is the Voigt upper shear modulus bound, the gold dashed line is the lower Reuss shear modulus bound and the black line is the Hill shear modulus average plotted from a 50-50 mixture of the alloying elements X and Y to Ti.

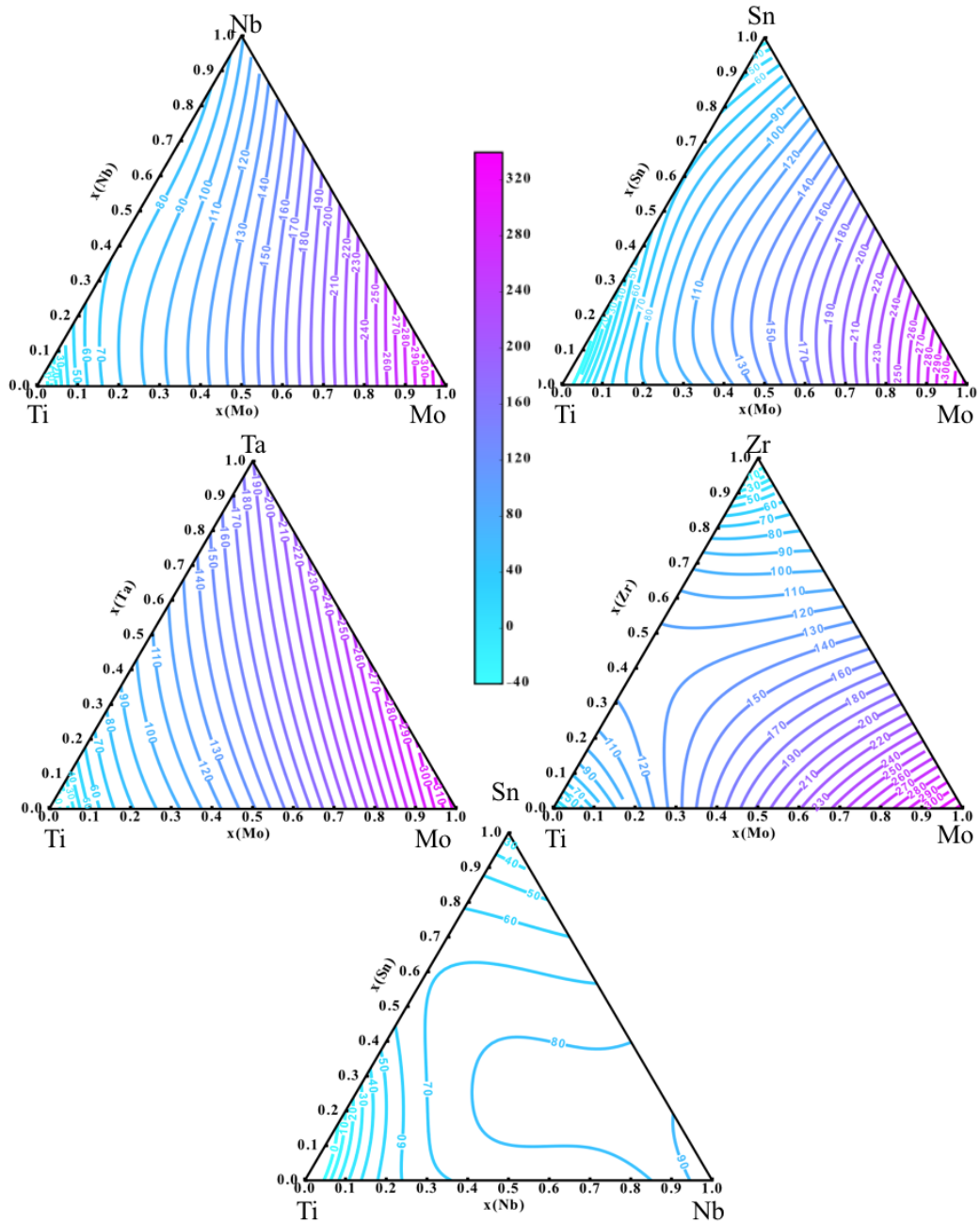


Figure 6.14. The Young's modulus is mapped as a function of composition in GPa for the Ti-Mo-Nb, Ti-Mo-Sn, Ti-Mo-Ta, Ti-Mo-Zr and Ti-Nb-Sn alloy systems using pycalphad [40].

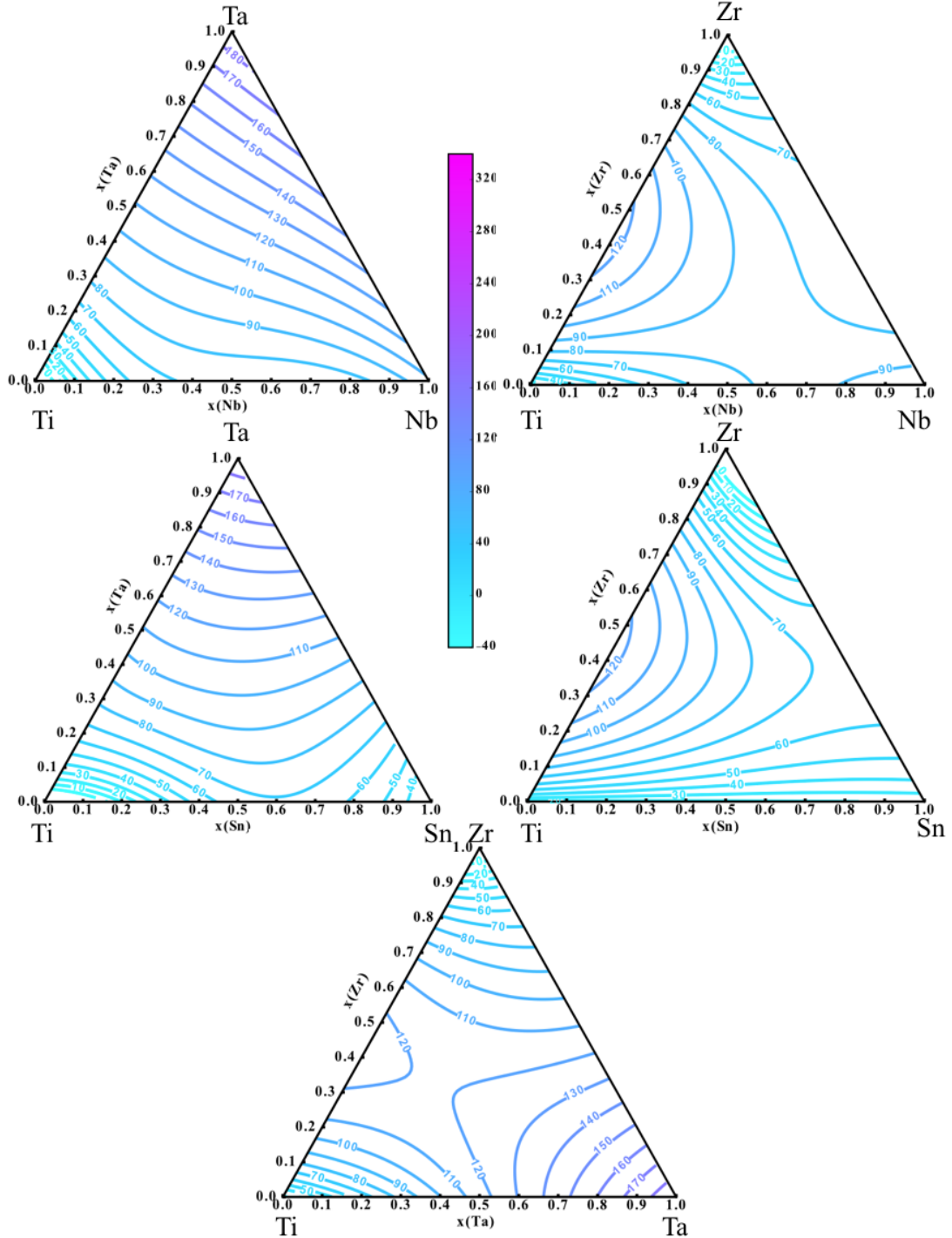


Figure 6.15. The Young's modulus is mapped as a function of composition in GPa for the Ti-Mo-Nb, Ti-Mo-Sn, Ti-Mo-Ta, Ti-Mo-Zr and Ti-Nb-Sn alloy systems using pycalphad [40].

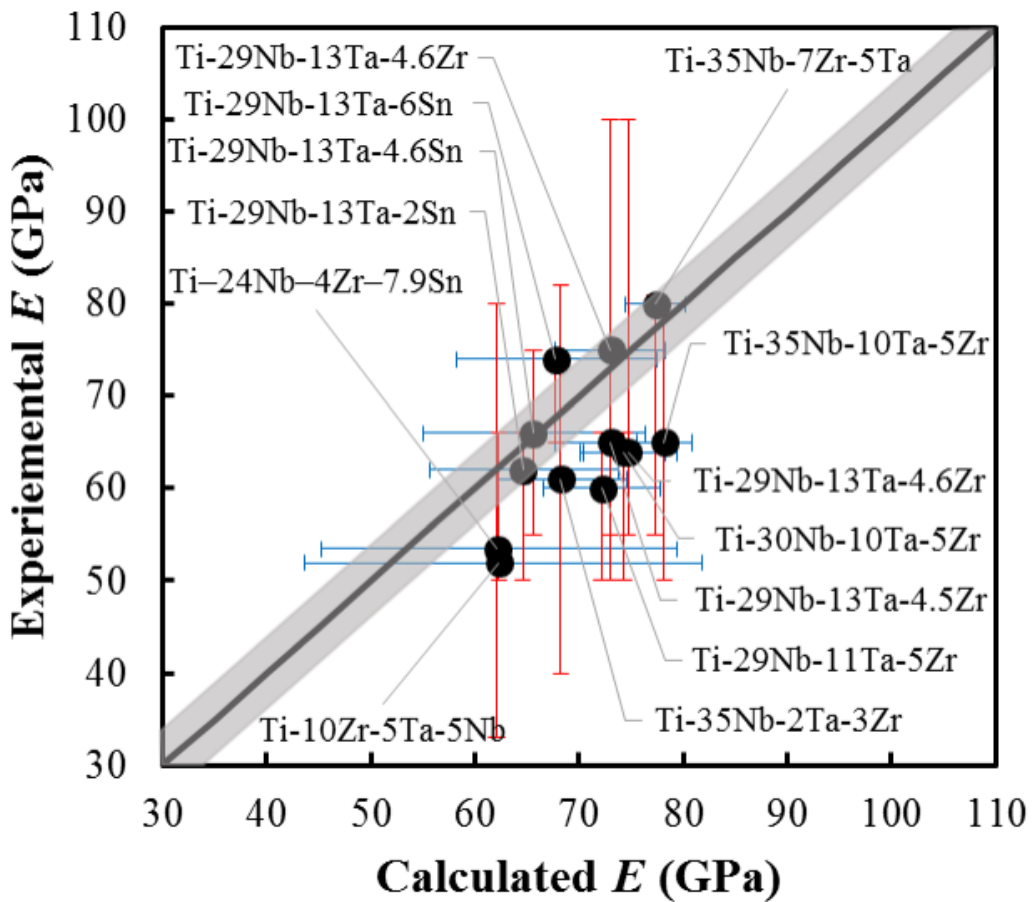


Figure 6.16. E of multicomponent bcc Ti alloys predicted from the completed database are compared with measured experimental results. Error bars plotted are from the variation in experimentally determined YoungâŽs modulus values for the specific multicomponent alloy. The grey region refers to the error in the first-principles calculations. More information on the alloys is Table 6.3 [35–37].

Chapter 7 |

Phase stability and elastic properties study of the Ti-Ta and Ti-Nb systems

7.1 Introduction

PUT IN AN INTRODUCTION ON THE PREVIOUS STUDIES OF THE PARTITION FUNCTION APPROACH

The present chapter is aimed at studying the formation of the metastable phases ω and α'' . The phase stability of bcc, hcp, *omega*, *alpha''* was calculated for the Ti-Ta and Ti-Nb alloys. Multiple structures were calculated across the entire Ti-Ta and Ti-Nb systems at 0 °K. The elastic properties of the four phases were then calculated systematically. CALPHAD modeling was completed to be able to predict the elastic properties as a function of composition. The partition function approach was then used to calculate the phase fraction formed. The predicted phase fractions were used to calculate the mixed force constants and phonon density of states as well as the elastic properties using the rule of mixtures. Inelastic neutron scattering experiments were completed to compare to the predicted phase fractions and phonon density of states. The elastic predictions were compared to experimental data in the literature.

7.2 Modeling and Calculations

7.2.1 Computational details

In the present work the Vienna ab-initio Simulation Package (VASP) [57] was employed to calculate the ground state energy and elastic properties of the pure elements and Ti-Nb and Ti-Ta systems in the bcc, hcp, ω , and α'' phases. The ion-electron interactions were described using the projector augmented wave (PAW) [58, 79] method and based on the previous work of comparing X-C functionals (Figure 2.1) the exchange-correlation functional of the generalized gradient approach depicted by Perdew, Burke, and Ernzerhof (PBE-GGA) was employed [54]. The energy convergence criterion was 10^{-6} eV/atom. The Brillouin zone sampling was done using the γ -centered Monkhorst-Pack scheme [80]. The ground state energy of 330 structures in the bcc phase, across the entire composition range, were calculated using 8x8x8 k-point meshes. The ground state energy of 21 structures in the hcp phase, across the entire composition range, were calculated using 10x10x13 k-point meshes. The ground state energy of 73 structures in the ω phase, across the entire composition range, were calculated using 13x13x7 k-point meshes. The ground state energy of 33 structures in the α'' phase, across the entire composition range, were calculated using 12x11x10 k-point meshes. The elastic properties were then calculated using a ± 0.01 magnitude of strain.

7.2.2 Modeling details

The elastic stiffness constants were modeled using the first-principles based DFT results. The modeling was completed by calculating the difference between the first-principles calculations and a linear extrapolation between pure elements. The differences were then used to fit to the interaction parameters. Due to the limitations within the PARROT module, a mathematica script was used to fit the interaction parameters. The mathematica script is appended in appendix C. The same modeling procedure used for the bcc phase, in Chapter 5 and 6, was used in the present work. The first-principles results with 70 at. % Ti or higher were weighted heavier (x6, according to the authors' practices) than the other points for the fittings. The best fit was found by comparing the fittings obtained with one interaction parameter or with two interaction parameters. The moduli values were then calculated using

pycalphad and the code in appendix D and E [40].

7.3 Results and discussion

7.3.1 First-principles calculations at 0 K

The phase stability is calculated as a function of composition for the Ti-Nb and Ti-Ta systems. Figure 7.1 shows the relative energy of the bcc, hcp, ω , and α'' phases from 100 at. % Ti to 100 at. % Nb. To calculate the relative energy, the ground state energies of the pure elements in the SER state are multiplied by the composition of the specific structure and then subtracted from the ground state energy of the structure being studied. Figure 7.2 is the relative energy of the bcc, hcp, ω , and α'' phases from 100 at. % Ti to 100 at. % Ta. Figure 7.1 and 7.2 are both at 0 °K. The figures show that the bcc and hcp phases are the lowest phases in energy. This shows that the ω and α'' phases are stabilized by entropy.

The Ti-Nb system is chosen to study more in depth due to the experimental work available in the literature which mapped the martensitic transformation temperature for Ti-Nb alloys between the 20 and 30 at. % Nb.

7.3.2 Elastic properties

For the Ti-Nb system, the elastic properties are calculated as a function of composition and are plotted in Figure 7.3. The calculations are shown as symbols and the results are listed in Table 7.3. The dotted lines are the fittings that use the interaction parameters in Table 7.2. The calculations show that the hcp elastic properties go from being positive at 100 at. % Ti to negative at 100 at. % Nb and vice versa for the bcc phase. A negative Young's modulus can indicate that the phase is not stable at that composition. From Figure 7.3, it can be seen that the Young's moduli of the ω and α'' phases are higher than the Young's moduli of the bcc phase for all the compositions. The Young's moduli of the ω and α'' phases are higher than the Young's moduli of the hcp phase at almost all compositions. This would explain why in Figure ?? the experimental Young's moduli increase in value with the formation of the metastable.

7.3.3 Neutron scattering results

7.3.3.1 Phonon density of states at 300 K

The phonon density of states was obtained at 300 °K for each set of samples at each Nb composition. The phonon density of states are plotted in Figure 7.4, 7.5, 7.6, 7.7. The samples at the same composition are plotted together for comparison. The phonon density of states of the slow cooled samples, that should contain the bcc and ω phases, are plotted with dashed lines and the phonon density of states of the quenched samples, that should contain the bcc and α'' phases, are plotted with solid lines. The fact that the different samples show different phonon DOS means that the quenching versus slow cooling worked and the samples should have different phases. The phonon DOS can be used to calculate the entropy by:

$$\left[\sum_{i=1}^N \left(-\frac{\hbar^2}{2m} \nabla_i^2 + V_{ext}(r_i) \right) + \sum_{i < j} U(r_i, r_j) \right] \Psi = E_s \Psi \quad (7.1)$$

comparison of the shows that the phonon DOS are different at the same compositions which is what Figure 7.4 shows that the different

7.3.3.2 Diffraction patterns at 300 K

7.3.3.3 Temperature dependent phonon density of states

7.3.3.4 Temperature dependent diffraction patterns

7.3.4 Partition function approach results

7.3.4.1 Phase fractions

7.3.4.2 Mixed force constants

7.3.5 Comparison of elastic properties

7.4 Conclusion

Table 7.1: First-principles calculations of the elastic stiffness constants in GPa for different atomic percent compositions in the α'' , bcc, hcp, and ω phases in the Ti-Nb system at 0 °K.

$Ti_{1-b}Nb_b$	c_{11}	c_{12}	c_{13}	c_{22}	c_{23}	c_{33}	c_{44}	c_{55}	c_{66}
α''									
Ti	198	69	84	197	84	189	40	40	63
TiNb ₂	A	B	C	D	E	F	G	H	I
TiNb ₃	106	112	123	152	45	138	25	17	38
TiNb ₁₃	A	B	C	D	E	F	G	H	I
TiNb ₉₄	307	94	119	248	143	214	31	-24	13
TiNb ₉₇	293	88	115	232	124	284	59	-58	8
TiNb ₉₈	A	B	C	D	E	F	G	H	I
Nb	306	88	125	240	135	284	47	-69	9
bcc									
Ti	93	115	-	-	-	-	41	-	-
TiNb ₂	93	115	-	-	-	-	35	-	-
TiNb ₁₃	116	116	-	-	-	-	37	-	-
TiNb ₂₅	140	116	-	-	-	-	34	-	-
TiNb ₅₀	181	121	-	-	-	-	31	-	-
TiNb ₇₅	208	130	-	-	-	-	15	-	-
TiNb ₉₄	242	134	-	-	-	-	18	-	-
TiNb ₉₈	242	134	-	-	-	-	18	-	-
Nb	245	144	-	-	-	-	27	-	-
hcp									
Ti	175	88	80	-	-	190	41	-	-
TiNb ₂	A	B	C	-	-	D	E	-	-
TiNb ₁₃	A	B	C	-	-	D	E	-	-
TiNb ₂₅	A	B	C	-	-	D	E	-	-
TiNb ₅₀	A	B	C	-	-	D	E	-	-
TiNb ₇₅	A	B	C	-	-	D	E	-	-
TiNb ₉₄	A	B	C	-	-	D	E	-	-
TiNb ₉₈	A	B	C	-	-	D	E	-	-

Table 7.1: First-principles calculations of the elastic stiffness constants in GPa for different atomic percent compositions in the α'' , bcc, hcp, and ω phases in the Ti-Nb system at 0 °K.

$Ti_{1-b}Nb_b$	c_{11}	c_{12}	c_{13}	c_{22}	c_{23}	c_{33}	c_{44}	c_{55}	c_{66}
Nb	24	18	11	-	-	25	-6	-	-
ω									
Ti	194	87	61	-	-	246	54	-	-
TiNb ₂	187	B	C	-	-	D	E	-	-
TiNb ₁₃	A	B	C	-	-	D	E	-	-
TiNb ₉₄	A	B	C	-	-	D	E	-	-
TiNb ₉₈	A	B	C	-	-	D	E	-	-
Nb	243	181	110	-	-	212	-55	-	-

Table 7.2. Evaluated interaction parameters L_0 and L_1 , using Eq. 2.35, for the elastic stiffness constants of the bcc, hcp, α'' and ω phases in the Ti-Nb systems.

Alloy	Interaction Parameter	α''	bcc	hcp	ω
c_{11}	L_0	A	B	C	D
	L_1	A	B	C	D
c_{12}	L_0	A	B	C	D
	L_1	A	B	C	D
c_{13}	L_0	A	N/A	C	D
	L_1	A	N/A	C	D
c_{22}	L_0	A	N/A	N/A	N/A
	L_1	A	N/A	N/A	N/A
c_{23}	L_0	A	N/A	N/A	N/A
	L_1	A	N/A	N/A	N/A
c_{33}	L_0	A	N/A	C	D
	L_1	A	N/A	C	D
c_{44}	L_0	A	B	C	D
	L_1	A	B	C	D
c_{55}	L_0	A	N/A	N/A	N/A
	L_1	A	N/A	N/A	N/A
c_{66}	L_0	A	N/A	N/A	N/A
	L_1	A	N/A	N/A	N/A

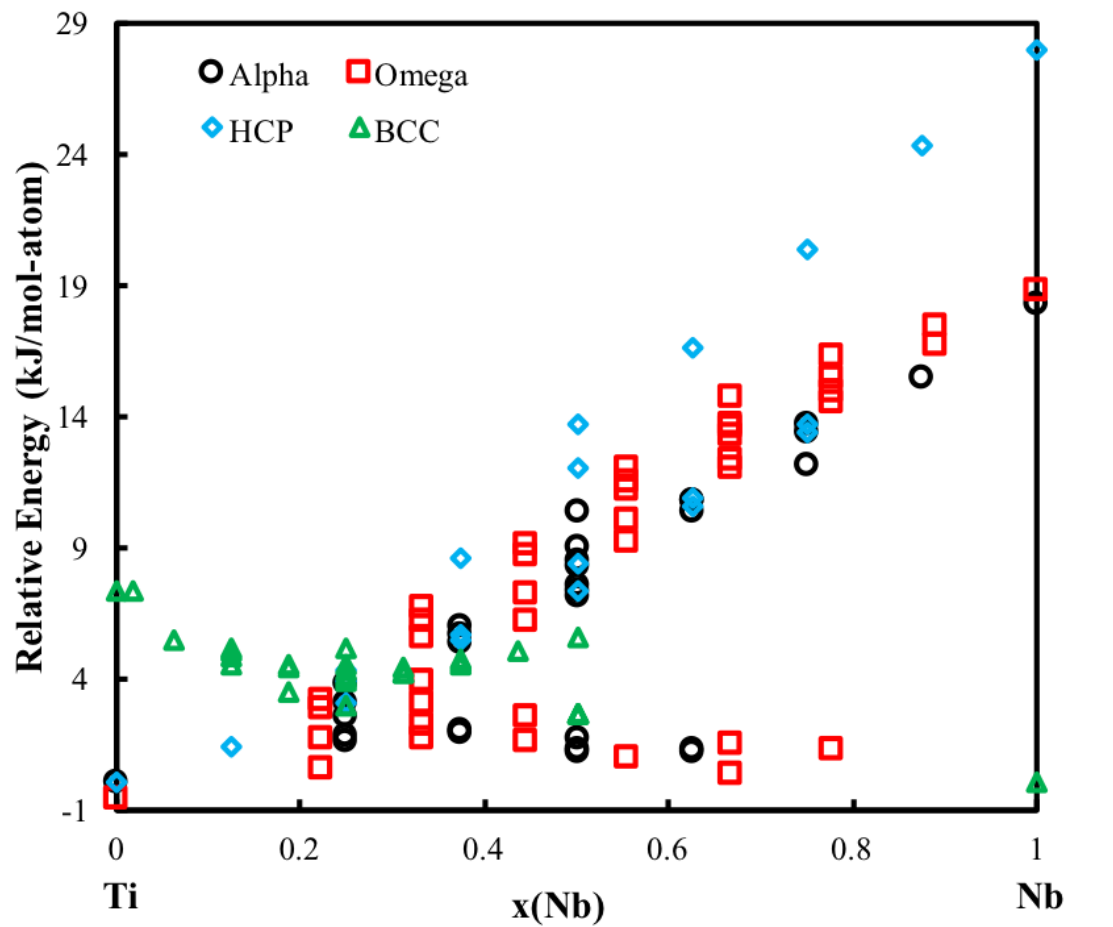


Figure 7.1. The relative energy of the bcc, hcp, ω , α'' phases in the Ti-Nb system are plotted from 100 at. % Ti to 100 at. % Nb.

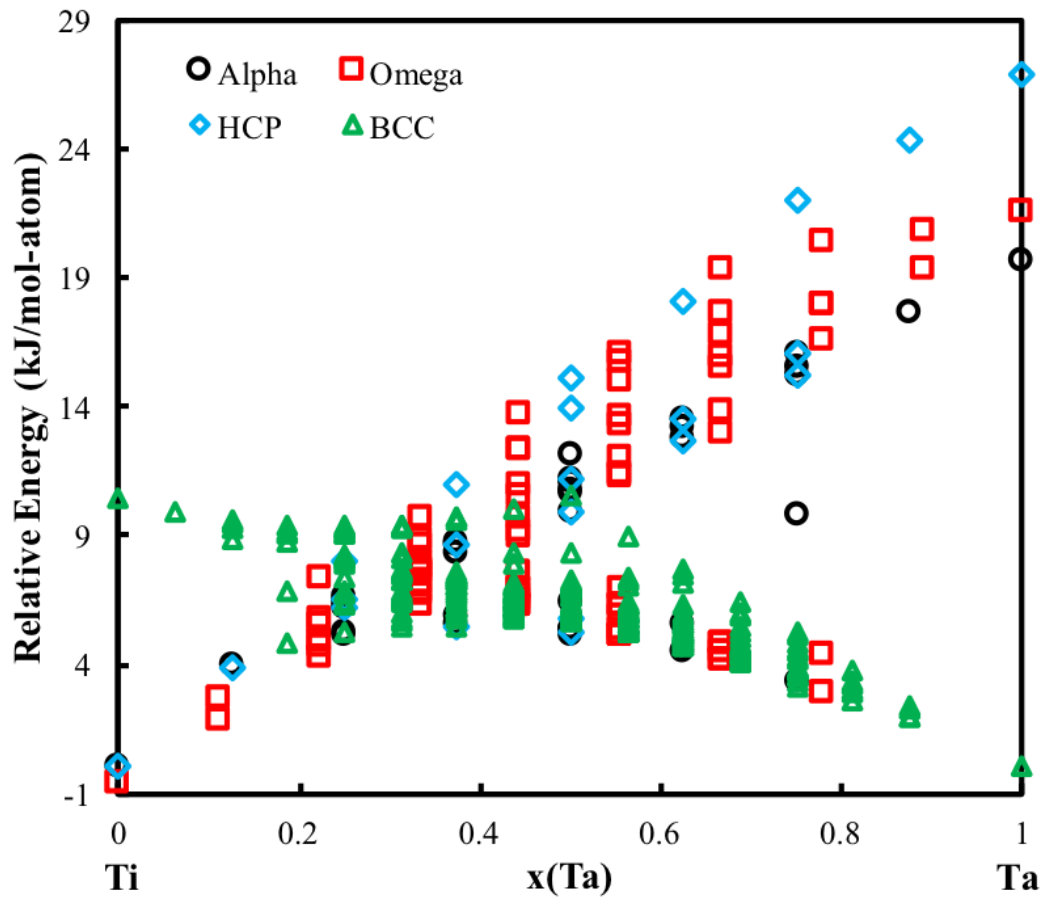


Figure 7.2. The relative energy of the bcc, hcp, ω , α'' phases in the Ti-Ta system are plotted from 100 at. % Ti to 100 at. % Ta.

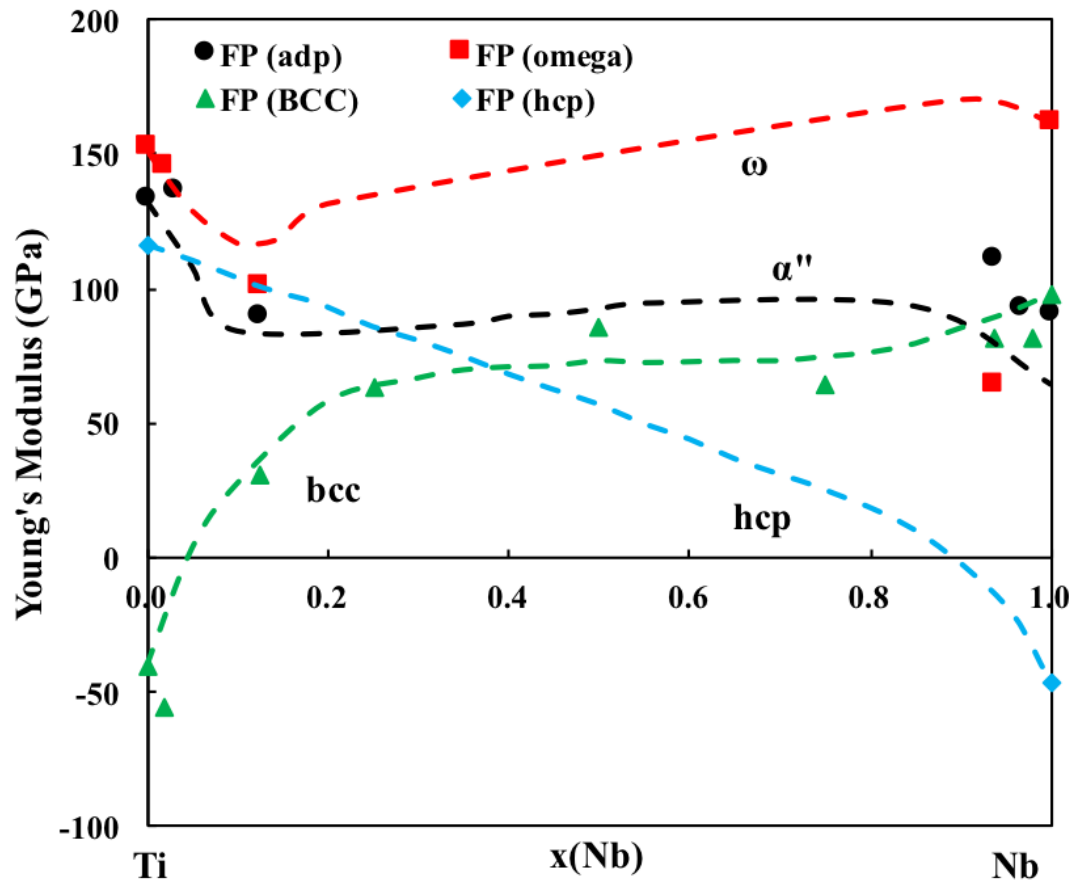


Figure 7.3. The elastic properties of the bcc, hcp, ω , α'' phases in the Ti-Nb system calculated from first-principles based on DFT are plotted as symbols. The CALPHAD fitting are plotted as the dashed lines. The figure is plotted from 100 at. % Ti to 100 at. % Nb.

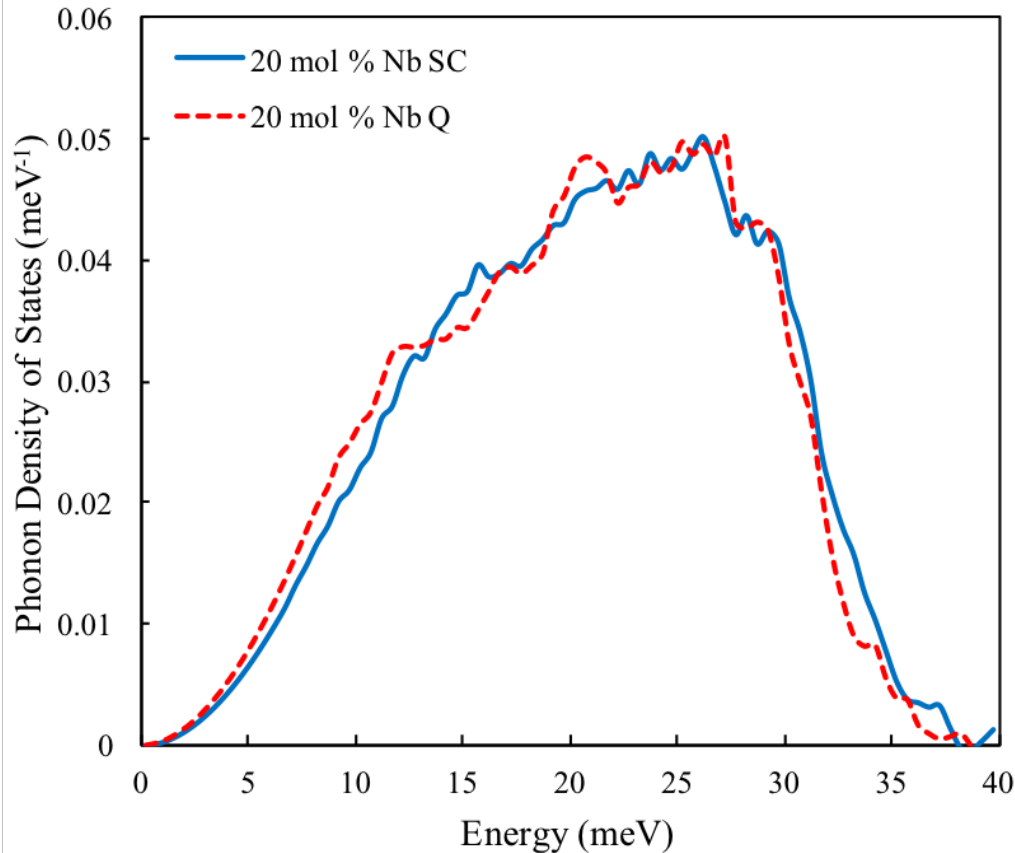


Figure 7.4. The phonon density of states is plotted for the TiNb alloy at 20 at. % Nb. The dashed line represents the slow cooled sample while the solid line represents the quenched sample.

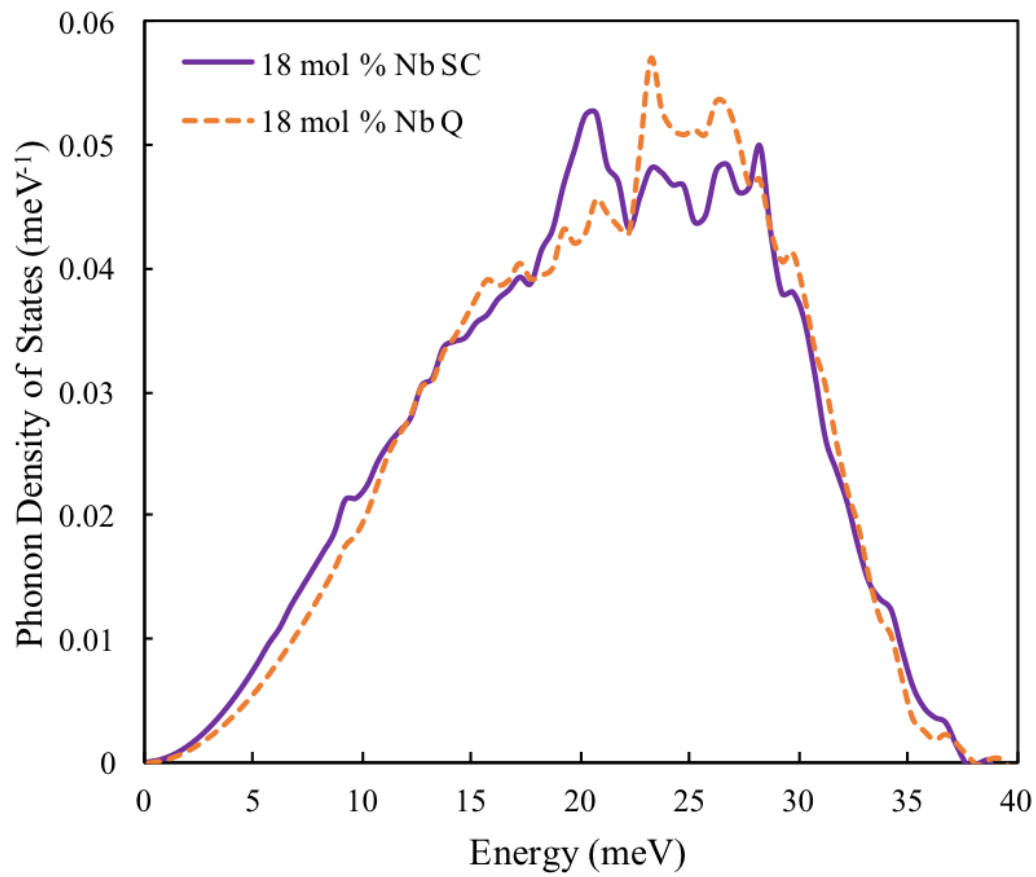


Figure 7.5. The phonon density of states is plotted for the TiNb alloy at 18 at. % Nb. The dashed line represents the slow cooled sample while the solid line represents the quenched sample.

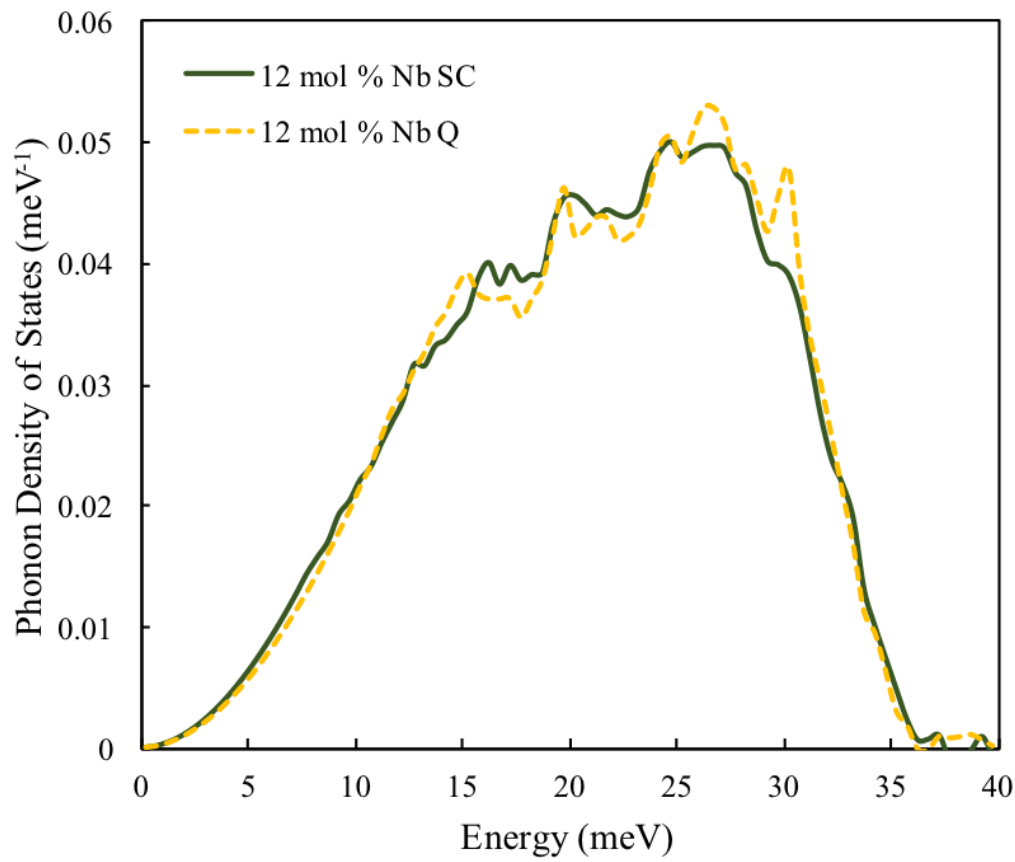


Figure 7.6. The phonon density of states is plotted for the TiNb alloy at 12 at. % Nb. The dashed line represents the slow cooled sample while the solid line represents the quenched sample.

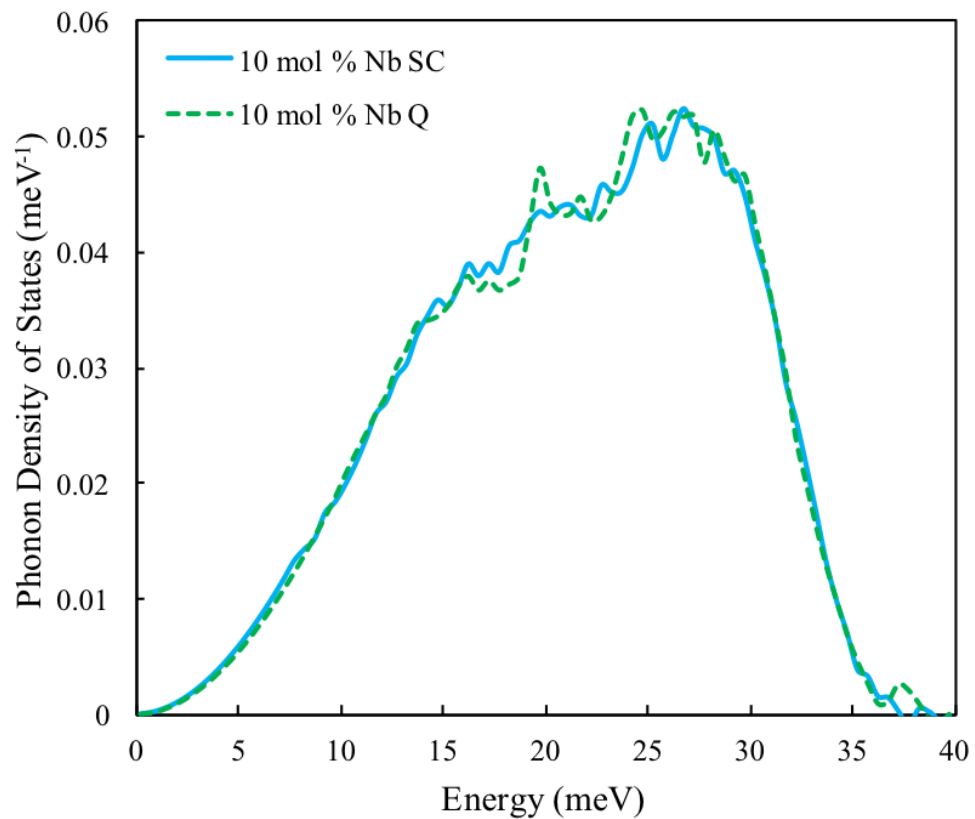


Figure 7.7. The phonon density of states is plotted for the TiNb alloy at 10 at. % Nb. The dashed line represents the slow cooled sample while the solid line represents the quenched sample.

Chapter 8 |

Conclusions and Future Work

8.1 Conclusions

ADD

8.2 Future Work

ADD

Appendix A | Ti-Mo-Nb-Ta-Zr Database

```
$*****  
$ The definition of the pure elements, vacancy and species  
$  
TEMPERATURE_LIMIT 0 6000.00 !  
ELEMENT /- ELECTRON_GAS 0.0000E+00 0.0000E+00 0.0000E+00!  
ELEMENT MO BCC_A2 95.94 4589.0 28.56 !  
ELEMENT NB BCC_A2 92.9064 5220.0 36.27 !  
ELEMENT TA BCC_A2 180.9479 5681.872 41.4718 !  
ELEMENT TI HCP_A3 4.7880E+01 4.8100E+03 3.0648E+01!  
ELEMENT ZR HCP_A3 9.1224E+01 5.5663E+03 3.9181E+01!  
ELEMENT VA VACUUM 0.0 0.0 0.0 !
```

```
$*****
```

```
$ The Gibbs energies of the elements  
$ in the stable and metastable forms from SGTE  
$  
$
```

```
* TI *
```

```
$  
$
```

```
FUNCTION GBCCTI
```

```
2.98150E+02 -1272.064+134.71418*T-25.5768*T*LN(T)
```

$-6.63845 \times 10^{-4} T^2 - 2.78803 \times 10^{-7} T^3 + 7208 T^*(-1); 1.15500 \times 10^3 Y$
 $+6667.385 + 105.366379 T - 22.3771 T \ln(T) + .00121707 T^2 - 8.4534 \times 10^{-7} T^3$
 $-2002750 T^*(-1); 1.94100 \times 10^3 Y$
 $+26483.26 - 182.426471 T + 19.0900905 T \ln(T) - .02200832 T^2$
 $+1.228863 \times 10^{-6} T^3 + 1400501 T^*(-1); 4.00000 \times 10^3 N$ REF:20 !

FUNCTION GHSERTI

$2.98150 \times 10^2 - 8059.921 + 133.615208 T - 23.9933 T \ln(T)$
 $-.004777975 T^2 + 1.06716 \times 10^{-7} T^3 + 72636 T^*(-1); 9.00000 \times 10^2 Y$
 $-7811.815 + 132.988068 T - 23.9887 T \ln(T) - .0042033 T^2 - 9.0876 \times 10^{-8} T^3$
 $+42680 T^*(-1); 1.15500 \times 10^3 Y$
 $+908.837 + 66.976538 T - 14.9466 T \ln(T) - .0081465 T^2 + 2.02715 \times 10^{-7} T^3$
 $-1477660 T^*(-1); 1.94100 \times 10^3 Y$
 $-124526.786 + 638.806871 T - 87.2182461 T \ln(T) + .008204849 T^2$
 $-3.04747 \times 10^{-7} T^3 + 36699805 T^*(-1); 4.00000 \times 10^3 N$ REF:20 !

FUNCTION GFCCTI

$2.98150 \times 10^2 + 6000.1 T + GHSERTI; 6.00000 \times 10^3 N$ REF:20 !

FUNCTION GLIQTI

$2.98150 \times 10^2 + 12194.415 - 6.980938 T + GHSERTI; 1.30000 \times 10^3 Y$
 $+368610.36 - 2620.99904 T + 357.005867 T \ln(T) - .155262855 T^2$
 $+1.2254402 \times 10^{-5} T^3 - 65556856 T^*(-1) + GHSERTI; 1.94100 \times 10^3 Y$
 $+104639.72 - 340.070171 T + 40.9282461 T \ln(T) - .008204849 T^2$
 $+3.04747 \times 10^{-7} T^3 - 36699805 T^*(-1) + GHSERTI; 6.00000 \times 10^3 N$ REF:20 !

\$

\$

* MO *

\$

\$

FUNCTION GHSERMO

$298.15 - 7746.302 + 131.9197 T - 23.56414 T \ln(T)$
 $-.003443396 T^2 + 5.662834 \times 10^{-7} T^3 + 65812.39 T^*(-1)$
 $-1.309265 \times 10^{-10} T^4; 2896.00 Y$
 $-30556.41 + 283.559746 T - 42.63829 T \ln(T)$
 $-4.849315 \times 10^{-9} T^*(-9); 4000.00 N$ REF:20 !

FUNCTION GLIQMO
298.15 41831.347-14.694912*T+4.24519E-22*T**7
+GHSERMO; 2896.00 Y
34095.373-11.890046*T+4.849315E33*T**(-9)+GHSERMO;
4000.00 N REF:20 !

FUNCTION GFCCMO
298.15 15200+0.63*T+GHSERMO; 4000.00 N REF:20 !

FUNCTION GHCPMO
298.15 11550+GHSERMO; 4000.00 N REF:20 !

\$_____

\$_____

* NB *

\$_____

\$_____

FUNCTION GHSERNB
2.98140E+02 -8519.353+142.045475*T
-26.4711*T*LN(T)+2.03475E-04*T**2-3.5012E-07*T**3
+93399*T**(-1); 2.75000E+03 Y
-37669.3+271.720843*T-41.77*T*LN(T)+1.528238E+32*T**(-9);
6.00000E+03 N REF:20 !

FUNCTION GHEXTNB
2.98150E+02 -8519.35+142.048*T
-26.4711*T*LN(T)+2.03475E-04*T**2-3.50119E-07*T**3
+93398.8*T**(-1); 6.00000E+03 N REF:23 !

FUNCTION GLIQNB
298.15 29781.555-10.816417*T
-3.06098E-23*T**7+GHSERNB; 2750.00 Y
+30169.901-10.964695*T-1.52824E32*T**(-9)+GHSERNB;
6000.00 N REF:20 !

FUNCTION GFCCNB
298.15 +13500+1.7*T+GHSERNB; 6000.00 N REF:20 !

FUNCTION GHCPNB
298.15 +10000+2.4*T+GHSERNB; 6000.00 N REF:20 !

\$
\$
* TA *
\$
\$

FUNCTION GHSERTA
2.98150E+02 -7285.889+119.139858*T
-23.7592624*T*LN(T)-.002623033*T**2+1.70109E-07*T**3
-3293*T**(-1); 1.30000E+03 Y
-22389.955+243.88676*T-41.137088*T*LN(T)+.006167572*T**2
-6.55136E-07*T**3+2429586*T**(-1); 2.50000E+03 Y
+229382.886-722.59722*T+78.5244752*T*LN(T)-.017983376*T**2
+1.95033E-07*T**3-93813648*T**(-1); 3.25800E+03 Y
-963392.734+2773.7774*T-337.227976*T*LN(T)+.039791303*T**2
-9.74251E-07*T**3+5.09949511E+08*T**(-1); 6.00000E+03 N REF:20 !
FUNCTION GFCCTA
2.98150E+02 +16000+1.7*T+GHSERTA; 6.00000E+03 N REF:20 !
FUNCTION GHCPTA
2.98150E+02 +12000+2.4*T+GHSERTA; 6.00000E+03 N REF:20 !
FUNCTION GLIQTA
2.98150E+02 +29160.975-7.578729*T+GHSERTA; 1.00000E+03 Y
+51170.228-181.121652*T+23.7872147*T*LN(T)-.009707033*T**2
+4.4449E-07*T**3-3520045*T**(-1)+GHSERTA; 1.30000E+03 Y
+66274.294-305.868555*T+41.1650403*T*LN(T)-.018497638*T**2
+1.269735E-06*T**3-5952924*T**(-1)+GHSERTA; 2.50000E+03 Y
-185498.547+660.615425*T-78.4965229*T*LN(T)+.00565331*T**2
+4.19566E-07*T**3+90290310*T**(-1)+GHSERTA; 3.29000E+03 Y
+1036069.47-2727.38037*T+320.319132*T*LN(T)-.043117795*T**2
+1.055148E-06*T**3-5.54714342E+08*T**(-1)+GHSERTA;
6.00000E+03 N REF:20 !
FUNCTION TATIB2
2.98150E+02 2500; 6.00000E+03 N REF:25 !
\$

\$
* ZR *
\$
\$
FUNCTION GLIQZR
2.98140E+02 +18147.69-9.080812*T
+1.6275E-22*T**7+GHSERZR; 2.12800E+03 Y
+17804.661-8.911574*T+1.342895E+31*T**(-9)+GHSERZR;
6.00000E+03 N REF:20 !
FUNCTION GBCCZR
2.98140E+02 -525.539+124.9457*T
-25.607406*T*LN(T)-3.40084E-04*T**2-9.729E-09*T**3
+25233*T**(-1)-7.6143E-11*T**4; 2.12800E+03 Y
-30705.955+264.284163*T-42.144*T*LN(T)+1.276058E+32*T**(-9);
6.00000E+03 N REF:20 !
FUNCTION GHSERZR
1.30000E+02 -7827.595+125.64905*T
-24.1618*T*LN(T)-.00437791*T**2+34971*T**(-1); 2.12800E+03 Y
-26085.921+262.724183*T-42.144*T*LN(T)-1.342895E+31*T**(-9);
6.00000E+03 N REF:20 !
\$
FUNCTION UN_ASS 298.15 0; 300 N !
\$

TYPE_DEFINITION % SEQ * !
TYPE_DEFINITION G SEQ * !
DEFINE_SYSTEM_DEFAULT SPECIE 5 !
DEFAULT_COMMAND DEF_SYS_ELEMENT VA !
\$

\$

PHASE LIQUID % 1 1.0 !

CONSTITUENT LIQUID :MO,TA,NB,TI,ZR: !

PARAMETER G(LIQUID, TI;0)
298.15 GLIQTI; 6000.00 N REF:20 !
PARAMETER G(LIQUID, MO;0)
298.15 GLIQMO; 6000.00 N REF:20 !
PARAMETER G(LIQUID, NB;0)
298.15 GLIQNB; 6000.00 N REF:20
PARAMETER G(LIQUID, TA;0)
298.15 GLIQT A; 6000.00 N REF:20 !
PARAMETER G(LIQUID, ZR;0)
298.15 +GLIQZR; 6000.00 N REF:20 !
PARAMETER G(LIQUID, MO, TI;0)
298.15 -9000.0+2*T; 6000.00 N REF:25 !
PARAMETER G(LIQUID, NB, TI;0)
298.15 +7406.1; 6000.00 N REF:23 !
PARAMETER G(LIQUID, TA, TI;0)
298.15 +1000; 6000.00 N REF:25 !
PARAMETER G(LIQUID, TA, TI;1)
298.15 -7000; 6000.00 N REF:25 !
PARAMETER G(LIQUID, TI, ZR;0)
298.15 -967.66; 6000.00 N REF:22 !
PARAMETER G(LIQUID, MO, NB;0) *
298.15 15253.7; 6000.00 N REF:21 !
PARAMETER G(LIQUID, MO, NB;1)
298.15 10594.2; 6000.00 N REF:21 !
PARAMETER G(LIQUID, MO, TA;0)
298.15 13978.9; 6000.00 N REF:21 !
PARAMETER G(LIQUID, MO, TA;1)
298.15 577.5; 6000.00 N REF:21 !
PARAMETER G(LIQUID, MO, ZR;0)
298.15 -24055.120+8.146158*T; 6000.00 N REF:26 !
PARAMETER G(LIQUID, MO, ZR;1)

298.15 -5132.1665+4.8041224*T; 6000.00 N REF:26 !

PARAMETER G(LIQUID,NB,TA;0)

298.15 0; 6000.00 N REF:21 !

PARAMETER G(LIQUID,NB,ZR;0)

298.15 10311; 6000.00 N REF:28 !

PARAMETER G(LIQUID,NB,ZR;1)

298.15 6709; 6000.00 N REF:28 !

PARAMETER G(LIQUID,TA,ZR;0)

298.15 13832.1; 6000.00 N REF:27 !

PARAMETER G(LIQUID,TA,ZR;1)

298.15 -7150; 6000.00 N REF:27 !

\$

PHASE BCC_A2 % 2 1 3 !

CONSTITUENT BCC_A2 :MO,TA,NB,TI,ZR:VA: !

PARAMETER G(BCC_A2,TI:VA;0)

298.15 +GBCCTI; 6000.0 N REF:20 !

PARAMETER G(BCC_A2,MO:VA;0)

298.15 +GHSERMO; 6000.00 N REF:20 !

PARAMETER G(BCC_A2,NB:VA;0)

298.15 +GHSERNB; 6000.00 N REF:20 !

PARAMETER G(BCC_A2,TA:VA;0)

298.15 +GHSERTA; 6000.00 N REF:20 !

PARAMETER G(BCC_A2,ZR:VA;0)

298.15 +GBCCZR; 6000.00 N REF:20 !

PARAMETER G(BCC_A2,MO,TI:VA;0)

298.15 2000.0; 6000.00 N REF:25 !

PARAMETER G(BCC_A2,MO,TI:VA;1)

298.15 -2000.0; 6000.00 N REF:25 !

PARAMETER G(BCC_A2,NB,TI:VA;0)

298.15 +13045.3; 6000.00 N REF:23 !

PARAMETER G(BCC_A2,TA,TI:VA;0)

298.15 12000; 6000.00 N REF:25 !

PARAMETER G(BCC_A2,TA,TI:VA;1)
298.15 -2500; 6000.00 N REF:25 !

PARAMETER G(BCC_A2,TI,ZR:VA;0)
298.15 -4346.16+5.48903*T; 6000.00 N REF:22 !

PARAMETER G(BCC_A2,MO,NB:VA;0)
298.15 -68202.6+29.85596*T; 6000.00 N REF:21 !

PARAMETER G(BCC_A2,MO,NB:VA;1)
298.15 8201.3; 6000.00 N REF:21 !

PARAMETER G(BCC_A2,MO,TA:VA;0)
298.15 -75129.2+30*T; 6000.00 N REF:21 !

PARAMETER G(BCC_A2,MO,TA:VA;1)
298.15 6039.24; 6000.00 N REF:21 !

PARAMETER G(BCC_A2,MO,ZR:VA;0)
298.15 +17935.985+3.102*T; 6000.00 N REF:26 !

PARAMETER G(BCC_A2,MO,ZR:VA;1)
298.15 -990.9911+4.299*T; 6000.00 N REF:26 !

PARAMETER G(BCC_A2,NB,TA:VA;0)
298.15 1298.02870; 6000.00 N REF:21 !

PARAMETER G(BCC_A2,NB,ZR:VA;0)
298.15 +15911+3.35*T; 6000.00 N REF:28 !

PARAMETER G(BCC_A2,NB,ZR:VA;1)
298.15 +3919-1.091*T; 6000.00 N REF:28 !

PARAMETER G(BCC_A2,ZR,TA:VA;0)
298.15 29499.6+2.6723*T; 6000.00 N REF:27 !

PARAMETER G(BCC_A2,ZR,TA:VA;1)
298.15 -4396.2+4.4302*T; 6000.00 N REF:27 !

PARAMETER G(BCC_A2,ZR,TA:VA;2)
298.15 -6353.3+4.9066*T; 6000.00 N REF:27 !

PARAMETER G(BCC_A2,MO,TA,TI:VA;0) 298.15 0; 6000.00 N !

PARAMETER G(BCC_A2,MO,TA,TI:VA;1) 298.15 0; 6000.00 N !

PARAMETER G(BCC_A2,MO,TA,TI:VA;2)
298.15 -1.5473118E+05; 6000.00 N !

PARAMETER G(BCC_A2,NB,TA,TI:VA;0)

2.98150E+02 -1.3660332E+05; 6.00000E+03 N !
PARAMETER G(BCC_A2,NB,TA,TI:VA;1)
2.98150E+02 -1.3660269E+05; 6.00000E+03 N !
PARAMETER G(BCC_A2,NB,TA,TI:VA;2)
2.98150E+02 0; 6.00000E+03 N !
\$

PHASE HCP_A3 % 2 1 .5 !
CONSTITUENT HCP_A3 :NB,TI%,ZR,TA,MO : VA% : !

PARAMETER G(HCP_A3,TI:VA;0)
298.15 +GHSERTI; 4000.00 N REF:20 !
PARAMETER G(HCP_A3,MO:VA;0)
298.15 +GHCPMO; 5000.00 N REF:20 !
PARAMETER G(HCP_A3,NB:VA;0)
298.15 +GHCPNB; 6000.00 N REF:20 !
PARAMETER G(HCP_A3,TA:VA;0)
298.15 +GHCPTA; 6000.00 N REF:20 !
PARAMETER G(HCP_A3,ZR:VA;0)
298.15 +GHSERZR; 6000.00 N REF:20 !
PARAMETER G(HCP_A3,MO,TI:VA;0)
298.15 22760-6*T; 6000.00 N REF:25 !
PARAMETER G(HCP_A3,NB,TI:VA;0)
298.15 +11742.4; 6000.00 N REF:23 !
PARAMETER G(HCP_A3,TA,TI:VA;0)
298.15 8500; 6000.00 N REF:25 !
PARAMETER G(HCP_A3,TI,ZR:VA;0)
298.15 +5133.02; 6000.00 N REF:22 !
PARAMETER G(HCP_A3,MO,ZR:VA;0)
298.15 +26753.79+4.556*T; 6000.00 N REF:26 !
PARAMETER G(HCP_A3,NB,ZR:VA;0)
298.15 24411; 6000.00 N REF:28 !
PARAMETER G(HCP_A3,ZR,TA:VA;0)
298.15 +30051.7; 6000.00 N REF:27 !

\$
TYPE_DEFINITION * GES A_P_D FCC_A1 MAGNETIC -3.0 2.80000E-01 !
PHASE FCC_A1 %* 2 1 1 !
CONSTITUENT FCC_A1 :MO,TA,ZR,NB : VA% : !

PARAMETER G(FCC_A1,TA:VA;0)
298.15 +GFCCTI; 4000.00 N REF:20 !
PARAMETER G(FCC_A1,MO:VA;0)
298.15 +GFCCMO; 5000.00 N REF:20 !
PARAMETER G(FCC_A1,NB:VA;0)
298.15 +GFCCNB; 6000.00 N REF:20 !
PARAMETER G(FCC_A1,TA:VA;0)
298.15 +GFCCTA; 6000.00 N REF:20 !
PARAMETER G(FCC_A1,MO,TA:VA;0)
298.15 16500.0; 6000.00 N REF:25 !
PARAMETER G(FCC_A1,TA,TI:VA;0)
298.15 8500; 6000.00 N REF:25 !

\$
PHASE AL3M_D022 % 2 3 1 !
CONSTITUENT AL3M_D022 :TI,MO : TA,TI,MO : !

PARAMETER G(AL3M_D022,TA:TI;0)
298.15 +4*GFCCTI; 6000.00 N REF:25 !
PARAMETER G(AL3M_D022,MO:MO;0)
298.15 +4*GFCCMO; 6000.00 N REF:25 !
PARAMETER G(AL3M_D022,TI:MO;0)
298.15 GFCCMO+3.0*GFCCTI; 6000.00 N REF:25 !
PARAMETER G(AL3M_D022,MO:TI;0)
298.15 3*GFCCMO+GFCCTI; 6000.00 N REF:25 !
PARAMETER G(AL3M_D022,TA:TA;0)
298.15 +3*GFCCTI+GFCCTA; 6000.00 N REF:25 !

TYPE_DEFINITION & GES A_P_D ALM_D019 MAGNETIC -3.0 2.80000E-01 !

PHASE ALM_D019 %& 2 3 1 !

CONSTITUENT ALM_D019 :MO,TA,TI% : MO,TA,TI : !

PARAMETER G(ALM_D019,TA:TI;0)
298.15 +4.0+4.0*GHSERTI; 6000.00 N REF:25 !
PARAMETER G(ALM_D019,TA:MO;0) 298.15 0; 6000 N!
PARAMETER G(ALM_D019,MO:TA;0) 298.15 0; 6000 N!
PARAMETER G(ALM_D019,MO:MO;0)
298.15 +4.0*GHCPMO; 6000.00 N REF:25 !
PARAMETER G(ALM_D019,TA:TA;0)
298.15 +4.0*GHCPTA; 6000.00 N REF:25 !
PARAMETER G(ALM_D019,TI:MO;0)
298.15 +17072.0-4.5*T+GHCPMO+3.0*GHSERTI; 6000.00 N REF:25 !
PARAMETER G(ALM_D019,MO:TI;0)
298.15 +17072.0-4.5*T+3.0*GHCPMO+GHSERTI; 6000.00 N REF:25 !
PARAMETER G(ALM_D019,TI:TA;0)
298.15 +6376+3.0*GHSERTI+GHCPTA; 6000.00 N REF:25 !
PARAMETER G(ALM_D019,TA:TI;0)
298.15 +6376+3.0*GHCPTA+GHSERTI; 6000.00 N REF:25 !
PARAMETER G(ALM_D019,MO,TI:MO;0)
298.15 +51212-13.5*T; 6000.00 N REF:25 !
PARAMETER G(ALM_D019,MO,TI:TI;0)
298.15 +51212-13.5*T; 6000.00 N REF:25 !
PARAMETER G(ALM_D019,MO:MO,TI;0)
298.15 +5692-1.5*T; 6000.00 N REF:25 !
PARAMETER G(ALM_D019,TI:MO,TI;0)
298.15 +5692-1.5*T; 6000.00 N REF:25 !
PARAMETER G(ALM_D019,TA,TI:TA;0)
298.15 +19128; 6000.00 N REF:25 !
PARAMETER G(ALM_D019,TA,TI:TI;0)
298.15 +19128; 6000.00 N REF:25 !
PARAMETER G(ALM_D019,TA:TA,TI;0)
298.15 2128; 6000.00 N REF:25 !

```
PARAMETER G(ALM_D019, TI:TA, TI;0)
298.15 +2128; 6000.00 N REF:25 !
$-----
TYPE_DEFINITION 'GES A_P_D ALTI MAGNETIC -1.0 4.00000E-01 !
PHASE ALTI %' 2 1 1 !
CONSTITUENT ALTI :MO,TA,TI : MO,TA,TI% : !
```

```
PARAMETER G(ALTI, TI:TI;0)
298.15 +2*GFCCTI; 6000.00 N REF:25 !
PARAMETER G(ALTI, MO:MO;0)
298.15 +2*GFCCMO; 6000.00 N REF:25 !
PARAMETER G(ALTI, TA:TA;0)
298.15 +2*GFCCTA; 6000.00 N REF:25 !
PARAMETER G(ALTI, TI:MO;0)
298.15 8250+GFCCMO+GFCCTI; 6000.00 N REF:25 !
PARAMETER G(ALTI, MO:TI;0)
298.15 8250+GFCCMO+GFCCTI; 6000.00 N REF:25 !
PARAMETER G(ALTI, TI:TA;0)
298.15 +4250+GFCCTI+GFCCTA; 6000.00 N REF:25 !
PARAMETER G(ALTI, TA:TI;0)
298.15 +4250+GFCCTA+GFCCTI; 6000.00 N REF:25 !
PARAMETER G(ALTI, MO, TI:MO;0)
298.15 8250; 6000.00 N REF:25 !
PARAMETER G(ALTI, MO, TI:TI;0)
298.15 8250; 6000.00 N REF:25 !
PARAMETER G(ALTI, MO:MO, TI;0)
298.15 8250; 6000.00 N REF:25 !
PARAMETER G(ALTI, TI:MO, TI;0)
298.15 8250; 6000.00 N REF:25 !
PARAMETER G(ALTI, TA, TI:TA;0)
298.15 4250; 6000.00 N REF:25 !
PARAMETER G(ALTI, TA, TI:TI;0)
298.15 4250; 6000.00 N REF:25 !
```

PARAMETER G(ALTI,TA:TA,TI;0)
298.15 4250; 6000.00 N REF:25 !
PARAMETER G(ALTI,TI:TA,TI;0)
298.15 4250; 6000.00 N REF:25 !
\$_____

TYPE_DEFINITION) GES AMEND_PHASE_DESCRIPTION
BCC_B2 DIS_PART BCC_A2,,,!
PHASE BCC_B2 %) 3 .5 .5 3 !
CONSTITUENT BCC_B2 :MO,NB,TA,TI,ZR : MO,NB,TA,TI%,ZR : VA : !

PARAMETER G(BCC_B2,MO:MO:VA;0) 298.15 0; 6000 N REF:25!
PARAMETER G(BCC_B2,TA:TA:VA;0) 298.15 0; 6000 N REF:25 !
PARAMETER G(BCC_B2,TI:TI:VA;0) 298.15 0; 6000 N REF:25 !
PARAMETER G(BCC_B2,TI:MO:VA;0)
298.15 10000.0; 6000.00 N REF:25 !
PARAMETER G(BCC_B2,MO:TI:VA;0)
298.15 10000.0; 6000.00 N REF:25 !
PARAMETER G(BCC_B2,TI:TA:VA;0)
298.15 +5000.0; 6000.00 N REF:25 !
PARAMETER G(BCC_B2,TA:TI:VA;0)
298.15 +5000.0; 6000.00 N REF:25 !
\$_____

PHASE BCT_A5 % 1 1.0 !
CONSTITUENT BCT_A5 :TI : !

PARAMETER G(BCT_A5,TI;0)
298.15 +4602.2+GHserti; 3000.00 N REF:20 !
\$_____

PHASE CBCC_A12 % 2 1 1 !
CONSTITUENT CBCC_A12 :TI : VA : !

PARAMETER G(CBCC_A12,TI:VA;0)
298.15 +4602.2+GHserti; 6000.00 N REF:20 !

\$

PHASE CUB_A13 % 2 1 1 !
CONSTITUENT CUB_A13 :TI : VA : !

PARAMETER G(CUB_A13, TI:VA;0)
298.15 +7531.2+GHserti; 6000.00 N REF:20 !

\$

PHASE DIAMOND_A4 % 1 1.0 !
CONSTITUENT DIAMOND_A4 :TI : !

PARAMETER G(DIAMOND_A4, TI;0)
298.15 +25000+GHserti; 6000.00 N REF:20 !

\$

PHASE LAVES_C14 % 2 2 1 !
CONSTITUENT LAVES_C14 :TI : TI% : !

PARAMETER G(LAVES_C14, TI:TI;0)
298.15 +15000+3*GHserti; 6000.00 N REF:20 !

\$

PHASE LAVES_C15 % 2 2 1 !
CONSTITUENT LAVES_C15 :TI,MO,ZR : TI,MO,ZR : !

PARAMETER G(LAVES_C15, TI:TI;0)
298.15 +15000+3*GHserti; 6.00000E+03 N REF:24!

PARAMETER G(LAVES_C15, MO:MO;0)

298.15 +3*GHSERMO+15000; 6000 N REF:26 !

PARAMETER G(LAVES_C15, ZR:ZR;0)

298.15 +3*GHSERZR+15000; 6000 N REF:26 !

PARAMETER G(LAVES_C15, TI:MO;0)

298.15 +GHSERMO+2*GHserti+15000; 6000 N REF:24 !

PARAMETER G(LAVES_C15, MO:TI;0)

298.15 +2*GHSERMO+GHserti+15000; 6000 N REF:24 !

PARAMETER G(LAVES_C15, TI:ZR;0)

298.15 +2*GHSERTI+GHSERZR+9000; 6000 N REF:24 !
PARAMETER G(LAVES_C15,ZR:TI;0)
298.15 +GHSERTI+2*GHSERZR+15000; 6000 N REF:24 !
PARAMETER G(LAVES_C15,MO:ZR;0)
298.15 +2*GHSERMO+GHSERZR-21734.78+0.1441789*T; 6000 N REF:26 !
PARAMETER G(LAVES_C15,ZR:MO;0)
298.15 +GHSERMO+2*GHSERZR+21734.78-0.1441789*T; 6000 N REF:26 !
PARAMETER G(LAVES_C15,MO:MO,ZR;0) 298.15 +60000; 6000 N REF:26 !
PARAMETER G(LAVES_C15,ZR:MO,ZR;0) 298.15 +60000; 6000 N REF:26 !
PARAMETER G(LAVES_C15,MO,ZR:MO;0) 298.15 +100000; 6000 N REF:26 !
PARAMETER G(LAVES_C15,MO,ZR:ZR;0) 298.15 +100000; 6000 N REF:26 !
PARAMETER G(LAVES_C15,TI:MO,ZR;0) 298.15 +60000; 6000 N REF:27 !
PARAMETER G(LAVES_C15,MO,ZR:TI;0) 298.15 +100000; 6000 N REF:27 !
\$

PHASE OMEGA % 2 1 .5 !
CONSTITUENT OMEGA :NB,TI% : VA% : !

PARAMETER G(OMEGA,ZR;0)
298.15 -8878.082+144.432234*T
-26.8556*T*LN(T)-.002799446*T**2+38376*T**(-1); 2128 Y
-29500.524+265.290858*T-42.144*T*LN(T)
+7.17445E+31*T**(-9); 6000 N REF:20 !
PARAMETER G(OMEGA,TI:VA;0)
298.15 1886.7-0.15161*T+GHSERTI; 4.00000E+03 N REF:23 !
PARAMETER G(OMEGA,NB:VA;0)
2.98150E+02 15000+2.4*T++GHSERNB; 6.00000E+03 N REF:23 !
PARAMETER G(OMEGA,NB,TI:VA;0)
298.15 -3775.9; 6000.00 N REF:23 !
\$

PHASE SI3TI5 % 3 2 3 3 !
CONSTITUENT SI3TI5 :TI : TI : TI : !

PARAMETER G(SI3TI5,TI:TI:TI;0)

298.15 +40000+20*T+8*GHSERTI; 6000.00 N REF:20 !

\$-----

PHASE SNTI3 % 2 1 3 !

CONSTITUENT SNTI3 :TI : TI% : !

PARAMETER G(SNTI3,TI:TI;0)

298.15 +4*GHSERTI+4; 6000.00 N REF:20 !

\$-----

PHASE ORTHORHOMBIC_A20 % 1 1.0 !

CONSTITUENT ORTHORHOMBIC_A20 :ZR : !

PARAMETER G(ORTHORHOMBIC_A20,ZR;0)

298.15 +4474.461+124.9457*T

-25.607406*T*LN(T)-3.40084E-04*T**2-9.729E-09*T**3

+25233*T**(-1)-7.6143E-11*T**4; 2128 Y

-25705.955+264.284163*T-42.144*T*LN(T)

+1.276058E+32*T**(-9); 6000 N REF:20 !

\$-----

PHASE TETRAGONAL_U % 1 1.0 !

CONSTITUENT TETRAGONAL_U :ZR : !

PARAMETER G(TETRAGONAL_U,ZR;0)

298.15 +4474.461+124.9457*T

-25.607406*T*LN(T)-3.40084E-04*T**2-9.729E-09*T**3

+25233*T**(-1)-7.6143E-11*T**4; 2128 Y

-25705.955+264.284163*T-42.144*T*LN(T)

+1.276058E+32*T**(-9); 6000 N REF:20 !

\$-----

DATABASE_INFO 'FOR THE TI_MO_NB_TA_ZR SYSTEM' !

LIST_OF_REFERENCES

NUMBER SOURCE

20 'A.T. Dinsdale, SGTE Data for Pure Elements, CALPHAD.

-
- 15 (1991) 317-425.'
- 21 'W. Xiong, Y. Du, Y. Liu, B.Y. Huang, H.H. Xu, H.L. Chen, et al., Thermodynamic assessment of the Mo-Nb-Ta system, Calphad-Computer Coupling Phase Diagrams Thermochem. 28 (2004) 133-140.'
- 22 'K.C.H. Kumar, P. Wollants, L. Delaey, Thermodynamic assessment of the Ti-Zr system and calculation of the Nb-Ti-Zr phase-diagram, J. Alloys Compd. 206 (1994) 121-127.'
- 23 'Y.L. Zhang, H.S. Liu, Z.P. Jin, Thermodynamic assessment of the Nb-Ti system, Calphad-Computer Coupling Phase Diagrams Thermochem. 25 (2001) 305-317.'
- 24 'S. Kar, D.M. Lipkin, A CALPHAD-based phase equilibrium model of Mo-Ti-Zr-C, in: TMS 2008 Annu. Meet. Suppl. Proceedings, Vol 2 Mater. Charact. Comput. Model., Minerals, Metals & Materials Soc, Warrendale, 2008: pp. 237-243.'
- 25 'I. Ansara, A.T. Dinsdale, M.H. Rand, COST 507: thermochemical database for light metal alloys, European Communities, Brussels and Luxembourg, 1998.'
- 26 'R.J. Perez, B. Sundman, Thermodynamic assessment of the Mo-Zr binary phase diagram, Calphad-Computer Coupling Phase Diagrams Thermochem. 27 (2003) 253-262.'
- 27 'A.F. Guillermet, Phase-diagram and thermochemical properties of the Zr-Ta system - an assessment based on Gibbs energy modeling, J. Alloys Compd. 226 (1995) 174-184.'
- 28 'A.F. Guillermet, Thermodynamic analysis of the stable phases in the Zr-Nb system and calculation of the phase-diagram, Zeitschrift Fur Met. 82 (1991) 478-487.'
- !
-

Appendix B |

Sn-Ta Database

```
$*****  
$ The definition of the pure elements, vacancy and species  
$-----  
ELEMENT /- ELECTRON_GAS 0.0000E+00 0.0000E+00 0.0000E+00!  
ELEMENT VA VACUUM 0.0000E+00 0.0000E+00 0.0000E+00!  
ELEMENT SN BCT_A5 1.1871E+02 6.3220E+03 5.1195E+01!  
ELEMENT TA BCC_A2 1.8095E+02 5.6819E+03 4.1472E+01!
```

```
$*****
```

```
$ The Gibbs energies of the elements  
$ in the stable and metastable forms from SGTE  
$-----  
$-----
```

* TA *

```
$-----  
$-----
```

FUNCTION GHSERTA

```
298.15 -7285.889+119.139857*T-23.7592624*T*LN(T)  
.002623033*T**2+1.70109E-07*T**3-3293*T**(-1); 1300 Y  
-22389.955+243.88676*T-41.137088*T*LN(T)+.006167572*T**2  
-6.55136E-07*T**3+2429586*T**(-1); 2500 Y  
+229382.886-722.59722*T+78.5244752*T*LN(T)-.017983376*T**2
```

+1.95033E-07*T**3-93813648*T**(-1); 3290 Y
-1042384.01+2985.49125*T-362.159132*T*LN(T)+.043117795*T**2
-1.055148E-06*T**3+5.54714342E+08*T**(-1); 6000 N REF20 !

FUNCTION GFCCTA

298.15 +8714.111+120.839857*T-23.7592624*T*LN(T)
.002623033*T**2+1.70109E-07*T**3-3293*T**(-1); 1300 Y
-6389.955+245.58676*T-41.137088*T*LN(T)+.006167572*T**2
-6.55136E-07*T**3+2429586*T**(-1); 2500 Y
+245382.886-720.89722*T+78.5244752*T*LN(T)-.017983376*T**2
+1.95033E-07*T**3-93813648*T**(-1); 3290 Y
-1026384.01+2987.19125*T-362.159132*T*LN(T)+.043117795*T**2
-1.055148E-06*T**3+5.54714342E+08*T**(-1); 6000 N REF20 !

FUNCTION GHCPTA

298.15 +4714.111+121.539857*T-23.7592624*T*LN(T)
.002623033*T**2+1.70109E-07*T**3-3293*T**(-1); 1300 Y
-10389.955+246.28676*T-41.137088*T*LN(T)+.006167572*T**2
-6.55136E-07*T**3+2429586*T**(-1); 2500 Y
+241382.886-720.19722*T+78.5244752*T*LN(T)-.017983376*T**2
+1.95033E-07*T**3-93813648*T**(-1); 3290 Y
-1030384.01+2987.89125*T-362.159132*T*LN(T)+.043117795*T**2
-1.055148E-06*T**3+5.54714342E+08*T**(-1); 6000 N REF20 !

FUNCTION GLIQTA

298.15 +21875.086+111.561128*T-23.7592624*T*LN(T)
.002623033*T**2+1.70109E-07*T**3-3293*T**(-1); 1000 Y
+43884.339-61.981795*T+.0279523*T*LN(T)-.012330066*T**2
+6.14599E-07*T**3-3523338*T**(-1); 3290 Y
-6314.543+258.110873*T-41.84*T*LN(T); 6000 N REF20 !

\$_____

\$_____

* SN *

\$_____

\$_____

FUNCTION GHSERSN

100 -7958.517+122.765451*T-25.858*T*LN(T)
+5.1185E-04*T**2-3.192767E-06*T**3+18440*T**(-1); 250 Y
-5855.135+65.443315*T-15.961*T*LN(T)-.0188702*T**2+3.121167E-06*T**3
-61960*T**(-1); 505.08 Y
+2524.724+4.005269*T-8.2590486*T*LN(T)-.016814429*T**2
+2.623131E-06*T**3-1081244*T**(-1)-1.2307E+25*T**(-9); 800 Y
-8256.959+138.99688*T-28.4512*T*LN(T)-1.2307E+25*T**(-9); 3000 N REF20 !

FUNCTION GBCCSN

100 -3558.517+116.765451*T-25.858*T*LN(T)
+5.1185E-04*T**2-3.192767E-06*T**3+18440*T**(-1); 250 Y
-1455.135+59.443315*T-15.961*T*LN(T)-.0188702*T**2+3.121167E-06*T**3
-61960*T**(-1); 505.08 Y
+6924.724-1.994731*T-8.2590486*T*LN(T)-.016814429*T**2
+2.623131E-06*T**3-1081244*T**(-1)-1.2307E+25*T**(-9); 800 Y
-3856.959+132.99688*T-28.4512*T*LN(T)-1.2307E+25*T**(-9); 3000 N REF20 !

FUNCTION GA12SN

100 -5958.517+122.765451*T-25.858*T*LN(T)
+5.1185E-04*T**2-3.192767E-06*T**3+18440*T**(-1); 250 Y
-3855.135+65.443315*T-15.961*T*LN(T)-.0188702*T**2+3.121167E-06*T**3
-61960*T**(-1); 505.08 Y+4524.724+4.005269*T-8.2590486*T*LN(T)
-.016814429*T**2+2.623131E-06*T**3-1081244*T**(-1)-1.2307E+25*T**(-9); 800 Y
-6256.959+138.99688*T-28.4512*T*LN(T)-1.2307E+25*T**(-9); 3000 N REF20 !

FUNCTION GA13SN

100 -5958.517+122.765451*T-25.858*T*LN(T)
+5.1185E-04*T**2-3.192767E-06*T**3+18440*T**(-1); 250 Y
-3855.135+65.443315*T-15.961*T*LN(T)-.0188702*T**2+3.121167E-06*T**3
-61960*T**(-1); 505.08 Y
+4524.724+4.005269*T-8.2590486*T*LN(T)-.016814429*T**2
+2.623131E-06*T**3-1081244*T**(-1)-1.2307E+25*T**(-9); 800 Y
-6256.959+138.99688*T-28.4512*T*LN(T)-1.2307E+25*T**(-9); 3000 N REF20 !

FUNCTION GDIAMOND

100 -9579.608+114.007785*T-22.972*T*LN(T)-.00813975*T**2
+2.7288E-06*T**3+25615*T**(-1); 298.15 Y

-9063.001+104.84654*T-21.5750771*T*LN(T)-.008575282*T**2
+1.784447E-06*T**3-2544*T**(-1); 800 Y
-10909.351+147.396535*T-28.4512*T*LN(T); 3000 N REF20 !

FUNCTION GFCCSN
298.15 -345.135+56.983315*T-15.961*T*LN(T)-.0188702*T**2
+3.121167E-06*T**3-61960*T**(-1); 505.08 Y
+8034.724-4.454731*T-8.2590486*T*LN(T)-.016814429*T**2
+2.623131E-06*T**3-1081244*T**(-1)-1.2307E+25*T**(-9); 800 Y
-2746.959+130.53688*T-28.4512*T*LN(T)-1.2307E+25*T**(-9); 3000 N REF20 !

FUNCTION GHCPSN
298.15 -1955.135+57.797315*T-15.961*T*LN(T)
-.0188702*T**2+3.121167E-06*T**3-61960*T**(-1); 505.08 Y
+6424.724-3.640731*T-8.2590486*T*LN(T)-.016814429*T**2
+2.623131E-06*T**3-1081244*T**(-1)-1.2307E+25*T**(-9); 800 Y
-4356.959+131.35088*T-28.4512*T*LN(T)-1.2307E+25*T**(-9); 3000 N REF20 !

FUNCTION GHCPZN_S
298.15 -1950.135+57.797315*T-15.961*T*LN(T)
-.0188702*T**2+3.121167E-06*T**3-61960*T**(-1); 505.08 Y
+6429.724-3.640731*T-8.2590486*T*LN(T)-.016814429*T**2
+2.623131E-06*T**3-1081244*T**(-1)-1.2307E+25*T**(-9); 800 Y
-4351.959+131.35088*T-28.4512*T*LN(T)-1.2307E+25*T**(-9); 3000 N REF20 !

FUNCTION GLIQSN
100 -855.425+108.677684*T-25.858*T*LN(T)+5.1185E-04*T**2
-3.192767E-06*T**3+18440*T**(-1)+1.47031E-18*T**7; 250 Y
+1247.957+51.355548*T-15.961*T*LN(T)-.0188702*T**2+3.121167E-06*T**3
-61960*T**(-1)+1.47031E-18*T**7; 505.08 Y
+9496.31-9.809114*T-8.2590486*T*LN(T)-.016814429*T**2
+2.623131E-06*T**3-1081244*T**(-1); 800 Y
-1285.372+125.182498*T-28.4512*T*LN(T); 3000 N REF20 !

FUNCTION GA7SN
100 -5923.517+122.765451*T-25.858*T*LN(T)
+5.1185E-04*T**2-3.192767E-06*T**3+18440*T**(-1); 250 Y
-3820.135+65.443315*T-15.961*T*LN(T)-.0188702*T**2+3.121167E-06*T**3

$-61960*T^{**}(-1); 505.08 \text{ Y}$
 $+4559.724+4.005269*T-8.2590486*T*LN(T)-.016814429*T^{**}2$
 $+2.623131E-06*T^{**}3-1081244*T^{**}(-1)-1.2307E+25*T^{**}(-9); 800 \text{ Y}$
 $-6221.959+138.99688*T-28.4512*T*LN(T)-1.2307E+25*T^{**}(-9); 3000 \text{ N REF20 !}$
 FUNCTION GA6SN
 $298.15 -468.135+57.181195*T-15.961*T*LN(T)-.0188702*T^{**}2$
 $+3.121167E-06*T^{**}3-61960*T^{**}(-1); 505.08 \text{ Y}$
 $+7911.724-4.256851*T-8.2590486*T*LN(T)-.016814429*T^{**}2$
 $+2.623131E-06*T^{**}3-1081244*T^{**}(-1)-1.2307E+25*T^{**}(-9); 800 \text{ Y}$
 $-2869.959+130.73476*T-28.4512*T*LN(T)-1.2307E+25*T^{**}(-9); 3000 \text{ N REF20 !}$
 \$

FUNCTION UN_ASS 298.15 +0.0; 300 N !

\$

TYPE_DEFINITION % SEQ *!

DEFINE_SYSTEM_DEFAULT ELEMENT 2 !

DEFAULT_COMMAND DEF_SYS_ELEMENT VA /- !

\$

\$

TYPE_DEFINITION & GES A_P_D BCC_A2 MAGNETIC -1.0 4.00000E-01 !

PHASE BCC_A2 %& 2 1 3 !

CONSTITUENT BCC_A2 :SN,TA : VA : !

PARAMETER G(BCC_A2,SN:VA;0)

100 +GBCCSN; 3000 N REF20 !

PARAMETER G(BCC_A2,TA:VA;0)

298.15 +GHSERTA; 6000 N REF20 !

PARAMETER G(BCC_A2,SN,TA:VA;0)

298.15 7.0451375E+04; 6000 N !

PARAMETER G(BCC_A2,SN,TA:VA;1)

298.15 1.1223739E+05; 6000 N !

\$

PHASE BCT_A5 % 1 1.0 !

CONSTITUENT BCT_A5 :SN : !

PARAMETER G(BCT_A5,SN;0)

100 +GHSERSN; 3000 N REF20 !

\$

TYPE_DEFINITION ' GES A_P_D CBCC_A12 MAGNETIC -3.0 2.80000E-01 !
 PHASE CBCC_A12 %' 2 1 1 !
 CONSTITUENT CBCC_A12 :SN : VA : !

PARAMETER G(CBCC_A12,SN:VA;0) 100 +GA12SN; 3000 N REF20 !

\$

PHASE CUB_A13 % 2 1 1 !
 CONSTITUENT CUB_A13 :SN : VA : !

PARAMETER G(CUB_A13,SN:VA;0) 100 +GA13SN; 3000 N REF20 !

\$

PHASE DIAMOND_A4 % 1 1.0 !
 CONSTITUENT DIAMOND_A4 :SN : !

PARAMETER G(DIAMOND_A4,SN;0) 100 +GDIAMOND; 3000 N REF20 !

\$

TYPE_DEFINITION (GES A_P_D FCC_A1 MAGNETIC -3.0 2.80000E-01 !
 PHASE FCC_A1 %(2 1 1 !
 CONSTITUENT FCC_A1 :SN,TA : VA : !

PARAMETER G(FCC_A1,SN:VA;0) 298.15 +GFCCSN; 3000 N REF20 !
 PARAMETER G(FCC_A1,TA:VA;0) 298.15 +GFCCTA; 6000 N REF20 !

\$

TYPE_DEFINITION) GES A_P_D HCP_A3 MAGNETIC -3.0 2.80000E-01 !
 PHASE HCP_A3 %) 2 1 .5 !
 CONSTITUENT HCP_A3 :SN,TA : VA : !

PARAMETER G(HCP_A3,SN:VA;0) 298.15 +GHCPSEN; 3000 N REF20 !
 PARAMETER G(HCP_A3,TA:VA;0) 298.15 +GHCPATA; 6000 N REF20 !

\$

PHASE HCP_ZN % 2 1 .5 !
 CONSTITUENT HCP_ZN :SN : VA : !

PARAMETER G(HCP_ZN,SN:VA;0) 298.15 +GHCPZN_S; 3000 N REF20 !
\$-----

PHASE LIQUID % 1 1.0 !
CONSTITUENT LIQUID :SN,TA : !

PARAMETER G(LIQUID,SN;0) 100 +GLIQSN; 3000 N REF20 !
PARAMETER G(LIQUID,TA;0) 298.15 +GLIQT; 6000 N REF20 !
PARAMETER G(LIQUID,SN,TA;0) 298.15 -1.7117919E+04; 6000 N !
\$-----

PHASE RHOMBOHEDRAL_A7 % 1 1.0 !
CONSTITUENT RHOMBOHEDRAL_A7 :SN : !

PARAMETER G(RHOMBOHEDRAL_A7,SN;0) 100 +GA7SN; 3000 N REF20 !
\$-----

PHASE TA3SN % 2 3 1 !
CONSTITUENT TA3SN :TA : SN : !

PARAMETER G(TA3SN,TA:SN;0)
298.15 -68843.951-6.00E+00*T+3*GHSERTA+GHSERSN; 3000 N !
\$-----

PHASE TASN2 % 2 1 2 !
CONSTITUENT TASN2 :TA : SN : !

PARAMETER G(TASN2,TA:SN;0)
298.15 -29678.180-4.202*T+GHSERTA+2*GHSERSN; 3000 N !
\$-----

PHASE TETRAGONAL_A6 % 1 1.0 !
CONSTITUENT TETRAGONAL_A6 :SN : !

PARAMETER G(TETRAGONAL_A6,SN;0) 298.15 +GA6SN; 3000 N REF20 !
\$-----

\$*****

LIST_OF_REFERENCES

NUMBER SOURCE

20 'A.T. Dinsdale, SGTE Data for Pure Elements,
CALPHAD.15 (1991) 317-425. '

!

Appendix C | Mathematica Interaction Parameter Fitting

input: $n = 0, 0, 0.019, -2.81, 0.019, -2.81, 0.019, -2.81, 0.019, -2.81, 0.019, -2.81, 0.019, -2.81, 0.125, 4.00, 0.125, 4.00, 0.125, 4.00, 0.125, 4.00, 0.125, 4.00, 0.125, 4.00, 0.125, 4.00, 0.25, 8.67, 0.25, 8.67, 0.25, 8.67, 0.25, 8.67, 0.25, 8.67, 0.25, 8.67, 0.50, 12.00, 0.75, 1.00, 0.938, 6.42, 0.981, -0.11, 1, 0$

output: $0, 0, 0.019, -2.81, 0.019, -2.81, 0.019, -2.81, 0.019, -2.81, 0.019, -2.81, 0.125, 4., 0.125, 4., 0.125, 4., 0.125, 4., 0.125, 4., 0.25, 8.67, 0.25, 8.67, 0.25, 8.67, 0.25, 8.67, 0.5, 12., 0.75, 1., 0.938, 6.42, 0.981, -0.11, 1, 0$

input: $gp = \text{ListPlot}[n, \text{PlotMarkers} \rightarrow \square, 10, \text{PlotStyle} \rightarrow \text{Blue}]$ input: $\text{Fit}[n, (x^*(1 - x)), ((x^*(1 - x))^*(x - (1 - x))), x]$ (For a two parameter fit) input: $\text{Fit}[n, (x^*(1 - x)), x]$ (For a one parameter fit) input: $\text{Plot}[\%, x, 0, 1, \text{PlotRange} \rightarrow -100, 100]$ input: $\text{Show}[\%, gp]$

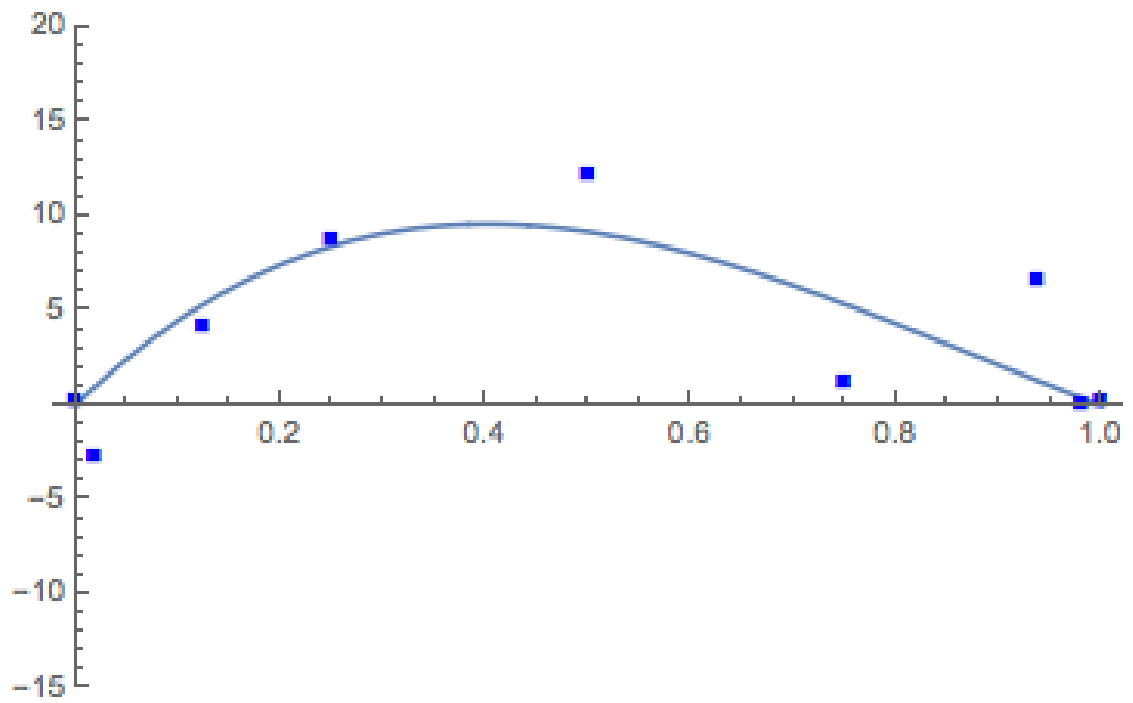


Figure C.1.

Appendix D | Ti Elastic Database

```
$*****  
$ The definition of the pure elements, vacancy and species  
$-----  
TEMPERATURE_LIMIT 0 6000.00 !  
ELEMENT /- ELECTRON_GAS 0.0000E+00 0.0000E+00 0.0000E+00!  
ELEMENT VA VACUUM 0.0 0.0 0.0 0.0 !  
ELEMENT TI BCC_A2 !  
ELEMENT MO BCT_A5 !  
ELEMENT NB BCC_A2 !  
ELEMENT SN BCT_A5 !  
ELEMENT TA BCC_A2 !  
ELEMENT ZR BCT_A5 !
```

```
$*****  
$-----  
FUNCTION C11BCCTI 298.15 +93; 6000 N !  
FUNCTION C12BCCTI 298.15 +115; 6000 N !  
FUNCTION C44BCCTI 298.15 +41; 6000 N !  
FUNCTION C11BCCMO 298.15 +475; 6000 N !  
FUNCTION C12BCCMO 298.15 +164; 6000 N !  
FUNCTION C44BCCMO 298.15 +108; 6000 N !
```

FUNCTION C11BCCNB	298.15 +245;	6000 N !
FUNCTION C12BCCNB	298.15 +144;	6000 N !
FUNCTION C44BCCNB	298.15 +27;	6000 N !
FUNCTION C11BCCSN	298.15 +50;	6000 N !
FUNCTION C12BCCSN	298.15 +52;	6000 N !
FUNCTION C44BCCSN	298.15 +29;	6000 N !
FUNCTION C11BCCTA	298.15 +278;	6000 N !
FUNCTION C12BCCTA	298.15 +164;	6000 N !
FUNCTION C44BCCTA	298.15 +81;	6000 N !
FUNCTION C11BCCZR	298.15 +86;	6000 N !
FUNCTION C12BCCZR	298.15 +91;	6000 N !
FUNCTION C44BCCZR	298.15 +32;	6000 N !
FUNCTION UN_ASS	298.15 +0;	300 N !
\$		
FUNCTION UN_ASS	298.15 0;	300 N !
\$		
\$*****		
TYPE_DEFINITION % SEQ *		!
TYPE_DEFINITION G SEQ *		!
DEFINE_SYSTEM_DEFAULT SPECIE 5		!
DEFAULT_COMMAND DEF_SYS_ELEMENT VA		!
\$		
\$*****		
\$*****		
\$		
TYPE_DEFINITION & GES A_P_D BCC_A2 MAGNETIC -1.0 4.00000E-01		!
PHASE BCC_A2 %& 2 1 3		!
CONSTITUENT BCC_A2 :TI,MO,NB,SN,TA,ZR : VA :		!
PARAMETER C11(BCC_A2, TI:VA;0)		
298.15 +C11BCCTI;	6000 N !	
PARAMETER C11(BCC_A2, MO:VA;0)		
298.15 +C11BCCMO;	6000 N !	

PARAMETER C11(BCC_A2,NB:VA;0)
298.15 +C11BCCNB; 6000 N !

PARAMETER C11(BCC_A2,SN:VA;0)
298.15 +C11BCCSN; 6000 N !

PARAMETER C11(BCC_A2,TA:VA;0)
298.15 +C11BCCTA; 6000 N !

PARAMETER C11(BCC_A2,ZR:VA;0)
298.15 +C11BCCZR; 6000 N !

PARAMETER C11(BCC_A2,TI,MO:VA;0)
298.15 -22.16; 6000 N !

PARAMETER C11(BCC_A2,TI,NB:VA;0)
298.15 +40.46; 6000 N !

PARAMETER C11(BCC_A2,TI,SN:VA;0)
298.15 +119.46; 6000 N !

PARAMETER C11(BCC_A2,TI,TA:VA;0)
298.15 +83.65; 6000 N !

PARAMETER C11(BCC_A2,TI,TA:VA;1)
298.15 -67.76; 6000 N !

PARAMETER C11(BCC_A2,TI,ZR:VA;0)
298.15 +246.97; 6000 N !

PARAMETER C11(BCC_A2,TI,ZR:VA;1)
298.15 -135.95; 6000 N !

PARAMETER C11(BCC_A2,TI,MO,NB:VA;0)
298.15 -29.97; 6000 N !

PARAMETER C11(BCC_A2,TI,MO,SN:VA;0)
298.15 -83.85; 6000 N !

PARAMETER C11(BCC_A2,TI,MO,TA:VA;0)
298.15 -106.53; 6000 N !

PARAMETER C11(BCC_A2,TI,MO,ZR:VA;0)
298.15 -245.27; 6000 N !

PARAMETER C11(BCC_A2,TI,NB,SN:VA;0)
298.15 -41.52; 6000 N !

PARAMETER C11(BCC_A2,TI,NB,TA:VA;0)

298.15 -93.77; 6000 N !
PARAMETER C11(BCC_A2, TI, NB, ZR:VA;0)
298.15 -220.35; 6000 N !
PARAMETER C11(BCC_A2, TI, SN, TA:VA;0)
298.15 -95.39; 6000 N !
PARAMETER C11(BCC_A2, TI, SN, ZR:VA;0)
298.15 -155.34; 6000 N !
PARAMETER C11(BCC_A2, TI, TA, ZR:VA;0)
298.15 -149.67; 6000 N !
\$—————
PARAMETER C12(BCC_A2, TI:VA;0)
298.15 +C12BCCTI; 6000 N !
PARAMETER C12(BCC_A2, MO:VA;0)
298.15 +C12BCCMO; 6000 N !
PARAMETER C12(BCC_A2, NB:VA;0)
298.15 +C12BCCNB; 6000 N !
PARAMETER C12(BCC_A2, SN:VA;0)
298.15 +C12BCCSN; 6000 N !
PARAMETER C12(BCC_A2, TA:VA;0)
298.15 +C12BCCTA; 6000 N !
PARAMETER C12(BCC_A2, ZR:VA;0)
298.15 +C12BCCZR; 6000 N !
PARAMETER C12(BCC_A2, TI, MO:VA;0)
298.15 -36.40; 6000 N !
PARAMETER C12(BCC_A2, TI, NB:VA;0)
298.15 -32.39; 6000 N !
PARAMETER C12(BCC_A2, TI, SN:VA;0)
298.15 +15.90; 6000 N !
PARAMETER C12(BCC_A2, TI, SN:VA;1)
298.15 -146.80; 6000 N !
PARAMETER C12(BCC_A2, TI, TA:VA;0)
298.15 +38.05; 6000 N !
PARAMETER C12(BCC_A2, TI, ZR:VA;0)

298.15 -110.53; 6000 N !
PARAMETER C12(BCC_A2, TI, ZR:VA;1)
298.15 +78.00; 6000 N !
PARAMETER C12(BCC_A2, TI, MO, NB:VA;0)
298.15 +13.97; 6000 N !
PARAMETER C12(BCC_A2, TI, MO, SN:VA;0)
298.15 +31.80; 6000 N !
PARAMETER C12(BCC_A2, TI, MO, TA:VA;0)
298.15 -12.35; 6000 N !
PARAMETER C12(BCC_A2, TI, MO, ZR:VA;0)
298.15 +50.43; 6000 N !
PARAMETER C12(BCC_A2, TI, NB, SN:VA;0)
298.15 +25.52; 6000 N !
PARAMETER C12(BCC_A2, TI, NB, TA:VA;0)
298.15 -15.80; 6000 N !
PARAMETER C12(BCC_A2, TI, NB, ZR:VA;0)
298.15 +72.10; 6000 N !
PARAMETER C12(BCC_A2, TI, SN, TA:VA;0)
298.15 -10.94; 6000 N !
PARAMETER C12(BCC_A2, TI, SN, ZR:VA;0)
298.15 +68.86; 6000 N !
PARAMETER C12(BCC_A2, TI, TA, ZR:VA;0)
298.15 -8.91; 6000 N !
\$

PARAMETER C44(BCC_A2, TI:VA;0)
298.15 +C44BCCTI; 6000 N !
PARAMETER C44(BCC_A2, MO:VA;0)
298.15 +C44BCCMO; 6000 N !
PARAMETER C44(BCC_A2, NB:VA;0)
298.15 +C44BCCNB; 6000 N !
PARAMETER C44(BCC_A2, SN:VA;0)
298.15 +C44BCCSN; 6000 N !
PARAMETER C44(BCC_A2, TA:VA;0)

298.15 +C44BCCTA; 6000 N !
PARAMETER C44(BCC_A2,ZR:VA;0)
298.15 +C44BCCZR; 6000 N !
PARAMETER C44(BCC_A2,TI,MO:VA;0)
298.15 -142.90; 6000 N !
PARAMETER C44(BCC_A2,TI,NB:VA;0)
298.15 -41.54; 6000 N !
PARAMETER C44(BCC_A2,TI,NB:VA;1)
298.15 -41.95; 6000 N !
PARAMETER C44(BCC_A2,TI,SN:VA;0)
298.15 +59.75; 6000 N !
PARAMETER C44(BCC_A2,TI,SN:VA;1)
298.15 -94.38; 6000 N !
PARAMETER C44(BCC_A2,TI,TA:VA;0)
298.15 -51.96; 6000 N !
PARAMETER C44(BCC_A2,TI,ZR:VA;0)
298.15 +70.06; 6000 N !
PARAMETER C44(BCC_A2,TI,MO,NB:VA;0)
298.15 +9.72; 6000 N !
PARAMETER C44(BCC_A2,TI,MO,SN:VA;0)
298.15 +74.73; 6000 N !
PARAMETER C44(BCC_A2,TI,MO,TA:VA;0)
298.15 +5.27; 6000 N !
PARAMETER C44(BCC_A2,TI,MO,ZR:VA;0)
298.15 -44.96; 6000 N !
PARAMETER C44(BCC_A2,TI,NB,SN:VA;0)
298.15 +67.85; 6000 N !
PARAMETER C44(BCC_A2,TI,NB,TA:VA;0)
298.15 +4.25; 6000 N !
PARAMETER C44(BCC_A2,TI,NB,ZR:VA;0)
298.15 -55.29; 6000 N !
PARAMETER C44(BCC_A2,TI,SN,TA:VA;0)
298.15 +67.85; 6000 N !

```
PARAMETER C44(BCC_A2, TI, SN, ZR:VA;0)
298.15 +3.85; 6000 N !
PARAMETER C44(BCC_A2, TI, TA, ZR:VA;0)
298.15 -23.70; 6000 N !
$*****
*****LIST_OF_REFERENCES
NUMBER SOURCE
!
```

Appendix E | Pycalphad script

This code is used in pycalphad to plot the elastic moduli and elastic properites as a function of composition. A tdb file must be loaded into the script. In the present work the tdb file in Appendix D is used.

```
import matplotlib
from matplotlib.axes import Axes
from matplotlib.patches import Polygon
from matplotlib.path import Path
from matplotlib.ticker import NullLocator, Formatter, FixedLocator
from matplotlib.transforms import Affine2D, BboxTransformTo, IdentityTransform
from matplotlib.projections import register_projection
import matplotlib.spines as mspines
import matplotlib.axis as maxis
import matplotlib.pyplot as plt

import numpy as np

class TriangularAxes(Axes):
    """
    A custom class for triangular projections.
    """

    name = 'triangular'

    def __init__(self, *args, **kwargs):
        Axes.__init__(self, *args, **kwargs)
        self.set_aspect(1, adjustable='box', anchor='SW')
        self.cla()
```

```

def __init__(self):
    self.xaxis = maxis.XAxis(self)
    self.yaxis = maxis.YAxis(self)
    self._update_transScale()

def cla(self):
    """
    Override to set up some reasonable defaults.
    """
    # Don't forget to call the base class
    Axes.cla(self)

    x_min = 0
    y_min = 0
    x_max = 1
    y_max = 1
    x_spacing = 0.1
    y_spacing = 0.1
    self.xaxis.set_minor_locator(NullLocator())
    self.yaxis.set_minor_locator(NullLocator())
    self.xaxis.set_ticks_position('bottom')
    self.yaxis.set_ticks_position('left')
    Axes.set_xlim(self, x_min, x_max)
    Axes.set_ylim(self, y_min, y_max)
    self.xaxis.set_ticks(np.arange(x_min, x_max+x_spacing, x_spacing))
    self.yaxis.set_ticks(np.arange(y_min, y_max+y_spacing, y_spacing))

def __set__lim_and__transforms(self):
    """
    This is called once when the plot is created to set up all the
    transforms for the data, text and grids.
    """
    # There are three important coordinate spaces going on here:
    #
    # 1. Data space: The space of the data itself
    #
    # 2. Axes space: The unit rectangle (0, 0) to (1, 1)
    # covering the entire plot area.
    #
    # 3. Display space: The coordinates of the resulting image,
    # often in pixels or dpi/inch.

```

```

# This function makes heavy use of the Transform classes in
# ``lib/matplotlib/transforms.py``. For more information, see
# the inline documentation there.

# The goal of the first two transformations is to get from the
# data space (in this case longitude and latitude) to axes
# space. It is separated into a non-affine and affine part so
# that the non-affine part does not have to be recomputed when
# a simple affine change to the figure has been made (such as
# resizing the window or changing the dpi).

# 1) The core transformation from data space into
# rectilinear space defined in the HammerTransform class.
self.transProjection = IdentityTransform()
# 2) The above has an output range that is not in the unit
# rectangle, so scale and translate it so it fits correctly
# within the axes. The peculiar calculations of xscale and
#yscale are specific to a Aitoff-Hammer projection, so don't
# worry about them too much.
self.transAffine = Affine2D.from_values(
    1., 0, 0.5, np.sqrt(3)/2., 0, 0)
self.transAffinedep = Affine2D.from_values(
    1., 0, -0.5, np.sqrt(3)/2., 0, 0)
#self.transAffine = IdentityTransform()

# 3) This is the transformation from axes space to display
# space.
self.transAxes = BboxTransformTo(self.bbox)

# Now put these 3 transforms together -- from data all the way
# to display coordinates. Using the '+' operator, these
# transforms will be applied "in order". The transforms are
# automatically simplified, if possible, by the underlying
# transformation framework.
self.transData = \
    self.transProjection + \
    self.transAffine + \
    self.transAxes

# The main data transformation is set up. Now deal with

```

```

# gridlines and tick labels.

# Longitude gridlines and ticklabels. The input to these
# transforms are in display space in x and axes space in y.
# Therefore, the input values will be in range (-xmin, 0),
# (xmax, 1). The goal of these transforms is to go from that
# space to display space. The tick labels will be offset 4
# pixels from the equator.

self._xaxis._pretransform = IdentityTransform()
self._xaxis._transform = \
    self._xaxis._pretransform + \
    self.transData
self._xaxis._text1._transform = \
    Affine2D().scale(1.0, 0.0) + \
    self.transData + \
    Affine2D().translate(0.0, -20.0)
self._xaxis._text2._transform = \
    Affine2D().scale(1.0, 0.0) + \
    self.transData + \
    Affine2D().translate(0.0, -4.0)

# Now set up the transforms for the latitude ticks. The input to
# these transforms are in axes space in x and display space in
# y. Therefore, the input values will be in range (0, -ymin),
# (1, ymax). The goal of these transforms is to go from that
# space to display space. The tick labels will be offset 4
# pixels from the edge of the axes ellipse.

self._yaxis._transform = self.transData
yaxis_text_base = \
    self.transProjection + \
    (self.transAffine + \
    self.transAxes)
self._yaxis._text1._transform = \
    yaxis_text_base + \
    Affine2D().translate(-8.0, 0.0)
self._yaxis._text2._transform = \
    yaxis_text_base + \
    Affine2D().translate(8.0, 0.0)

```

```

def get_xaxis_transform(self, which='grid'):
    assert which in ['tick1', 'tick2', 'grid']
    return self._xaxis_transform

def get_xaxis_text1_transform(self, pad):
    return self._xaxis_text1_transform, 'bottom', 'center'

def get_xaxis_text2_transform(self, pad):
    return self._xaxis_text2_transform, 'top', 'center'

def get_yaxis_transform(self, which='grid'):
    assert which in ['tick1', 'tick2', 'grid']
    return self._yaxis_transform

def get_yaxis_text1_transform(self, pad):
    return self._yaxis_text1_transform, 'center', 'right'

def get_yaxis_text2_transform(self, pad):
    return self._yaxis_text2_transform, 'center', 'left'

def _gen_axes_spines(self):
    dep_spine = mspines.Spine.linear_spine(self,
                                             'right')
    # Fix dependent axis to be transformed the correct way
    dep_spine.set_transform(self.transAffinedep + self.transAxes)
    return {'left': mspines.Spine.linear_spine(self,
                                                'left'),
            'bottom': mspines.Spine.linear_spine(self,
                                                 'bottom'),
            'right': dep_spine}

def _gen_axes_patch(self):
    """
    Override this method to define the shape that is used for the
    background of the plot. It should be a subclass of Patch.
    Any data and gridlines will be clipped to this shape.
    """
    return Polygon([[0, 0], [0.5, np.sqrt(3)/2], [1, 0]], closed=True)

# Interactive panning and zooming is not supported with this projection,

```

```

# so we override all of the following methods to disable it.
def can_zoom(self):
    """
    Return True if this axes support the zoom box
    """
    return False

def start_pan(self, x, y, button):
    pass

def end_pan(self):
    pass

def drag_pan(self, button, key, x, y):
    pass

# Now register the projection with matplotlib so the user can select
# it.
register_projection(TriangularAxes)

import pycalphad.io.tdb_keywords
pycalphad.io.tdb_keywords.TDB_PARAM_TYPES.extend\
([ 'EM', 'BULK', 'SHEAR', 'C11', 'C12', 'C44' ])
from pycalphad import Database, Model, equilibrium, calculate
import numpy as np
import pycalphad.variables as v
import sympy
from tinydb import where

class ElasticModel(Model):
    def build_phase(self, dbe):
        phase = dbe.phases[self.phase_name]
        param_search = dbe.search
        # EM, BULK, SHEAR, C11, C12, C44
        for prop in [ 'EM', 'BULK', 'SHEAR', 'C11', 'C12', 'C44' ]:
            prop_param_query = (
                (where('phase_name') == phase.name) & \
                (where('parameter_type') == prop) & \
                (where('constituent_array').test(self._array_validity)))

```

```

)
prop_val = self.redlich_kister_sum \
(phase, param_search, prop_param_query).subs(dbe.symbols)
setattr(self, prop, prop_val)

dbf = Database('ElasticTi.tdb')
mod = ElasticModel(dbf, ['TI', 'SN', 'ZR', 'VA'], 'BCC_A2')
symbols = dict([(sympy.Symbol(s), val) for s, val in dbf.symbols.items()])
mod.C11 = mod.C11.xreplace(symbols)
mod.C12 = mod.C12.xreplace(symbols)
mod.C44 = mod.C44.xreplace(symbols)
x1 = np.linspace(0,1, num=100)
x2 = np.linspace(0,1, num=100)
mesh = np.meshgrid(x1, x2)
X = mesh[0]
Y = mesh[1]
mesh_arr = np.array(mesh)
mesh_arr = np.moveaxis(mesh_arr, 0, 2)
dep_col = 1 - np.sum(mesh_arr, axis=-1, keepdims=True)
mesh_arr = np.concatenate((mesh_arr, dep_col), axis=-1)
mesh_arr = np.concatenate((mesh_arr, np.ones(mesh_arr.shape[:-1] + (1,))), axis=-1)
orig_shape = tuple(mesh_arr.shape[:-1])
mesh_arr = mesh_arr.reshape(-1, mesh_arr.shape[-1])
mesh_arr[np.any(mesh_arr < 0, axis=-1), :] = np.nan
res_c11 = calculate(dbf, ['TI', 'SN', 'TA', 'VA'], 'BCC_A2', T=300, P=101325,
    model=mod, output='C11', points=mesh_arr)
res_c11 = res_c11.C11.values.reshape(orig_shape)
res_c12 = calculate(dbf, ['TI', 'SN', 'TA', 'VA'], 'BCC_A2', T=300, P=101325,
    model=mod, output='C12', points=mesh_arr)
res_c12 = res_c12.C12.values.reshape(orig_shape)
res_c44 = calculate(dbf, ['TI', 'SN', 'TA', 'VA'], 'BCC_A2', T=300, P=101325,
    model=mod, output='C44', points=mesh_arr)
res_c44 = res_c44.C44.values.reshape(orig_shape)

```

```

import numpy as np
def compute_moduli(c11, c12, c44):
    """Consume elastic stiffness constants and, under symmetry assumptions, compute
    bulk modulus, shear modulus, and Young's modulus.

```

Parameters

c11: float64 array-like
c12: float64 array-like
c44: float64 array-like

Returns

```

B, G, Y : tuple of float64 array-likes """
# Ported from a matlab code
c11 = np.array(c11)
c12 = np.array(c12)
c44 = np.array(c44)
cij = np.zeros(c11.shape + (6,6))
cij [..., 0, 0] = cij [..., 1, 1] = cij [..., 2, 2] = c11
cij [..., 0, 1] = cij [..., 1, 0] = cij [..., 0, 2] = \
cij [..., 2, 0] = cij [..., 1, 2] = cij [..., 2, 1] = c12
cij [..., 3, 3] = cij [..., 4, 4] = cij [..., 5, 5] = c44
sij = np.linalg.inv(cij)
A_c = (cij [..., 0, 0] + cij [..., 1, 1] + cij [..., 2, 2]) / 3.
B_c = (cij [..., 0, 1] + cij [..., 0, 2] + cij [..., 1, 2]) / 3.
C_c = (cij [..., 3, 3] + cij [..., 4, 4] + cij [..., 5, 5]) / 3.
A_s = (sij [..., 0, 0] + sijs [..., 1, 1] + sijs [..., 2, 2]) / 3.
B_s = (sij [..., 0, 1] + sijs [..., 0, 2] + sijs [..., 1, 2]) / 3.
C_s = (sij [..., 3, 3] + sijs [..., 4, 4] + sijs [..., 5, 5]) / 3.
Bv = (A_c + 2*B_c) / 3.
Gv = (A_c - B_c + 3*C_c) / 5.
Br = 1. / (3*A_s + 6*B_s)
Gr = 5. / (4*A_s - 4*B_s + 3*C_s)
Bvrh = (Br + Bv) / 2.
Gvrh = (Gr + Gv) / 2.
Yvrh = (9*Bvrh*Gvrh) / (Gvrh + 3*Bvrh)
return Bvrh, Gvrh, Yvrh

```

bulk_modulus, shear_modulus, young_modulus = \

```

compute_moduli(res_c11, res_c12, res_c44)

%matplotlib inline
import matplotlib.pyplot as plt

fig = plt.figure(figsize=(12,12))
ax = fig.gca(projection='triangular')
CS = ax.contour(X, Y, bulk_modulus, linewidths=4, \
levels=list(range(100, 300, 10)), cmap='cool')
ax.clabel(CS, inline=1, fontsize=13, fmt='%1.0f')
#PCM=ax.get_children()[0] #get the mappable,
#the 1st and the 2nd are the x and y axes
#plt.colorbar(PCM, ax=ax)
ax.set_xlabel('x(Mo)', fontsize=18)
ax.set_ylabel('x(Nb)', fontsize=18, rotation=60, labelpad=-180)
ax.tick_params(axis='both', which='major', labelsize=18)
ax.tick_params(axis='both', which='minor', labelsize=18)
ax.set_title('Bulk modulus')
#fig.savefig('TiMoNb-Bulk.pdf')

%matplotlib inline
import matplotlib.pyplot as plt

fig = plt.figure(figsize=(12,12))
ax = fig.gca(projection='triangular')
CS = ax.contour(X, Y, shear_modulus, linewidths=4, \
levels=list(range(0, 150, 5)), cmap='cool')
ax.clabel(CS, inline=1, fontsize=13, fmt='%1.0f')
#PCM=ax.get_children()[0] #get the mappable,
#the 1st and the 2nd are the x and y axes
#plt.colorbar(PCM, ax=ax)
ax.set_xlabel('x(Mo)', fontsize=18)
ax.set_ylabel('x(Nb)', fontsize=18, rotation=60, labelpad=-180)

```

```

ax.tick_params(axis='both', which='major', labelsize=18)
ax.tick_params(axis='both', which='minor', labelsize=18)
ax.set_title('Shear_modulus')
#fig.savefig('TiMoNb-Shear.pdf')

%matplotlib inline
import matplotlib.pyplot as plt

fig = plt.figure(figsize=(12,12))
ax = fig.gca(projection='triangular')
CS = ax.contour(X, Y, young_modulus, linewidths=4, \
levels=list(range(0, 350, 10)), cmap='cool')
ax.clabel(CS, inline=1, fontsize=13, fmt='%1.0f')
#PCM=ax.get_children()[0] #get the mappable,
#the 1st and the 2nd are the x and y axes
#plt.colorbar(PCM, ax=ax)
ax.set_xlabel('x(Mo)', fontsize=18)
ax.set_ylabel('x(Nb)', fontsize=18, rotation=60, labelpad=-180)
ax.tick_params(axis='both', which='major', labelsize=18)
ax.tick_params(axis='both', which='minor', labelsize=18)
ax.set_title('Young\s_modulus')
#fig.savefig('TiMoNb-Young.pdf')

```

Bibliography

- [1] WU, C., Y. XIN, X. WANG, and J. LIN (2010) “Effects of Ta content on the phase stability and elastic properties of β Ti-Ta alloys from first-principles calculations,” *Solid State Sciences*, **12**(12), pp. 2120–2124.
- [2] IKEHATA, H., N. NAGASAKO, T. FURUTA, A. FUKUMOTO, K. MIWA, and T. SAITO (2004) “First-principles calculations for development of low elastic modulus Ti alloys,” *Physical Review B*, **70**(17), p. 174113.
- [3] ZHOU, Y. L., M. NIINOMI, and T. AKAHORI (2004) “Effects of Ta content on Young’s modulus and tensile properties of binary Ti-Ta alloys for biomedical applications,” *Materials Science and Engineering: A*, **371**(1-2), pp. 283–290.
- [4] ZHOU, Y.-L. and M. NIINOMI (2009) “Ti₆₂Ta alloy with the best mechanical compatibility in Ti-Ta alloys for biomedical applications,” *Materials Science and Engineering: C*, **29**(3), pp. 1061–1065.
- [5] FEDOTOV, S., T. CHELIDZE, Y. KOVNERISTYY, and V. SANADZE (1985) “Phase structure, critical points MS and AS of martensitic transformations and elastic properties of metastable alloys of the Ti-Ta system,” *Phys. Met. Metall.*, **60**(3), pp. 139–143.
- [6] TIMOSHEVSKII, A., S. YABLONOVSKII, and O. IVASHIN (2011) “First-principles calculations atomic structure and elastic properties of Ti-Nb alloys,” *arXiv preprint arXiv:1111.7182*.
- [7] OZAKI, T., H. MATSUMOTO, S. WATANABE, and S. HANADA (2004) “Beta Ti Alloys with Low Young’s Modulus,” *MATERIALS TRANSACTIONS*, **45**(8), pp. 2776–2779.
- [8] FRIÁK, M., W. COUNTS, D. MA, B. SANDER, D. HOLEC, D. RAABE, and J. NEUGEBAUER (2012) “Theory-guided materials design of multi-phase Ti-Nb alloys with bone-matching elastic properties,” *Materials*, **5**(10), pp. 1853–1872.

- [9] KARRE, R., M. NIRANJAN, and S. DEY (2015) “First principles theoretical investigations of low Young’s modulus beta Ti_xNb and Ti_xNb_{1-x}Zr alloys compositions for biomedical applications,” *Materials Science and Engineering: C*, **50**, pp. 52–58.
 URL <http://www.sciencedirect.com/science/article/pii/S0928493115000715>
- [10] MATSUMOTO, H., S. WATANABE, N. MASAHASHI, and S. HANADA (2006) “Composition dependence of Young’s modulus in Ti-V, Ti-Nb, and Ti-V-Sn alloys,” *Metallurgical and Materials Transactions A*, **37**(11), pp. 3239–3249.
- [11] ANSARA, I., A. DINSDALE, and M. RAND (1998) *COST 507: thermochemical database for light metal alloys*, vol. 2, European Communities, Brussels and Luxembourg.
- [12] MURRAY, J. (1981) “The Mo-Ti (Molybdenum-Titanium) system,” *Bulletin of Alloy Phase Diagrams*, **2**(2), pp. 185–192.
 URL <http://dx.doi.org/10.1007/BF02881476>
- [13] ZHANG, Y., H. LIU, and Z. JIN (2001) “Thermodynamic assessment of the Nb-Ti system,” *Calphad-Computer Coupling of Phase Diagrams and Thermochemistry*, **25**(2), pp. 305–317.
- [14] KUMAR, K., P. WOLLANTS, and L. DELAEY (1994) “Thermodynamic calculation of Nb-Ti-V phase diagram,” *CALPHAD*, **18**(1), pp. 71–79.
- [15] MURRAY, J. L. (1987) “Phase diagrams of binary titanium alloys,” *ASM International, 1987*, p. 354.
- [16] KUMAR, K., P. WOLLANTS, and L. DELAEY (1994) “Thermodynamic assessment of the Ti-Zr system and calculation of the Nb-Ti-Zr phase-diagram,” *Journal of Alloys and Compounds*, **206**(1), pp. 121–127.
- [17] XIONG, W., Y. DU, Y. LIU, B. HUANG, H. XU, H. CHEN, and Z. PAN (2004) “Thermodynamic assessment of the Mo-Nb-Ta system,” *Calphad-Computer Coupling of Phase Diagrams and Thermochemistry*, **28**(2), pp. 133–140.
- [18] PEREZ, R. and B. SUNDMAN (2003) “Thermodynamic assessment of the Mo-Zr binary phase diagram,” *Calphad-Computer Coupling of Phase Diagrams and Thermochemistry*, **27**(3), pp. 253–262.
- [19] GUILLERMET, A. (1991) “Thermodynamic analysis of the stable phases in the Zr-Nb system and calculation of the phase-diagram,” *Zeitschrift Fur Metallkunde*, **82**(6), pp. 478–487.

- [20] ABRIATA, J. P. and J. C. BOLCICH (1982) “The Nb-Zr (Niobium-Zirconium) system,” *Bulletin of alloy phase diagrams*, **3**(1), pp. 34–44.
- [21] GUILLERMET, A. (1995) “Phase-diagram and thermochemical properties of the Zr-Ta system - an assessment based on Gibbs energy modeling,” *Journal of Alloys and Compounds*, **226**(1-2), pp. 174–184.
- [22] NIKITIN, P. and V. MIKHEYEV (1971) “Examination of titanium corner of Ti-Ta-Mo equilibrium diagram,” *Russian Metallurgy-Metally-USSR*, (1), pp. 144–147.
URL http://scholar.google.com/scholar?hl=en&q=ti-ta-mo+nikitin&btnG=&as_&sdt=1%2C39&as_&sdtpp=%#
- [23] KAR, S. and D. LIPKIN (2008) “A CALPHAD-based phase equilibrium model of Mo-Ti-Zr-C,” in *TMS 2008 Annual Meeting Supplemental Proceedings, Vol 2: Materials Characterization, Computation and Modeling*, Minerals, Metals & Materials Soc, Warrendale, pp. 237–243.
- [24] PROKOSHKIN, D. A. and M. I. ZAKHAROVA (1967) “Phase equilibrium in the molybdenum-titanium-zirconium system(Ternary phase diagram of Mo-Ti-Zr system from eleven isothermal cross sections),” in *AKADEMIIA NAUK SSSR, DOKLADY*, vol. 172, pp. 1382–1384.
- [25] NA, L. and W. WARNE (2001) “Estimation of the Nb-Ti-Ta phase diagram,” *Ieee Transactions on Applied Superconductivity*, **11**(1), pp. 3800–3803.
- [26] TOKUNAGA, T., S. MATSUMOTO, H. OHTANI, and M. HASEBE (2007) “Thermodynamic calculation of phase equilibria in the Nb-Ni-Ti-Zr quaternary system,” *Materials transactions*, **48**(2), pp. 89–96.
- [27] LIN, L., L. DELAEY, O. VANDERBIEST, and P. WOLLANTS (1996) “Calculation of isothermal sections of three ternary Ti-Zr-X systems,” *Scripta Materialia*, **34**(9), pp. 1411–1416.
- [28] HOCH, M. and D. BUTRYMOW (1964) “System tantalum-titanium-zirconium-oxygen at 1500 degrees C,” *Transactions of the Metallurgical Society of AIME*, **230**(1), pp. 186–192.
- [29] TAIOLI, S., C. CAZORLA, M. J. GILLAN, and D. ALFÈ (2007) “Melting curve of tantalum from first principles,” *Physical Review B*, **75**(21), p. 214103.
- [30] OLIJNYK, H. (1992) “Pressure dependence of Raman phonons of metallic β -Sn,” *Physical Review B*, **46**(10).
- [31] DINSDALE, A. (1991) “SGTE Data for Pure Elements,” *CALPHAD*, **15**(4), pp. 317–425.

- [32] ZHANG, W.-D., Y. LIU, H. WU, M. SONG, T.-Y. ZHANG, X.-D. LAN, and T.-H. YAO (2015) “Elastic modulus of phases in Ti_xMo alloys,” *Materials Characterization*, **106**, pp. 302–307.
- [33] BOYER, R., G. WELSCH, and E. COLLINGS (1994) “Materials Properties Handbook: Titanium Alloys,” *ASM International, Materials Park, OH*.
- [34] SUNG, B.-S., T.-E. PARK, and Y.-H. YUN (2015) “Microstructures and electrochemical behavior of Ti-Mo alloys for biomaterials,” *Advances in Materials Science and Engineering*, **2015**(Article ID 872730), pp. 1–7.
- [35] TANE, M., S. AKITA, T. NAKANO, K. HAGIHARA, Y. UMAKOSHI, M. NIINOMI, H. MORI, and H. NAKAJIMA (2010) “Low Young’s modulus of Ti_xNb_yTa_zZr alloys caused by softening in shear moduli c₄₄ and c₄₄ near lower limit of body-centered cubic phase stability,” *Acta Materialia*, **58**(20), pp. 6790–6798.
- [36] GEETHA, M., A. SINGH, R. ASOKAMANI, and A. GOGIA (2009) “Ti based biomaterials, the ultimate choice for orthopaedic implants – A review,” *Progress in Materials Science*, **54**(3), pp. 397–425.
- [37] MOHAMMED, M., Z. KHAN, and A. SIDDIQUEE (2014) “Beta titanium alloys: the lowest elastic modulus for biomedical applications: a review,” *International Journal of Chemical, Molecular, Nuclear, Materials and Metallurgical Engineering*, **8**(8), pp. 788–793.
- [38] NIINOMI, M., M. NAKAI, and J. HIEDA (2012) “Development of new metallic alloys for biomedical applications,” *Acta Biomaterialia*, **8**(11), pp. 3888–3903.
- [39] NOZOE, F., H. MATSUMOTO, T. K. JUNG, S. WATANABE, T. SABURI, and S. HANADA (2007) “Effect of Low Temperature Aging on Superelastic Behavior in Biocompatible. BETA. TiNbSn Alloy,” *Materials transactions*, **48**(11), pp. 3007–3013.
- [40] OTIS, R. and Z.-K. LIU (2017) “pycalphad: CALPHAD-based Computational Thermodynamics in Python,” *Journal of Open Research Software*, **5**(1).
- [41] LONG, M. and H. RACK (1998) “Titanium alloys in total joint replacement materials science perspective,” *Biomaterials*, **19**(18), pp. 1621–1639.
- [42] KURTZ, S. (2007) “Projections of primary and revision hip and knee arthroplasty in the United States from 2005 to 2030,” *The Journal of Bone and Joint Surgery (American)*, **89**(4), pp. 780–785.

- [43] KRISHNA, B., S. BOSE, and A. BANDYOPADHYAY (2007) “Low stiffness porous Ti structures for load-bearing implants,” *Acta biomaterialia*, **3**(6), pp. 997–1006.
- [44] NIINOMI, M. (2003) “Recent research and development in titanium alloys for biomedical applications and healthcare goods,” *Science and Technology of Advanced Materials*, **4**(5), pp. 445–454.
- [45] ITO, A., Y. OKAZAKI, T. TATEISHI, and Y. ITO (1995) “In vitro biocompatibility, mechanical properties, and corrosion resistance of Ti-Zr-Nb-Ta-Pd and Ti-Sn-Nb-Ta-Pd alloys,” *Journal of Biomedical Materials Research*, **29**(7), pp. 893–899.
- [46] MEI, Z. G. (2011) *First-principles Thermodynamics of Phase Transition: from Metal to Oxide*, Ph.D. thesis.
- [47] BRAILOVSKI, V., S. PROKOSHIN, M. GAUTHIER, K. INAEKYAN, S. DUBINSKIY, M. PETRZHIK, and M. FILONOV (2011) “Bulk and porous metastable beta $Ti_{x}Nb_{y}Zr$ (Ta) alloys for biomedical applications,” *Materials Science and Engineering: C*, **31**(3), pp. 643–657.
- [48] TANE, M., S. AKITA, T. NAKANO, K. HAGIHARA, Y. UMAKOSHI, M. NIINOMI, and H. NAKAJIMA (2008) “Peculiar elastic behavior of $Ti_{x}Nb_{y}Zr$ single crystals,” *Acta Materialia*, **56**(12), pp. 2856–2863.
- [49] KHACHATURIAN, A. (1985) “Theory of structural transformations in solids. 1983,” *Wiley, New York, Jacobs AE, Phys. Rev. B*, **31**, p. 5984.
- [50] SALJE, E. (1990) “Phase transitions in ferroelastic and co-elastic crystals,” *Ferroelectrics*, **104**(1), pp. 111–120.
- [51] HOHENBERG, P. and W. KOHN (1964) “Inhomogeneous Electron Gas,” *Physical Review*, **136**(3B), pp. B864–B871.
URL <http://link.aps.org/doi/10.1103/PhysRev.136.B864>
- [52] KOHN, W. and L. SHAM (1965) “Self-Consistent Equations Including Exchange and Correlation Effects,” *Phys. Rev.*, **140**, pp. 1133–1138.
- [53] PERDEW, J. and Y. WANG (1992) “Accurate and simple analytic representation of the electron-gas correlation energy,” *Physical Review B*, **45**(23), p. 13244.
- [54] PERDEW, J., K. BURKE, and M. ERNZERHOF (1996) “Generalized gradient approximation made simple,” *Physical Review Letters*, **77**(18), pp. 3865–3868.
- [55] CEPERLEY, D. M. and B. J. ALDER (1980) “Ground state of the electron gas by a stochastic method,” *Physical Review Letters*, **45**(7), p. 566.

- [56] SHANG, S., Y. WANG, D. KIM, and Z.-K. LIU (2010) “First-principles thermodynamics from phonon and Debye model: Application to Ni and Ni₃Al,” *Computational Materials Science*, **47**(4), pp. 1040–1048.
- [57] KRESSE, G. and J. FURTHMÜLLER (1996) “Efficiency of ab-initio total energy calculations for metals and semiconductors using a plane-wave basis set,” *Computational Materials Science*, **6**(1), pp. 15–50.
- [58] KRESSE, G. and D. JOUBERT (1999) “From ultrasoft pseudopotentials to the projector augmented-wave method,” *Physical Review B*, **59**(3), pp. 1758–1775.
- [59] WANG, A., S. SHANG, D. ZHAO, J. WANG, L. CHEN, Y. DU, Z.-K. LIU, T. XU, and S. WANG (2012) “Structural, phonon and thermodynamic properties of fcc-based metal nitrides from first-principles calculations,” *Calphad*, **37**, pp. 126–131.
- [60] MORUZZI, V. L., J. F. JANAK, and K. SCHWARZ (1988) “Calculated thermal properties of metals,” *Physical Review B*, **37**(2), pp. 790–799.
- [61] LIU, X. L., B. K. VANLEEUWEN, S. SHANG, Y. DU, and Z.-K. LIU (2015) “On the scaling factor in Debye–Grüneisen model: A case study of the Mg–Zn binary system,” *Computational Materials Science*, **98**, pp. 34–41.
- [62] WANG, Y., Z.-K. LIU, and L.-Q. CHEN (2004) “Thermodynamic properties of Al, Ni, NiAl, and Ni₃Al from first-principles calculations,” *Acta Materialia*, **52**(9), pp. 2665–2671.
- [63] SHANG, S., Y. WANG, and Z.-K. LIU (2007) “First-principles elastic constants of alpha- and theta-Al₂O₃,” *Applied Physics Letters*, **90**(10), pp. 101909–1–101909–3.
- [64] SIMMONS, G. and H. WANG (1971) *Single Crystal Elastic Constants and Calculated Aggregate Properties: A Handbook*, M.I.T. Press, Cambridge.
- [65] ZUO, Y. and Y. CHANG (1993) “Thermodynamic calculation of the Mg–Cu phase diagram,” *Zeitschrift für Metallkunde*, **84**(10), pp. 662–667.
- [66] CHUNG, D. H. and W. R. BUESSEM (1967) “The Voigt–Reuss–Hill Approximation and Elastic Moduli of Polycrystalline MgO, CaF₂, β-ZnS, ZnSe, and CdTe,” *Journal of Applied Physics*, **38**(6), pp. 2535–2540.
- [67] BORN, M. and K. HUANG (1998) *Dynamical Theory of Crystal Lattices*, Oxford University Press.
- [68] NYE, J. (1985) *Physical Properties of Crystals: Their Representation by Tensors and Matrices*, Oxford University Press.

- [69] JIANG, C., C. WOLVERTON, J. SOFO, L.-Q. CHEN, and Z.-K. LIU (2004) “First-principles study of binary bcc alloys using special quasirandom structures,” *Physical Review B*, **69**(21), pp. 214202–1–214202–10.
- [70] JIANG, C. (2009) “First-principles study of ternary bcc alloys using special quasi-random structures,” *Acta Materialia*, **57**(16), pp. 4716–4726.
- [71] LIU, Z. K. and Y. WANG (2016) *Computational Thermodynamics of Materials*, Cambridge University Press.
- [72] ANDERSSON, J.-O., T. HELANDER, L. HÖGLUND, P. SHI, and B. SUNDMAN (2002) “Thermo-Calc & DICTRA, computational tools for materials science,” *Calphad*, **26**(2), pp. 273–312.
- [73] REDLICH, O. and A. T. KISTER (1948) “Algebraic representation of thermodynamic properties and the classification of solutions,” *Industrial & Engineering Chemistry*, **40**(2), pp. 345–348.
- [74] ZACHERL, C., S. SHANG, A. SAENGDEEJING, and Z.-K. LIU (2012) “Phase stability and thermodynamic modeling of the Re–Ti system supplemented by first-principles calculations,” *Calphad*, **38**, pp. 71–80.
URL <http://www.sciencedirect.com/science/article/pii/S0364591612000442>
- [75] SHANG, S., J. SAAL, Z. MEI, Y. WANG, and Z.-K. LIU (2010) “Magnetic thermodynamics of fcc Ni from first-principles partition function approach,” *Journal of Applied Physics*, **108**(12), p. 123514.
- [76] YOUNG, R. and A. LARSON (1998) “Rietveld analysis of X-ray and neutron powder diffraction patterns,” *Atlanta (GA): School of*.
URL <http://debian.ccp14.ac.uk/ccp/web-mirrors/dbws/downloads/young/guide99.pdf>
- [77] TORAYA, H. (1986) “Whole-Powder-Pattern Fitting Without Reference to a Structural Model: Application to X-ray Powder Diffractometer Data,” *J. Appl. Cryst.*, **19**, pp. 440–447.
- [78] MANLEY, M. E. (2001) *From elementary excitations to microstructures: The thermodynamics of metals and alloys across length scales*.
- [79] BLÖCHL, P. (1994) “Projector augmented-wave method,” *Physical Review B*, **50**(24), p. 17953.
- [80] MONKHORST, H. and J. PACK (1976) “Special points for Brillouin-zone integrations,” *Physical Review B*, **13**(12), pp. 5188–5192.

- [81] PREDEL, B. (1997) “Mo-Ti (Molybdenum-Titanium) BT - Li-Mg - Nd-Zr,” Springer Berlin Heidelberg, Berlin, Heidelberg, pp. 1–3.
URL http://dx.doi.org/10.1007/10522884{_}2106
- [82] HOFFMAN, J. R., E. RUDY, S. T. WINDISCH, and A. J. STOSICK (1967) “The constitution of binary molybdenum-carbon alloys(Binary molybdenum-carbon system investigated using X-ray, metallographic, thermoanalytical and melting-point techniques),” *AIME, TRANSACTIONS*, **239**, pp. 1247–1267.
- [83] ENGLISH, J. (1961) *Binary and Ternary Phase Diagrams of Columbium, Molybdenum, Tantalum, and Tungsten, Tech. rep.*
- [84] SHANG, S., A. SAENGDEEJING, Z. MEI, D. KIM, H. ZHANG, S. GANE-SHAN, Y. WANG, and Z.-K. LIU (2010) “First-principles calculations of pure elements: Equations of state and elastic stiffness constants,” *Computational Materials Science*, **48**(4), pp. 813–826.
- [85] WOLFRAM RESEARCH, I., “Matematica,” .
- [86] DICKINSON, J. and P. ARMSTRONG (1967) “Temperature dependence of the elastic constants of molybdenum,” *Journal of Applied Physics*, **38**(2), pp. 602–606.
- [87] BOLEF, D. (1961) “Elastic constants of single crystals of the bcc transition elements V, Nb, and Ta,” *Journal of Applied Physics*, **32**(1), pp. 100–105.
- [88] TRECO, R. M. (1953) “Effect of small additions of oxygen on lattice constants and hardness of zirconium,” *Transactions of the American Institute of Mining, Metallurgical and Petroleum Engineers*, **197**, pp. 344–348.
- [89] BERGERHOFF, G., R. HUNDT, R. SIEVERS, and I. D. BROWN (1983) “The inorganic crystal structure data base,” *Journal of Chemical Information and Computer Sciences*, **23**(2), pp. 66–69.
URL <http://pubs.acs.org/doi/abs/10.1021/ci00038a003>
- [90] KARLSRUHE, F. I. Z., “Inorganic Crystal Structure Database,” .
URL <http://icsd.fiz-karlsruhe.de>
- [91] “Materials Project,” .
URL <http://www.materialsproject.org>
- [92] KURODA, D., M. NIINOMI, M. MORINAGA, Y. KATO, and T. YASHIRO (1998) “Design and mechanical properties of new β type titanium alloys for implant materials,” *Materials Science and Engineering: A*, **243**(1), pp. 244–249.

- [93] HE, G. and M. HAGIWARA (2004) “Ti-Cu-Ni (Fe, Cr, Co)-Sn-Ta (Nb) alloys with potential for biomedical applications,” *Materials Transactions*, **45**(4), pp. 1120–1123.
- [94] ——— (2006) “Ti alloy design strategy for biomedical applications,” *Materials Science and Engineering: C*, **26**(1), pp. 14–19.
- [95] LIU, Z.-K. (2009) “First-Principles Calculations and CALPHAD Modeling of Thermodynamics,” *Journal of Phase Equilibria and Diffusion*, **30**(5), pp. 517–534.
- [96] OKAMOTO, H. (2003) “Sn-Ta (Tin-Tantalum),” *Journal of Phase Equilibria*, **24**(5), p. 484.
- [97] STUDNITZKY, T. and R. SCHMID-FETZER (2002) “Phase Formation and reaction Kinetics in M-Sn systems (M=Zr, Hf, Nb, Ta, Mo),” *Zeitschrift Fur Metallkunde*, **93**(9), pp. 894–903.
- [98] BASILE, F. (1971) “Cristallographic study and supraconductive properties of compounds V₃Sn and Ta₂Sn₃,” in *Annales de chimie*, vol. 6, pp. 241–244.
- [99] YUE, Q., Y. LIU, M. CHU, and J. SHEN (2009) “Thermodynamic modeling of the Sn–V binary system,” *Calphad*, **33**(3), pp. 539–544.
- [100] TOFFOLON, C., C. SERVANT, and B. SUNDMAN (1998) “Thermodynamic assessment of the Nb-Sn system,” *Journal of Phase Equilibria*, **19**(5), pp. 479–485.
- [101] TOFFOLON, C., C. SERVANT, J. GACHON, and B. SUNDMAN (2002) “Re-assessment of the Nb-Sn system,” *Journal of Phase Equilibria*, **23**(2), pp. 134–139.
- [102] COURTNEY, T., G. PEARSALL, and J. WULFF (1965) “Effect of Processing History on the Superconducting Properties and LongâĂŖRange Order of Ta₃Sn,” *Journal of Applied Physics*, **36**(10), pp. 3256–3260.
- [103] PREDMORE, R. and R. ARSENAULT (1970) “Short range order of Ta-Mo B.C.C. alloys,” *Scripta Metallurgica*, **4**(3), pp. 213–217.
- [104] ALLEN, W. and J. PEREPEZKO (1991) “Solidification of undercooled Sn-Sb peritectic alloys: Part I. Microstructural evolution,” *Metallurgical Transactions A*, **22**(3), pp. 753–764.
- [105] ARROYAVE, R. and Z.-K. LIU (2006) “Intermetallics in the Mg-Ca-Sn ternary system: Structural, vibrational, and thermodynamic properties from first principles,” *Physical Review B*, **74**(17), p. 174118.

- [106] CALVERT, L. and P. VILLARS (1991) "Pearson's Handbook of Crystallographic Data for Intermetallic Phases," *ASM, Materials Park, OH*.
- [107] PELTZER Y BLANCÁ, E. L., A. SVANE, N. E. CHRISTENSEN, C. O. RODRÍGUEZ, O. M. CAPPANNINI, and M. S. MORENO (1993) "Calculated static and dynamic properties of β -Sn and Sn-O compounds," *Physical Review B*, **48**(21), pp. 15712–15718.
- [108] JOUAULT, F. and P. LECOCQ (1967) "Etude comparee des trois diagrammes V-Sn, Nb-Sn, Ta-Sn," *Colloques Internationaux du Centre National de la Recherche Scientifique*, **157**, pp. 229–235.
- [109] GELLER, S., B. T. MATTHIAS, and R. GOLDSTEIN (1955) "Some new intermetallic compounds with the beta.-wolfram structure," *Journal of the American Chemical Society*, **77**, pp. 1502–1504.
- [110] WANG, Y., S. CURTAROLO, C. JIANG, R. ARROYAVE, T. WANG, G. CEDER, L.-Q. CHEN, and Z.-K. LIU (2004) "Ab initio lattice stability in comparison with CALPHAD lattice stability," *Calphad*, **28**(1), pp. 79–90.
- [111] ARROYAVE, R. and Z.-K. LIU (2006) "Thermodynamic modelling of the Zn–Zr system," *Calphad*, **30**(1), pp. 1–13.

Vita
Cassie Marker

The details of my childhood are inconsequential.